University of Alberta

Utilization of Semiconductors Piezoresistive Properties in Mechanical Strain Measurements under Varying Temperature Conditions for Structural Health Monitoring Applications

by

Ahmed Ahmed Shehata Mohammed

A thesis submitted to the Faculty of Graduate Studies and Research
in partial fulfillment of the requirements for the degree of

Doctor of Philosophy

Mechanical Engineering Department

Dedication

To my parents, my grandmother, and my family... the persons who sacrificed themselves infinitely for the sake of my success, I dedicate this work ... with my deep love and gratitude.

Abstract

Strain gauges have been powerful tools in experimental stress analysis. This importance is expected to continue, even though other means of strain measurement are continually introduced to the market. The strain gauge is a simple device that can be easily installed to measure mechanical strain. By far, the one-dimensional single-filament has been the most common strain gauge. Conventional strain gauges are typically made from thin-foil metal; thus the resistivity change under stress is insignificant. On the other hand, semiconductor material demonstrated considerable resistivity change as a result of the applied mechanical strain or stress.

In this work, the piezoresistive characteristics of silicon crystal are investigated to realize a robust Micro Electro Mechanical (MEMS) strain sensor. This sensor has been developed to withstand harsh environmental conditions, such as those in Structural Health Monitoring (SHM) applications. Silicon strain gauges have demonstrated higher gauge factor, sensitivity, and accuracy compared to conventional thin-foil strain gauges. Unfortunately, silicon strain gauges suffer from large temperature effect, which influences their performance dramatically. This temperature effect puts various challenges on the development and application of semiconductor sensors. On top of these challenges are the temperature compensation of the output signal, packaging, and fabrication. In addition, transferring strain through different structural layers causes substantial loss in the sensed strain values.

Piezoresistivity theory is presented and applied to develop a new MEMS strain sensor. Taking into account all geometric and material characteristics, various tools and techniques, such as indicial equations, Finite Element Modeling (FEM) (ANSYS10.0®), and experimental evaluation, were employed to go through the development cycle of the piezoresistive strain sensor. In addition, alignment errors during microfabrication have been investigated. The proper microfabrication parameters and piezoresistors configuration were selected by investigating the silicon crystal material properties based on the crystallographic

directions. A microfabrication process flow has been developed exploring a group of fabrication processes available at the University of Alberta micromachining and nanofabrication facility (NanoFab).

In order to minimize the loss in the transferred strain, geometric features were created in the silicon substrate. These geometric features have resulted in stress discontinuity in their vicinity, which introduced the concept of geometrical gauge factor. The geometrical gauge factor is a new concept that can 'virtually' improve the performance of any piezoresistive sensor by utilizing the silicon carrier to increase the differential stress around the piezoresistive sensing elements. The main limitation to use this concept is whether or not material properties will accommodate the resulted stress concentration without failing the sensor.

The developed sensor was evaluated, tested, and characterized at the University of Alberta and Syncrude Canada Edmonton Development Research Center. Uniaxial tension was utilized to calibrate a number of chip designs. The temperature coefficient of resistance (TCR) was also evaluated. Preliminary packaging procedure was proposed and applied. Comparing the performance characteristics of the developed MEMS strain sensor to a 350Ω thin-foil strain gauge showed that the piezoresistive MEMS strain sensor had better performance characteristics: sensitivity and resolution, with room for significant improvements. In addition, the MEMS strain sensor can be successfully applied under varying temperature conditions.

The solution of the above challenges and the small size of MEMS sensors have resulted in a novel MEMS-based strain sensor with low power consumption, compared to conventional strain gauges. This low power consumption promotes this sensor in wireless SHM systems as the sensing unit, which can extend such technology to wider range of applications. The MEMS strain sensor has potential to provide a valuable tool to improve the current SHM systems as well as allowing higher number of sensors to be economically deployed. As a result, the reliability of both the SHM system and equipment will be enhanced, which will reflect positively on the economic performance of the equipment.

Acknowledgments

Table of Contents

List of Tables

List of Illustrations

Chapter 1 – Introduction

This chapter discusses Structural Health Monitoring (SHM) as an important field of applied research and various sensors used in SHM. It also provides the motivation and significance of the current study, which is reflected in research objectives and contributions. The last section of this chapter describes the organization of the thesis.

1.1.   Structural Health Monitoring

Structural Health Monitoring (SHM) is defined as the diagnostic monitoring of integrity or condition of a structure. SHM of engineering structures is an important field of research. Measurements from SHM systems provide valuable input in maintenance planning. Traditionally, wired systems are deployed in SHM applications. Conventional wired sensors have many advantages, such as ease of data transmission, low sensor cost and availability of various sensor choices. However, to instrument large structures such as bridges, huge amounts of wires and large number of sensors are required, which may affect reliability of data transmission and increase the maintenance requirements of SHM systems. In addition, the cost of complete wired monitoring systems tends to limit the number of sensing nodes that can be economically installed on large structures. Finally, there might be cases in which wires can not be used, for example in the case of moving and rotating equipment. Fortunately, with the development of wireless communication and Micro Electro Mechanical Systems (MEMS), wireless sensing platforms have been developed rapidly, and used gradually to construct Wireless Sensors Networks (WSNs) in SHM applications [1-4]. Using Complementary Metal Oxide Semiconductor (CMOS) enables implementation of true single chip solutions called System-on-Chip (SoC).

1.2.   Sensors in Structural Health Monitoring

Strain and vibration sensors are the most common types of sensors used in SHM [2, 5, 9-13]. Strain, normalized deformation, is one of the most fundamental engineering quantities. Various structural variables can be determined from mechanical strain measurements. Conventionally, strain sensors found applications not only in the most sophisticated structures but also in very common and simple applications. Therefore, it is not surprising that strain sensors have been extensively studied. Recoded strain measurements allow load history data to be logged. Unexpected changes in strain values can indicate the presence of, or be used to predict, structural damage. For this reason, strain sensing is a central feature in SHM sensor research [14].

Several sensing principles have been researched to develop strain sensing devices including the modulation of optical [15-19], capacitive [9, 20, 21], piezoelectric [4, 22], frequency shift [23-25] and piezoresistive properties [11, 12, 24, 26-38]. Optical sensors face significant challenge to achieve the required accuracy of light intensity modulation. In addition, the signal temperature drift places huge burden on the conditioning circuitry and electronics. Moreover, optical fibers are susceptible to damage. As a result, higher number of fiber redundancies is required, which reflects on the cost per sensing node.

Capacitive sensors require high input power to reach the required sensitivity. Moreover, they have limited measurement range compared to piezoresistive and piezoelectric sensors [39]. Response of piezoelectric sensors, on the other hand, is highly dependent on temperature. In addition, piezoelectric sensors are not compatible with microelectronics integration processes. More important, they are still immature in their fabrication technology to reach the required signal stability. MEMS resonant strain sensors [23, 24] have been demonstrated to achieve high performance by converting input strain to shift in the device resonant frequency, but due to the high structural coupling coefficients, they require high operating voltage to overcome the energy loss in the sensor structural supports. Therefore, they are undesirable for low-voltage and low-power integrated systems.

Piezoresistive strain sensors based on MEMS technology, on the other hand, are more favorable and attractive than piezoelectric, capacitive, optical fiber sensors due to a number of key advantages such as high sensitivity [26], low noise [27], low cost and the ability to have conditioning electronic circuits further away from the sensor or on the same sensing board. Moreover, they have high potential for monolithic integration with low-power CMOS electronics. Finally, piezoresistive strain sensors need less complicated conditioning compared to piezoelectric, capacitive, optical fiber sensors circuit [40].

Due to their superior performance characteristics over thin-foil metal gauges, semiconductors strain sensors have received extensive research efforts to realize different piezoresistive strain and stress sensing devices [28, 32, 33, 38, 41-56]. Unfortunately, experimental and analytical results indicated the high dependence of the piezoresistive properties of the doped silicon on operating temperature [34, 36, 54, 57-66]. The temperature dependence can be related to two sources; temperature coefficient of resistance (TCR) and temperature coefficient of gauge factor (TCGF). Many researchers focused their efforts to overcome the dependence of piezoresistive sensors on temperature, which made the development of piezoresistive semiconductors' strain or stress sensor more appealing [67].

1.3. Motivation and Significance of the Current Study

The mechanical properties of silicon have been studied over the last few decades. The results of these studies demonstrated silicon as the material of choice to fabricate high performance strain sensors using surface micromachining [68]. MEMS technology borrows a significant amount of knowledge from Integrated Circuit (IC) technology. The three main sensing phenomena that are commonly used to develop MEMS devices are piezoresistive, piezoelectric and capacitive. Table 1 compares between these three major sensing principles based on certain characteristics. A numeric value is given to compare between the three sensing principles, which is called performance index. For example, it is better to have wide measurement range. Therefore, piezoresistive and piezoelectric sensors have

performance indices of 3. On the other hand, because sensing range of capacitive sensors is limited by the size of the sensing electrodes, a performance index of 1 was assigned. The individual performance indices were summed to provide a relative measure that can help to justify selection of piezoresistive phenomenon over piezoelectric and capacitive. In the decision matrix, the sensing characteristics were assumed to have the same weight (importance). If certain characteristics are more important of critical to the application, weighing factors can be used to reflec the relative importance. Figure 1 presents summary results drawn from the decision matrix shown in Table 1. From this figure, it is clear that piezoresistive sensing has the best performance characteristics. It is worth to mention that depending on the research advancements the decision matrix in Table 1, and hence Figure 1, may be changed to give different output.

Regardless of the extensive research efforts, the problem of thermal errors during calibration and measurement still limits the development of piezoresistive sensors. This problem appears to be very serious when performing measurements over wide temperature range. It was reported in some cases that piezoresistive semiconductor sensors have higher sensitivity to temperature than the intended measurand [35, 36, 63, 69]. Thus, the application of silicon piezoresistive sensors under varying temperature conditions was limited and, therefore, silicon piezoresistive stress/strain sensors have found their applications over a very narrow temperature range and sometimes at constant temperature, such as in medical applications. Moreover, most of the piezoresistive MEMS stress sensors were especially developed to monitor stresses in electronics packages. Therefore, it is important to investigate a feasible methodology to reduce temperature dependence of the piezoresistive properties while maintaining reasonable strain sensitivity.

Various researchers [59-63, 70, 71] reported on the possibility of utilizing high doping concentration to develop piezoresistive sensing elements with improved temperature dependence. Unfortunately, there is no application along the line of this idea. One main reason for that is the improvement in signal stability comes at

the expense of the sensor sensitivity. For example, by using doping concentration of 10^{20} atoms/cm^3 instead of 10^{17} atoms/cm^3, 70%-80% of the sensing sensitivity is lost . Therefore, if high doping concentrations are to be used in the microfabrication process, then special considerations have to be taken into account to recover part of the sensitivity loss.

Table 1 Decision matrix to compare between the characteristics of piezoresistive, piezoelectric and capacitive sensing phenomena using performance index

Sensing Phenomena / Characteristics	Piezoresistive	Piezoelectric	Capacitive
Measuring range	Wide (3)	Wide (3)	Limited (1)
Sensitivity	High (3)	Medium (3)	Low (3)
Temperature dependence	High (1)	High (1)	Low (3)
Conditioning circuitry	Simple (3)	Complex (1)	Complex (1)
Consumed power	Low (3)	Low (3)	High (1)
Output signal strength	High (3)	High (3)	Low (3)
Signal stability	Stable (3)	Unstable (1)	Stable (3)
Out of plane Accuracy	Low (3)	Low (3)	High (1)
Microfabrication	Well developed (3)	Undeveloped (1)	Developed (2)
Total merit index	**25**	**19**	**18**
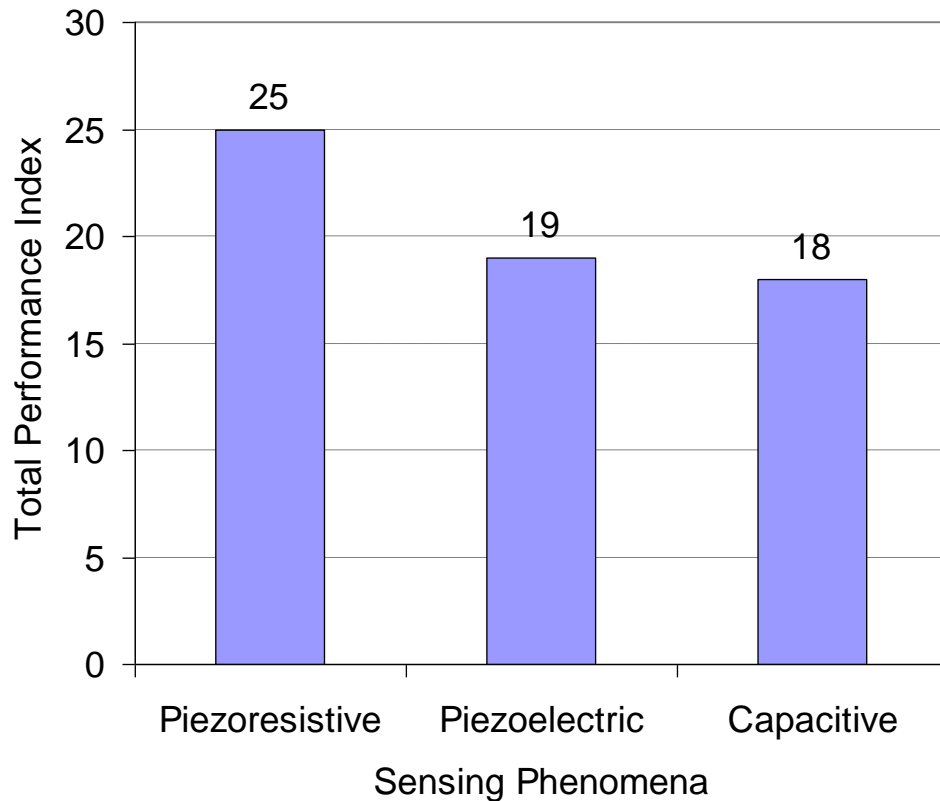
Figure 1 Graphical representation of the decision matrix results

The limited application of the piezoresistive effect in developing sensors that can work over wide temperature range initiated this study. In addition, the high potential of improving the piezoresistive properties by utilizing ion implantation process provided the feasibility. Further, the limited published literature on results from ion implantation studies provided another motivation. The results of this work document the piezoresistive behavior of semiconductor elements (single crystal silicon) over a wide temperature range, from -50°C to +50°C. This range is typical for SHM applications. Moreover, in this study a strain-based representation of the piezoresistive theory is provided. Finally, the research findings are directed to guide the development methodology of MEMS-based piezoresistive sensors.

1.4.   Research Objectives

The general goal of this research effort is to explore the opportunity of improving silicon thermal piezoresistive properties while maintaining acceptable level of mechanical strain sensitivity. The primary focus of the research work is to develop a piezoresistive strain sensor utilizing the results achieved in the general goal. The temperature range of interest in this study is from -50$^{\text{o}}$C to +50$^{\text{o}}$C. Therefore, to reach these goals the piezoresistive properties of doped single crystal silicon to measure surface mechanical strain over temperature range from -50$^{\text{o}}$C to +50$^{\text{o}}$C have been investigated. One proposed method of achieving this goal is to utilize the high doping concentration along with the silicon carrier geometry to alter the strain field around the piezoresistors' locations. Therefore, studying the piezoresistive properties of boron-implanted layers in silicon, especially the effect of using different implantation doses on the sensor performance was crucial. This goal is achieved through different studies. First, finite element method (FEM) is used to investigate the effect of utilizing full-microbridge configuration compared to a single piezoresistive element. Second, FEM is employed to study the effect of introducing geometric features, namely surface trenches, in the silicon carrier. Third, FEM is employed to perform sensitivity analysis of the sensing chip parameters. All of the simulated parameters using FEM were experimentally investigated through the evaluation of the different chip layouts.

1.5.   Thesis Organization

This thesis is organized into seven chapters. Chapter (1) discusses the need for reliable semiconductor strain sensing capabilities under varying temperature conditions. Moreover, it presents the different sensing phenomena showing their strengths and weaknesses. This chapter concludes that the piezoresistive effect has high potential to be employed in mechanical strain measurements under varying temperature environments, if thermal drift of the piezoresistive elements can be minimized. Finally, it summarizes research objectives and structure of the thesis. Chapter (2) introduces a comprehensive summary of the related literature

7

and the utilized methodologies in temperature compensation of piezoresistive devices. Chapter (3) presents the piezoresistive theory in two forms; stress-based and strain-based. Moreover, it forms the basis of modeling based on band structure of silicon. Chapter (4) provides details of the finite element studies to investigate the feasibility of the proposed approach. Chapter (5) describes the experimental procedure to perform the research work in this thesis. Chapter (6) presents, discusses and suggests explanations for the experimental results. Finally, Chapter (8) concludes the thesis and briefly outlines proposed future work.

Chapter 2 – Literature Review

This chapter summarizes research efforts in various fields related to the topic of this thesis. It starts by introducing reasons why Wireless Sensors Networks (WSNs) are needed in Structural Health Monitoring (SHM) and how MEMS devices can improve performance of WSNs. Piezoresistivity, as transduction technique, is also introduced. Then, a summary description of the piezoresistive effect in semiconductors is provided to give context for design aspects of piezoresistive devices. The effect of operating temperature on the performance of piezoresistive devices and various techniques to minimize, compensate, and/or eliminate such effect are also discussed. Other sensing phenomena are outside the scope of this chapter.

2.1. Need of WSNs and MEMS Sensors in Structural Health Monitoring

Traditional schemes of scheduling downtime for inspection or periodic evaluation of civil infrastructure cost millions of dollars in maintenance due to either downtime or lack of timely maintenance. This has resulted in the high need of the so-called condition-based maintenance (CBM). CBM requires SHM systems to transmit information related to key health indicators, such as vibration and strain values. CBM gradually replaces time-based management. A key benefit of real-time wireless sensors is allowing appropriate actions to be taken. Real-time SHM involves systematic, real-time sampling and analysis of signal, from onboard sensors to determine the condition of the structure. This can be used to carry out immediate repairs as well as to predict failures. One main problem limiting the applications of wireless SHM is the scarcity of power, especially in applications where wires can not be deployed, e.g. in rotating equipment.

The use of Wireless Sensor Networks (WSNs) in routine monitoring is becoming very common in a wide variety of fields [14, 72]. In a review of WSNs, Akyildiz et *al*. [14] summarized possible application fields including health, industry, military and environmental. In the past, inspections in these applications have

mainly been based on visual methods, with occasional employment of conventional non-destructive techniques. However, this methodology is time consuming, costly and does not necessarily provide quantitative measures of the structural damage and is not suitable for some applications. Therefore, permanently installed sensors are more favorable. For example, one of the approaches to detect cracks is to embed fiber-optic strain measuring sensors into structures [73, 74]. This approach, however, may cause reductions in static and fatigue strengths, as shown by Seo and Lee [75]. Moreover, it is a difficult method to adapt as a wireless sensor. Another work by Todoroki et $al.$ [76, 77] has proposed an electrical resistance change method of the fibers in composite material [77, 78], which does not require expensive instruments. This method avoids the previous problem discussed by Seo and Lee [75], and it can be used on existing structures. Although this method is efficient, the main issue was power consumption of conventional sensors.

The miniature size of micro MEMS sensors can potentially solve the power consumption problem. As described by Trimmer [79], small devices, such as sensors or actuators, consume less power compared to conventional full-size sensors. In addition, MEMS devices have other advantages such as survivability, high accuracy and high cost reduction, when produced on the batch production basis.

2.2. Piezoresistivity

Change in bulk resistivity of a solid material as a result of the application of mechanical strain is called elastoresistive effect. Alternatively, it is called piezoresistive effect when the change in resistivity is caused by the application of mechanical stress. Smith [71] was the first to quantitatively report the piezoresistive effect in semiconductors. In 1954, he noted that silicon and germanium have much larger piezoresistive effect compared to metals. In his work [71], Smith measured the three independent piezoresistive coefficients; π_{11}, π_{12} and π_{44}. Since then, extensive research efforts have been devoted to this subject for many reasons. First, the piezoresistive effect can be used as a powerful

tool to study the energy band structure and scattering mechanisms in semiconductors [71, 80-82], and hence material properties and behavior of semiconductors. Second, piezoresistive effect in semiconductors, especially silicon, has found a wide range of applications in numerous piezoresistive devices [24, 26-31, 38] to measure strain, pressure, force, torque, position, velocity, acceleration, temperature…etc. Additionally, this property is the main foundation to measure deformation of a sensing piezoresistive element material by monitoring the change in the gauge resistance.

Almost all materials have piezoresistive response but with different values. Doped silicon has been demonstrated as a common semiconductor material that exhibits strong piezoresistive effect [65, 71, 82, 86]. Piezoresistive effect in silicon has been traditionally modeled using stress-based formulae. In this case, the stress-strain relations and elastic material constants of silicon are not required. However, strain-based expressions possess advantages when measuring the interface strains. Although the stress components across the interface are different, the strain values at neighboring points in two materials are equal according to the compatibility relations. For strain-based theories, the stress-strain relations and the elastic material constants of silicon are always needed prior to both the application of sensors and calibration of the elastoresistive coefficients of the sensing piezoresistive elements. Moreover, the successful application of piezoresistive sensors requires accurate values of the piezoresistive coefficients of the sensing piezoresistors elements as well as the recognition of the potential sources of errors, which may affect the results during the calibration process [34, 36].

2.3. Physical Explanation of Piezoresistivity in Semiconductors

In metals, the change in the sensing element resistivity is mainly attributed to the geometrical effect. The volume (geometrical) changes affect the energy band gap between the valence and the conduction bands leading to a change in the number of carriers, and thus, change in electrical resistance. On the other hand, in semiconductors, in addition to the geometrical effect, the resistance change is caused by the change in specific resistivity originating from the strain or stress-

dependency of the resistivity. The effect of the specific resistivity was explained by the many-valley energy band gap model. The resistance change caused by specific resistivity effect is much higher than that caused by geometrical effect. The piezoresistive effect in silicon can be understood by examining the *E-k* band structure. Silicon has an indirect band gap. Conduction band minima are found in the six equivalent <100> directions. The valence band is centered at the origin and is composed from three bands: heavy hole, light hole and split-off. The resistivity of semiconductors is given by

$$\rho = \frac{1}{q\mu_n n + q\mu_p p} \tag{1}$$

where q is the charge of an electron, μ is the mobility of an electron or hole, and n and p are equilibrium concentrations of electrons and holes. For non-degenerate doping levels, carrier concentrations are given by

$$n = N_c e^{-\left(\frac{E_c - E_f}{k_B T}\right)}$$

$$\tag{2}$$

$$p = N_v e^{-\left(\frac{E_f - E_v}{k_B T}\right)}$$

where N_c and N_v, E_c and E_v, E_f, k_B, T are density of states in the conduction and valence bands, conduction band minima and valence band maxima energies, Fermi energy, Boltzmann's constant, and absolute temperature. The mobility can be related to effective mass (m^*) or *E-k* curvature by

$$\mu \propto \frac{1}{m^*} \propto \frac{\partial^2 E}{\partial k^2} \tag{3}$$

From the above equations, it can be seen that resistivity change is affected by either changing the shape of a band or by changing the energy level of a band.

12

2.3.1. Energy Band Structure

The experimental work of Smith [71] described the linear effect in silicon. Later, Herring and Vogt [80] used the many-valley carrier transport framework to explain Smith's data. When pure silicon forms into the diamond crystal structure, all four valence electrons covalently bond with neighboring silicon atoms. This crystal structure has a full valence band and an empty conduction band. These energy bands represent the energy levels in which electrons can reside. The energy band is, in a sense, a region of available energy positions for electrons in the crystalline solid. How easily electrons or holes can reach the conduction band is the key to determining the conductivity or resistivity of the material.

For semiconductors in general, a small energy gap, called the energy band gap, separates the conduction and valence energy bands. This band gap represents the energy required by the highest electron in the valence band to enter the empty conduction band. For insulators, the band gap is large, meaning that more external energy is required for electrons in the valence band to reach the conduction band and move throughout the solid. When the band gap is reduced or the energy level of the highest valence electron is increased, the conductivity of the crystal increases, since it becomes easier for electrons to conduct throughout the solid. Once the highest valence electron has received the necessary energy (E_g) to overcome the band gap, it will be able to move throughout the crystal structure. The movement of electrons throughout the crystal is what constitutes current flow through a material. Electrons moving through a crystal are called charge carriers, as they are the means of transporting charge throughout a solid. Holes are also charge carriers since they have a charge equal in magnitude but opposite in sign to the charge of an electron. Moreover, it can be transported throughout the crystalline lattice.
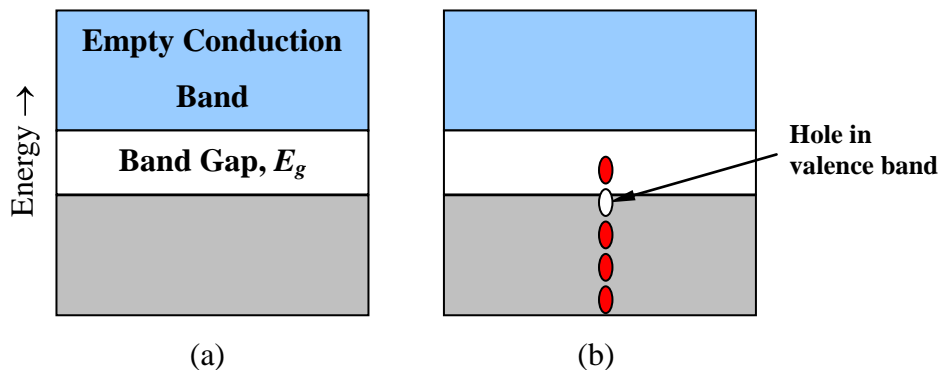
(a) (b)

13

2.3.2. Carrier Transport in Doped Silicon

The boron-doped (p-type) silicon is shown in Figure 3. In Figure 3.a, the impurity boron atoms, which has three valence electrons, bonds to the silicon crystal and contributes a hole to the lattice. When subjected to an external electric field, the hole is transferred to another crystal as it switches with the electron in that bond, as shown in Figure 3.b. The hole in motion becomes the charge carrier. In the presence of an electric field the holes located in p-type silicon will flow in a direction opposite to the electric field. The actual velocity of the hole, termed as the carrier drift velocity, does not follow a straight line but is scattered, since the carrier's motion is impeded and redirected as it collides with other barriers. The complex band structure of p-type silicon complicates the analysis of its piezoresistive behavior. Some physicists assign the piezoresistive behavior of p-type silicon to the separation of heavy and light hole valence bands [3].

The piezoresistive behavior of phosphorous doped (n-type) silicon, on the other hand, is attributed to the creation of an extra electron energy level near the top of the energy band gap. Electrons in this energy level are more easily excited into the conduction band under an applied stress or strain. The ability of a material to transport carriers (electrons or holes) in this manner is one way of describing the conductivity of the material. For a material to be highly conductive, therefore, it requires a high number of mobile charge carriers. The concentration of charge carriers in a material depends on the concentration of impurity atoms (dopant level) as well as the temperature. Similarly, the carrier drift velocity, as a function of the carrier mobility, is also affected by the dopant level and the magnitude of thermal vibrations (temperature).

The electrical conductivity, σ, of a material is a function of the number of charge carriers and their respective mobility. From this equation it is obvious that increasing the concentration of holes or electrons and/or increasing their respective mobility will increase the conductivity and decrease the resistivity of the material. However, it should be noted that carrier mobility is a function of carrier concentration and an increase in concentration does not directly result in an equivalent increase in conductivity.

(a)   (b)
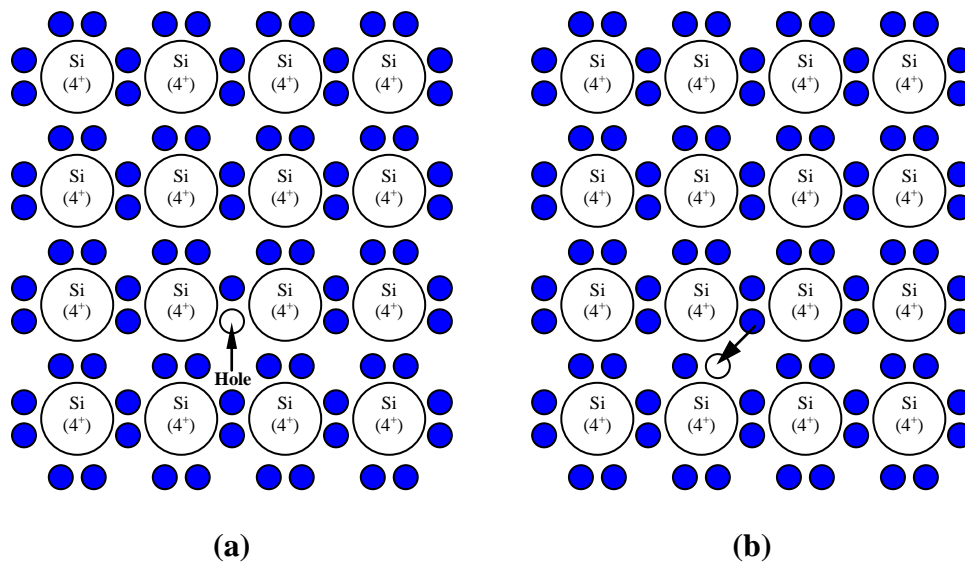
Figure 3 Hole transport of boron-doped (p-type) silicon due to external electric field (reproduced from ref. [87])

2.4. Review of Piezoresistive Effect in Semiconductors

The piezoresistive effect was first reported by Bridgman [88]. He observed that applying transverse and longitudinal stresses along certain crystals orientation changed their electrical resistance. Later, experimental measurements of the piezoresistive effect in semiconductors (silicon and germanium) were performed by other researchers [71, 89, 90]. The early theory of piezoresistivity for silicon and germanium was developed by Smith [71], who introduced the piezoresistive effect as a major sensing principle to develop mechanical sensors. Smith [71, 82]

described the physical background of the effect and experimentally measured the three independent piezoresistive on-axis coefficients; π_{11}, π_{12} and π_{44}. In 1961, Pfann and Thurston [51] derived the equivalent longitudinal and transverse piezoresistive coefficients for various orientations in cubic crystals such as silicon, as a function of the three independent piezoresistive coefficients. These formulations were later refined using tensor analysis by Mason and Thurston [48], Thurston [55], and Smith [82]. Since then, many researchers have studied the piezoresistive coefficients of silicon, both analytically and experimentally.

A detailed theory for silicon piezoresistive sensors was introduced by Bittle et al. [33]. Kang [38] explored piezoresistivity theory for silicon on various wafer planes. Based on the literature values of piezoresistive coefficients by Smith [71], Kanda [61] offered a graphical representation of the piezoresistance coefficients in silicon. In his work [61], Kanda plotted the theoretical longitudinal and transverse piezoresistance coefficients at room temperature as a function of the crystal orientation for (001), (110) and (211) crystallographic planes. Richter et al. [91] presented experimental results of the piezoresistive effect in p-type silicon. Richter et al. [91] measured longitudinal and transverse components for the [110] direction on the (001) silicon.

This early work, generally, ignored the effects of crystallographic misalignment and temperature-induced errors. Another effect that was not studied in this research is the nonlinearity of the piezoresistive effect. Jaeger and Suhling [34] showed that temperature variations and measurement errors play a vital role in the application results of piezoresistive sensors. They demonstrated the significance of thermally-induced errors in the calibration of silicon piezoresistive sensors. Moreover, they concluded that the temperature sensitivity of the piezoresistive elements can be more than one order of magnitude higher than their stress sensitivity. Matsuda [69] measured the nonlinearity in the piezoresistive effect for silicon and presented theoretical and experimental values of piezoresistive coefficients. Yamada et al. [92] addressed the nonlinearity of the piezoresistive effect based on the applied stress level.

The temperature dependence of the piezoresistance of high-purity silicon and germanium was described by Morin [63]. Tufte and Stelzer [65, 66] measured the temperature dependence of the large piezoresistive coefficients (π_{44} for p-type silicon and π_{11} for n-type silicon) as a function of impurity concentration. Suhling et al. [54] used piezoresistive sensors to investigate thermally-induced stresses. Lenkkeri [93] presented experimental values of the piezoresistance coefficients at $77^{o}K$ and $300^{o}K$. Jaeger et al. [35] presented experimental results for the piezoresistive coefficients of silicon, π_{44} and (π_{11}-π_{12}), as a function of temperature from $25^{o}C$ to $140^{o}C$. Using the off-axis direction of silicon, Lund [62] measured the piezoresistive coefficients in p-type silicon over temperature range from $5^{o}C$ to $140^{°}C$. Gniazdowski [94] measured the longitudinal and transverse components of the piezoresistive coefficient in p-type silicon along [110] orientation over the temperature range $25^{o}C$ to $105^{o}C$. Toriyama [56] derived an approximate piezoresistance equation for p-type silicon as a function of impurity concentration and temperature taking into account the spin-orbit interaction. Kozlovskiy [95] calculated the piezoresistive coefficients, π_{44} in p-type silicon and π_{11} in n-type silicon as a function of temperature for different impurity concentrations.

As can be noticed from the above paragraphs, piezoresistance, as a sensing phenomenon received significant research efforts over the last few decades. However, there has been limited application in mechanical strain measurements under varying temperature conditions. This limitation is attributed to the dependence of piezoresistive properties on temperature, which has been discussed by many researchers [56, 60-63, 65, 66, 70, 71, 91]. It is well reported [28, 34, 36-38, 45, 59-63, 65, 66, 69-71, 92, 93] that increasing doping level decreases the TCR and the TCGF of the piezoresistive elements. Nevertheless, this performance stability comes on the expense of the sensitivity of piezoresistive elements to stress or strain. Therefore, a new methodology to utilize high doping concentrations in mechanical strain measurements under varying temperature conditions was required. This methodology has to address the physical phenomenon and the effect of different parameters on the sensing mechanism.

17

Moreover, it has to provide a compensating method to account for the sensitivity loss.

Ion implantation has evolved as a microfabrication technique, which is used to develop piezoresistive elements. Ion implantation has the potential to control the piezoresistive properties more precisely compared to diffusion. Pisciotta and Gross [96] studied piezoresistive elements built by ion-implanted silicon. However, the published data from this work were obtained from a limited number of test samples and, hence, are incomplete. In this work, Pisciotta and Gross studied the effect of incomplete annealing on the temperature dependence of resistivity and gauge factor in aluminum and phosphorous implanted silicon-on-sapphire. They found that: (1) it is possible, for a given dose, to reduce the TCR at room temperature to substantially lower values by choosing a partial annealing temperature and, (2) there is no significant change in the magnitude and temperature dependence of the gauge factor for the partial annealing used.

2.5. Temperature Dependence of Piezoresistive Effect in Semiconductors

Semiconductor strain gauges used in sensing applications are almost never intrinsic, or purely made of one type of material such as Si or Ge. This is because the piezoresistive effect in intrinsic semiconductors is so susceptible to temperature change that it is very difficult to characterize them for strain measurements. Therefore, strain gauges are generally fabricated out of semiconductors in which certain impurities or carriers have been introduced in the crystalline structure.

The magnitude of TCR and TCGF are primarily determined by the doping concentrations of silicon. The most common method of reducing the temperature dependence of a piezoresistive device is by changing the impurity concentration. These efforts have been partially successful. Chu [67] concluded that the minimum value of TCR for p-type silicon occurs at impurity concentration of about 1.5×10^{19} cm^{-3}. Unfortunately, at this doping level, TCGF is still fairly high. The minimum TCGF values occur for p-type silicon at impurity concentration as

high as 10^{20} cm^{-3}. At this impurity concentration, the gauge factor is markedly reduced. From this discussion, it is clear that if the impurity concentration is varied, the TCR and the TCGF can be reduced to relatively small values, but not simultaneously, and that if a small TCGF is desired, the gauge factor must be sacrificed. Ion implantation appears to offer a more feasible solution to this problem as will be discussed in later sections.

2.6. Review of Temperature Compensation Techniques in Piezoresistive Devices

Different techniques have been suggested to overcome the problem of temperature dependence of piezoresistive properties [97-109]. For example, it was suggested to use two identical sensors. The first sensor is used to measure strain and the second sensor is used to compensate for the temperature effect. In this case, the first sensor is subjected to strain and temperature while the second sensor is subjected only to temperature. By subtracting the outputs of the two sensors, response to mechanical strain can be extracted. The applicability of this method is highly dependent on the microfabrication process, which can result in high variability in the material properties even within few millimeters on the same microfabricated silicon substrate. Another temperature compensation method is to use software to build a chart that accounts for the thermal effect at different temperatures. This technique is not successful due to the high nonlinearity of semiconductors thermal behavior. Moreover, this technique did not consider the applied stress/strain level, which has been proven to affect the sensor response [69, 92, 93, 110]. Other researchers used special circuitry to increase the input voltage based on the applied stress/strain level. This technique was partially successful, especially when using low to medium doping concentrations to build the piezoresistive elements. The last technique to improve the thermal behavior of doped silicon as strain sensing material is to increase the doping level during the development of the piezoresistive elements. Increasing doping concentration reduces the temperature dependence of silicon piezoresistive properties; however this leads to significant decrease in strain sensitivity [28, 60, 61, 63, 70, 71, 82,

19

86]. In this thesis, the last methodology, increasing doping level to reduce thermal behavior of piezoresistive properties, was adapted. As mentioned before, increasing doping concentration significantly reduces the sensor sensitivity and gauge factor to mechanical strain/stress. However, an alternative mechanism to compensate for sensitivity loss, due to high doping level, is needed.

Chapter 3 – Piezoresistivity Effect in Cubic Semiconductors

Piezoresistive effect describes the cha nge in bulk electrical resistivity (opposite to conductivity) when a semiconductor is subjected to mechanical stress. It is a useful mechanism to measure stress or strain. The piezoresistive behavior has been observed in many materials, but much of today's research focuses on the piezoresistive behavior in semiconductors, as they are the prime material to develop MEMS and IC devices using microfabrication processes. Semiconductors produce anisotropic mobility alteration based on the utilized crystallographic direction of the piezoresistive element in the silicon crystal lattice [111]. Understanding the basic formulation governing the piezoresistive effect in doped silicon (as an example of semiconductors) is, therefore, critical to realize the behavior of the piezoresistive elements in response to mechanical stress or strain. Many models and empirical relationships have been proposed in attempt to predict the piezoresistive response of silicon under various loading and environmental conditions. Nevertheless, opinions vary as to which crystalline, environmental and loading conditions play a more significant role in the piezoresistive behavior of the material. This chapter is dedicated to discuss this phenomenon and provide insight background information regarding the crystal structure of silicon and the piezoresistivity theory. This discussion is based on the work done by Kanda, Kloeck and de Rooij 1994 [60, 111]. In this chapter presents the important physics that determine the effect and where the assumptions are made. This chapter is a necessary foundation for subsequent chapters.

3.1. Silicon Crystalline Structure

Silicon wafers are single crystals with a diamond type lattice, as shown in Figure 4. The diamond lattice can be viewed as orderly constructed bonded tetrahedron silicon atoms. This crystal structure provides a variety of plane atom densities, depending on the orientation of the plane to the crystal lattice, as illustrated in

Figure 5. The number of bonds holding each atom in exposed planes of silicon atoms is dependent on the orientation of the plane in the crystal lattice. As shown in Figure 4 and Figure 5, the exposed planes of {111} atoms have three bonds holding the atom in the crystal lattice. Moreover, these atoms have a higher net bonding energy than exposed atoms in {100}, {110} and higher order planes that are held by only two bonds [112].

Silicon structure can be seen as an intermediate metal. It has four valence electrons, which are available for covalent or ionic bonding with other silicon or impurity atoms. As shown in Figure 4, pure silicon forms highly symmetric diamond cubic crystal structure. In this diamond cubic crystal structure, each silicon atom is covalently bonded with four adjacent atoms. When silicon is doped with impurity atoms, these impurities add free electrons or holes to the crystalline lattice. For example, silicon doped with boron (B) receives holes in the crystal lattice, and the resultant crystal is called p-type silicon. Conversely, when doped with phosphorous (P), silicon receives extra free electrons, resulting in n-type silicon. The crystal lattice that results from doping silicon has an important effect on the piezoresistive behavior.
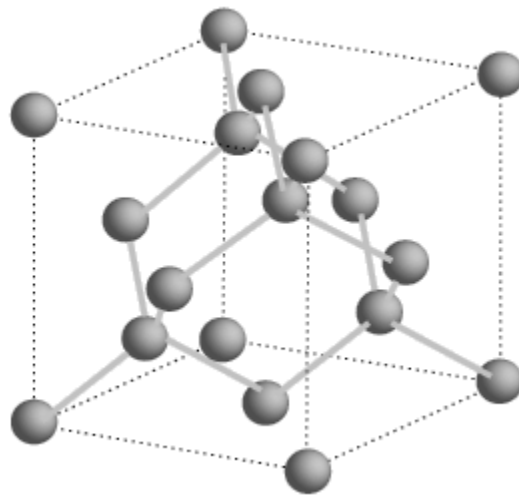
Figure 4 Diamond crystal structure of silicon

(001)　　　　(100)　　　　(010)

(101)　　　　(110)　　　　(011)

(111)　　　　$(1\bar{1}1)$　　　　$(\bar{1}11)$
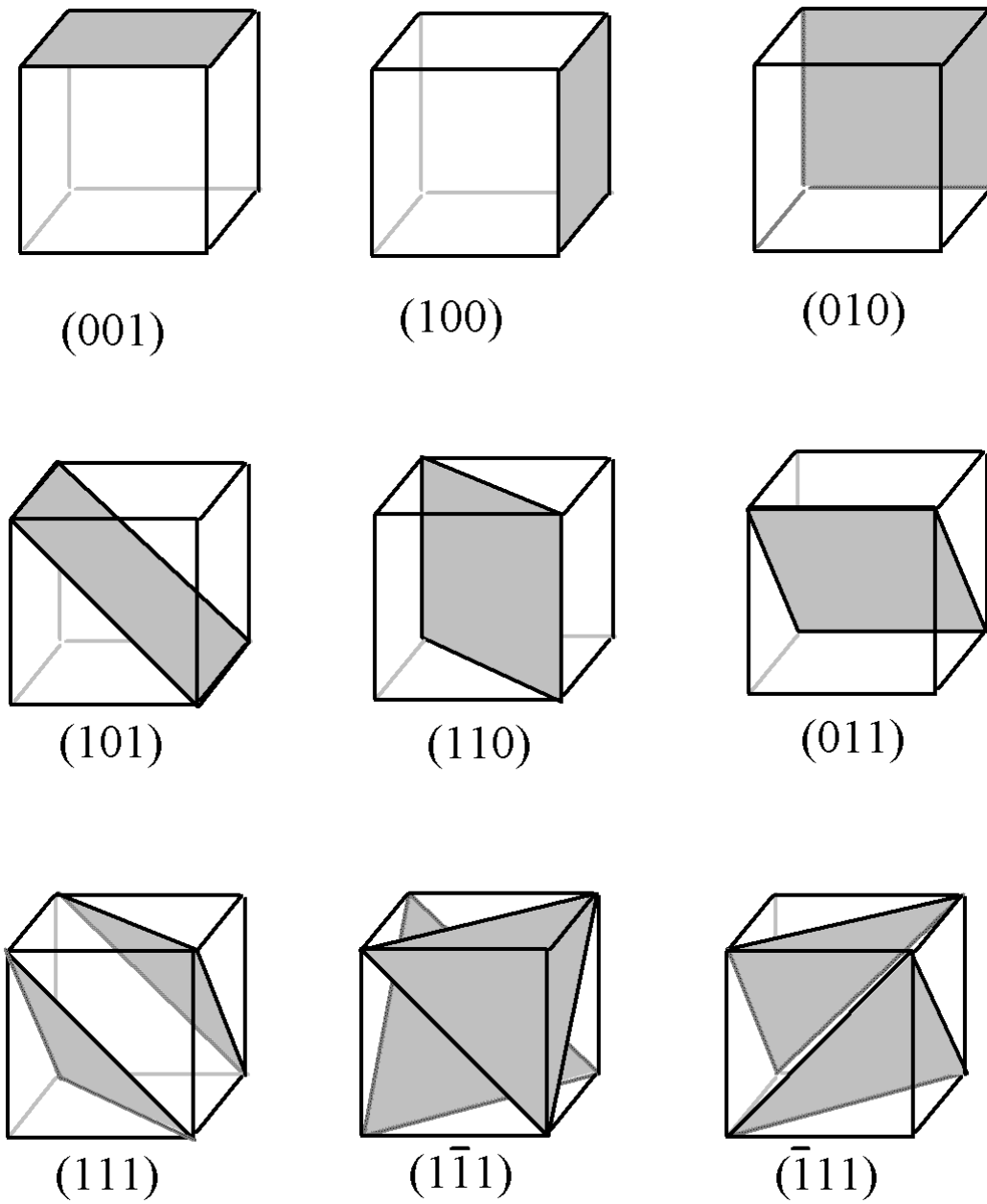
Figure 5 Planes with different Miller indices in cubic crystals ref. [113]

3.2. Elastoresistance in Semiconductors

The application of mechanical strain to semiconductor crystal changes its electrical resistivity, $\Delta\rho_{\alpha\beta}$. Referring to the standard Cartesian notation and

considering the linear strain approximation, the electrical resistivity can be written as

$$\frac{\Delta\rho_{\alpha\beta}}{\rho_o} = \sum_{\gamma,\delta=1}^{3} m_{\alpha\beta,\gamma\delta}\, \varepsilon_{\gamma\delta} \qquad\qquad (4)$$

where $\varepsilon_{\gamma\delta}$ are the components of strain tensor, ρ_o is the isotropic resistivity of the unstrained crystal and $m_{\alpha\beta,\gamma\delta}$ are the components of a dimensionless fourth rank tensor, which is symmetric with respect to interchanging of indices within each pair

$$m_{\alpha\beta,\gamma\delta} = m_{\beta\alpha,\gamma\delta} = m_{\beta\alpha,\delta\gamma} = m_{\alpha\beta,\delta\gamma} \qquad\qquad (5)$$

$m_{\alpha\beta,\gamma\delta}$ are known as the components of the elastoresistance tensor. It is more convenient to define the components of the elastoresistance tensor in terms of strain-induced changes in conductivity as

$$\frac{\Delta\sigma_{\alpha\beta}}{\sigma_o} = m_{\alpha\beta,\gamma\delta}^{(\sigma)}\, \varepsilon_{\gamma\delta} \qquad\qquad (6)$$

In cubic crystals, such as silicon and germanium, it has been shown that $m_{\alpha\beta,\gamma\delta}^{(\sigma)} = -m_{\alpha\beta,\gamma\delta}$ [114]. The form and the number of independent components of the elastoresistance tensor depend on crystal structure and symmetry of the tensor relative to the permutation of indices. In case of cubic crystals such as silicon and germanium, only three of the elastoresistance tensor components differ from zero.

Since all of the components of tensors, $\underline{m}$, $\underline{\rho}$ and $\underline{\varepsilon}$, depend only on a pair of indices, $\alpha\beta$, it is more suitable to adopt a simplified notation to reduce each pair of indices to only one [$\alpha\alpha \rightarrow \alpha$, $\alpha\beta \rightarrow 9-(\alpha+\beta)$]. The resistivity tensor and the strain tensor are now characterized by a single index and the tensor $\underline{m}$ becomes a 6×6 matrix.

$$\varepsilon_{11} \rightarrow \varepsilon_1, \varepsilon_{22} \rightarrow \varepsilon_2, \varepsilon_{33} \rightarrow \varepsilon_3,$$
$$2\varepsilon_{23} \rightarrow \varepsilon_4, 2\varepsilon_{31} \rightarrow \varepsilon_5, 2\varepsilon_{12} \rightarrow \varepsilon_6$$

$$\rho_{11} \rightarrow \rho_1, \rho_{22} \rightarrow \rho_2, \rho_{33} \rightarrow \rho_3,$$
$$2\rho_{23} \rightarrow \rho_4, 2\rho_{31} \rightarrow \rho_5, 2\rho_{12} \rightarrow \rho_6$$

(7)

Thus, Eq. (4) can be rewritten in the form of

$$\frac{\Delta\rho_i}{\rho_o} = \sum_{j=1}^{6} m_{ij}\, \varepsilon_j \tag{8}$$

As a special case of cubic crystals, with the 1-, 2- and 3- axis taken along, [100], [010] and [001], the elastoresistance tensor takes the form

$$\begin{bmatrix} m_{11} & m_{12} & m_{12} & 0 & 0 & 0 \\ m_{12} & m_{11} & m_{12} & 0 & 0 & 0 \\ m_{12} & m_{12} & m_{11} & 0 & 0 & 0 \\ 0 & 0 & 0 & m_{44} & 0 & 0 \\ 0 & 0 & 0 & 0 & m_{44} & 0 \\ 0 & 0 & 0 & 0 & 0 & m_{44} \end{bmatrix} \tag{9}$$

3.3. Piezoresistance in Semiconductors

To determine the piezoresistive effect, one usually applies stress to the crystal and measures the relative change in resistivity per unit stress in a given direction; therefore, in practice, it will be more convenient to describe the piezoresistive effect in terms of a piezoresistance tensor, with components expressed as:

$$\frac{\Delta \rho_{\alpha\beta}}{\rho_o} = \sum_{\gamma,\delta=1}^{3} \pi_{\alpha\beta,\gamma\delta}\, P_{\gamma\delta} \tag{10}$$

where $P_{\gamma\delta}$ are the components of stress tensor, ρ_o is the isotropic resistivity of the crystal and $\pi_{\alpha\beta,\gamma\delta}$ are the components of piezoresistance tensor having the same symmetric properties as $m_{\alpha\beta,\gamma\delta}$. In a simplified notation, the components of $P_{\gamma\delta}$ and $\pi_{\alpha\beta,\gamma\delta}$ can be expressed as

$$P_{11} \rightarrow P_1, P_{22} \rightarrow P_2, P_{33} \rightarrow P_3,$$
$$P_{23} \rightarrow P_4, P_{31} \rightarrow P_5, P_{12} \rightarrow P_6$$

$$\tag{11}$$

$$\pi_{11} \rightarrow \pi_1, \pi_{22} \rightarrow \pi_2, \pi_{33} \rightarrow \pi_3,$$
$$\pi_{23} \rightarrow \pi_4, \pi_{31} \rightarrow \pi_5, \pi_{12} \rightarrow \pi_6$$

Similarly, Eq. (10) can be rewritten in the form of Eq. (8)

$$\frac{\Delta \rho_i}{\rho_o} = \sum_{j=1}^{6} \pi_{ij}\, P_j \tag{12}$$

Components of piezoresistance tensor (π_{ij}) are analogous to (m_{ij}), and has the form of Eq. (9).

Eq. (12) can be explicitly expressed in terms of the components of electric field, current and piezoresistance tensor as follows:

$$\frac{E_1}{\rho_o} = J_1[1 + \pi_{11}P_1 + \pi_{12}(P_2 + P_3)] + \pi_{44}(J_2P_6 + J_3P_5)$$

$$\frac{E_2}{\rho_o} = J_2[1 + \pi_{11}P_2 + \pi_{12}(P_3 + P_1)] + \pi_{44}(J_3P_4 + J_1P_6) \tag{13}$$

$$\frac{E_3}{\rho_o} = J_3[1 + \pi_{11}P_3 + \pi_{12}(P_1 + P_2)] + \pi_{44}(J_1P_5 + J_2P_4)$$

For sufficiently small deformations, strain is directly proportional to stress.

$$P_i = \sum_{j=1}^{6} C_{ij}\varepsilon_j \tag{14}$$

C_{ij} are components of the elastic stiffness tensor, which are analogous to m_{ij} and π_{ij}, and can be expressed by a matrix form in Eq. (9). Substituting Eq. (14) into Eq. (10) and using the fact that, for cubic crystals, $\rho_{\alpha\beta}/\rho_o = -\sigma_{\alpha\beta}/\sigma_o$, it can be shown that the elastoresistance tensor and the piezoresistance tensor satisfy a relation analogous to Eq. (14).

$$m_{ij} = \sum_{k=1}^{6} C_{kj}\pi_{ik} \tag{15}$$

For cubic crystals, Eq. (15) can be written approximately as

$$m_{11} = C_{11}\pi_{11} + 2C_{12}\pi_{12}$$
$$m_{12} = C_{12}\pi_{11} + (C_{11} + C_{12})\pi_{12} \tag{16}$$
$$m_{44} = C_{44}\pi_{44}$$

or conversely,

$$\pi_{11} = \frac{(C_{11}+C_{12})m_{11} - 2C_{12}m_{12}}{(C_{11}-C_{12})(C_{11}+2C_{12})}$$
$$\pi_{12} = -\frac{C_{12}m_{11} - C_{11}m_{12}}{(C_{11}-C_{12})(C_{11}+2C_{12})} \tag{17}$$
$$\pi_{44} = \frac{m_{44}}{C_{44}}$$

For silicon, where $m_{12} = -0.5m_{11}$, the relation is

$$\pi_{11} = \frac{m_{11}}{(C_{11}-C_{12})}$$
$$\pi_{12} = \frac{m_{12}}{(C_{11}-C_{12})} \tag{18}$$
$$\pi_{44} = \frac{m_{44}}{C_{44}}$$

3.4.   Rotation of Axes on (001) Silicon Wafers

Since silicon is anisotropic material, it is desirable to find the piezoresistive coefficients for arbitrary direction in a crystal. (001) is one of the most commonly used crystallographic planes in the MEMS field, as a result, an example will be presented in this section on transformation of axes on this plane. The general

28

transformation equations for the piezoresistance tensor have been worked out by Mason [115], and Pfann and Thurston [51]. The effect of rotation of coordinate system on the piezoresistance tensor is

$$\pi_{\alpha'\beta'\gamma'\delta'} = \sum_{mnpq} \frac{\partial x'_\alpha}{\partial x_m} \frac{\partial x'_\beta}{\partial x_n} \frac{\partial x'_\gamma}{\partial x_p} \frac{\partial x'_\delta}{\partial x_q} \pi_{mnpq} \qquad (19)$$

where the unprimed components refer to the old axes, and the primed components refer to the new axes. The partial derivatives are the direction cosines defined as

$$x'_\alpha = \frac{\partial x'_\alpha}{\partial x_1} x_1 + \frac{\partial x'_\alpha}{\partial x_2} x_2 + \frac{\partial x'_\alpha}{\partial x_3} x_3 = l_\alpha x_1 + m_\alpha x_2 + n_\alpha x_3 \qquad (20)$$

Once the direction cosines between the two coordinate systems are determined, the transformation of the fourth rank tensor is straightforward, though extremely tedious. As an example, consider the change in resistivity of cubic crystal under stress when the current flow is along the <110> directions. The coordinate systems are designated as follows: $x_1 = [100]$, $x_2 = [010]$, $x_3 = [001]$, $x'_1 = [001]$, $x'_2 = [1\bar{1}0]$ and $x'_3 = [110]$. The direction cosines between the two sets of axes are

$$\begin{bmatrix} l_1 & m_1 & n_1 \\ l_2 & m_2 & n_2 \\ l_3 & m_3 & n_3 \end{bmatrix} = \begin{bmatrix} 0 & 0 & 1 \\ \dfrac{1}{\sqrt{2}} & \dfrac{-1}{\sqrt{2}} & 0 \\ \dfrac{1}{\sqrt{2}} & \dfrac{1}{\sqrt{2}} & 0 \end{bmatrix} \qquad (21)$$

29

Using Eq. (21), the piezoresistance tensor in the new coordinate systems is found to be

$$
\pi_{ij}^{'} =
\begin{bmatrix}
\pi_{11} & \pi_{12} & \pi_{12} & 0 & 0 & 0 \\
\pi_{12} & \dfrac{1}{2}\left(\pi_{11}+\pi_{12}+\pi_{44}\right) & \dfrac{1}{2}\left(\pi_{11}+\pi_{12}-\pi_{44}\right) & 0 & 0 & 0 \\
\pi_{12} & \dfrac{1}{2}\left(\pi_{11}+\pi_{12}-\pi_{44}\right) & \dfrac{1}{2}\left(\pi_{11}+\pi_{12}+\pi_{44}\right) & 0 & 0 & 0 \\
0 & 0 & 0 & \pi_{11}-\pi_{12} & 0 & 0 \\
0 & 0 & 0 & 0 & \pi_{44} & 0 \\
0 & 0 & 0 & 0 & 0 & \pi_{44}
\end{bmatrix}
\quad \text{(22)}
$$

The conduction equation along the <110> direction is then given by

$$
\frac{E_3^{'}}{\rho_o} = J_3^{'}\left[1 + \pi_{12}P_1^{'} + \frac{1}{2}\left(\pi_{11}+\pi_{12}-\pi_{44}\right)P_2^{'} + \frac{1}{2}\left(\pi_{11}+\pi_{12}+\pi_{44}\right)P_3^{'}\right]
\quad \text{(23)}
$$

Generally, for a semiconductor filament arbitrarily oriented in a crystallographic coordinate system, where $x_1 = [100]$, $x_2 = [010]$, $x_3 = [001]$ are the principal directions of the cubic silicon crystal, the general expression for the normalized resistance change of the piezoresistive, as a function of stress components $\sigma_i^{'}$, element can be obtained as [32, 38, 116]

$$
\frac{\Delta R}{R} = \pi_{1\alpha}^{'}\sigma_{\alpha}^{'}\, l^{'2} + \pi_{2\alpha}^{'}\sigma_{\alpha}^{'}\, m^{'2} + \pi_{3\alpha}^{'}\sigma_{\alpha}^{'}\, n^{'2}
$$
$$
+ 2\,\pi_{4\alpha}^{'}\sigma_{\alpha}^{'}\, l^{'}n^{'} + 2\,\pi_{5\alpha}^{'}\sigma_{\alpha}^{'}\, m^{'}n^{'}
\quad \text{(24)}
$$
$$
+ 2\,\pi_{6\alpha}^{'}\sigma_{\alpha}^{'}\, l^{'}m^{'} + \alpha_1\Delta T + \alpha_2\Delta T^2 + ...
$$

where $\pi'_{\alpha\beta}$ (α, β = 1, 2,..., 6) are the off-axis temperature dependent piezoresistive coefficients. α_1, α_2,…etc. are the temperature coefficients of resistance, and $\Delta T = T_m - T_{ref}$ is the difference between the measurement temperature (T_m) and reference temperature (T_{ref}), and l', m', n' are the direction cosines of the conductor orientation with respect to the x'_1, x'_2 and x'_3 axes, respectively. Equation (24) assumes that geometric changes are neglected.

In practice, it is more convenient especially for p-type silicon, to refer Eq. (24) to the primed axes instead of the unprimed axes. In this case, the reference axes will be parallel and perpendicular to the primary wafer flat. Therefore, when the primed axes are aligned with the unprimed crystallographic axes, Eq. (24) reduces to [32, 33, 35, 38, 54, 116, 117]

$$\frac{\Delta R}{R} = \left[\pi_{11}\sigma_{11} + \pi_{12} \ \sigma_{22} + \sigma_{33} \ \right]\cos^2\phi + \left[\pi_{11}\sigma_{22} + \pi_{12} \ \sigma_{11} + \sigma_{33} \ \right]\sin^2\phi$$
$$+ \pi_{44}\sigma_{12}\sin \ 2\phi \ + \ \alpha_1\Delta T + \alpha_2\Delta T^2 + ...$$
(25)

In the new reference system, ϕ is the angle between the [110] and resistor orientation, as shown in Figure 6. Further simplification can be attained to yield

$$\frac{\Delta R}{R} = \left[\left(\frac{\pi_{11} + \pi_{12} + \pi_{44}}{2} \right)\sigma_{11} + \left(\frac{\pi_{11} + \pi_{12} - \pi_{44}}{2} \right)\sigma_{22} \right]\cos^2\phi$$
$$+ \left[\left(\frac{\pi_{11} + \pi_{12} - \pi_{44}}{2} \right)\sigma_{11} + \left(\frac{\pi_{11} + \pi_{12} + \pi_{44}}{2} \right)\sigma_{22} \right]\sin^2\phi$$
$$+ \pi_{12}\sigma_{33} + \ \pi_{11} - \pi_{12} \ \sigma_{12}\sin \ 2\phi \ + \ \alpha_1\Delta T + \alpha_2\Delta T^2 + ...$$
(26)

Equation (26) indicates that the out-of-plane shear stresses σ'_{13} and σ'_{23} do not influence the resistances of stress sensors fabricated on (001) wafers. This means that a sensor rosette on (001) silicon may at best measure four of the six unique components of the stress tensor. All three of the unique piezoresistive coefficients

for silicon (π_{11}, π_{12} and π_{44}). Moreover, this equation is useful to calculate the potential alignment errors during the microfabrication and application processes. Table 2 presents the results of different transformations of the piezoresistive coefficients. These results are expressed in main quantities; π_l and π_t. Where π_l is the longitudinal piezoresistive coefficient and π_t is the transverse piezoresistive coefficient. It is clear that π_l and π_t are functions of the independent piezoresistive on-axis coefficients; π_{11}, π_{12} and π_{44}, originally calculated by Smith [71].
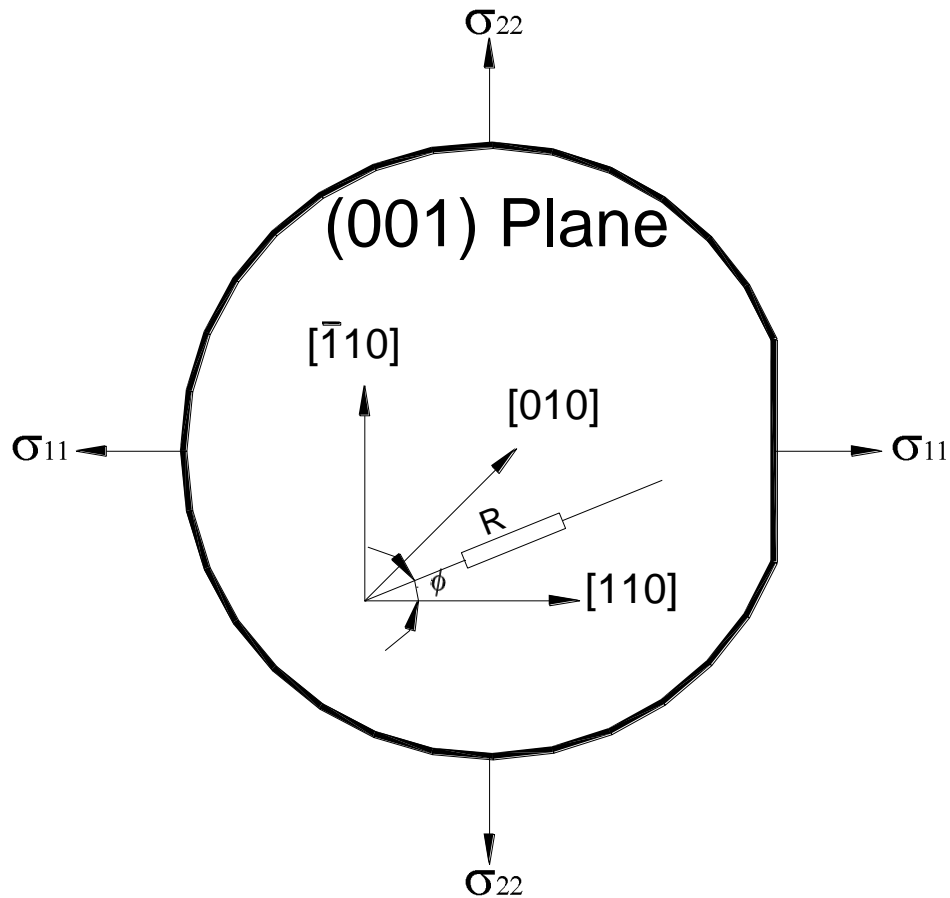
Figure 6 General (001) silicon wafer

Table 2 Longitudinal and transverse piezoresistive coefficients for common cubic crystalline directions, adapted from ref. [111]

Longitudinal Direction	$l_1\, m_1\, n_1$	π_l	Transverse Direction	$l_2\, m_2\, n_2$	π_t
[100]	1 0 0	π_{11}	[010]	010	π_{12}
[001]	0 0 1	π_{11}	[110]	$\dfrac{1}{\sqrt{2}}\ \dfrac{1}{\sqrt{2}}\ 0$	π_{12}
[111]	$\dfrac{1}{\sqrt{3}}\ \dfrac{1}{\sqrt{3}}\ \dfrac{1}{\sqrt{3}}$	$\dfrac{1}{3}\left(\pi_{11}+2\pi_{12}+2\pi_{44}\right)$	[1$\bar{1}$0]	$\dfrac{1}{\sqrt{2}}\ \dfrac{-1}{\sqrt{2}}\ 0$	$\dfrac{1}{3}\left(\pi_{11}+2\pi_{12}+2\pi_{44}\right)$
[110]	$\dfrac{1}{\sqrt{2}}\ \dfrac{1}{\sqrt{2}}\ 0$	$\dfrac{1}{2}\left(\pi_{11}+\pi_{12}+\pi_{44}\right)$	[111]	$\dfrac{1}{\sqrt{3}}\ \dfrac{1}{\sqrt{3}}\ \dfrac{1}{\sqrt{3}}$	$\dfrac{1}{3}\left(\pi_{11}+2\pi_{12}+2\pi_{44}\right)$
[110]	$\dfrac{1}{\sqrt{2}}\ \dfrac{1}{\sqrt{2}}\ 0$	$\dfrac{1}{2}\left(\pi_{11}+\pi_{12}+\pi_{44}\right)$	[001]	0 0 1	π_{12}
[110]	$\dfrac{1}{\sqrt{2}}\ \dfrac{1}{\sqrt{2}}\ 0$	$\dfrac{1}{2}\left(\pi_{11}+\pi_{12}+\pi_{44}\right)$	[1$\bar{1}$0]	$\dfrac{1}{\sqrt{2}}\ \dfrac{-1}{\sqrt{2}}\ 0$	$\dfrac{1}{2}\left(\pi_{11}+\pi_{12}-\pi_{44}\right)$

3.5.   Silicon as a Piezoresistive Material

Silicon is widely used in semiconductor industry and MEMS field. The piezoresistive behavior of silicon was first documented by Smith in 1954 [71]. Silicon is well suited for applications involving piezoresistivity for many reasons [118, 119]:

1. Gauge factor of semiconductors is more than an order of magnitude higher than that of metals.
2. Silicon is a very robust material with high fracture strength.
3. Good matching of the piezoresistive elements is possible, which is particularly useful if a Wheatstone bridge configuration is employed.
4. The piezoresistive effect is very suitable for miniaturization of the sensors.

5. Mass production can be achieved utilizing the available technology of IC's.

6. It is possible to integrate electronic circuitry directly on the sensor chip, for signal amplification and temperature compensation.

7. Finally, equations describing the large deflections inherent in compliant mechanism motion are well documented and allow for accurate analysis of these devices [120].

As a results of the above properties, the piezoresistive behavior in silicon has been employed in many applications [121-123]:

1. Acceleration detection
2. Pressure sensing
3. Flow sensing
4. Displacement sensing and nano-positioning
5. Force and torque detection, as in atomic force microscopy, biological research, and gauge calibration
6. Acoustic wave detection in microphones

Many of these devices utilize the Wheatstone bridge, with one, two or variable piezoresistors, which are developed on the surface of the beam, diaphragm or deflecting member. Therefore, to be successfully implemented in any of these applications, the piezoresistive behavior of each resistor must be accurately modeled.

3.6. Gauge Factor

While the longitudinal and transverse piezoresistive coefficients are useful for designing piezoresistive devices, the further refinement of gauge factors is even more helpful. The gauge factor is a key component to model piezoresistance. The general definition of gauge factor comes from resistance equations. The gauge factor, G, can be defined as the fractional change in resistance per unit strain. The

derivation of the gauge factor begins with the simple relationship between resistance (R) and resistivity (ρ):

$$R = \frac{\rho L}{A} \tag{27}$$

where L is the length of the resistor in the direction of the current flow and A is the cross sectional area of the resistor. By differentiation

$$DR = \left(\frac{L}{A}\right)d\rho + \left(\frac{\rho}{A}\right)dL - \left(\frac{\rho L}{A^2}\right)dA \tag{28}$$

Further simplification leads to

$$\frac{dR}{R} = \frac{d\rho}{\rho} + \frac{dL}{L} - \frac{dA}{A} \tag{29}$$

Therefore, the gauge factors can be computed based on the applied state of stress. More importantly, the crystal anisotropy has to be considered.

Using Hooke's Law and the mechanics of materials principles, Eq. 29 can be reduced to

$$\frac{dR}{R} = \frac{d\rho}{\rho} + \frac{dL}{L} + 2v\frac{dL}{L} = \frac{d\rho}{\rho} + \left(1 + 2v\right)\varepsilon \tag{30}$$

Where ε is the applied mechanical strain. Further simplifications can be attained using Eqs. (12) and (14) as

$$\frac{dR}{R} = \pi\sigma + \left(1+2v\right)\varepsilon = \pi C\varepsilon + \left(1+2v\right)\varepsilon = \left[\pi C + \left(1+2v\right)\right]\varepsilon \tag{31}$$

From the above definition of the gauge factor and considering the small size of the piezoresistive elements, the piezoresistive gauge factor can be extracted as

$$G = \left[\pi C + \left(1+2v\right)\right] = \left(\frac{dR}{R}\right)\Big/\varepsilon \tag{32}$$

It is well reported that the piezoresistive gauge factor depends on the fabrication method, whether it is diffusion, ion-implantation or epitaxial growth. Moreover, as mentioned above, it depends on the crystallographic directions; dopant level and type. In addition, the subsequent annealing step after diffusion, ion-implantation or the epitaxial growth plays a crucial rule in the final properties of the microfabricated piezoresistive elements including contact resistance, sheet resistivity, dopant distribution profile, noise…etc. All of these properties contribute to the performance characteristics of the piezoresistor as a sensing element. Finally, the operating temperature of the developed piezoresistive elements is as important as the other factors; however, the effect of the operating temperature decreases with the increase of the doping concentration.

Stress concentration concept can be used to improve the sensitivity of piezoresistive sensors. For example, sensing elements in load cells have layouts to increase sensitivity in the direction of interest.

Chapter 4 – Finite Element Investigation and Analytical Modeling

In 1943, based on Ritz method, Richard Courant introduced Finite Element Analysis (FEA) as an engineering and research tool for numerical analysis. During the 1970's, FEA became a powerful method and was mainly utilized in aerospace and automotive industries. Later, FEA included different physics such as electromagnetic, fluid flow…etc., which has led to the appearance of coupled-field FEA modeling. FEA is commonly used to analyze complex structures with load configurations that can not be modeled using closed form equations or do not have simple analytical models. It is considered one of the most accurate methods for stress-strain analysis. FEA has been utilized in the current research work to facilitate the development cycle of the MEMS piezoresistive strain sensor. Additionally, detailed investigation of the sensor performance was carried out through sensitivity analysis to select the proper microfabrication variables. Figure 7 illustrates the development cycle of the piezoresistive MEMS-based strain sensor highlighting the role of FEA. Finite element simulations were used to determine the states of stress in the silicon chip. The finite element model predictions were used to approximate trends of the various stress component distributions, so that the experimental data could be better understood.

The following sections discuss the various FEA models that were used to investigate the effect of different factors on the characteristics of the MEMS-based sensor. The presented FEA models were constructed and solved following a common procedure [124-127]. First, the model geometry was constructed according to the physical dimensions of the sensing chip, solid model. Second, the solid model was converted into small pieces called elements, meshing. These elements have specific constitutive equations that describe their performance during the solution process. Material properties (structural, electrical and electromechanical or piezoresistive) were then defined. Some material properties were isotropic (strained surface and boding material) and some properties were

anisotropic (piezoresistive elements and silicon chips). Loadings and boundary conditions were defined and applied on the meshed model. In addition, solution controls and load application method was defined to properly describe the model behavior. Finally, the solution process was initiated. Subsequently, FEA results were collected and analyzed, post processing. Using FEA results key performance characteristics of the sensor were calculated.
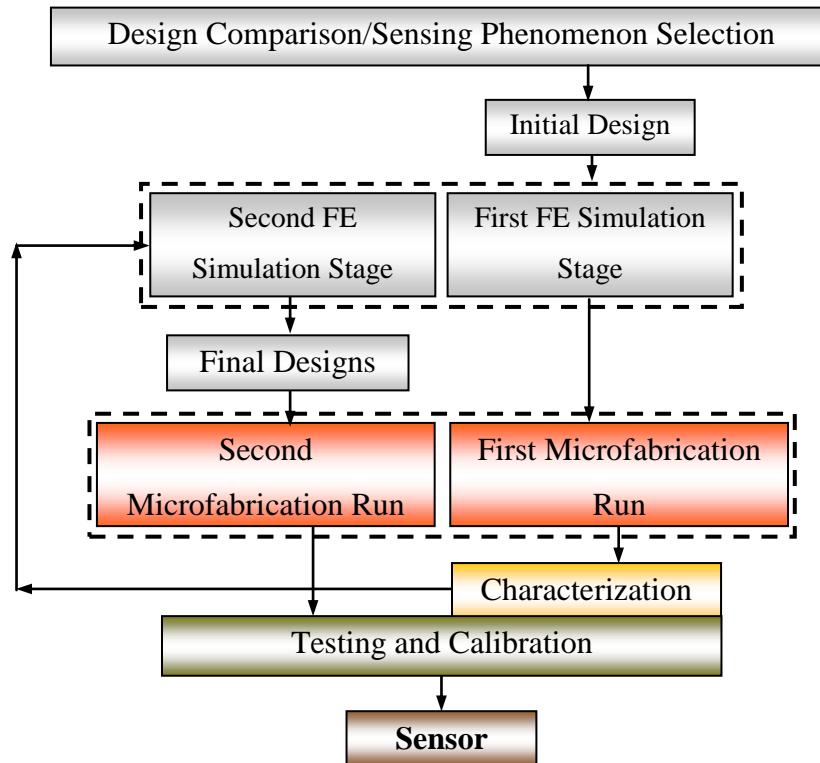
Figure 7 Development cycle of the MEMS-based piezoresistive strain sensor

4.1. Verification of FEA Modeling – Simplified FEA Model

Although FEA is a well-recognized analysis method, it is highly dependent on the modeling procedure. For example meshing and boundary conditions can significantly affect the results accuracy. To verify the efficiency and reliability of

the FEA modeling process in this research work, a simplified analytical model was constructed. This simplified model was then analyzed using FEA.

As depicted in Figure 8, the simplified FEA model is 10mm×10mm square chip. The chip thickness is 500μm. On the silicon chip, four piezoresistive elements were implanted and connected in a full-bridge configuration. The piezoresistive elements are rectangular with the dimensions of 20μm×100μm with junction depth of 1μm. Properties of the simplified model are listed in Table 3. The silicon chip dimensions (length, width and thickness), piezoresistors dimensions (length, width and depth) were selected to match the corresponding variables of the full FEA model.
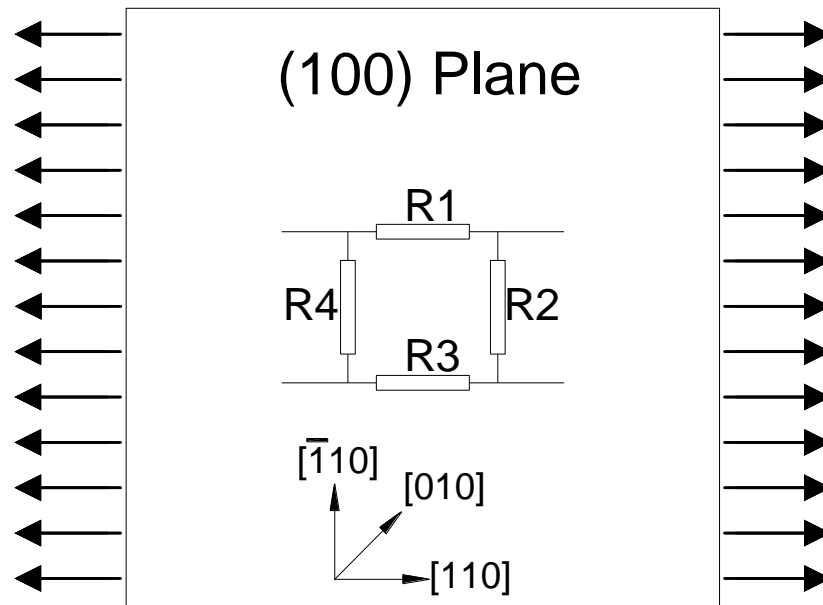
Figure 8 Schematic of verification (simplified) FE model: 10mm×10mm sensing chip with four 100μm×20μm sensing elements

Table 3 Finite element model details

Structural Layer	Modeling Element Characteristics	Model Input Properties [128-131]
Silicon carrier	*Anisotropic* 20-node tetrahedral elements	Elastic constants C_{11}= 165.7 GPa C_{12}= 63.9 GPa C_{44}= 79.6 GPa
Piezoresistors	*Anisotropic* 20-node tetrahedral elements with piezoresistive behavior	Elastic constants C_{11}= 165.7 GPa C_{12}= 63.9 GPa C_{44}= 79.6 GPa Piezoresistive Coefficients π_{11}= 66 TPa^{-1} π_{12}= - 11 TPa^{-1} π_{44}= 1381 TPa^{-1}

4.2. Analytical Equations of the Simplified Model

For a semiconductor resistor with cross-sectional area A_R, the normalized resistance change is given by

$$\left.\frac{\Delta R}{R}\right|_{\substack{Unit \\ Load}} = \frac{1}{A_R} \int_0^{A_R} \pi_l \sigma_l + \pi_t \sigma_t \ \partial A + \alpha \Delta T \qquad (33)$$

where π_l is the longitudinal piezoresistive coefficient, π_t is the transverse piezoresistive coefficient, σ_l is the longitudinal stress and σ_t is the transverse stress. Due to the small size of the piezoresistive elements, the applied stresses can be assumed constant over the length of the piezoresistive element. Therefore, Eq. (33) is expressed as

$$\frac{\Delta R}{R} = \pi_l \sigma_l + \pi_t \sigma_t + \alpha \Delta T \qquad (34)$$

In case of p-type silicon, π_{44} is more dominant over the other two piezoresistive coefficients, π_{11} and π_{12}. Therefore, along <110> directions, the above equation can be approximated by

$$\frac{\Delta R}{R} = \frac{\pi_{44}}{2}\frac{\sigma_l - \sigma_t}{2} + \alpha\Delta T \qquad (35)$$

From Eq. (35), it is clear that the normalized resistance change ($\Delta R/R$) is increased by maximizing the differential stress (σ_l-σ_t), which can be achieved by magnifying σ_l and decreasing σ_t. Therefore, a uniaxial stress case along the longitudinal axis ([110]) can be assumed, i.e. σ_t =0. Eq. (35) can be reduced to

$$\frac{\Delta R}{R} = \frac{\pi_{44}\sigma_l}{2} + \alpha\Delta T \qquad (36)$$

Equation (36) assumes one active resistor in [110] direction; however, in case of two active piezoresistive elements in a full-bridge configuration, the normalized resistance change is described by

$$\frac{\Delta R}{R} = \pi_{44}\sigma_l \qquad (37)$$

Equation (37) is the approximate form for a full-bridge configuration on a flat silicon chip. The validity of the different assumptions is tested in the following paragraphs. First, it was assumed that the stress is constant over the piezoresistor length. This assumption is valid in case of extremely small piezoresistive elements and small junction depth compared to the sensing chip dimensions. In the current project, the piezoresistive elements are rectangular with dimensions of 20µm×100µm and a junction depth of 1µm.

The second approximation is the uniaxial stress case. Due to the piezoresistive element cross-sensitivity This assumption will be hard to achieve in the real

world. However, careful design can significantly reduce the effect of cross-sensitivity by reducing the transferred transvers strain to the sensing elements. The third approximation comes from neglecting the π_{11} and π_{12}. The applicability of this assumption is dependent on the utilized crystal orientation and microfabrication doping concentration. The last approximation can be examined comparing Eqs. (36) and (37). From these equations, one can notice that TCR of both transverse and longitudinal piezoresistive element are assumed to be equal. This assumption is confirmed by visiting figure 5 in reference [35]. Moreover, for piezoresistive elements with high doping concentrations, the induced error from this assumption is minimal. Other factors can introduce inaccuracy in the calculations results using Eq. (37) such as initial imbalance of the full-bridge due to microfabrication variability. This can be tackled by isolating the initial shift at stress-free condition from the measurements.

4.2.1. Wheatstone Bridge

Wheatstone bridge is useful for measuring resistance, capacitance and inductance. Its precise comparison of resistance makes it very suitable for measuring small changes in resistance of stain gauges. The piezoresistors on the sensing chip and the dummy resistors are connected to form a full-bridge configuration. The bridge output (V_{out}) is the differential voltage, which can be expressed as a function of the excitation voltage (V_{in}) and all the resistors in the bridge by [40]

$$V_{out} = \left[\frac{R_1}{R_1 + R_2} - \frac{R_4}{R_3 + R_4} \right] V_{in} \tag{38}$$

The differential change in the Wheatstone bridge output becomes

$$dV_{out} = \left[\frac{R_1 R_2}{{R_1 + R_2}^2} \left(\frac{dR_1}{R_1} - \frac{dR_2}{R_2} \right) + \frac{R_3 R_4}{{R_3 + R_4}^2} \left(\frac{dR_3}{R_3} - \frac{dR_4}{R_4} \right) \right] V_{in} \tag{39}$$

If $R_1 = R_2 = R_3 = R_4 = R$, the bridge is balanced. The differential change in output yields

$$dV_{out} = \frac{1}{4}\left[\frac{dR_1}{R_1} - \frac{dR_2}{R_2} + \frac{dR_3}{R_3} - \frac{dR_4}{R_4}\right]V_{in} \qquad (40)$$

Based on the bridge configuration and chip dimensions, it was expected that only two resistors will be subjected to mechanical stain and the other two resistors will experience relatively low stress. Assuming that R_1 and R_3 will be the stressed resistors, Eq. (40) reduces to

$$\frac{dR}{2R} = \frac{dV_{out}}{V_{in}} \qquad (41)$$

When any temperature change occurs equally in all resistors, the bridge output will not be sensitive to thermal expansion or contraction. On the other hand, depending on the doping level the sensing chip output will change. The full-bridge configuration also reduces the total noise of the sensor. Most Wheatstone bridges use DC voltage to excite the resistive bridge elements for simplicity. Hence, DC voltage was adopted in all simulations and experiments. However, a higher performance can be achieved with AC (sine wave) excitation technology allowing more accurate measurements. The AC excitation is more stable as it is essentially immune to thermocouple effects at the terminals and connectors. It is also an effective way to remove DC-offset voltages in series with bridge output.

4.2.2. Noise and Resolution

Intrinsic noise affects the resolution of the piezoresistive sensors. Specifically, Johnson noise and $1/f$ noise are the two main sources of noise in piezoresistive sensors [132, 133]. The following sections discuss the mathematical formulation governing these noise sources. This mathematical formulation was used in conjunction with FEA to predict and evaluate the sensor key performance

characteristics, which were later compared to experimental results. In addition, it was used to understand, discuss and explain the discrepancies, if any, between experimental and theoretical results.

4.2.2.1. Johnson Noise

Johnson noise originates from the random motion of the charge carriers within resistors, which leads to thermal fluctuations in electron density. Similar to white noise, its spectral density is independent of frequency. It can be evaluated by the thermal energy of the carriers in the piezoresistive elements, i.e. it is dependent only on the resistance value and the operating temperature. The voltage noise power density ($S_{Johnson}$) is calculated by [134]

$$S_{Johnson} = 4k_B TR \tag{42}$$

where k_B is the Boltzmann's constant (1.38×10^{-23} J/K), T is the operating temperature in degrees Kelvin, and R is the resistance in ohms. The resistance of the piezoresistive element is determined by its geometry and the utilized doping concentration during microfabrication. Johnson noise power for a given geometry as a function of the junction depth (z) can be obtained from

$$\overline{V}^2_{Johnson} = \frac{16k_B Tl}{wt\mu(z)qN(z)} \quad f_{max} - f_{min} \tag{43}$$

where f_{max} and f_{min} are the upper limit and the lower limit of the bandwidth, respectively, and (f_{max}-f_{min}) is the sensor bandwidth. For piezoresistors with uniform dopant concentration, Johnson noise power can be simplified to

$$\overline{V}^2_{Johnson} = \frac{16k_B Tl}{wt\mu qN} \quad f_{max} - f_{min} \tag{44}$$

where N is the impurity concentration, and μ is the hole mobility at N.

44

4.2.2.2. *1/f* Noise

The electric current flowing through the piezoresistive elements results in fluctuations in resistivity or conductivity. This leads to what is commonly called *1/f* noise. Although there may be other sources for *1/f* noise, Hooge noise usually dominates *1/f* noise source [132, 133, 135]. Hooge put an empirical model to describe this noise [134]

$$S_{Hooge} = \frac{\alpha V_{in}^2}{N_c f}$$

(45)

where V_{in} is the input voltage to the bridge circuit or the biased voltage across a resistor. The resistor has a total number of charge carriers of N_c, and is operating under frequency f is the frequency. Hooge noise source has a spectrum proportional to *1/f*, making the measurement at low frequencies difficult. After integration from f_{min} to f_{max}, the voltage noise power is given by

$$\overline{V}_{Hooge}^2 = \frac{\alpha V_{in}^2}{N_c} \ln\left(\frac{f_{max}}{f_{min}}\right)$$

(46)

where α is a dimensionless parameter called Hooge constant. It has been reported that this parameter is dependent on annealing conditions of piezoresistive elements [133, 134]. In Eq. (46), the total number of charge carrier can be obtained by integrating the dopant concentration through the volume of the resistor. For rectangular resistor with constant doping concentration, it can be calculated as the product of doping concentration and the volume of the piezoresistive element, i.e., $N_c = N \times (l \times w \times t)$. Where, $(l \times w \times t)$ is the product of the element length, width and depth, respectively. Therefore, Eq. (46) can be rewritten as

$$\overline{V}_{Hooge}^2 = \frac{\alpha V_{in}^2}{N \ l \times t \times w} \ln\left(\frac{f_{max}}{f_{min}}\right)$$

(47)

Thus, the *1/f* noise power density is inversely proportional to the volume of the piezoresistors and their doping concentration.

4.2.2.3.   Resolution Calculations

Resolution is defined as the minimum detectable value of the quantity. Mathematically, it is calculated by dividing total noise by sensitivity, and can be obtained when V_{out} equals noise. From Eqs. (32), (37), (44) and (47), the minimum detectable strain can be obtained by

$$\varepsilon_{min} = \frac{\sqrt{\left[\dfrac{\alpha V_{in}^2}{N\ l \times t \times w}\ln\left(\dfrac{f_{max}}{f_{min}}\right)\right] + \left[\dfrac{16 k_B T l}{wt\mu qN}\ f_{max} - f_{min}\right]}}{\pi_{44}C_{44}V_{in}} \tag{48}$$

The first term in the numerator in Eq. (48) is the contribution of Hooge noise, and the second term is the contribution of Johnson noise. It is evident that resolution is determined by more parameters than sensitivity. The parameters that affect the resolution can be divided into two categories: the dimensions of the piezoresistive elements and the doping concentration in addition to the input voltage to the bridge. However, considering the low frequency applications, Johnson noise can be neglected compared to *1/f* noise.

4.2.3. Results of Simplified Finite Element Model

As described above, a 10mm×10mm flat square piece of silicon with a full-bridge arrangement was analyzed using FEA to test the reliability and accuracy of the FEA modeling process. This configuration is very similar to the sensing unit of the full FEA model of the MEMS sensor. This configuration eases the transition from the simplified FEA model to the full FEA model, which ensures transferring the reliability of the modeling process for subsequent geometric modifications. Therefore, it was logical to adapt it. The piezoresistive elements are aligned along the <110> and its in-plane transverse. These directions are the orientations on the

sensing piezoresistors on the MEMS sensing chips. The FEA simulation of the flat sensing chip (simplified model) served two main purposes. First, the results of the FEA helped to test the accuracy of the assumptions, such as neglecting π_{11} and π_{12}. Second, the results of the simplified model were used as a reference for subsequent comparison to the final sensing chips.

To verify the reliability of the FEA modeling process, the results from the flat sensing chip, shown in Figure 8, were compared to the results calculated from Eq. (37). This comparison is presented in Figure 9. The FEA results and the analytical calculations of the simplified model are in close agreement, especially at high doping concentration. Differences between the FEA simulation results and the analytical model were calculated and presented in Figure 10 as error percentage (error %). The error % was calculated according to

$$Error\% = \frac{Analytical - FEA}{Analytical} \times 100\% \qquad (49)$$

The error percentage was found to decrease as the doping concentration increases. Generally, the output signal from the analytical solution is higher than FEA results. The difference between analytical and FEA solutions can be attributed to the algebraic approximation of the element type, mesh size of the FEA model and/or neglecting π_{11} and π_{12}. This was examined by refining the mesh size. After refining the mesh, the same trend was found, *i.e.*, analytical solution was higher than FEA solution. The maximum % error (at light doping concentration) was less than 5% error decreased as the doping concentration increased. The difference between the two solutions decreased as the doping concentration increased. This can be the result of neglecting π_{11} and π_{12}. At high doping concentrations (more than 1×10^{19} atoms/cm^3), π_{11} and π_{12} are approximately 25% of their values at light doping levels [61]. Bearing in mind that high doping level is favorable under varying temperature conditions, the FEA modeling procedure was considered highly descriptive to the analytical model and later to the fabricated sensing chips.

47
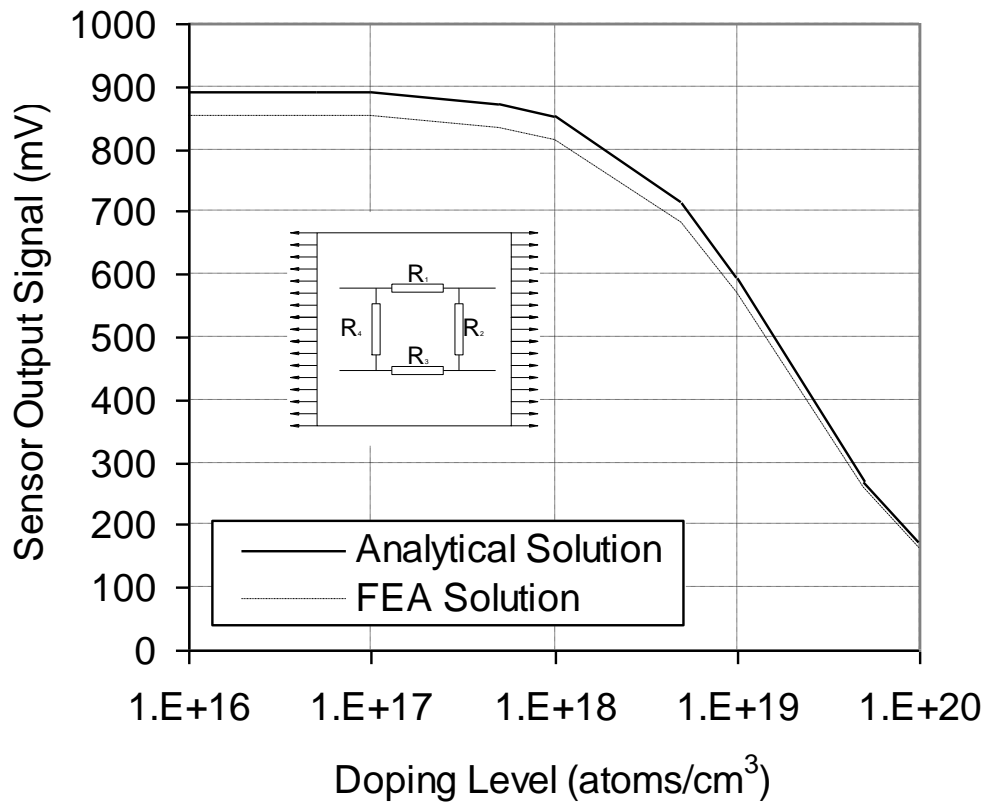
Figure 9 Comparison between analytical calculations model and the FEA results at different doping concentrations for a flat silicon chip with four piezoresistors along [110] and its in-plane transverse (full-bridge configuration), V_{in} = 5 volts. Kanda's model [61] was used to scale the piezoresistive coefficients
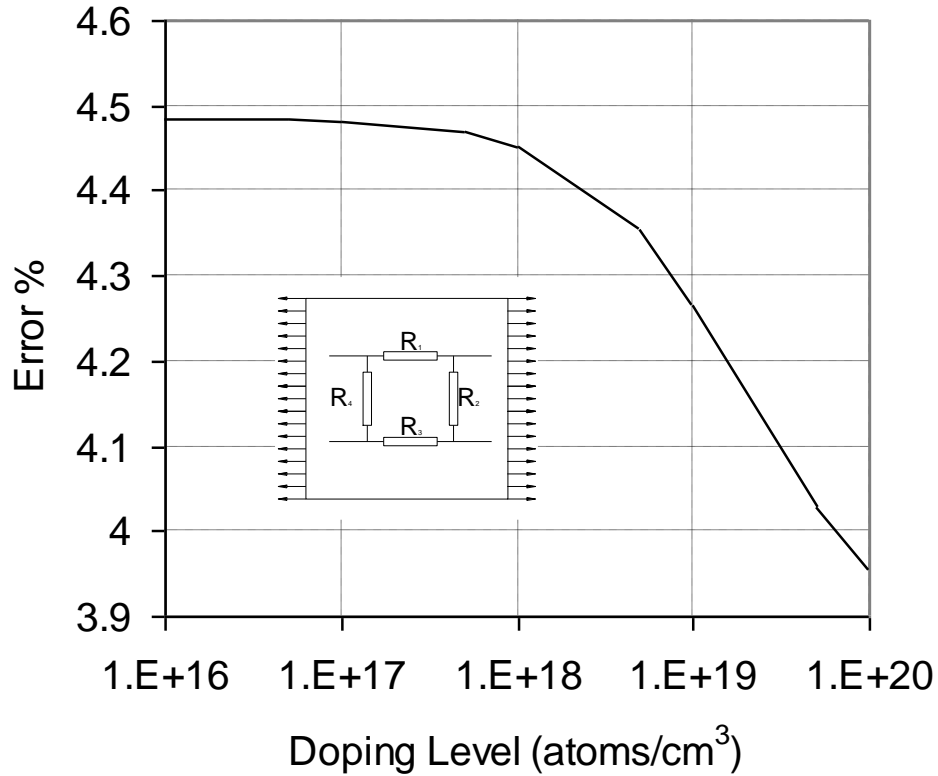
Figure 10 Error % in the sensor output signal calculated from analytical model and FEA model at different doping concentrations for a flat silicon chip with four piezoresistors along [110] and its in-plane transverse (full-bridge configuration), $V_{in} = 5$. Kanda's model [61] was used to scale the piezoresistive coefficients

4.3. Full Finite Element Model

One important goal of numerical simulation is to understand the effect of different variables and, in particular, how design, fabrication, and operating parameters determine, enhance, or limit the sensor performance with respect to the quantity under consideration, strain/stress in the our case. The full finite element code can be found in Appendix A. As shown in Figure 11, the full finite element model is composed from two models. The first model is a silicon chip that was geometrically modified from the simplified element model, as discussed above. Stress concentration regions (SCRs) or geometric features (surface trenches) were

incorporated around the sensing unit. The results of this model were compared to reference results to evaluate the feasibility of surface features to magnify the sensor output signal. The second FEA model was constructed by including strained surface and bonding material layer to the second FEA model. The results of the second FEA model were used to discuss the effect of bonding adhesive characteristics (material properties and thickness) to guide the selection of bonding material and installation procedure. Further, this model is used to quantify the signal loss through the bonding material.

Each simulation involved three submodels [136]; mechanical, electrical and electromechanical (piezoresistive). The silicon chip was built and assigned anisotropic structural properties. Then, the piezoresistive elements were incorporated in the silicon chip. In addition to the anisotropic structural properties, the piezoresistive elements had electrical properties that are coupled to the stress experienced during loading. Next to the geometry definition, the solid model was meshed. The mesh was refined to ensure stable solution. The meshed FEA model of the silicon chip was composed from approximately 47,000 3D solid elements.

The effect of boundary conditions was isolated by analyzing the sensing chip dimensions. The piezoresistive properties of the silicon crystal at different doping concentrations were calculated using the piezoresistance factor from Kanda's model [61]. Finally, constant displacement equivalent to $1500\mu\varepsilon$ was applied on the chip edges (in the case of the first and the second FEA simulation submodels) and on the strained surface edges (in the case of the third FEA simulation submodel). A schematic of the applied boundary conditions on the different FEA models is shown in Figure 12.

Using the commercial FEA software, ANSYS® Multiphysics, a model of the sensor structure was constructed to verify the effect of doping concentration and geometric features on the sensor sensitivity. In addition, FEA was applied to investigate the effect of the bonding adhesive characteristics on the overall signal loss. The following sections discuss different aspects in the FEA modeling process. Then, FEA results of the full-model are presented.
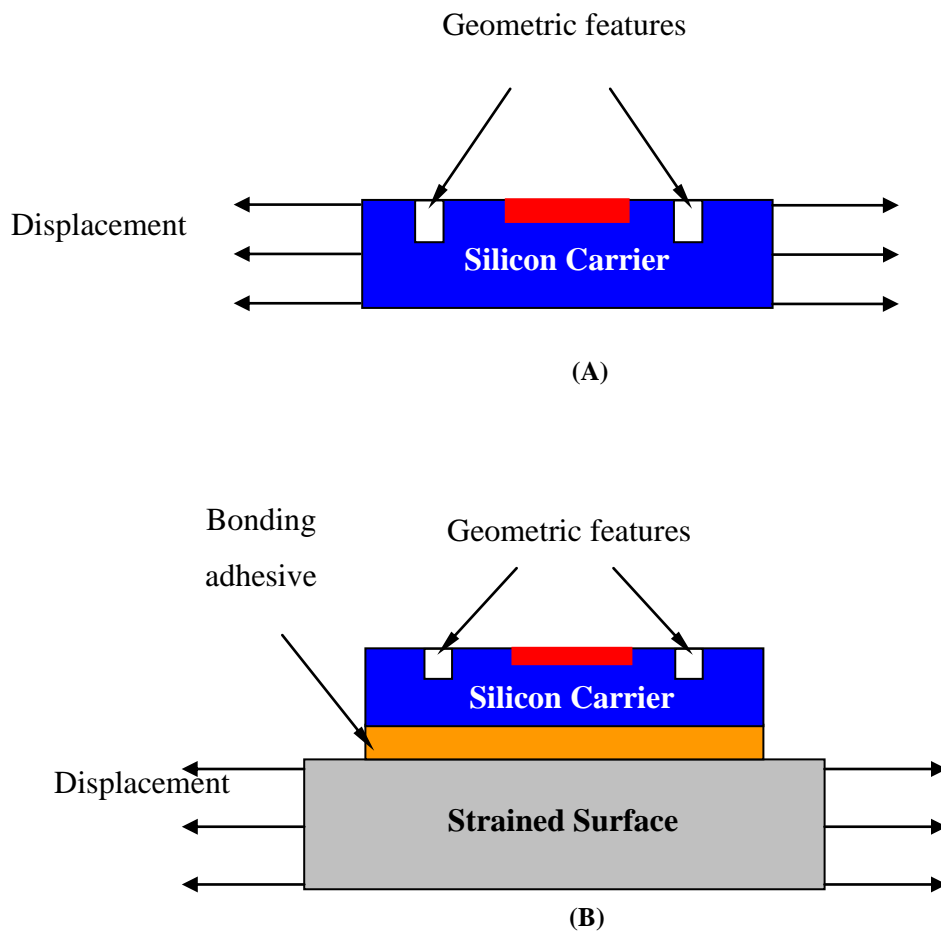
Figure 11 Schematic of the different FEA models (A) sensing chip with surface trenches and (B) full-model (strained surface, bonding layer and sensing chip with geometric features). Chip dimensions 10mm (length)×10mm (width)×500μm (thickness)
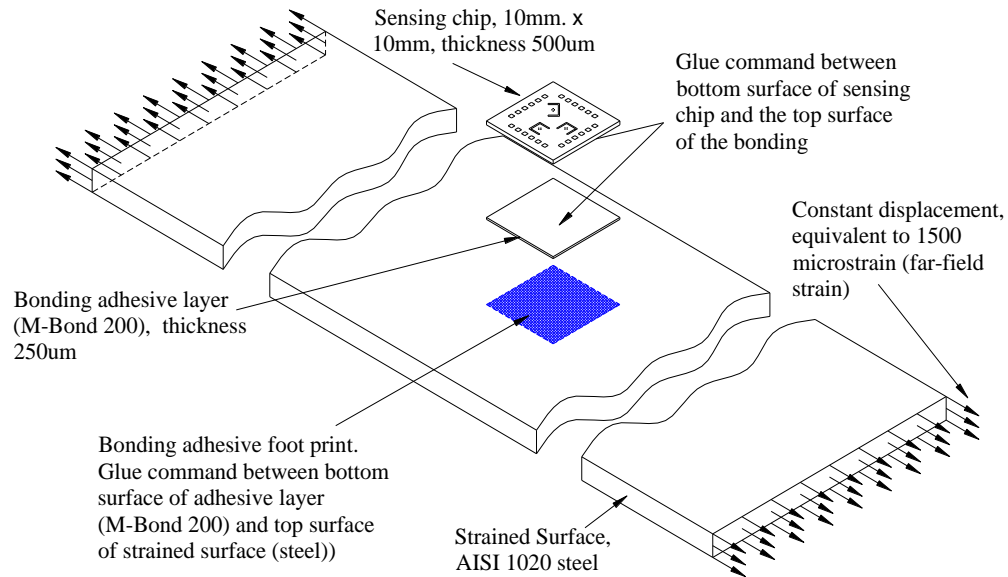
Sensing chip, 10mm. x
10mm, thickness 500um

Glue command between
bottom surface of sensing
chip and the top surface
of the bonding

Constant displacement,
equivalent to 1500
microstrain (far-field
strain)

Bonding adhesive layer
(M-Bond 200), thickness
250um

Bonding adhesive foot print.
Glue command between bottom
surface of adhesive layer
(M-Bond 200) and top surface
of strained surface (steel))

Strained Surface,
AISI 1020 steel

The individual resistor and the aluminum interconnections are removed from the 3D view for clarity.

Figure 12 Three dimensional representation of the full FEA model (strained surface, bonding layer and sensing chip with geometric features) illustrating boundary conditions between the different structural layers

4.3.1. Sensor Design Considerations

Due to their small size, MEMS devices place a challenge on handling process during development and application. To ease the chip handling, it was designed as 10mm×10mm square. These dimensions were considered appropriate to put more than one sensing unit and characterization structures on one sensing chip. Further, 10mm×10mm squares were convenient for subsequent packaging. Moreover, four piezoresistive elements were implanted on the top surface of the silicon carrier (chip) and connected in a full Whitestone bridge configuration. This full bridge serves two main functions; improves the temperature dependency of the sensor

characteristics by reducing the equivalent TCR of the full bridge and enhances the signal strength as discussed in Eqs. (36) and (37).

Additionally, the self-heating (Joule heating) of the gauge resistor has limited the input voltage of the sensor, which limits the output signal strength. The upper limit of the resistance value is set by Johnson noise. Although, dimensions of the piezoresistive elements do not appear in any equation, from the assumptions discussed during the development of the simplified model, small dimensions were favorable to reduce the strain gradient over the sensing element length. Therefore, 20μm×100μm with a junction depth of 1μm was considered acceptable. The doping concentration was investigated to determine the optimum value that will reduce temperature effect while maintaining reasonable sensor sensitivity.

Because p-type silicon has higher sensitivity compared to n-type silicon, it was selected to develop the sensing elements [71]. Moreover, it is more favorable from fabrication standpoint. After searching the available literature, no enough reliable data was found on the value of piezoresistive coefficients at different operating temperatures and different doping concentrations. Therefore, Kanda piezoresistance factor, P(N,T), was utilized to calculate (scale) the piezoresistive properties at different temperatures and various doping levels [61]. The piezoresistance factor is defined as the ratio between the piezoresistive coefficient at light doping concentration (less than 10^{17} atoms/cm^3) and room temperature (~ 25°C) and the piezoresistive coefficient at doping concentration (N) and temperature (T).

Figure 13 provides a schematic representation of the working principle of the sensing chip. As shown in this figure, the application of mechanical strain generates stress field, which alters the resistance of the gauges and hence contributes to the bridge imbalance in form of output voltage. Numerous sensor layouts were considered during the various stages of this study. However, only six sensor layouts went through full FEA simulation process. The results of all sensor designs are presented in Appendix F. To ensure solution convergence, the finite element mesh was refined.

Output

Voltage

| Applied | Chip | Stress/Strain | Gauge | Resistance | Bridge | Output |

Applied → Chip → Stress/Strain Field → Gauge → Resistance Change → Bridge → Output Voltage

Strain
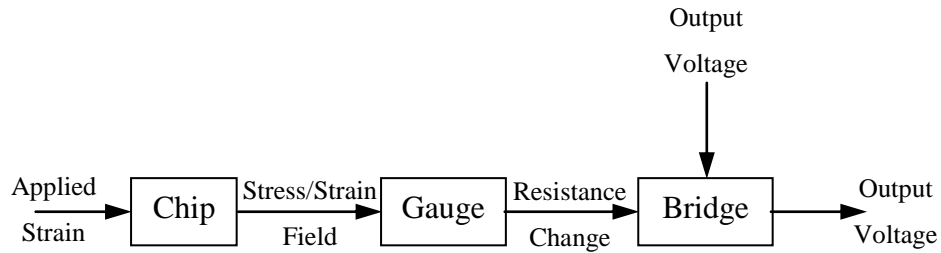
Figure 13 Schematic representation of the sensing chip working principle

4.3.2. Finite Element Analysis of the MEMS Sensor

As mentioned above, six sensor designs went through full FEA simulation. Figure 14 shows the different sensor layouts labeled from Design 1 to Design 6. Individual piezoresistors to characterize the sensing chips and to evaluate material properties were included on the same chip. The various sensor designs can be classified in four groups. The first group consists from Design 1 and Design 2 to test for the aspect ratio of the sensing unit. The second group consists from Design 2, Design 3 and Design 4 to test for the effect of the SCRs geometry with the same aspect ratio. The third group consists from Design 4 and Design 5 to test the aspect ratio of the sensing unit as well as the aspect ratio of the surface trenches. The last group consists from the Design 5 and Design 6 to test for trench geometry.

As shown in Figure 13, the silicon carrier is stressed in response to the applied mechanical strain. Accordingly, stress field is generated. Due to the existence of the SCRs around the sensing unit, the stress field is altered resulting in high stress intensity around the sensing unit. This has led to sensing sensitivity enhancement. As shown in Table 3, two elements types are used to construct the FEA model. In ANSYS® FEA computer package, SOLID187 is a 20-node tetrahedral 3D structural solid element with anisotropic material capabilities. This element is used to model the silicon chip carrier, which is mainly used as a transfer medium

54

for mechanical strain. Therefore, no piezoresistive properties are defined for this part of the FEA model. The second element type is SOLID226, which is a 20-node tetrahedral 3D structural solid element with anisotropic material capabilities. In addition, it is able to handle piezoresistive behavior and link it to the applied mechanical stress on the element, which is transferred through the silicon carrier.

The geometry of the sensing chip is constructed following a similar procedure described above for the simplified verification FEA model. Additional geometric features, namely surface trenches, are inserted in the top surface of the silicon carrier to act as stress raisers, which improves the sensor sensitivity. Three sensing unites are included on the sensing chip with three different orientations with respect to the applied strain direction, -45°, 0° and +45°. Each sensing unit is composed from four sensing piezoresistive elements that are connected in a full-bridge configuration, which is surrounded by the surface trenches. A three dimensional sample schematic of the sensor design is shown in Figure 16.

The input bridge voltage was 5 volts. The load was applied on the FEA model as a constant displacement equivalent to 1500 microstrain ($\mu\varepsilon$). The output results for this model are the bridge imbalance. Therefore, this output voltage is used to calculate the sensor sensitivity and the equivalent normalized resistance change of the sensing unit, which is then used to evaluate the piezoresistive gauge factor of the sensing unit. Johnson and 1/f noise level are calculated analytically and the MEMS strain sensor resolution is calculated using the sensitivity and the noise data. In this modeling process, uniform doping concentration is considered to carry out all the simulations. Moreover, Kanda's model [61] was utilized to simulate the effect of the varying operating temperature and doping concentrations.

The FEA model was meshed and mesh sensitivity analysis was carried out to ensure solution stability. The mesh sensitivity analysis was performed on each structural layer separately. Results of the mesh sensitivity are shown in Figure 17 through Figure 20. As shown in Figure 20, the piezoresistive sensing elements were the least sensitive part of the finite element model.
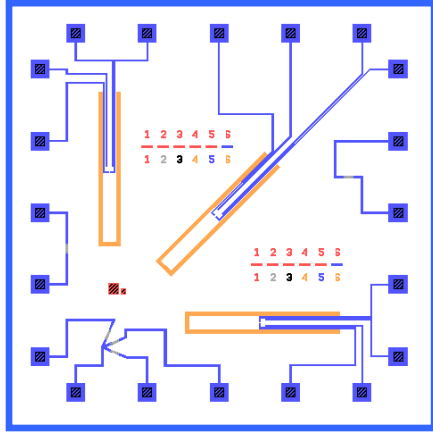
Design 1
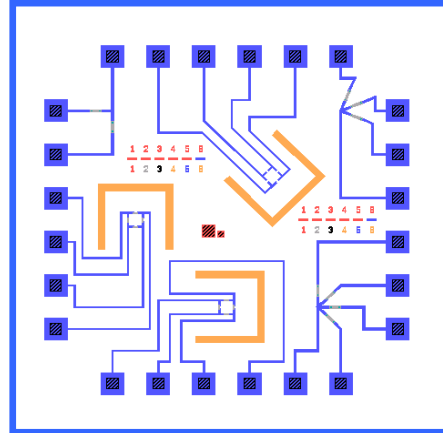
Design 2
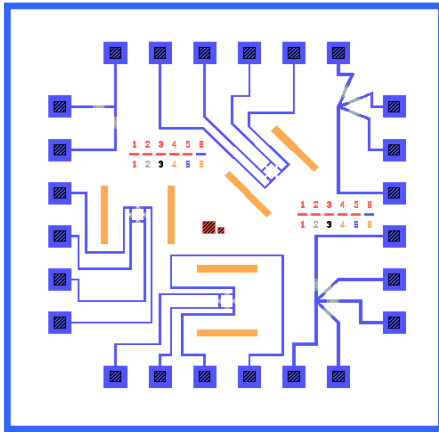
Design 3
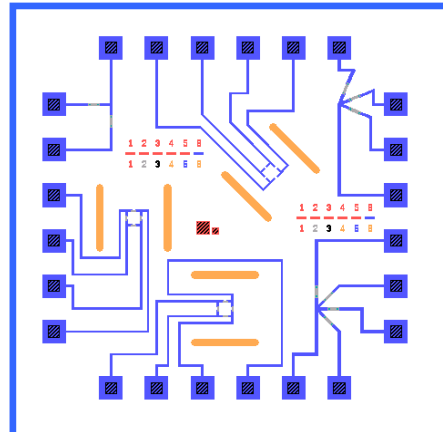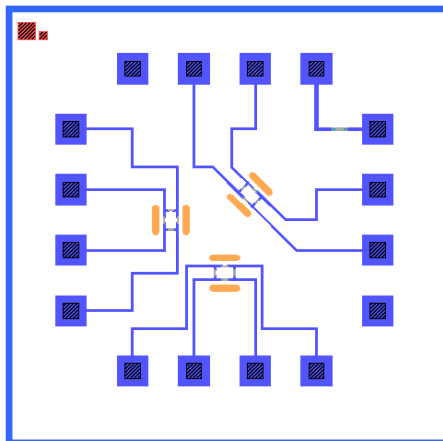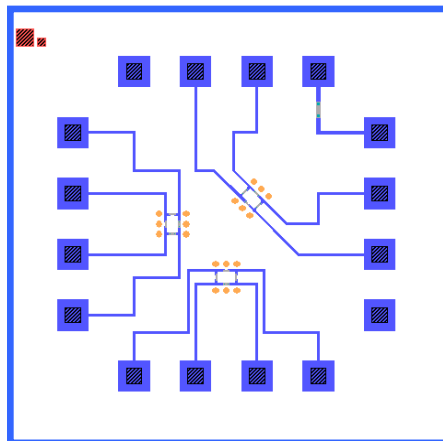
Design 4

Design 5

Design 6

Figure 14 Schematic of the different sensing chip designs as shown on the microfabrication masks. Figure 15 provides dimensions of various sensing units

56
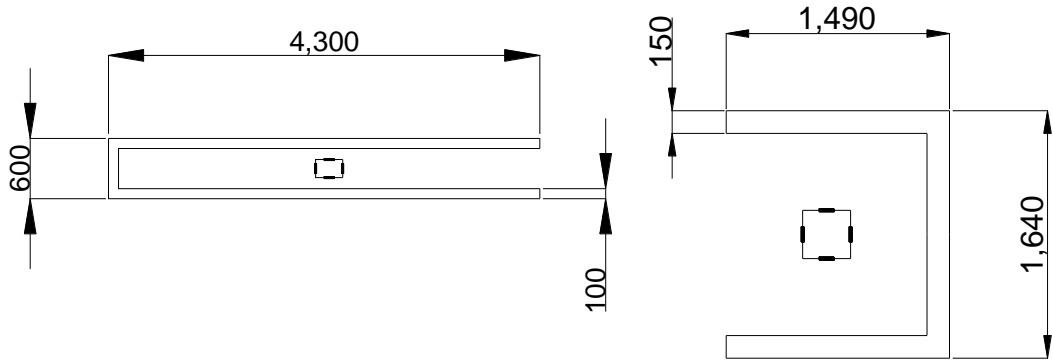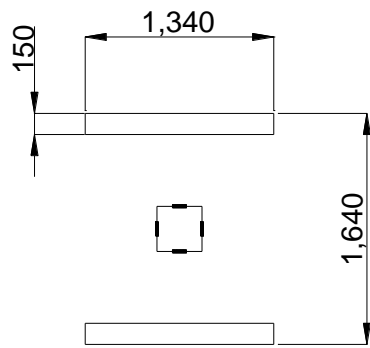
Design 1
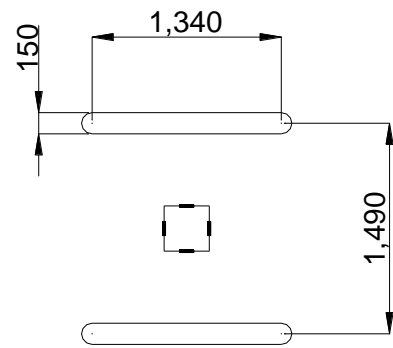
Design 2
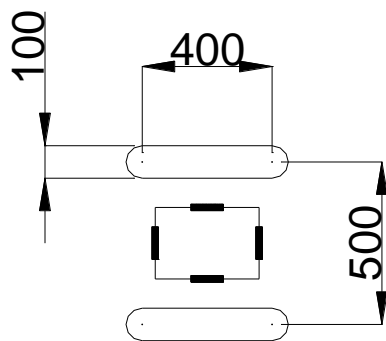
Design 3
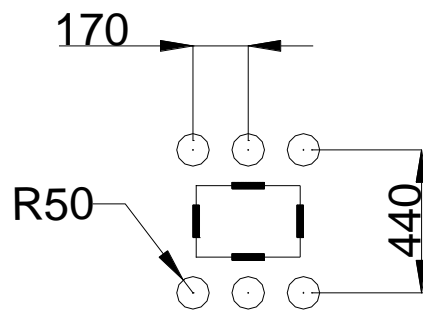
Design 4

Design 5

Design 6

Figure 15 Dimensions of various sensing units
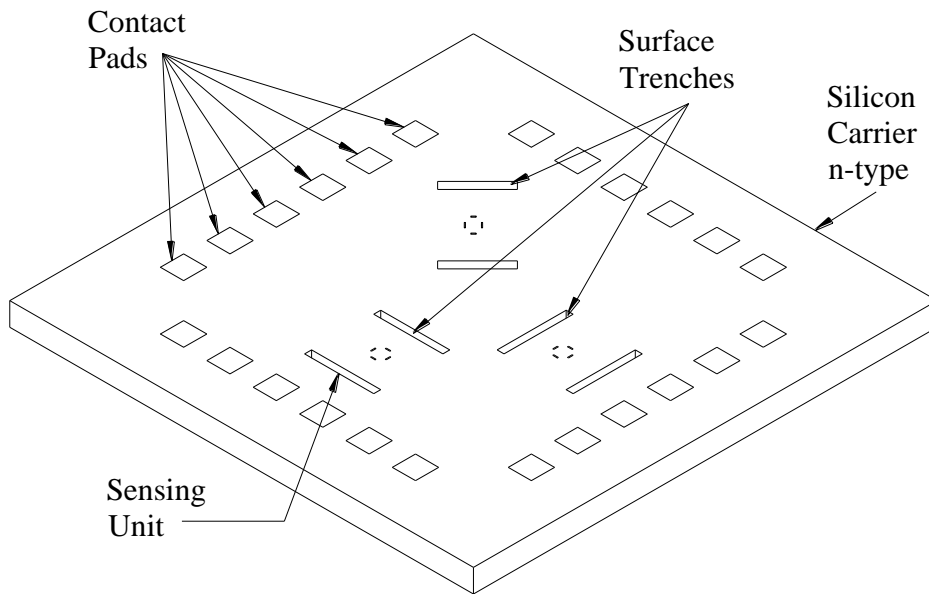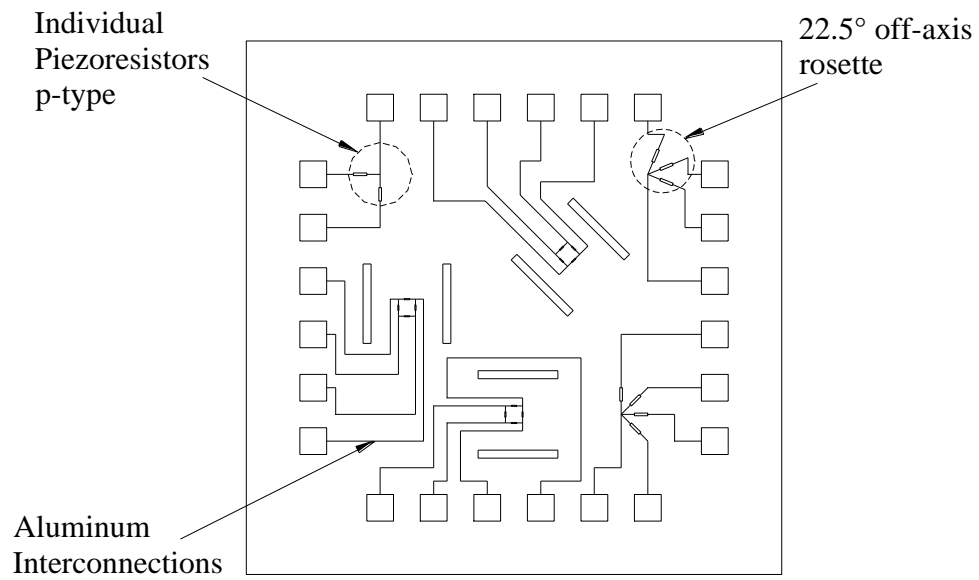
Individual
Piezoresistors
p-type

22.5° off-axis
rosette

Aluminum
Interconnections

Contact
Pads

Surface
Trenches

Silicon
Carrier
n-type

Sensing
Unit

*The individual resistor and the aluminum interconnections are
removed from the 3D view for clarity.*

**Figure 16 Schematic of the sensing chip (Design 3) showing the three sensing units and the
full bridge configuration. Chip dimensions 10mm (length)×10mm (width)×500μm (thickness)**
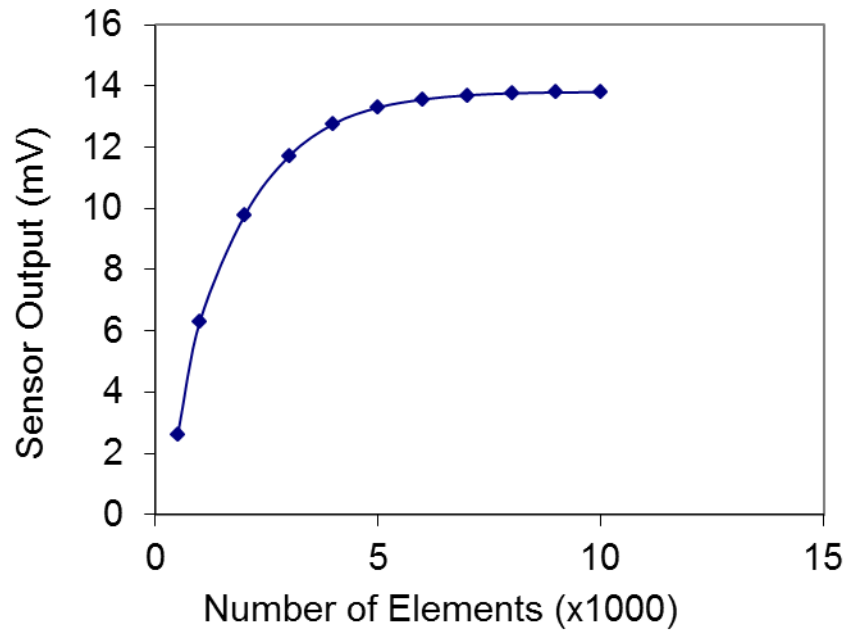
Figure 17 Results of mesh sensitivity analysis of strained surface
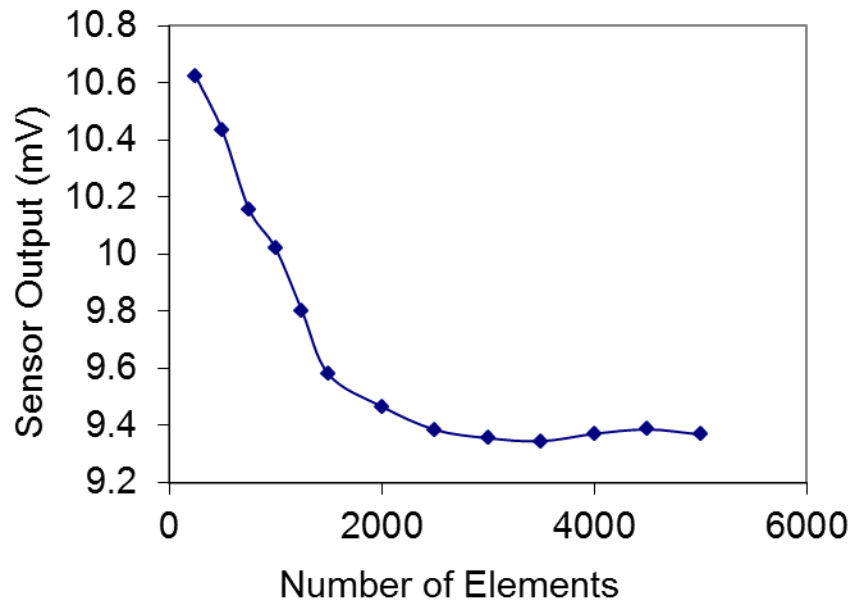
Figure 18 Results of mesh sensitivity analysis of bonding adhesive layer
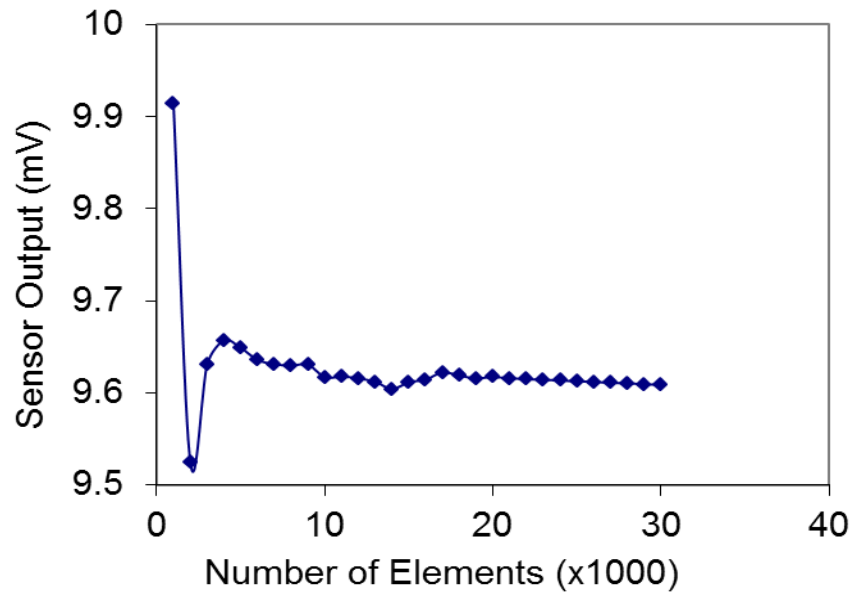
Figure 19 Results of mesh sensitivity analysis of sensor silicon carrier
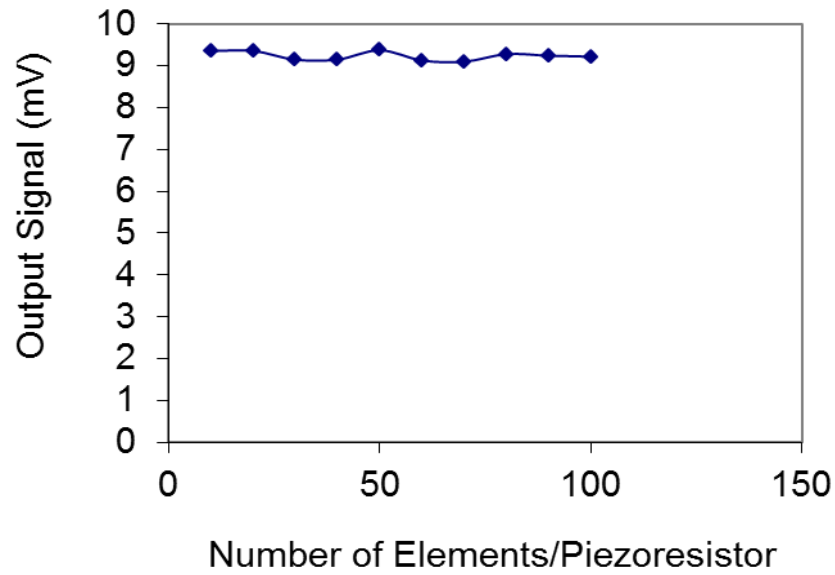
Figure 20 Results of mesh sensitivity analysis of piezoresistive sensing elements

60

4.4. Results of Finite Element Modeling

Design 1 was simulated first to determine the optimum doping concentration to prototype the proposed sensing chip. It is worth to mention that two microfabrication runs were performed in this study. The first microfabrication run was used to experiment with the microfabrication parameters. Only Design 1 was used in the first prototyping stage. In addition, this design was initially simulated to guide the development process.

4.4.1. Sensor Performance Analysis

The typical electrical resistance of the commercial semiconductor strain gauges is minimum of 1 kΩ and in metal foil gauges is 120 Ω or 350 Ω. Results from the FEA simulation showed that current sensor design has 15 KΩ/doped piezoresistors. This value can be adjusted (increased or decreased) and tuned based on the microfabrication parameters and piezoresistor dimensions. As result of the high resistance, the piezoresistive MEMS sensor is suitable for low-current and low-power applications. The decrease in doping level showed to increase the sensor sensitivity, however it has undesirable effect on the noise level; both *1/f* and Johnson.

The simulation results have been combined with the analytical modeling to construct the characteristic curves of the MEMS strain sensor. Figure 21 and Figure 22 illustrate the dependence of both Johnson and *1/f* noises on the doping concentration at different operating temperatures, respectively. Referring to Eq. (46), *1/f* noise does not appear to depend on the operating temperature. However, this noise source follows the same trend as Johnson noise with doping concentration. *1/f* noise was found to decrease as doping concentration increases.

On the other hand, due to the nature of Johnson noise as thermal energy fluctuation of the resistors, it was found to increase as the operating temperature increases. This trend is generally correct up to doping level of 10^{19} atoms/cm^3. At this doping level, all the curves tend to coincide and Johnson noise becomes temperature independent. It was also noted that increasing the doping level beyond 5×10^{18} atoms/cm^3 reduces the noise dependence on the operating

temperature and its absolute value, which improves the sensor performance. In addition, it is clear from Figure 21 and Figure 22 that the value of Johnson noise is lower than the value of *1/f* noise by more than two orders of magnitude, which makes the *1/f* noise dominating at low frequency range (1 Hz-1 kHz).

Figure 23 and Figure 24 depict the sensor output signal and sensitivity, respectively, versus doping level at different operating temperatures. It is clear that increasing doping level lowers the output signal and hence reduces the sensitivity. Moreover, working at high doping levels (more than 10^{19}atoms/cm^3) stabilizes the output signal and makes it temperature-independent. Further, when doping level more than 10^{19} atoms/cm^3 is used, the sensor output signal and sensitivity are reduced significantly. For example, piezoresistors with doping concentration of 10^{19} atoms/cm^3 lose approximately 35 percent of its sensitivity at low to moderate doping levels (10^{16}-10^{18} atoms/cm^3) at room temperature.

Generally, sensor sensitivity aspects favor low doping concentrations. However, another variable must be considered to develop the sensor. That variable is the sensor resolution. Resolution is defined as the minimum measurable value. Figure 25 shows the sensor resolution decreases with doping concentration. At high doping concentrations (more than 10^{19} atoms/cm^3), the sensor resolution is approximately 1 microstrain ($\mu\varepsilon$). However, continuous increase of the doping level results in a substantial decrease in the sensor sensitivity. Therefore, the competing performance parameters, resolution and sensitivity, reveals that optimum doping concentration can be evaluated, which will be used later in the prototyping process. It is worth mentioning that a trend might exist on Figure 25 beyond doping concentration of 5×10^{19} atoms/cm^3. Studying this trend, if any, is an interesting research point.

To select the optimum doping level, the signal to noise ratio (SNR) was plotted versus doping concentration under different temperature conditions. From Figure 26 it is found that doping level of 5×10^{19} atoms/cm^3 produces the highest SNR with temperature independent signal over temperature range of ±50 ^{o}C (225-325 ^{o}K). The sensor input voltage (V_i) is another parameter that can affect the sensor performance stability. At this stage of the work, the input voltage was selected

based on the SNR. In the upcoming sections, the sensor input voltage will be selected experimentally. From Figure 27 and Figure 28, it is clear that increasing the input voltage increases *1/f* noise and SNR. Moreover, sensitivity at this doping level is constant regardless of the operating temperature, as shown in Figure 24. Based on these results, input voltage from 3 to 8 V is selected for both the MEMS sensor and the microelectronics in the conditioning circuit.
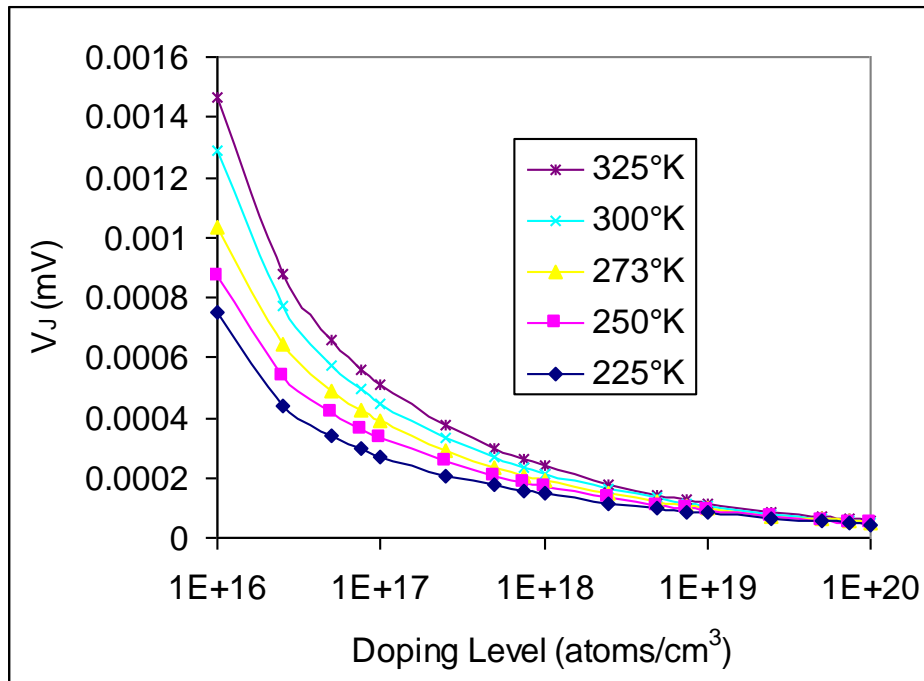
Figure 21 Johnson noise versus doping level at different operating temperatures
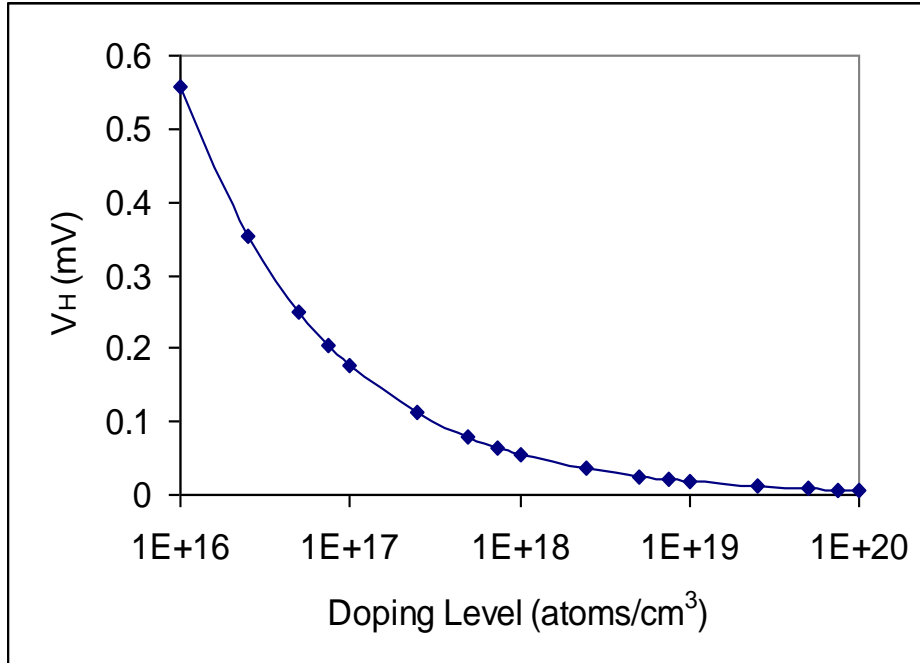
Figure 22 *1/f* **noise versus doping level at different operating temperatures for bridge input**
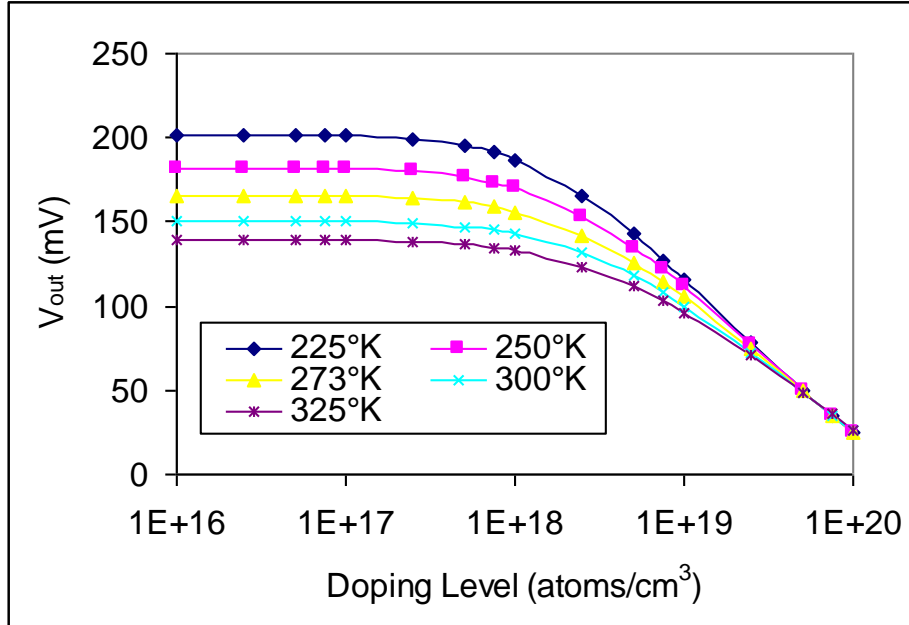
of 3V

Figure 23 Sensor output versus doping level at different operating temperatures for bridge
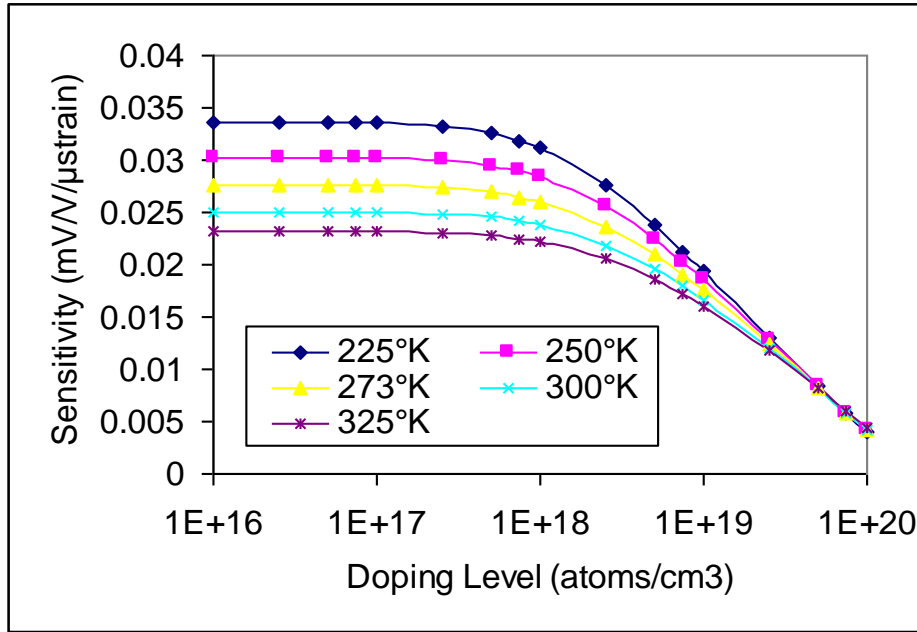
input of 3V

Figure 24 Sensor sensitivity versus doping level at different operating temperatures
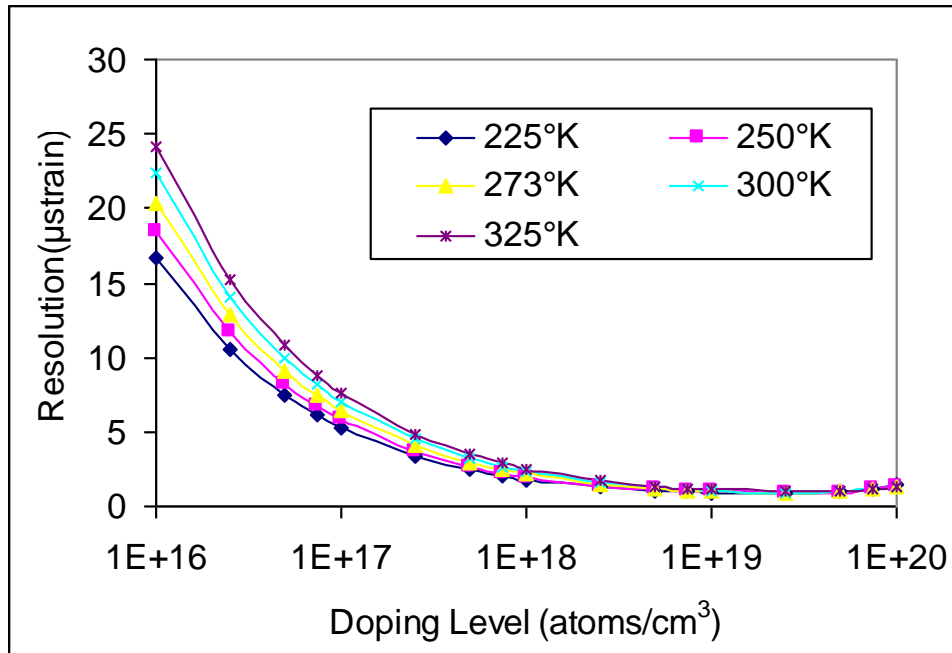
Figure 25 Sensor resolution versus doping level at different operating temperatures for bridge input of 3V
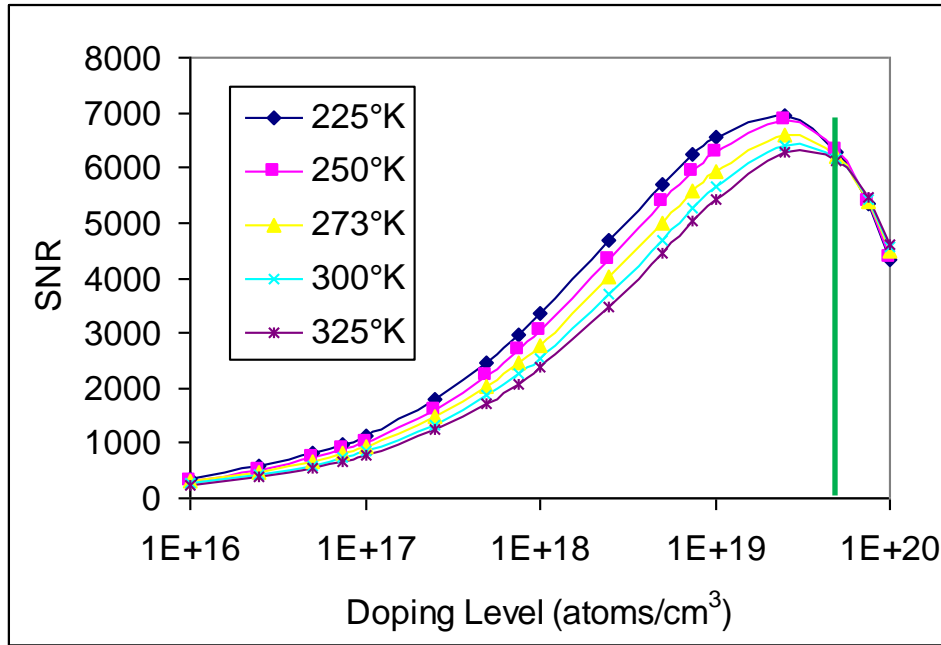
Figure 26 Signal to Noise Ratio (SNR) versus doping level at different operating temperatures for bridge input of 3V
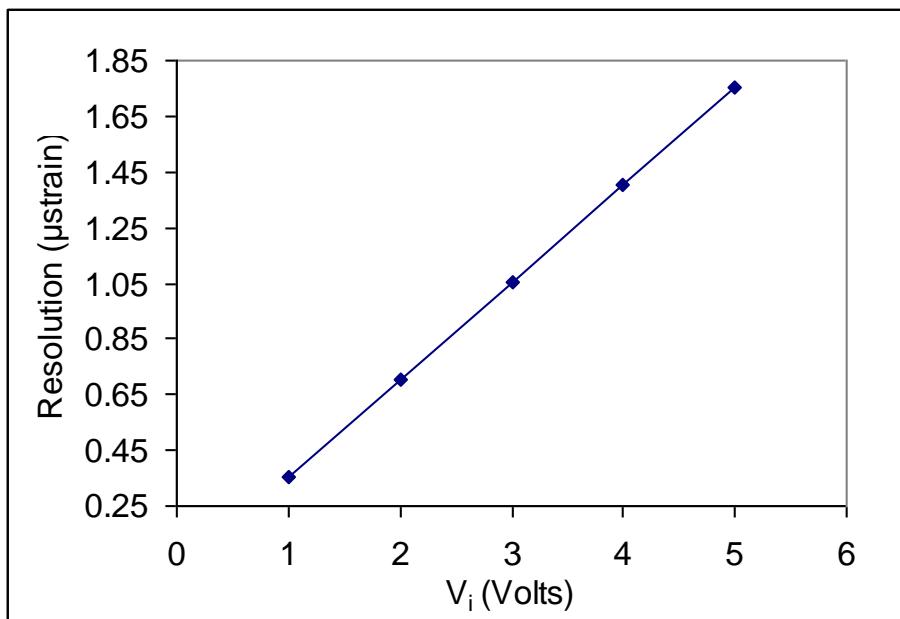
Figure 27 Sensor resolution dependence on the bridge input for doping level of 5×10^{19} atoms/cm^3
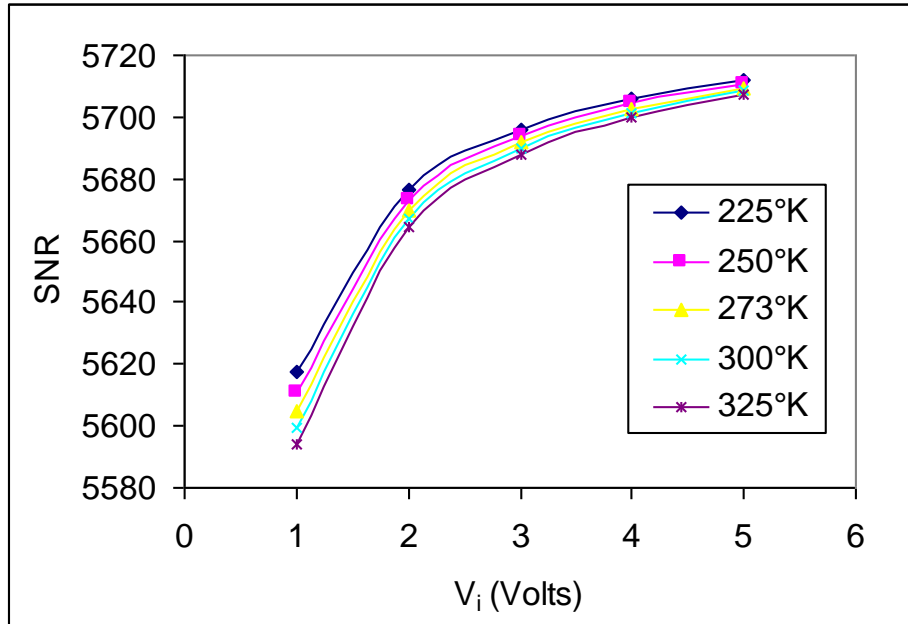
Figure 28 Signal to Noise Ratio (SNR) dependence on the bridge input for doping level of 5×10^{19} atoms/cm^3 at different temperatures

4.4.2. Effect of Bonding Adhesive on Sensor Performance

Before presenting the results in this section, it is crucial to differentiate between two quantities; sensor equivalent gauge factor and piezoresistive gauge factor. The sensor equivalent gauge factor is defined as the ratio between the measured normalized resistance changes, from the sensing piezoresistors in response to the applied strain on the strained surface, far-field strain. On the other hand, piezoresistive gauge factor is defined as the ratio between the measured normalized resistance changes, from the sensing piezoresistor in response to the directly-applied mechanical strain on the sensing element, near-field strain.

Another key parameter that was considered in the FEA simulation is the effect of bonding material on the sensor signal loss. The signal loss is dependent on the modulus of elasticity and the layer thickness of the used bonding adhesive. Therefore, a parametric FEA study was performed to guide in the selection of the

67

boding adhesive and to help developing appropriate installation procedure. FEA was employed to evaluate the signal loss and the change in gauge factor using different modulus of elasticity and adhesive layer thickness. The results of this investigation are shown in Figure 29 and Figure 30. From these figures, it is clear that at low modulus of elasticity the effect of bonding layer thickness is negligible. However, as the modulus of elasticity increases, i.e. stiffer adhesive, the adhesive layer thickness has major influence. Therefore, it can be concluded that a thin layer of a bonder adhesive that has high modulus of elasticity after curing is highly recommended to minimize the signal loss and maximize the sensor equivalent gauge factor.
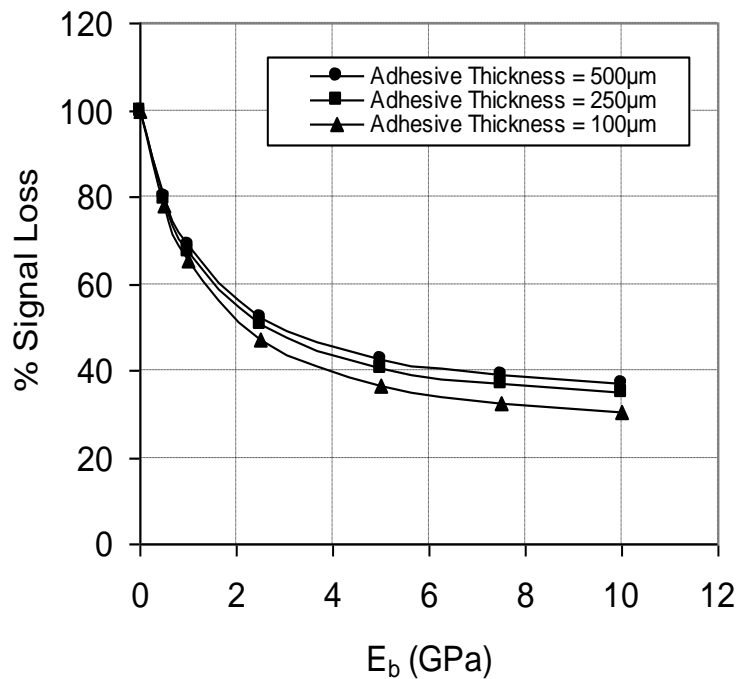
Figure 29 FEA simulation results describing effect of material properties of bonding adhesive (modulus of elasticity, E_b) and bonding adhesive thickness on percentage signal loss, $V_i = 5$ Volts, doping concentration = 5×10^{19} atoms/cm^3
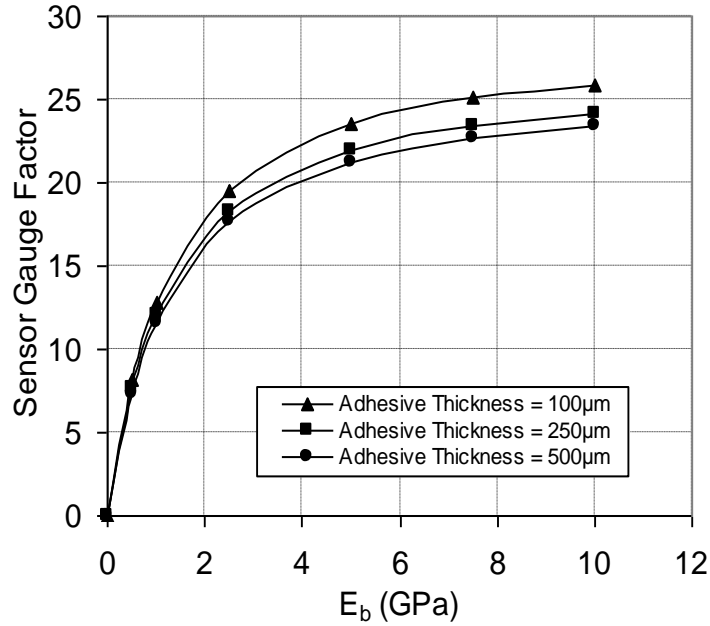
Figure 30 FEA simulation results describing effect of material properties of bonding adhesive (modulus of elasticity, E_b) and bonding adhesive thickness on sensor gauge factor, $V_i = 5$ Volts, doping concentration = 5×10^{19} atoms/cm^3

The M-bond 200 used in the sensor installation has a modulus of elasticity of ~ 0.5GPa. Material properties of the M-bond 200 was acquired from Vishay Precision Group [137]. Referring to Figure 49, the relation between the near-field strains to the far-field strain is approximately 16 %, which was evaluated experimentally using the testing specimen with thin-foil starin gauge and readings from the testing machine. If Figure 29 is used to evaluate the same ratio, it would be approximately 20%. This difference can be attributed to imperfection in the bonding adhesive after curing. However, the FEA can be considered accurate at this stage.

4.4.3. Sensitivity Analysis of Geometric Characteristics

Design 3 and Design 4 showed the highest performance. Therefore, they were selected for the sensitivity analysis. Finite element simulation was employed to evaluate the effect of the geometric features or stress concentration regions

(SCRs). These two designs were selected because they had the highest performance characteristics during mechanical testing. Three different values (0.5µm, 1µm and 2µm) of the piezoresistive element thickness (junction depth) were analyzed. The FEA simulation results showed that the output signal strength has minor dependency (less than 0.1% over the range 0.5µm-2µm) on the piezoresistors' thickness. From microfabrication standpoint, it is easier to create shallow piezoresistive elements with more uniform properties. Moreover, it is more favorable to have thin piezoresistive elements to minimize stress/strain gradient perpendicular to the chip surface. The analytical solution of flat sensing chip was calculated and taken as a reference. Generally, as mentioned above, due to neglecting π_{11} and π_{12}, the output signal from the analytical solution is higher than FEA results; however, the difference between the two solutions decreased as the doping concentration increased. At high doping concentrations (more than 1×10^{19} atoms/cm^3), π_{11} and π_{12} are approximately 25% of their values at light doping levels [61].

As expected, the SCRs altered the stress distribution within the sensing unit in both simulated sensor designs. Therefore, placing the full sensing bridge in locations with high stress concentration improved the sensing sensitivity. Figure 31 and Figure 32 show the longitudinal (x-direction) stress distribution for Design 3 and Design 4 in response to applied longitudinal and transverse strain, respectively. Although Design 3 has higher stress concentration in the proximity of the sensing elements due to the sharp corner effect, Design 4 (Figure 31-B and Figure 32-B) has more uniform stress concentration regions. The FEA mesh in the vicinity of the SCRs for Design 3 was further refined and the longitudinal stress was found to be similar to the first case. Therefore, if uniform stress distribution is required, Design 4 will be chosen. On the other hand, if higher stress concentration value is required, Design 3 is more favorable. Moreover, comparing these two figures confirmed that the introducing the SCRs in the silicon chip significantly reduced the sensor cross sensitivity.

The percentage signal change (% signal change) due to SCRs was calculated. The percentage signal change is defined as the increase or decrease in the sensor

output signal compared to a flat sensing chip divided by the output signal of a flat sensor. Therefore, percentage sensitivity change is proportional percentage signal change. Figure 33 and Figure 35 present the dependency of the percentage signal change of Design 3 and Design 4 on the SCRs depth at doping concentration of 5×10^{19} atoms/cm^3. The percentage signal change showed to increase as the depth of the trenches increases. Then, the sensitivity decreases after specific SCR depth. The SCRs depths at the peak values are 300µm and 400µm for percentage signal change (longitudinal) and percentage signal change (transverse), respectively. Due to the high similarity between the two SCRs designs, SCRs depths at peak values for both designs were the same; however, the percentage signal changes were different. This can be the result of the tendency of the top surface of the chip to bend beyond certain SCRs depth, which slightly counterbalances effect of the applied mechanical strain. Moreover, these two figures demonstrate that incorporating SCRs in the sensor silicon carrier enhanced the longitudinal sensitivity (positive percentage signal change in response to longitudinal loading). On the other hand, the SCRs showed to decrease the effect of the sensor cross sensitivity (negative percentage signal change in response to transverse loading).

In order to select the proper SCRs depth, the signal ratio (longitudinal sensitivity/transverse sensitivity) was calculated to understand the relative difference between Design 3 and Design 4. The results of these calculations are presented in Figure 34 and Figure 36 for Design 3 and Design 4, respectively. It was found that SCR depth of 400µm provides the maximum signal ratio for both designs. Opposing to the previous conclusion, Design 4 has higher signal ratio. The maximum signal ratios were approximately 25 and 40 for Design 3 and Design 4, respectively. In the case of a flat sensing chip, the sensitivity ratio is unity. Based on the simulation results, it is clear that the sensor sensitivity can be boosted by introducing SCRs in the sensor silicon carrier compared to a flat sensing chip design of the same thickness. The effect of doping concentration on the percentage signal change and the signal ratio was also investigated. It was found that doping concentration has minor influence on these parameters for constant temperatures. On the other hand, it only affects the output signal strength

and the sensor thermal drift when considering application under varying temperature conditions. The dependence of percentage signal change both longitudinal and transverse on SCR depth, shown in Figure 33 and Figure 35, were constructed using curves fitting. The curve fitting parameters are listed in Table 4 and Table 5.

(A) **(B)**
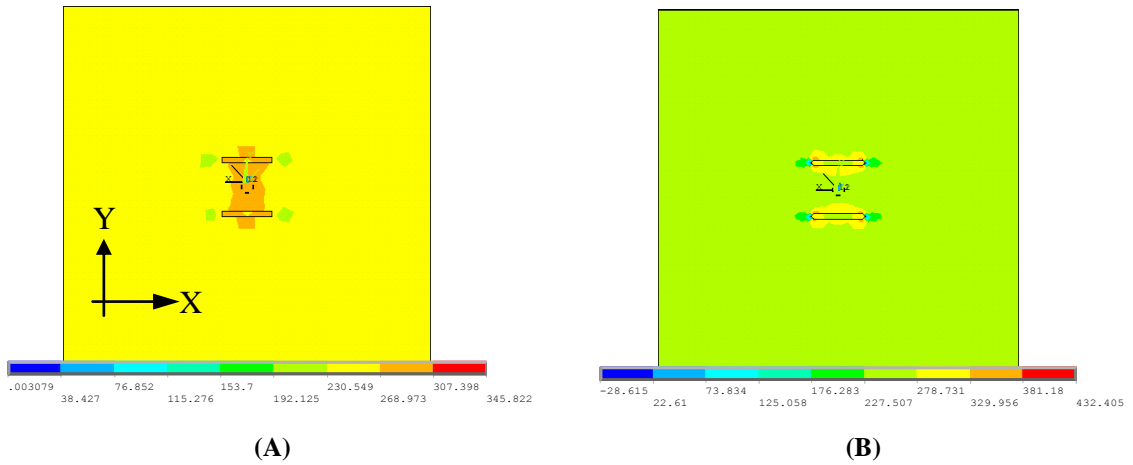
Figure 31 Longitudinal (x-direction) stress distribution in response to longitudinal loading (A) Design 3 and (B) Design 4, SCR depth = 300μm. Stress is expressed in MPa

(A) **(B)**
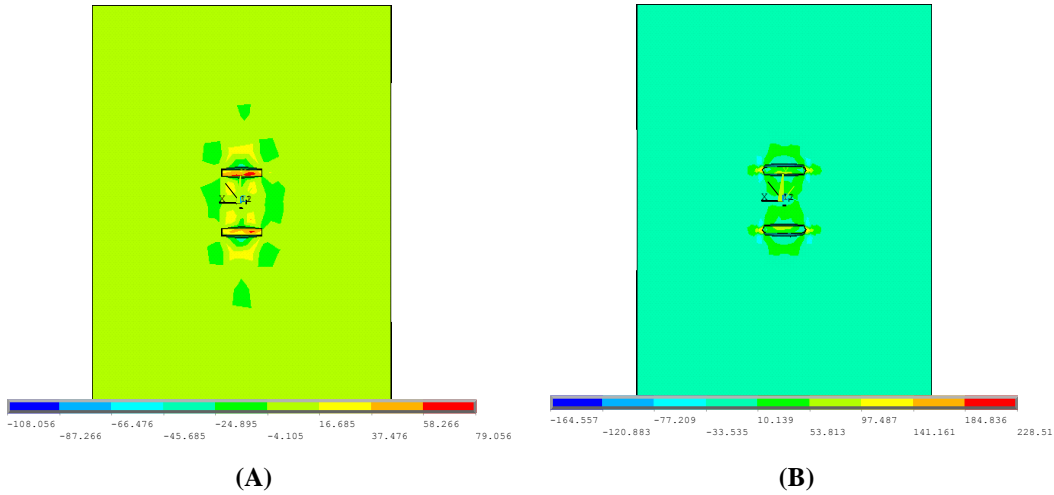
Figure 32 Longitudinal (x-direction) stress distribution in response to transverse loading (A) Design 3 and (B) Design 4, SCR depth = 300μm. Stress is expressed in MPa

72
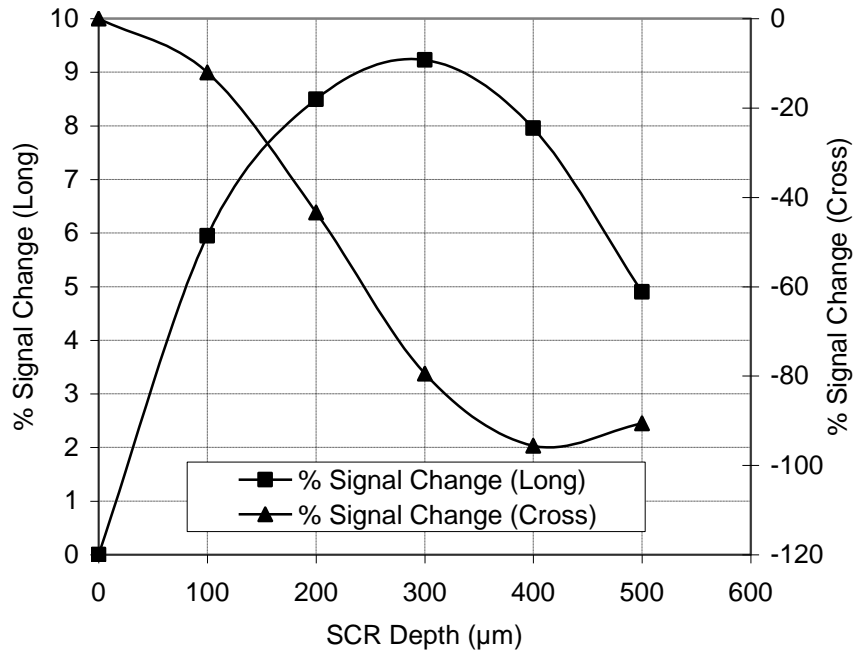
Figure 33 Effect the SCRs depth on the % signal change both longitudinal and transverse, V_i = 5 V, doping concentration of 5×10^{19} atoms/cm^3 (Design 3)
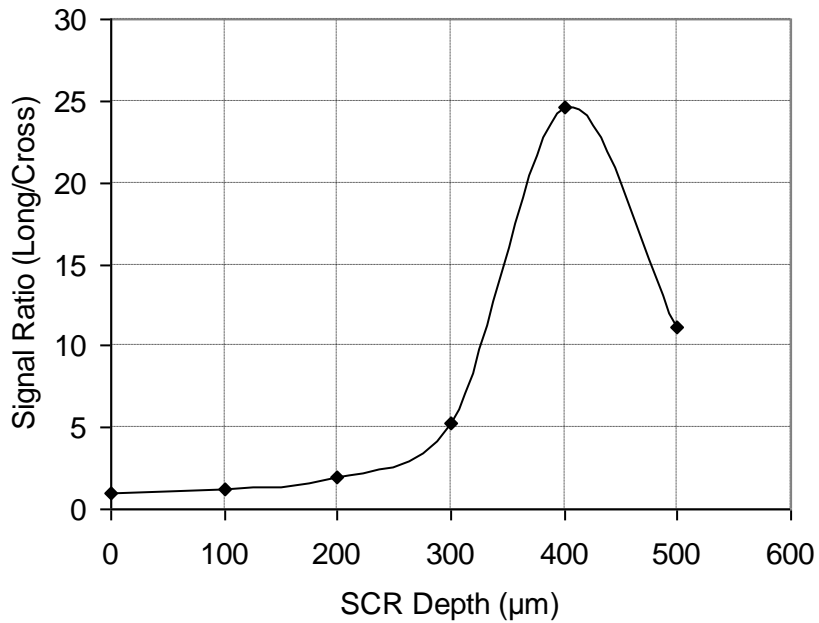
Figure 34 Effect the SCRs depth on signal ratio (longitudinal sensitivity/cross sensitivity), V_i = 5 V, doping concentration of 5×10^{19} atoms/cm^3 (Design 3)
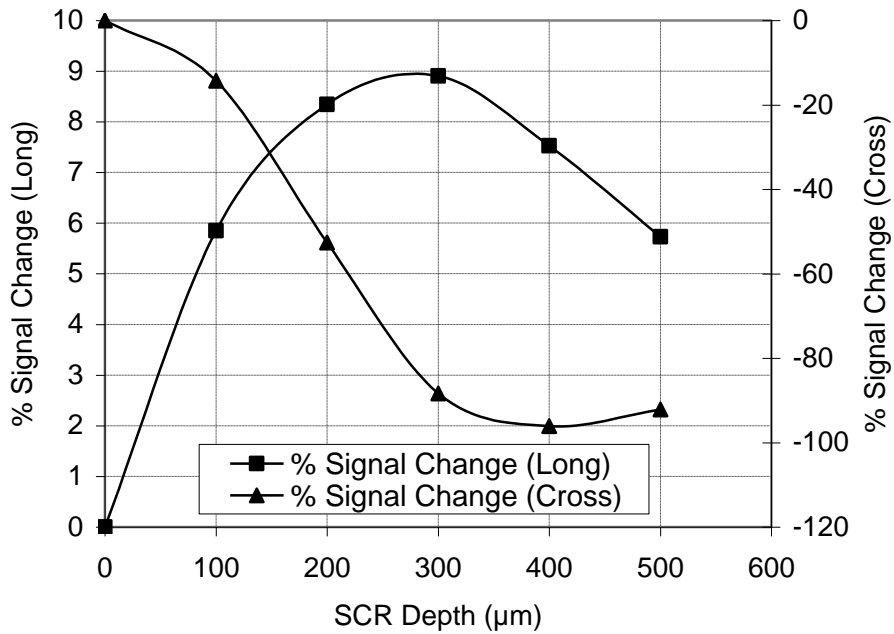
Figure 35 Effect the SCRs depth on the % signal change both longitudinal and transverse, V_i = 5 V, doping concentration of 5×10^{19} atoms/cm^3 (Design 4)
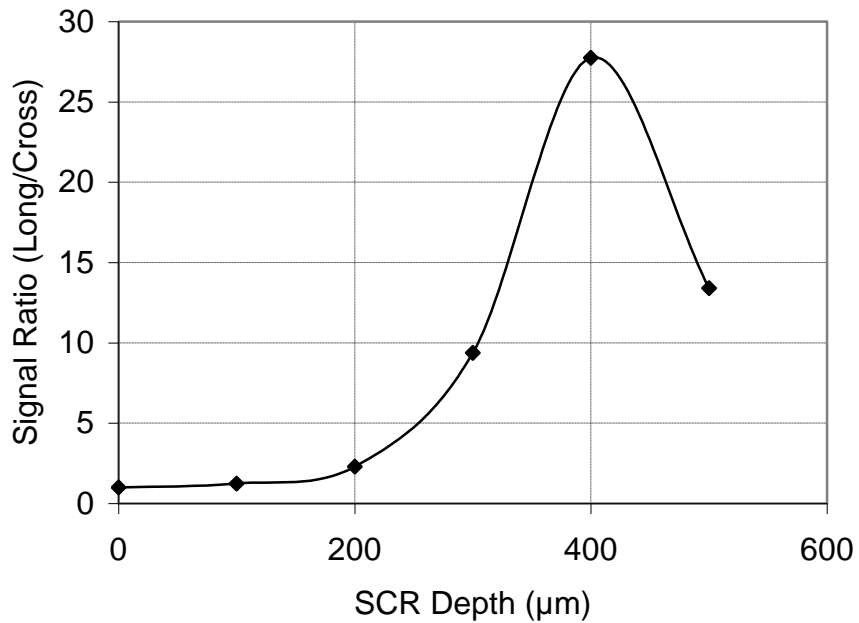
Figure 36 Effect the SCRs depth on signal ratio (longitudinal sensitivity/cross sensitivity), V_i = 5 V, doping concentration of 5×10^{19} atoms/cm^3 (Design 4)

Table 4 Curve fitting parameters of the relationship shown in Figure 33 and Figure 35 for % Signal Change (Long)

Shape of Formulae	$y = a + bx + cx^2 + dx^3 + ex^4$				
	a	b	c	d	e
Design 3	0.009	0.08	-0.00025	3.52×10^{-7}	-2.83×10^{-10}
Design 4	0.009	0.08	-0.00012	1.36×10^{-7}	0

Table 5 Curve fitting parameters of the relationship shown in Figure 33 and Figure 35 for % Signal Change (Cross)

Shape of Formulae	$y = a + b \times \cos(cx + d)$			
	a	b	c	d
Design 3	-48.78	48.91	0.0074	-0.018
Design 4	-50.25	51.56	0.0074	0.122

4.5. Limitations of the Finite Element Modeling

Although the FEA modeling process captured the most important characteristics properties of the physical model, there are some limitations on the FEA model. Most of these limitations are related to the microfabrication process. From a real world perspective, it is almost impossible to create sharp corners, which affect the developed stress field. Moreover, it is very hard to avoid the surface roughness inside the surface trenches, which is randomly developed. Additionally, the sensing noise is calculated analytically due to the limited capabilities of the FEA computer package. Finally, the charge carrier life has not been modeled due to the same reason; however, it is reported that the impurity concentration deteriorates due to the applied current/voltage effect, which can be considered an interesting area of research [131].

Chapter 5 – Sensor Microfabrication

Semiconductors devices are typically fabricated from circular slices of silicon referred as wafers, which have been cut from single crystal ingots. This chapter presents the prototyping process of the piezoresistive sensing chips. The mentionable achievement specific to this part of research is the standardization and repeatability of the microfabrication process. Moreover, this chapter highlights the selection of microfabrication parameters to improve the sensing chip sensitivity, which was achieved through sensitivity analysis using FEA, as described in Chapter 4. The following sections introduce the relevant efforts to the chip microfabrication process.

5.1. Selection of Sensor Substrate

In Micro Electro Mechanical Systems (MEMS) field, the majority of prototyped microdevices are fabricated from (100) silicon substrates. During microfabrication, in addition to easy handling, the sensor has to be robust enough to sustain the harsh operating conditions. Conventional thickness of double side polished (DSP) wafers is $500\pm25\mu m$. Therefore, the thickness of the sensing chip has the same value ($500\pm25\mu m$). Originally backside etching was planned. Therefore, DSP wafers were selected for proper backside alignment. However, due to technical limitations in the microfabrication facility, the backside alignment was extremely difficult. As a result, backside etch was not performed, i.e. single side polished wafers could have been used instead of the DSP ones.

5.2. Mask Design

AutoCAD® was used to construct the initial layouts of the microfabrication masks. AutoCAD® layouts were utilized to measure the relative distances between the different features. Subsequently, L-Edit® Software from MEMS-Pro® was used to design the microfabrication masks. Using L-Edit® Software, the different layers of the designed masks were converted into GDSII format. The GDSII files were used to develop the microfabrication masks. Figure 14 shows

the plan view of the microfabrication masks for the different sensor designs. The microfabrication of the sensing chips required five masks.

All masks are non-inverted except mask#4 (metallization). 36 sensing chips were fabricated per wafer. To properly align the five masks, different alignment marks have been employed. When designing the metallization mask, certain factors have been taken into account. First, the width of the aluminum traces have to be greater than the width of the piezoresistive element connected to them. Second, the overlap between the aluminum and the piezoresistive elements is a minimum of one square of piezoresistor. In this work, the width of the aluminum metallization was double the width of the piezoresistive element, which allowed reasonable tolerance for mask misalignment and aluminum over-etching. The alignment between the various masks was done with reference to one mask (mask#1 in the current case). This technique proved to minimize the mask alignment error and eliminated the progressive alignment error, i.e. only first order error is included, which reduced the total alignment error between masks during the microfabrication process.

5.3.   Process Overview

This section summarizes the microfabrication process flow. Appendix B provides the full details on the microfabrication procedure with specific values of the parameters. To study the geometric effect on the sensor sensitivity, various layouts are considered, which resulted in six sensor designs. All six designs have undergone through the same microfabrication steps using one microfabrication mask.

Figure 37 illustrates the top view of the so-called Design 3 sensing chip as shown on the microfabrication mask. The sensing chip has three sensing units. Each sensing unit is defined by two parallel deep SCRs etched along the sensing unit. The trenches make 0°, 45°, and 90° with [110] direction. Between the two SCRs, four piezoresistive elements are connected in a full-bridge configuration to partially compensate for the temperature effect. Moreover, piezoresistive rosettes with different number of elements are included on the same chip to facilitate

subsequent characterization. Figure 38 depicts the evolution of wafer cross-sectional during fabrication. To prototype the various layouts of the sensing chip, a five-mask microfabrication process flow is used to prototype the sensor. 4-inch (100) n-type double side polished silicon substrates with the primary flat along [110] direction is the starting material. The wafer has thickness of 500 ± 25 μm, bulk resistivity of 10 Ω.cm, and total thickness variation less than 1 μm. As shown in Figure 38, the microfabrication process flow starts by wafer cleaning in piranha solution (3 parts of H_2SO_4 + 1 part of H_2O_2). After wafer cleaning, the following fabrication steps are performed

1. Wet thermal oxidation to grow 1200nm of thermal oxide at 1000^oC for 8 hrs in wet N_2 atmosphere.
2. Lithography to pattern the first mask (alignment marks).
3. Reactive Ion Etching (RIE) and Deep Reactive Ion Etching (DRIE) to pattern the first mask in the silicon substrate.
4. Lithography to define the piezoresistors' locations using the second mask (doping windows).
5. RIE to open windows for ion implantation.
6. Boron ion implantation with different doses or fluences (5.20×10^{12}, 5.20×10^{13}, 5.20×10^{14}, 5.20×10^{15} and 5.20×10^{16} atoms/cm^2) at energy level of 100 keV to create the p-type piezoresistive elements.
7. Masking oxide layer removal using RIE.
8. Annealing at 1100^oC for 15 minutes.
9. Wet thermal oxidation to grow insulating oxide layer for one hour at 1000^oC.
10. Lithography to pattern the contact via for the aluminum contacts using the third mask (contact via openings).
11. RIE to open contact via.
12. Lithography to pattern the surface trenches using the fourth mask (surface features).

78

13. RIE then DRIE to pattern the fourth mask in the silicon substrate to a depth of about 100μm.

14. Aluminum sputtering for 30 minutes to get aluminum layer of thickness 500nm.

15. Lithography to define metallization traces and interconnects using the fifth mask (metallization and interconnections).

16. Aluminum etching.

17. Aluminum sintering to improve ohmic contact between the p-type silicon and aluminum.

18. Wafer dicing, preparation for wire bonding and testing.

To select the drive-in (annealing) conditions in step 8, which can achieve maximum activated fraction of implanted dose (fluence), trial test specimens were annealed at different temperatures and times. The annealing temperature varied from 950°C to 1200°C with intervals of 50°C, and the time was changed from 5 minutes to 30 minutes with intervals of 5 minutes. It was found that maximum activated fraction of the implanted fluence, approximately 41%, is attained at 1100°C for 15 minutes. These annealing conditions were used for subsequent work, i.e. all tested sensing chips have been annealed at 1100°C for 15 minutes. In addition, further oxidation (step 9) provided further annealing, which increased the fraction of the activated dose to approximately 43%. This improvement can be due to the fact that the annealing process (step 8) was able to partially recover the lattice damage and the oxidation-annealing step continued to activate the charge carriers. The fraction of the implanted dopant, which was not activated during annealing, was lost through diffusion. The percentage activation can be improved by rapid thermal annealing (RTA) before step 8. Alternatively, annealing with very short time at high temperature, denoted as spike annealing, can also minimize diffusion associated with a given portion of the dopant. Generally, in spike annealing, the activated fraction of boron increases monotonically with temperature and remains relatively insensitive to the implant fluence [138]. Unfortunately, spike annealing and RTA were not available to the authors of this

work at the time of fabrication. On the other hand, activation of the implants using these techniques, spike annealing and RTA, can leave residual lattice defects, and thus have influence on junction properties.
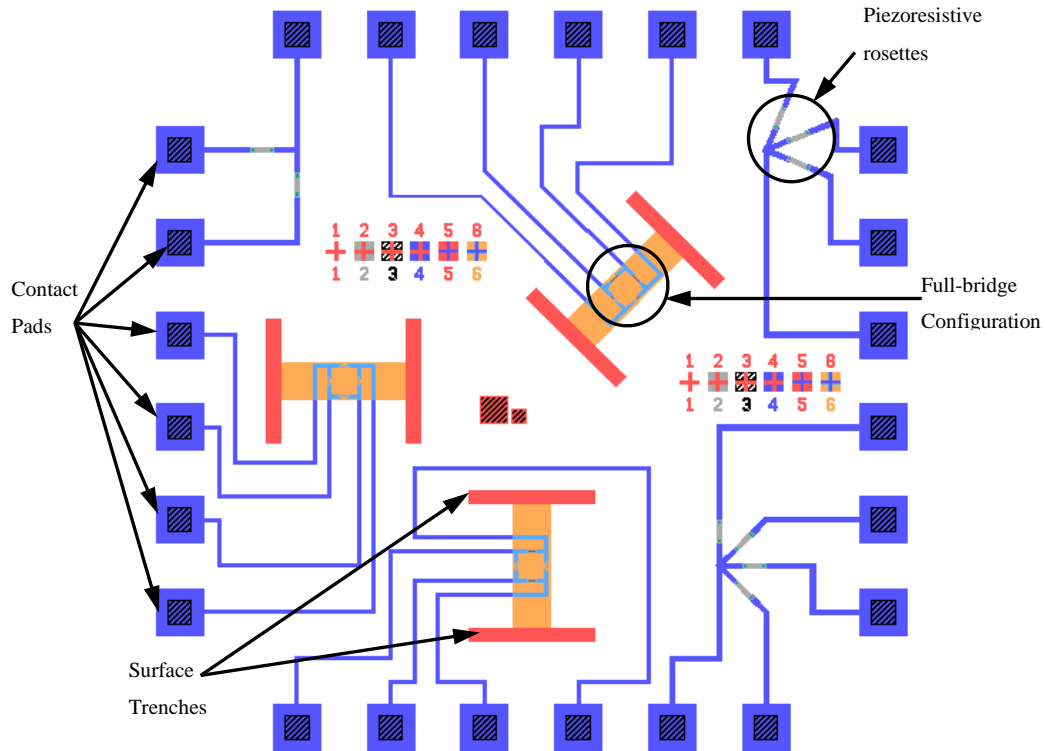
Figure 37 Top view of the sensor Design 3. The sensing units make 0°, 45°, and 90° with [110] direction. The four piezoresistive elements forming the sensing are connected in a full-bridge configuration that is parallel to the sensing unit

Wafer preparation and cleaning		Mask oxide removal Drive-in Thermal oxidation	
Thermal oxidation		Lithography (mask#3)	
Lithography (mask#1)		RIE	
Reactive ion etching (RIE)		Photoresist strip and cleaning	
Photoresist strip and cleaning		Aluminum sputtering	
Deep reactive ion etching (DRIE)		Lithography (mask#4)	
Lithography (mask#2)		Aluminum etching Photoresist strip and cleaning	
RIE		Lithography (mask#5)	
Photoresist strip and cleaning		RIE Photoresist strip and cleaning	
Boron ion implantation		DRIE Cleaning Dicing	

N-type silicon
Thermal oxide
Photoresist
P-type silicon
Aluminum

Sensing Unit
(Design#2)

Figure 38 Schematic of the microfabrication process to build the sensing unit

81

Chapter 6 – Experimental Method

The most common technique to calibrate stress/strain sensors involves subjecting the silicon chip to a known stress or strain. In this method, a controlled uniaxial stress state is applied and the sensor output signal is recorded. The sensing chips are loaded individually, which makes the calibration process tedious. Flaws introduced during chip installation can cause variability in the results. Therefore, the calibration process must be repeated more than once and a statistical technique is used to analyze the testing results.

After microfabrication, the wafers were diced into square chips along [110] direction and its in-plane transverse. In this chapter, preparation of the testing specimens, excremental test setup, characterization of sensing chips, process to evaluate the sensor temperature coefficients of resistance (TCRs), mechanical testing and calibration, quantification of signal losses, and finally, the proposed packaging scheme were described. The organization of this chapter corresponds, roughly, to the order in which different parts of the experiment were performed. The calibration process was performed under various temperature conditions.

6.1. Preparation of Testing Specimens

Figure 39 depicts an example of a diced sensing chip. To prepare for testing and characterization, the sensing chips were installed on steel testing specimens. The testing specimens were cut from cold rolled AISI 1020 steel flat bars. The steel specimens had the following dimensions; length 405 mm, width 25 mm, and thickness 3 mm. The surface of the steel specimens was prepared using degreaser, neutralizer, acetone and IPA to ensure reliable bonding. Each testing specimen was instrumented with 350 Ω thin-foil strain gauge from Vishay Instruments[®] in a quarter-bridge configuration from one side. The thin-foil gauge was used to verify the applied strain from the testing machine, which was called far-field strain. Moreover, the thin-foil gauge was used for performance comparison. On the other side of the steel specimen, a MEMS strain sensor was installed.

The bonding adhesive used in the installation process was M-Bond 200, which is a typical adhesive for thin-foil strain gauges. This bonding material proved to generate low stresses after curing at room temperature. To quantify the stress-induced due to adhesive curing, resistance of the piezoresistive sensing elements was measured before and after the sensing chip installation using a digital multimeter with resolution of 1 mΩ. The change of resistance due to adhesive curing was less than 0.005%, which is lower than literature values [59].

During calibration, it was difficult to maintain contact between testing probes and the sensing chip while cross heads of the testing machine are moving. As a result, testing printed circuit boards (pcb's) were designed and developed to serve as signal transfer medium between the MEMS sensor and the data acquisition (DAQ) system. The testing pcb is shown in Figure 40.

A pcb was bonded around the installed MEMS sensor. Following pcb installation, wire bonding was performed to connect the MEMS sensor and the pcb terminals. Electrical wires were then soldered to the pcb pads. Finally, a polymeric cap was placed to prevent any potential damage to the testing pcb, MEMS sensor or the fine bonded wires. A prepared testing specimen is shown in Figure 41.
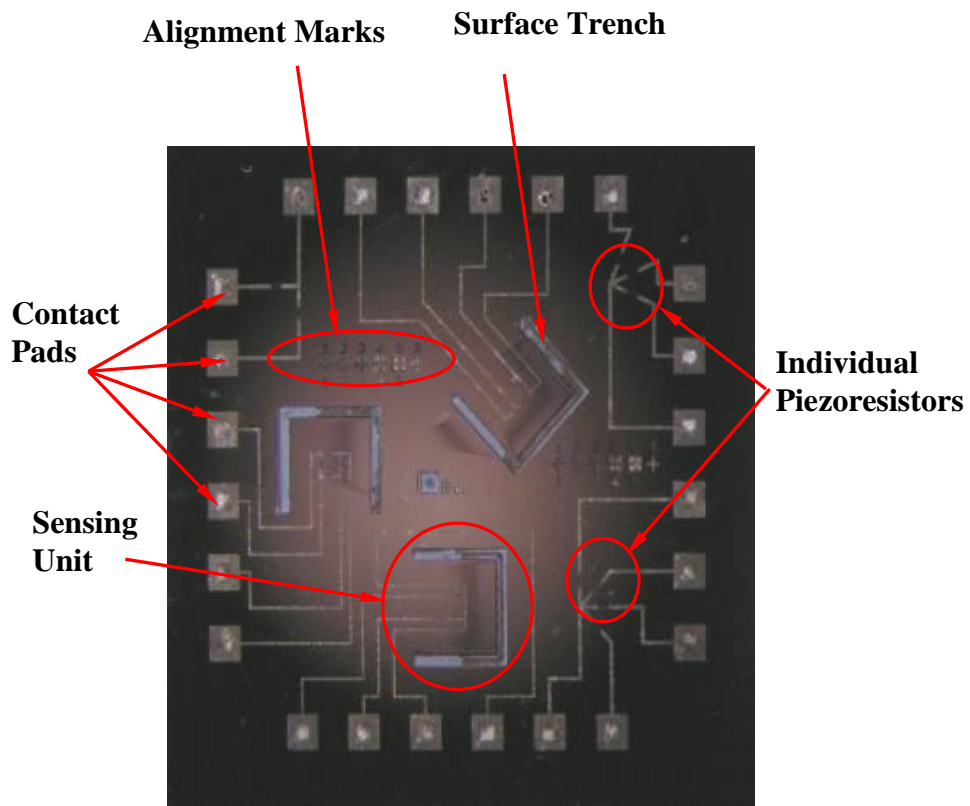
Figure 39 Fabricated sensing chip. Chip dimensions 10mm (length)×10mm (width)×500μm (thickness)
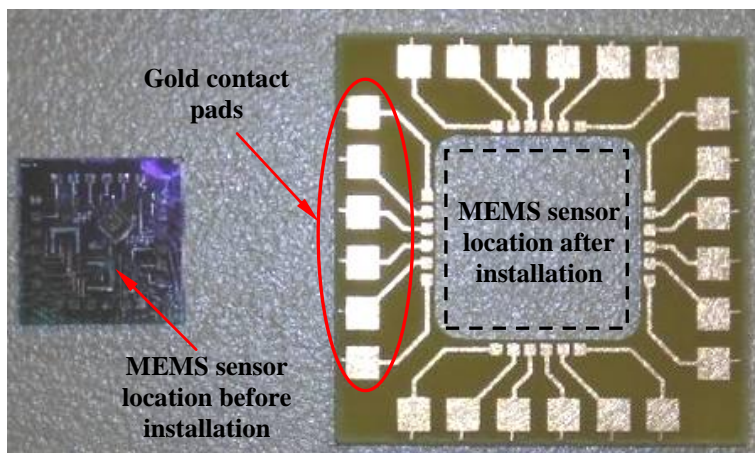
Figure 40 Testing printed circuit board
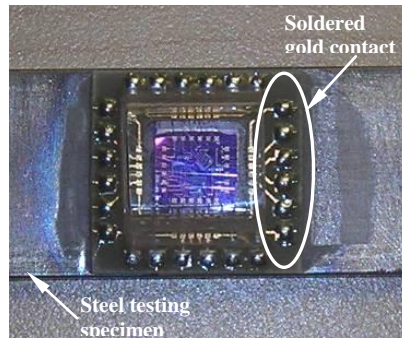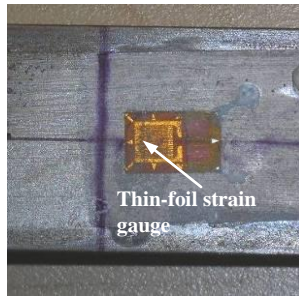
(B)
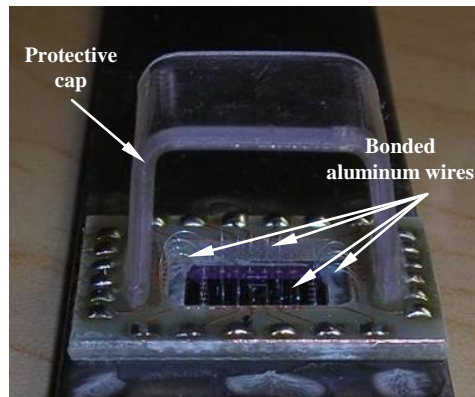
(C)

Figure 41 Preparation steps of the testing specimen. (A) installed thin-foil, (B) MEMS sensor and frame-like PCB after installation and (C) MEMS sensor, PCB and protective cap after wire bonding

6.2. Experimental Test Setup

To characterize and test the fabricated sensors, an experimental test setup was constructed. The basic elements of the testing apparatus for the microfabricated chips are shown in Figure 42 and Figure 43. This setup consisted of:

- Sensing chip holder (steel testing strips)
- Agilent DC power supply to provide excitation input voltage
- Instron Environmental test chamber
- Agilent Digital multimeter (DMM)
- Fluke Portable digital multimeter
- Instron Universal testing machine
- Data acquisition (DAQ) system equipped with National Instruments® DAQ box and LabView® Software

All equipment of the test setup had calibration records that were up to date at the time of experimental evaluation of the sensing chips.LabView® Software was used to automate the data acquisition process and to reduce inaccuracy due to human readout error. This approach allowed for lager amount of data to be logged. However, in order to analyze these data, a systematic manual approach was utilized using MS-Excel® spreadsheets. The MS-Excel® spreadsheets helped in various functions, such as:

- Making data files more readable
- Calculating strain from thin-foil strain gauges
- Calculating offset voltage, sensitivity and non-linearity
- Graphing sensor characteristics from separate data files
- Extracting sensor characteristics, e.g. sensitivity, resolution…etc.

The environmental test chamber was capable of achieving temperatures from -155 ^{o}C to +300°C with a 5°C resolution. The temperature range in the current study covered from -50°C to +50°C. For low temperatures, a liquid-nitrogen tank was hooked up to the test chamber. The increment of the temperature between sensor

readings was usually set to be 25°C, and the temperature at each step is maintained for at least 10 minutes before measurements were taken to ensure uniform temperature distribution around the silicon chip. In addition, the environmental chamber was equipped with internal fan to circulate the air inside the chamber, which provided uniform temperature distribution. During loading, force and displacement information were collected from testing machine control system. Displacement data from testing machine was used to calculate the applied strain. In addition, the applied strain was obtained from a thin-foil strain gauge. Calculated strain from testing machine was compared to measured strain from thin-foil gauge for verification purposes. Testing machine readings and thin-foil measurements are considered completely independent sources.

DAQ System

**Nitrogen
Source**

**Steel Testing
Specimen**

**Environmental
Chamber**

**Sensing
Chip**

**Testing Machine
Cross-Head**
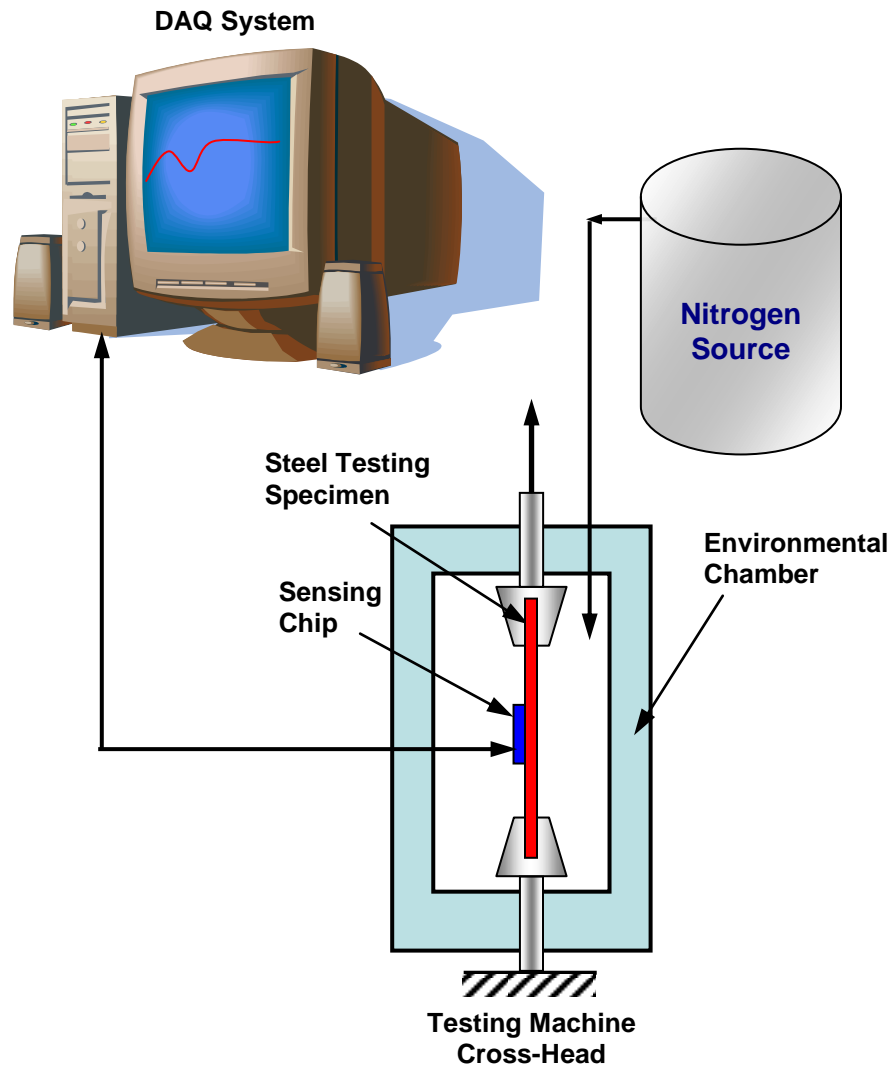
Figure 42 Schematic of the experimental test setup
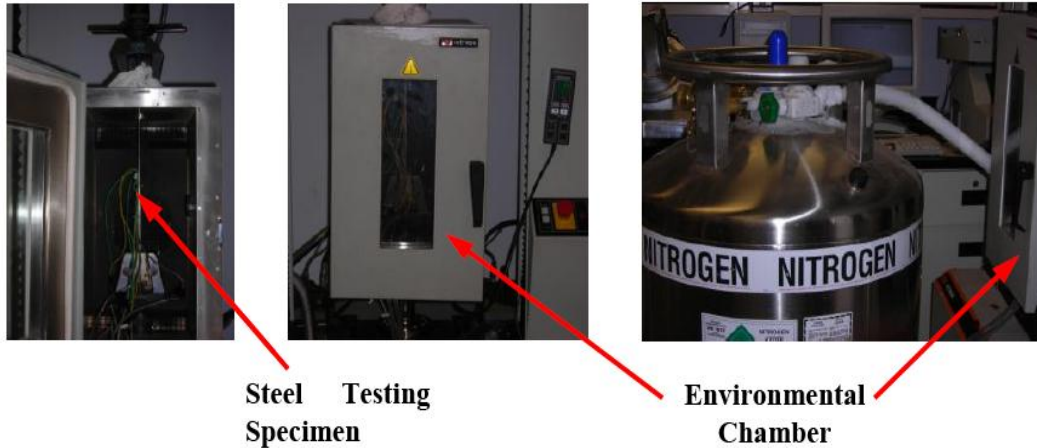
Figure 43 Experimental test setup

6.3. Characterization of Sensing Chips

To verify the suitability of the annealing process used in microfabrication, a burn-in step was done prior to testing. Burn-in is a commercial term describing the process used to stabilize the operation of the device. The device is hooked up to a power supply and the voltage increased up to a level where the resistors are burned in to the bonding pads. At this voltage level, any foreign layer between the pads and the resistor is removed. No change in the resistance was noticed before and after the burn-in. Therefore, the annealing process was considered correct. For the 100μm resistors, the burn-in voltage was 15V. The voltage was incremented from 0V to 15V.

Following the burn-in, the sensing chip characterization was started by initial resistance measurements at load-free condition. The sensor I-V characteristic curves were constructed to determine the suitable input voltage in order to operate the sensor within its linear range. Figure 44 shows an example of the room temperature I-V characteristic curves for five different doping concentrations; 1×10^{18} atoms/cm^3, 5×10^{18} atoms/cm^3, 1×10^{19} atoms/cm^3, 5×10^{19} atoms/cm^3 and 1×10^{20} atoms/cm^3.
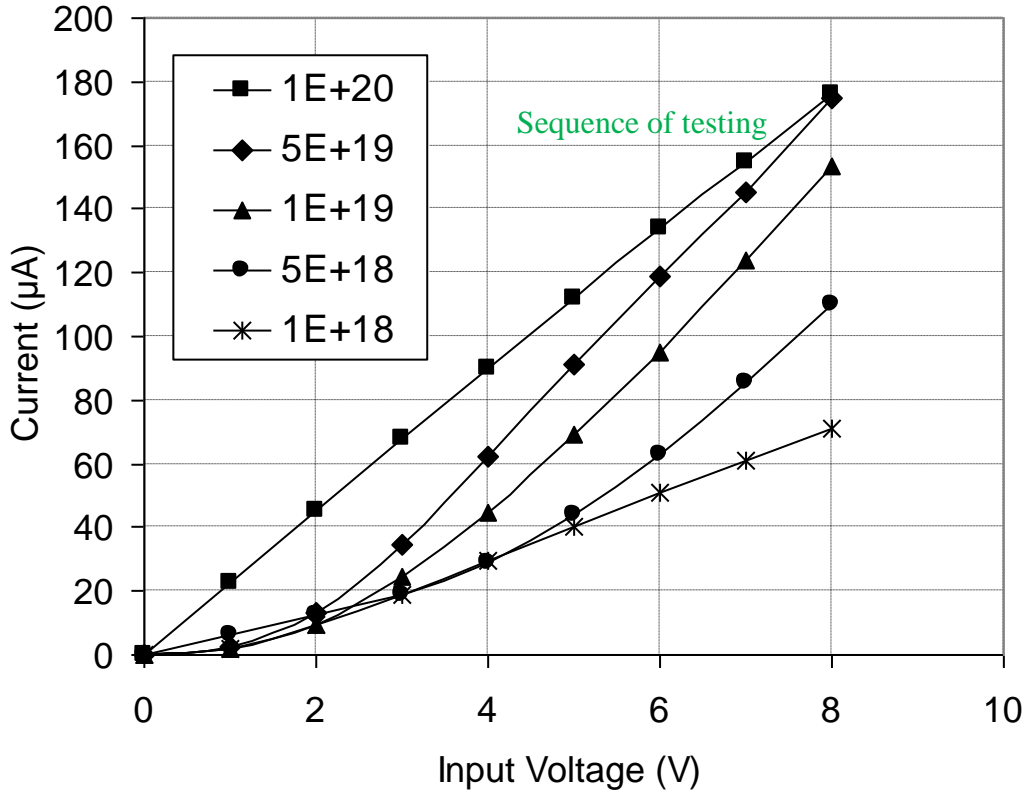
Figure 44 Sensor I-V characteristic curves for different doping concentrations at room temperature

Another quantity that needed to be evaluated was sheet resistance. Sheet resistance is an important quantity because it can be used to determine doping concentration. For electrical measurements on the ion-implanted samples, constant currents of 0.1, 1, 10 and 100µA were applied. Two high-impedance digital multimeters were used for voltage measurements: 4½ digits for routine measurements and 5½ digits for accuracy check.

To measure sheet resistance of the ion-implanted layer Van der Pauw Creek Cross structure, shown in Figure 45, was used. To perform such measurements, a constant current of 5 mA was used to provide I_{12} and the voltage output V_{34} in mV provides a direct readout in $(\Omega / \square)$. The advantage of this structure is that

voltage V_{34} of the element can be measured without disturbance of the current flow I_{12} through the element. The sheet resistance (R_s) of the element is given by

$$R_s = \frac{\pi}{\ln 2} \frac{V_{34}}{I_{12}} \qquad (\Omega/\square) \qquad\qquad \textbf{(50)}$$

Many studies have been conducted of symmetrical Van der Pauw structure with different geometries. The Greek Cross structure with the contact arm length greater than the contact arm width produces an error from the true sheet resistance that is less than 0.1 $\Omega/\square$ [139]
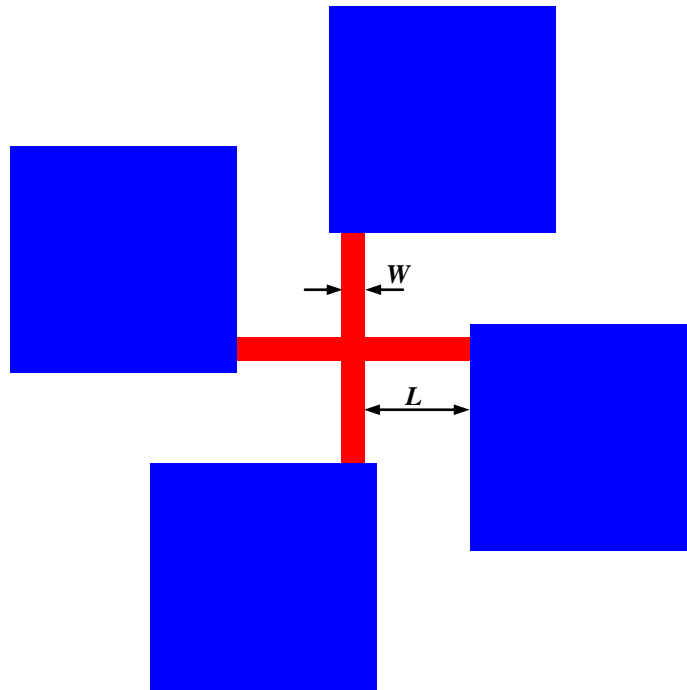
Figure 45 Greek Cross Van der Pauw structure. Van der Pauw structures are used to separate the current supply from the voltage readout to minimized testing error. The width (*w*) of the cross element is 10µm and the length (*L*) is 50µm. the contact pads are 400µm to a side

6.4. Evaluation of Temperature Coefficient of Resistance

Using the environmental chamber, the sensing chips were subjected to different temperatures, from -50°C to +50°C on 25°C interval, and the equivalent sensor resistance was recorded at load-free condition. Using the sensor resistance at room temperature (25°C) as a reference, the equivalent normalized resistance change was plotted versus temperature. The average slope of the individual curves represents the sensor average TCRs. Linear regression was used to calculate the average TCR for each doping level. An example of the normalized resistance change versus temperature is shown in Figure 46.
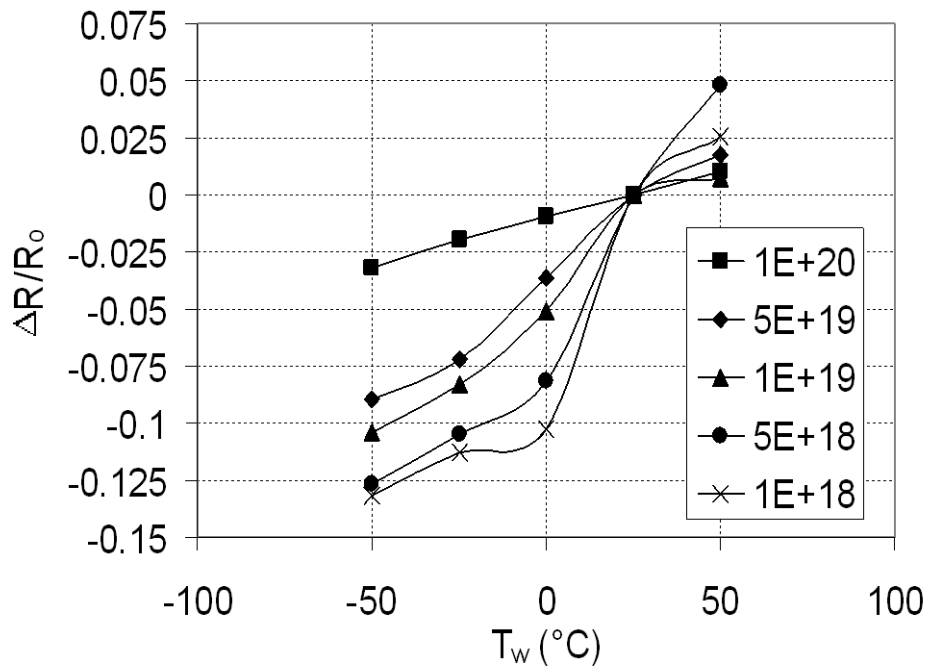
Figure 46 Example of normalized resistance change versus temperature at stress-free condition, the average slope = TCR

6.5. Sensor Mechanical Testing and Calibration

After evaluating the sensor TCRs, mechanical testing of the sensor was performed in accordance with ASTM E8 Standard [140], *Standard Test Methods for*

Tension Testing of Metallic Materials. During mechanical testing, the response of the thin-foil strain gauge was recorded to verify the applied strain on the steel testing specimen. The load applied approximately maximum mechanical strain of about 1550 $\mu\varepsilon$ on the steel testing specimen. The maximum applied strain value was selected based on the capacity of the testing machine. An example of the sensor calibration curves is shown in Figure 47.
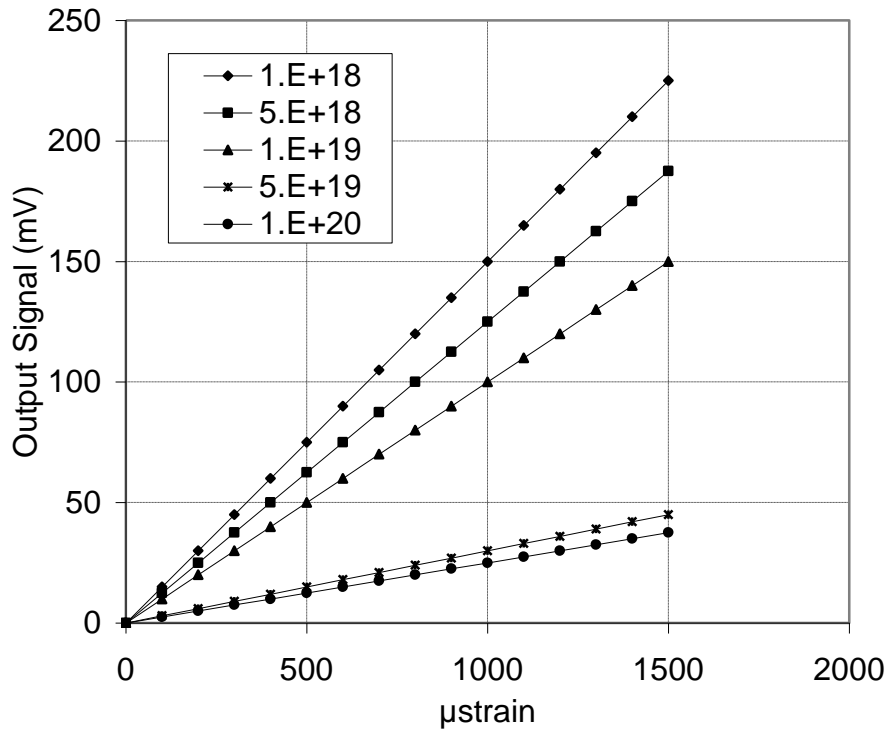
Figure 47 Example of sensor calibration curve for different doping concentrations at room temperature, input voltage = 5 V

As discussed above, the testing specimen consisted of different materials, such as bonding adhesive, whose material properties vary with temperatures. To examine the signal drift and load hysteresis, five sensing chips were mechanically retested at 25°C. This retest was performed approximately after 3 months from initial testing. Thermal hysteresis was tested on bare sensing chip before mounting. In thermal hysteresis tests, the temperature was originally at +25°C, cooled down to

93

-50°C, raised back to +25°C, continued to heat up to +50°C, and cooled back down to +25°C. Sensor outputs were recorded at all test temperature points.

6.6.   Quantification of Signal Losses

Due to differences in stiffness of sensing chip (silicon), bonding adhesive, and strained surface (steel), the transferred strain to the sensing piezoresistors (near-field strain) was different from the applied strain on strained surface from testing machine (far-field strain). This has resulted in strain field alteration, which affected the transferred strain value through the bonding material and sensing chip thickness. To quantify the signal loss due to bonding adhesive and silicon chip thicknesses, another testing specimen was prepared. On one side of this specimen, a 350 Ω thin-foil strain gauge was installed to measure the far-field strain. On the other side of this specimen, instead of a MEMS sensor, a 10 mm × 10 mm silicon square was bonded to the steel specimen then another 350 Ω thin-foil strain gauge was bonded on top of the silicon square to measure the near-field strain, after it undergone all of the signal losses. A schematic of the specimen used to evaluate the strain field alteration is shown in Figure 48. Since the thin-foil strain gauge calibration curve is well known from the manufacturer datasheet, the installed thin-foil strain gauges provided the relationship between the far-field strain and near-field strain. The relationship between the far-field strain and the near-field strain is plotted in Figure 49. The slope of this graph showed that about 16% of the applied strain is transferred through the bonding adhesive and the silicon carrier.
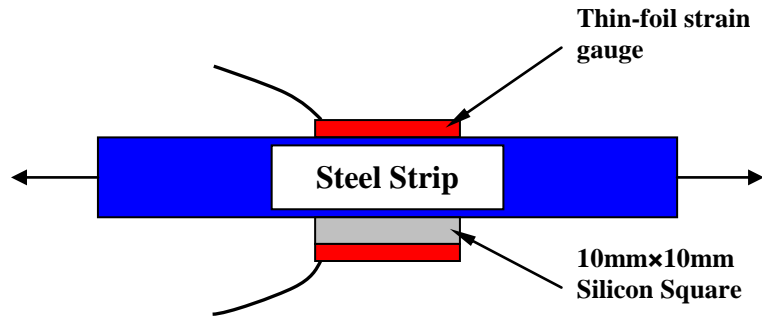
Figure 48 Schematic of the specimen used to evaluate the relation between near-field strain and the far-field strain
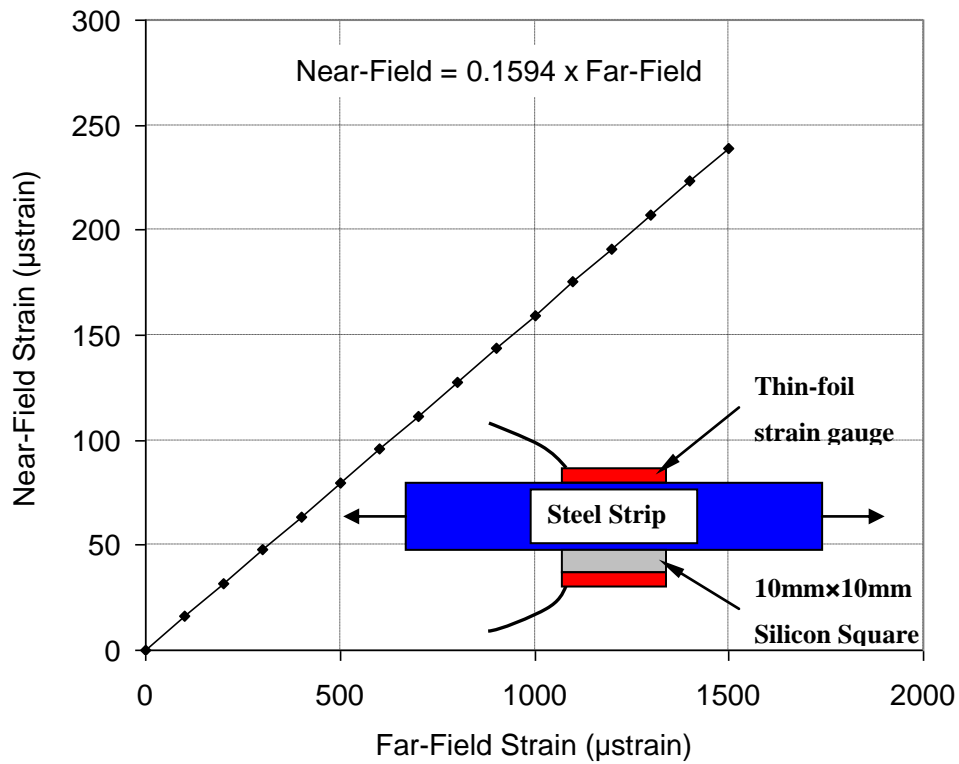
Figure 49 Relationship between far-field strain and near-field strain. The transferred (near-field) strain to the sensing elements is approximately 16% from the applied (far-field) strain

6.7. Proposed Packaging Scheme

Packaging pcb's were designed and constructed following flip chip scheme. Flip chip packages consist from multiple layers and thin film coatings. The pcb's have a similar layout to the layout on the sensing chips. The packaging process is summarized below:

- Chip and pcb cleaning - clean the fabricated chip and the pcb using acetone and IPA
- Chip mounting - mount the fabricated chip on the placing head
- Pcb placement - place the pcb on the heating chuck
- Epoxy placement - place anisotropic conductive epoxy on the pcb contact pads
- Epoxy curing - epoxy curing at 120°C

After packaging, initial sensor resistance data were measured to establish reference values. In reality, there are small stresses present in the chip due to the epoxy curing process. In this study, the introduced stress due to epoxy curing was negligible. Moreover, underfill between the packaging pcb and the sensing chip was unimportant. There is no single property of the packaging epoxy that can solely determine the induced stresses magnitude. However, several properties including the elastic modulus, coefficient of thermal expansion, and glass transition temperature are known to make significant contributions to the induced stresses in the packaged chip. It is worth to mention that the scope of this research project did not cover packaging. However, flip chip packaging was performed to test the chip packageability. A schematic of flip chip packaging process is shown in Figure 50.
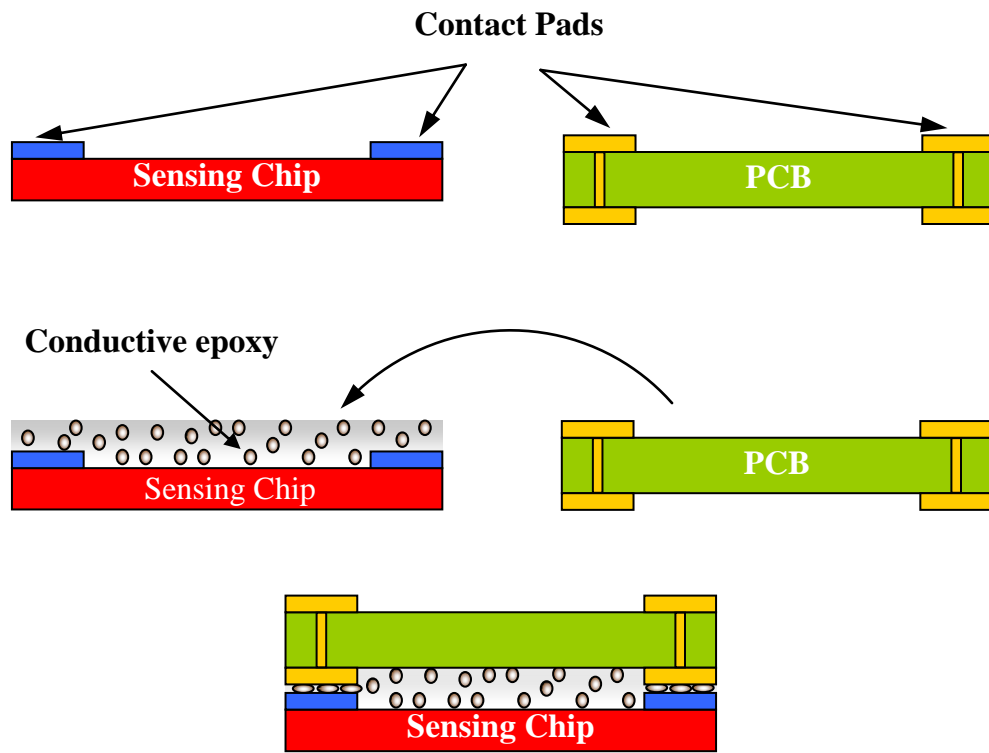
Figure 50 Flip chip packaging steps

Chapter 7 – Results and Discussion

This chapter presents experimental results. The microfabrication process flow, in Appendix B, was used to create six sensor layouts. Five doping concentrations were used to fabricate the sensor samples. Each concentration was applied to prototype 64 sensing chips. Therefore, a total of three hundred and twenty (320) sensors were available for characterization and calibration. Characterization structures were also fabricated on the same sensing chips. Not all fabricated sensing chips were successfully tested due to fabrication and cleanliness issues. The results of this research work were published in four separate studies [28-31]. As mentioned in Chapter 4, Design 3 and Design 4 showed the highest performance characteristics. Therefore, they have been selected for presentation in this chapter. The complete results of the six sensor layouts can be found in Appendix F.

The mentionable achievement specific to this phase of research is the standardization of microfabrication process and development of evaluation procedure and preliminary packaging scheme. Finite element results were utilized to understand the experimental results and explain discrepancies. Moreover, FEA predictions allowed identification of the limitations when using the sensing chips. It can be shown that FEA predictions are in reasonable agreement with the experimental results. However, FEA results over-predicted sensor response in some cases.

7.1. Procedure of Data Analysis

After data collection, a systematic procedure was used to calculate mean and standard deviation of the measurements. The following steps were carried out to process the output signal:

1. The sensor output signal was plotted as a normalized resistance change ($\Delta R/R$) versus temperature at load-free condition.

98

2. The slope of (ΔR/R) versus temperature was evaluated based on linear regression. This slope was multiplied by 10^6 to calculate the average sensor TCR in parts per million per degree Celsius (ppm/°C).

3. Mechanical strain was calculated using the applied load and steel testing specimen characteristics (dimensions and material properties).

4. The applied strain was verified using readings from thin-foil strain gauge.

5. Temperature effect was removed from the sensor output signal using the evaluated TCRs.

6. The sensor output signal was plotted as output voltage versus strain to construct the sensor calibration curves.

7. Initial offset was removed from the sensor calibration curves.

8. Sensor sensitivity was evaluated by calculating slopes of the different calibration curves using linear regression at different temperatures; −50°C, −25°C, 0°C, +25°C and +50°C.

7.2. I-V Characteristic Curves

The I-V characteristic curves were constructed to the individual sensing units. The I-V characteristic curves of the sensing units were closely matching; it was selected to evaluate the average curve of the three sensing units to present the I-V curve of the sensing chip. In addition, the characteristic curves of the sensing chips of the various chip layouts were very close for the same doping concentration. Hence, each doping level is represented by one curve on Figure 51. To construct the I-V characteristic curves, electrical voltage was applied to the input pads of the sensing unit and the passing current was measured. All I-V curves were constructed at room temperature.

Figure 51 shows the I-V characteristic curves for different doping concentrations at room temperature. It is depicted that at high doping concentration (1×10^{20} atoms/cm^3), the passing current is linearly related to the applied voltage, which is resulted from the good ohmic contact between the aluminum metallization and the p-type silicon. In the case of lower doping levels, the I-V curves started by a nonlinear portion, which indicates diode junction. Following the nonlinear zone,

99

the I-V curve is linear. Leakage current is dependent on operating temperature, which affects passing current through the sensing elements. This leads to nonlinear behavior of the sensor. Hence, the characteristics of the diode junction are considered temperature-dependent. Due to the firm link between the aluminum wires and the piezoresistive elements, the contact resistance of the bonds is excluded. In the case of I-V curves with nonlinear zones, the bridge input voltage was selected within the linear range. The bridge excitation voltage of all sensing chips for all subsequent testing is 5 Volts, see Figure 51.
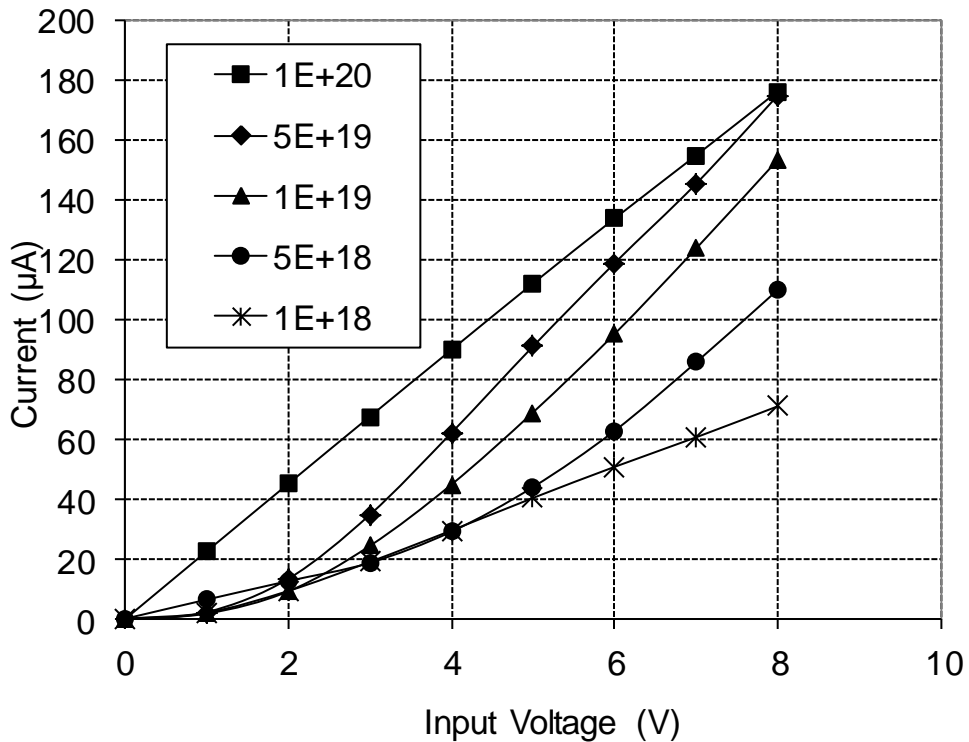
Figure 51 Sensor I-V characteristic curves for different doping concentrations at room temperature

The I-V curve of doping concentration of 1×10^{20} atoms/cm^3 has an equivalent nominal sensor resistance of approximately 45 KΩ. This high resistance reflected positively on the MEMS sensor power consumption. On the other hand, for 5

100

Volts bridge input, the current consumption of the 350 Ω thin-foil strain gauge and MEMS sensor with doping level of 1×10^{20} atoms/cm^3 are ~ 15 mA and ~ 0.11 mA, respectively. Hence, the power source will have a longer working life when used for the developed MEMS sensor compared to the 350 Ω thin-foil strain gauge. This demonstrates the MEMS sensing chip as a strong candidate for wireless structural health monitoring applications, where power consumption is a critical issue.

7.3.   Evaluation of Temperature Coefficient of Resistance

Using the experimental setup, shown in Figure 42 and Figure 43, the sensing chips were subjected to various temperatures at load-free condition. The change in the equivalent resistance of the sensing unit was measured. Taking the room temperature measurement as a reference, the normalized resistance change was calculated and plotted versus test temperature in Figure 52 through Figure 57. The average slopes of the individual graphs in these figures represent the average TCRs of the developed sensing chip.

Figure 58 shows the temperature response of the thin foil stain gauge used for comparison. On the vertical axis of Figure 58, the sensor output is plotted in microstrain units. Microstrain is directly proportional to the normalized resistance change. The foil gauge factor is the constant in this case. Therefore, Figure 58 can be used to compare temperature response of thin foil strain gauge and the piezoresistive MEMS sensor. As can be depicted from Figure 58, the thermal response of the thin-foil strain gauge is highly non-linear, similar the MEMS sensor with low doping concentration. This nonlinearity makes the thermal drift of the thin-foil gauge unpredictable and difficult to compensate. On the other hand, MEMS sensors with high doping concentration (10^{19} atoms/cm^3) have approximately linear temperature response. Additionally, the MEMS sensor has almost horizontal or zero TCR in the case of Design 3 as shown in Figure 54.

It is clear from the above discussion that a piezoresistive MEMS sensor can be developed with low or minimum temperature drift. Excluding microfabrication variability, which was low in the current project, all MEMS should have same or

identical temperature response, which is not the case, as can be seen in Figure 52 through Figure 57. This can be attributed to the combined effect of geometrical and piezoresistive TCRs. The piezoresistive TCR is what is widely known in the MEMS field and is highly predicable. On the other hand, the geometrical TCR is highly dependent on the geometrical features of the sensing chip, which is the main difference between the various designs at same doping level.
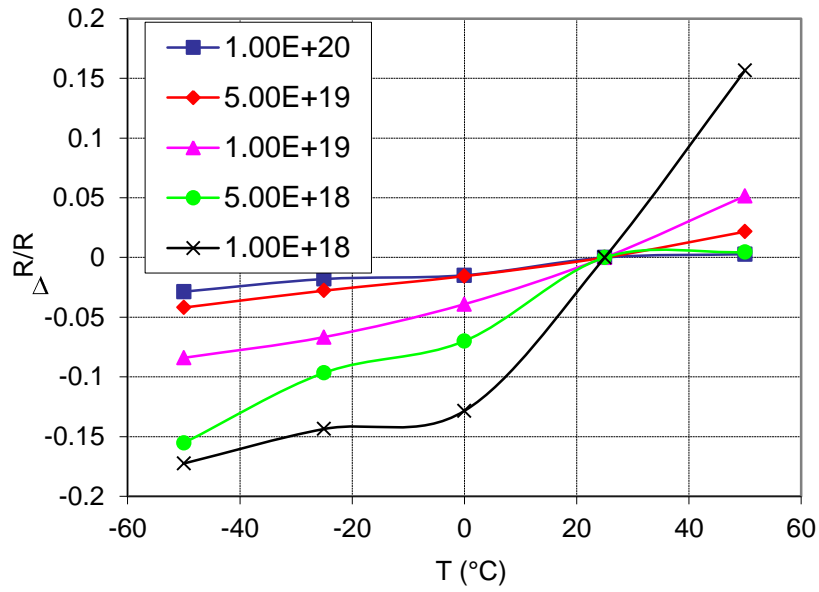
Figure 52 Normalized resistance change at stress free condition for different doping concentrations, slope of individual curves = TCR at different doping concentration, Design 1
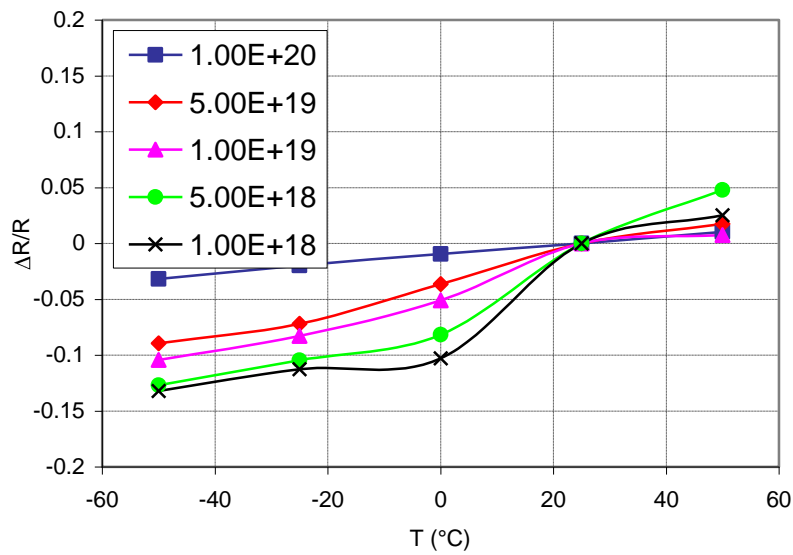
Figure 53 Normalized resistance change at stress free condition for different doping concentrations, slope of individual curves = TCR at different doping concentration, Design 2
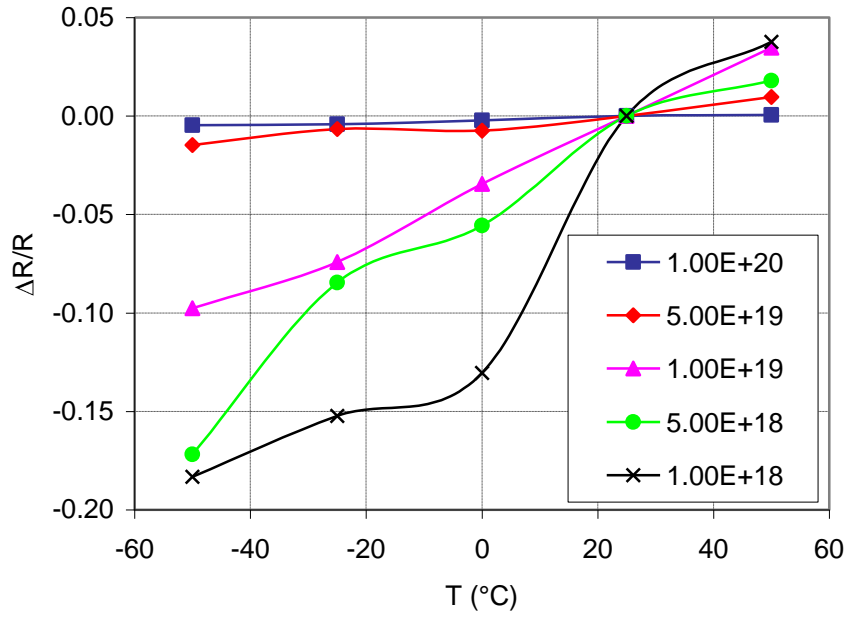
Figure 54 Normalized resistance change at stress free condition for different doping concentrations, slope of individual curves = TCR at different doping concentration, Design 3
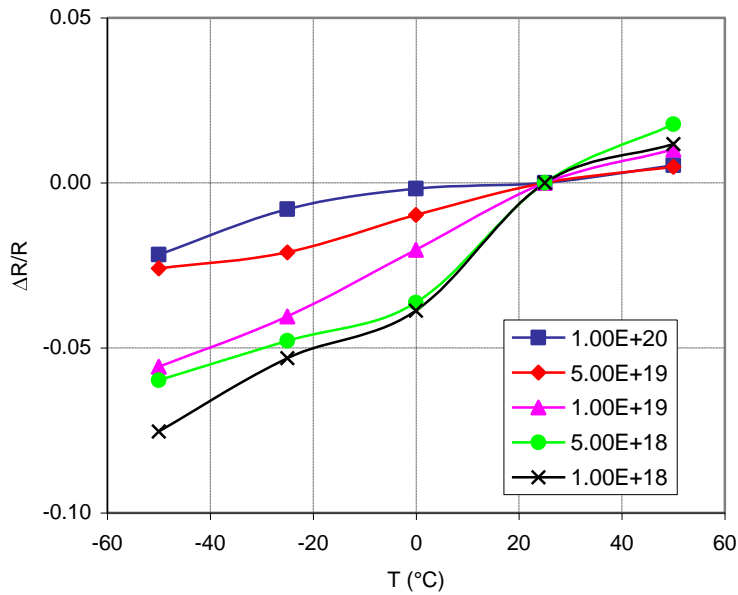
Figure 55 Normalized resistance change at stress free condition for different doping concentrations, slope of individual curves = TCR at different doping concentration, Design 4
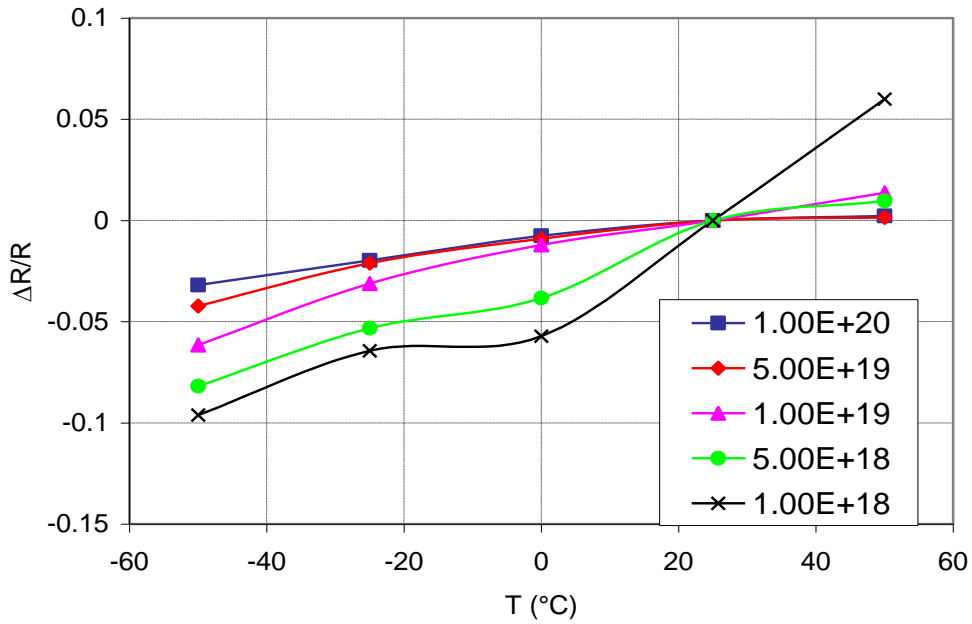
Figure 56 Normalized resistance change at stress free condition for different doping concentrations, slope of individual curves = TCR at different doping concentration, Design 5
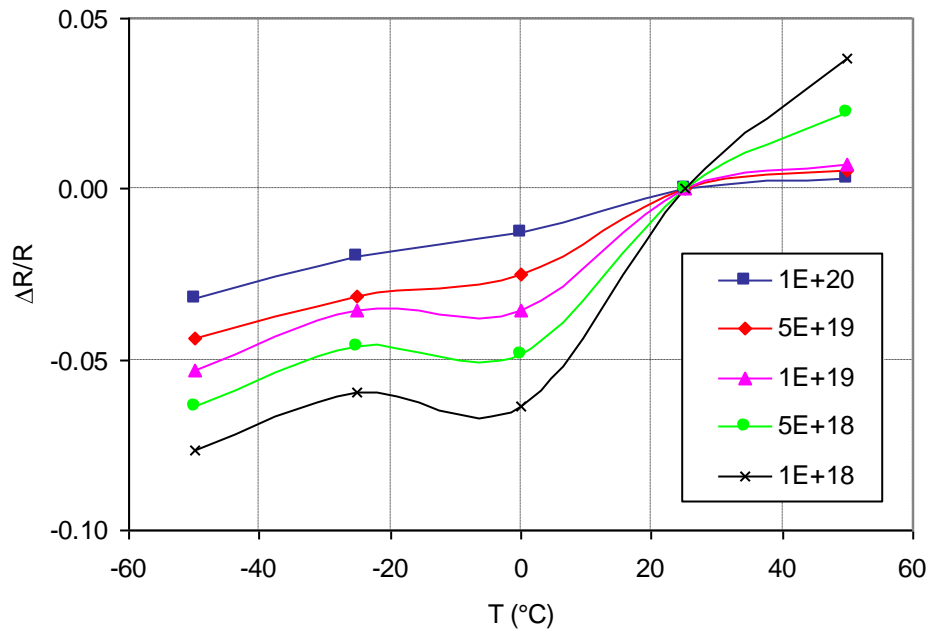
Figure 57 Normalized resistance change at stress free condition for different doping concentrations, slope of individual curves = TCR at different doping concentration, Design 6
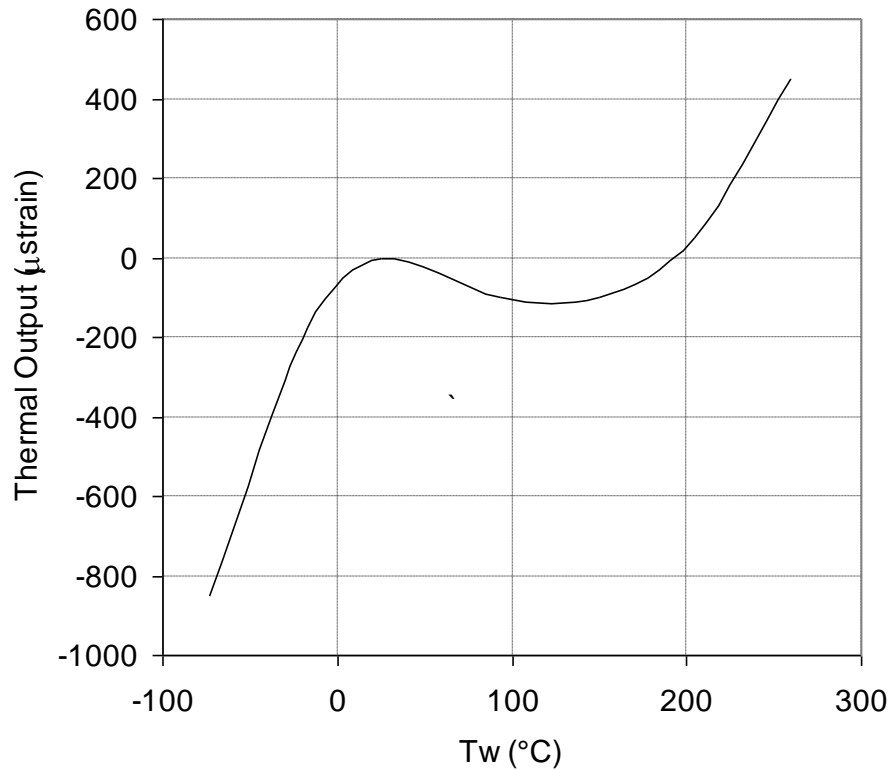
**Figure 58 Temperature dependence of thin-foil strain gauge on temperature, part number
LWK-06-W250B-350**

The average slopes of individual curves on Figure 52 through Figure 57 were evaluated using linear regression. Figure 59 through Figure 64 present the sensor TCRs. Generally, as the doping concentration increases the sensor TCR decreases. This trend agrees with most of the published literature [59, 61, 141, 142], with the exception of reference [70] by Boukabache and Pons. In 2002 Boukabache and Pons reported that first order TCR decreases with the increase in doping level until it reaches minimum value at doping concentration of approximately 5×10^{18} atoms/cm^3. Then, it increases again with doping concentration. It is worth to mention that TCRs in Figure 59 through Figure 64 are the results of the overall sensor TCR, which include first order, second order, higher order TCRs, and effect of geometric features, which can cause local deformations. Therefore, the TCRs behavior (decrease then increase) from

106

reference [70] can not be compared to the results presented in Figure 59 through Figure 64. In addition, a recent work [143] by Boukabache, Pons and other researchers demonstrated that there are significant disagreement between models in reference [70] and experiments using ion implantation. Therefore, the trend in reference [70] can be excluded from the comparison.

Figure 58 depicts the thermal behavior of the thin-foil strain gauge that was used during mechanical testing, part number LWK-06-W250B-350 from Vishay Micro-Measurements®. This figure was abstained from the thin-foil gauge datasheet provided by Vishay Micro-Measurements®. From this figure, at temperature of -50°C, the foil gauge has a thermal output equivalent to 600$\mu\epsilon$. On the other hand, a MEMS sensor with doping concentration of 1×10^{20} atoms/cm^3 has a thermal output equivalent to 727$\mu\epsilon$. This value was calculated using the normalized resistance change from sensor calibration curves and piezoresistive gauge factor. The sensor calibration curves will be presented later. It is clear that thin-foil gauge has relatively lower TCR compared to the MEMS sensor. However, as mentioned above, examination of both curves of temperature dependence confirms that MEMS sensor has highly linear behavior as opposed to the foil gauge. This linear performance is very helpful to predict the sensor thermal output at a given temperature. Therefore, the developed sensing chip can be considered to have better thermal characteristics compared to conventional metallic strain gauges.
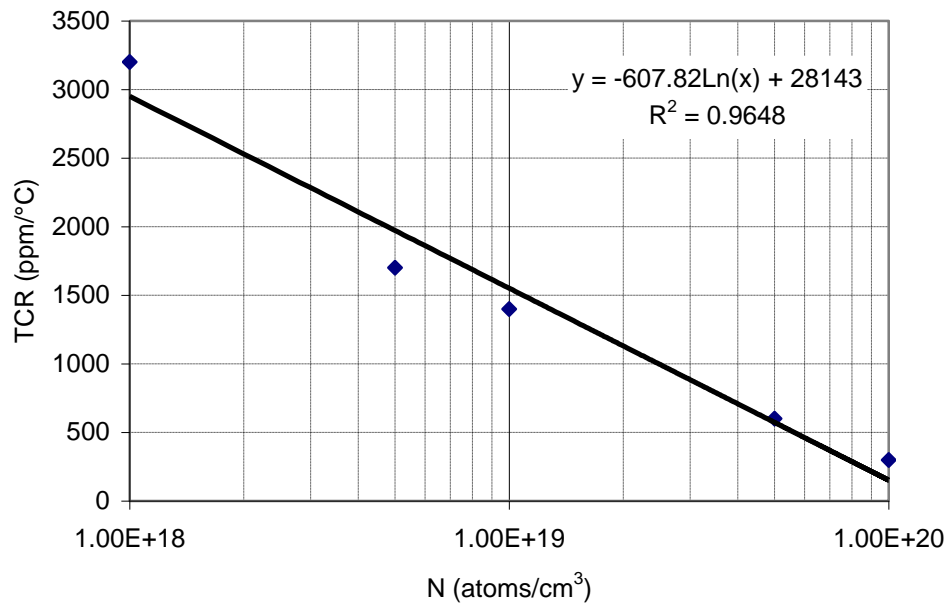
Figure 59 Temperature coefficient of resistance (TCR) at different doping concentrations to evaluate the sensor TCR, (Design 1)
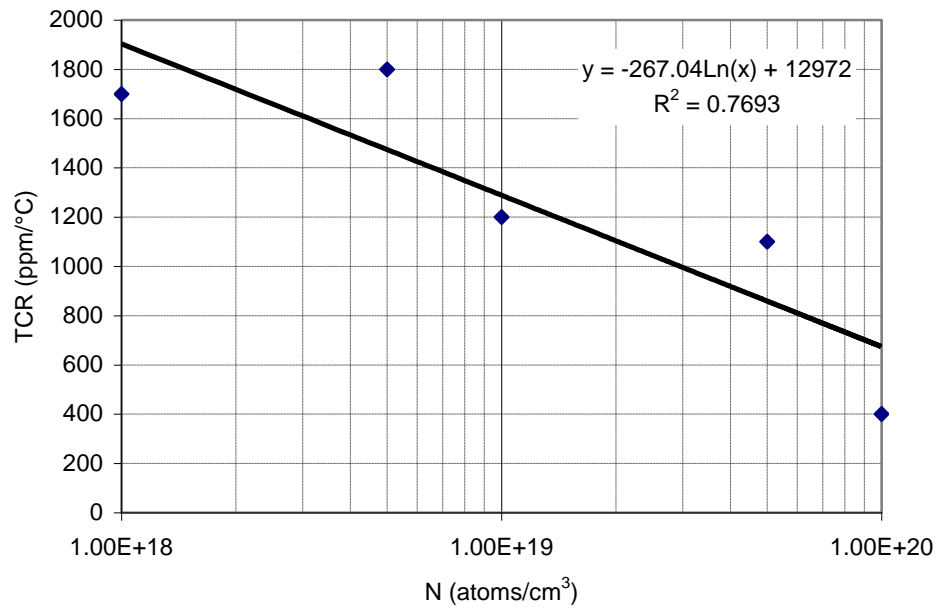
Figure 60 Temperature coefficient of resistance (TCR) at different doping concentrations to evaluate the sensor TCR, (Design 2)
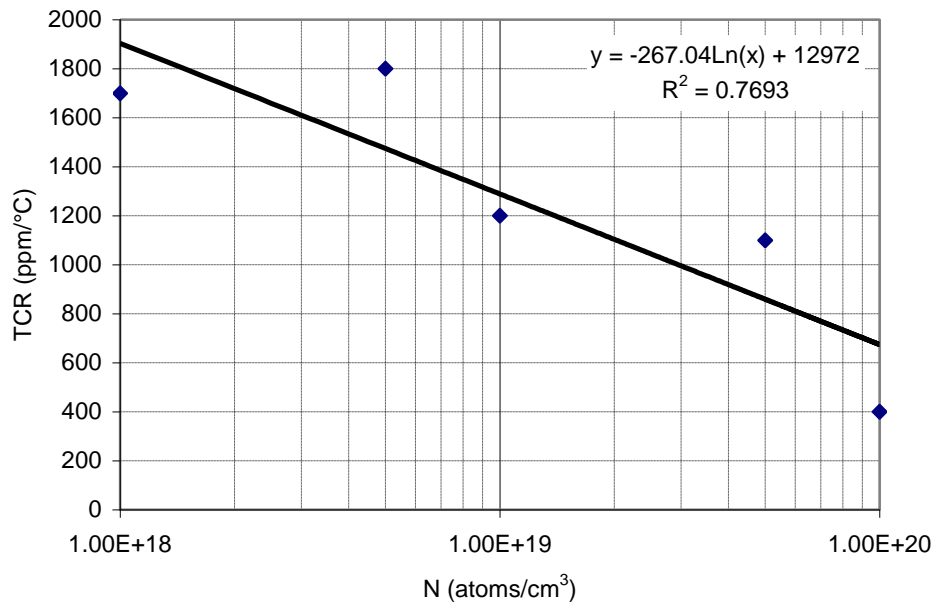
Figure 61 Temperature coefficient of resistance (TCR) at different doping concentrations to evaluate the sensor TCR, (Design 3)
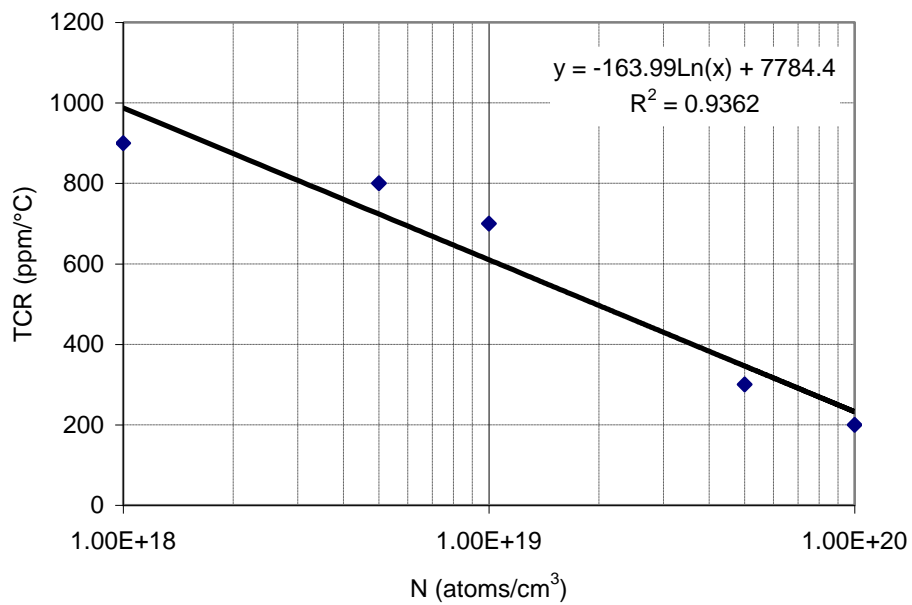
Figure 62 Temperature coefficient of resistance (TCR) at different doping concentrations to evaluate the sensor TCR, (Design 4)
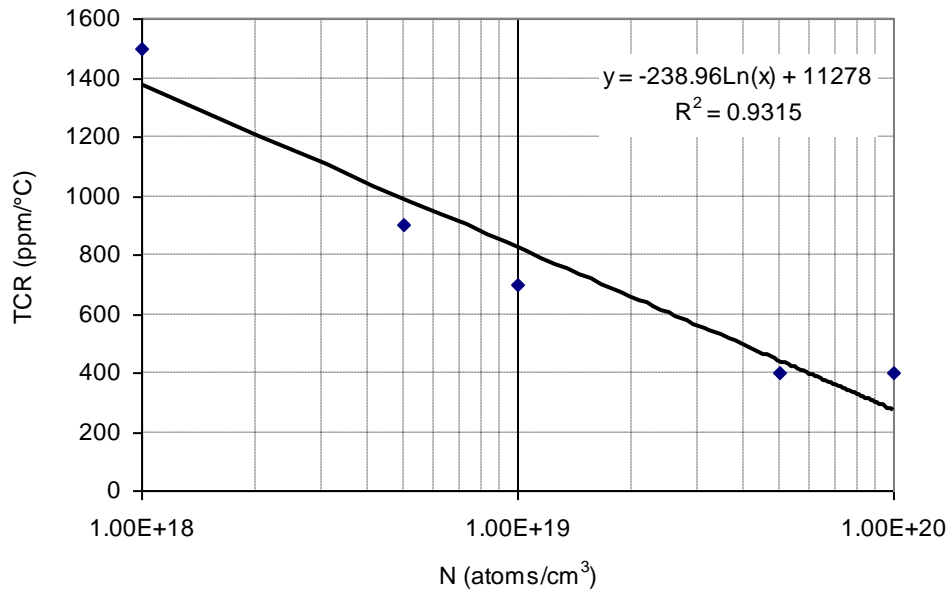
Figure 63 Temperature coefficient of resistance (TCR) at different doping concentrations to evaluate the sensor TCR, (Design 5)
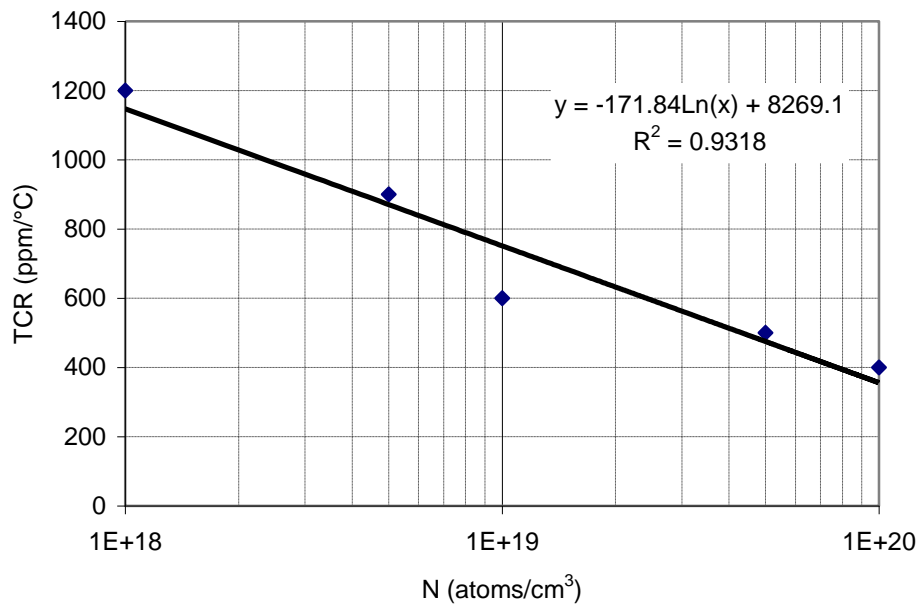
Figure 64 Temperature coefficient of resistance (TCR) at different doping concentrations to evaluate the sensor TCR, (Design 6)

Table 6 and Table 7 list TCR values collected from published literature and calculated using criteria shown on Figure 59 through Figure 64. It is noted that the criteria shown on Figure 59 through Figure 64 provide comparable results to some values from references [35, 70] for doping concentrations of 1.5×10^{18} and 1×10^{18}, respectively. By referring to Table 6 discrepancies can be found between researchers for a given doping level, e.g. references [35, 59, 70]. However, the evaluated trend (TCR decreases with the increase in doping concentration) applies within the same work, except in reference [70]. It is also reported that for constant doping level the TCRs of n- and p-type silicon are equal and the TCRs are nearly constant for different crystallographic directions [35].

Table 6 Summary of TCR values from literature

Reference#	Doping Level (atoms/cm^3)	TCR (ppm/^{o}C)
Figure 6 in ref. [64]	2×10^{19}	1600
Figure 22 in ref. [59]	2×10^{18}	940
Figure 5 in ref. [35]	1.5×10^{18}	1802
Figure 9 in ref. [141]	5×10^{19}	1187
Figure 8 in ref. [144]	1×10^{16}	2689
Figure 1 in ref. [70]	1×10^{18}	1900
Figure 1 in ref. [70]	2×10^{18}	1000
Figure 1 in ref. [70]	5×10^{18}	250
Table 3 in ref. [143]	1.25×10^{19}	561
Table 3 in ref. [143]	1.1×10^{18}	2699

Table 7 Summary of TCR values calculated from criteria shown on Figure 59 through Figure 64

Doping Level (atoms/cm^3)	Design 1 (ppm/^{o}C)	Design 2 (ppm/^{o}C)	Design 3 (ppm/^{o}C)	Design 4 (ppm/^{o}C)	Design 5 (ppm/^{o}C)	Design 6 (ppm/^{o}C)
1×10^{16}	5750	3134	1995	1743	2474	1938
1×10^{18}	2951	1904	1222	988	1374	1147
1.1×10^{18}	2893	1879	1206	972	1351	1131
1.5×10^{18}	2705	1796	1154	921	1277	1077
2×10^{18}	2530	1719	1105	874	1208	1028
5×10^{18}	1973	1474	951	724	989	870
1.25×10^{19}	1416	1230	797	573	770	713
2×10^{19}	1130	1104	719	496	658	632
5×10^{19}	573	859	565	346	439	475

7.4. Mechanical Testing and Sensitivity Evaluation

The ASTM E251-92 Standard [145] was adapted to evaluate the performance characteristics of the MEMS strain sensor. This Standard was originally developed to evaluate metallic bonded resistance strain gauges. Therefore, it was the most applicable standard to compare thin-foil gauges and the developed MEMS strain sensor. Because of the high sampling rate during sensor calibration, volume of the collected data was huge, which placed significant burden on graphing and presentation of data. Hence, it was decided to convert the original calibration curves to what is called simplified calibration curves. From this point forward calibration curve stands for simplified calibration curve. To convert the original calibration curves to simplified curves, a systematic approach was followed. The steps of this approach are presented in Appendix E.

To evaluate the electrical measurements as a function of temperature, the test specimens were soaked inside the environmental chamber, where the temperature could be controlled from $-50^{o}C$ to $+50^{o}C$ with accuracy better than $0.25\ ^{o}C$. To control temperature, a combination of heating by resistive coils and cooling by liquid nitrogen was done. Electrical measurements were taken only after thermal equilibrium was established. Much attention has to be given in order to reduce the error induced by measurement of temperature. To minimize the discrepancy from the set point, maintaining temperature of the oven at the set point for a long period of time was necessary.

Mechanical strain was applied by the universal testing machine on the steel testing specimen. This applied strain is called far-field strain. The mechanical strain is transferred to the MEMS sensor through steel specimen (strained surface), bonding adhesive and sensor silicon carrier. The strain sensed by the piezoresistive elements is called near-field strain. The calibration curves have been constructed using the far-field strain. To reduce the measurements uncertainty, the sensor sensitivity was evaluated using results from five different tests.

The calibration curves were constructed using the far-field strain. This method included the effect of bonding adhesive in measurements. Therefore, the

112

calculated gauge factor and sensitivity were called equivalent gauge factor and equivalent sensitivity, respectively. The relationships between the equivalent parameters (gauge factor and sensitivity) and their corresponding piezoresistive values can be defined experimentally or using FEA. Figure 49 illustrates the relationship between the far-field strain and the near-field strain, which is equivalent to the relationship between piezoresistive and equivalent parameters (gauge factor and sensitivity). Design 3 and Design 4 were found to have the best performance characteristics. Therefore, calibration curves of these designs are presented in this chapter, Figure 65 through Figure 74.

Table 8 through Table 13 summarize the sensitivity values calculated from calibration curves. Slopes of the individual calibration curves represent the sensing sensitivity. As expected, for low to moderate doping concentrations, when doping level decreases the sensing sensitivity increases. This can be explained by the higher piezoresistive coefficients at these doping levels. Likewise, as the operating temperature decreases, the sensitivity increases. This can be the result of the freeze out phenomenon that happens in the lightly to moderately doped semiconductors. On the other hand, at high doping concentrations, the sensitivity is lower compared to low and medium doping concentrations. However, the sensitivity is very stable, i.e. no significant change in sensor sensitivity over a wide temperature range, from -50°C to +50°C. This stable performance exists because the freeze out does not happen in heavily doped silicon [59]. Based on the quantum physics, the piezoresistance coefficients decrease with increasing impurity concentration. In addition, mathematical calculations based on the many-valley model predict a decrease of the piezoresistance effect with increasing temperature [63, 81].

It was expected that the sensing sensitivity declines with the increase in doping level and operating temperature. This is generally true. However, careful examination of Table 8 through Table 13 reveals some disagreement with this statement. For example, in case of Design 3 at doping concentration of 5×10^{18} atoms/cm^3, the trend is correct except at 25°C. Another example can be seen in Design 5 at doping level of 1×10^{19} atoms/cm^3 and 0°C. This can be due to some

air voids (pockets) in the bonding adhesive after curing. Another reason that may have contributed to these discrepancies is the existence of two or more competing mechanisms inside the material under stress and at various temperatures, e.g. freeze out and another mechanism.

To evaluate the equivalent sensor gauge factor, the calculated sensitivities must be multiplied by 10^6 (to convert from microstrain to strain). On the other hand to calculate the piezoresistive gauge factor, values of the equivalent sensor gauge factor must be divided by 0.16 to convert far-field to near-field.

Hysteresis is an important parameter, which determines the stability of the sensor performance. It measures the reliability of the sensor output. Ideally, the sensor should produce the same output regardless of measurement conditions. In this case, hysteresis value equals zero. In reality, sensors are affected by external conditions, i.e. nonzero hysteresis. Hysteresis can be expressed in one of the two forms; absolute value of the sensor output and percentage of the full scale (FS). Thermal and load hysteresis were tested in this study.

Normalized resistance change was calculated as a result of the thermal cycle applied on the bare sensing chips. Thermal hysteresis tests showed maximum hysteresis of 0.01% FS, which corresponds to $0.15\mu\varepsilon$. This value is less that the sensor resolution, and therefore, it can be neglected. This negligible thermal hysteresis can be due to errors in the measuring device. Hence, the bare sensing chip can be considered free of thermal hysteresis. Load hysteresis was evaluated by retesting of six sensors, one from each design layout. High doping concentration was selected for load hysteresis testing. The testing specimens were loaded and unloaded to examine the sensor hysteresis and repeatability. Five out of the six retested sensors suffered hysteresis less than 0.12% FS, which is equivalent to approximately to $2\mu\varepsilon$. The sixth sensor had extremely weak signal, i.e. high hysteresis. Further investigation of this sensing chip showed that the bonding adhesive experienced fatigue cracking due to thermal cycling.
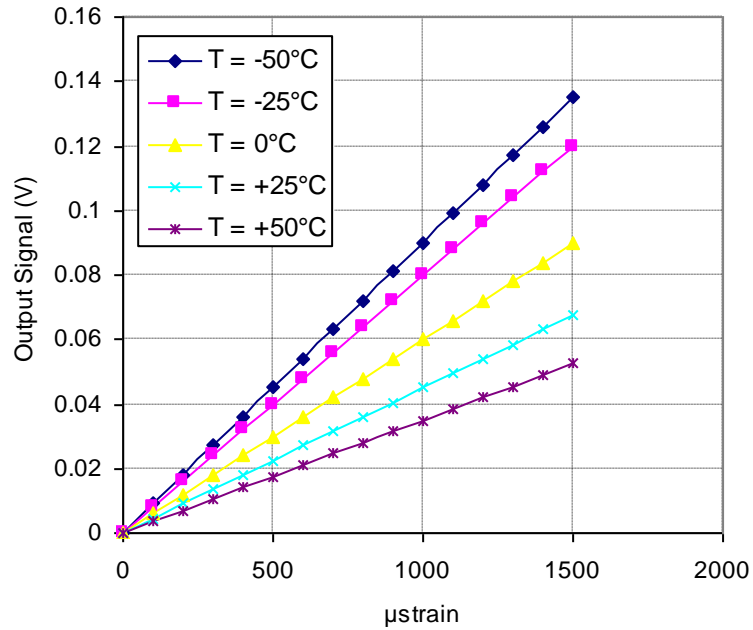
Figure 65 Simplified calibration curves at different temperatures for doping concentration of 1×10^{18} /cm^3 (Design 3)
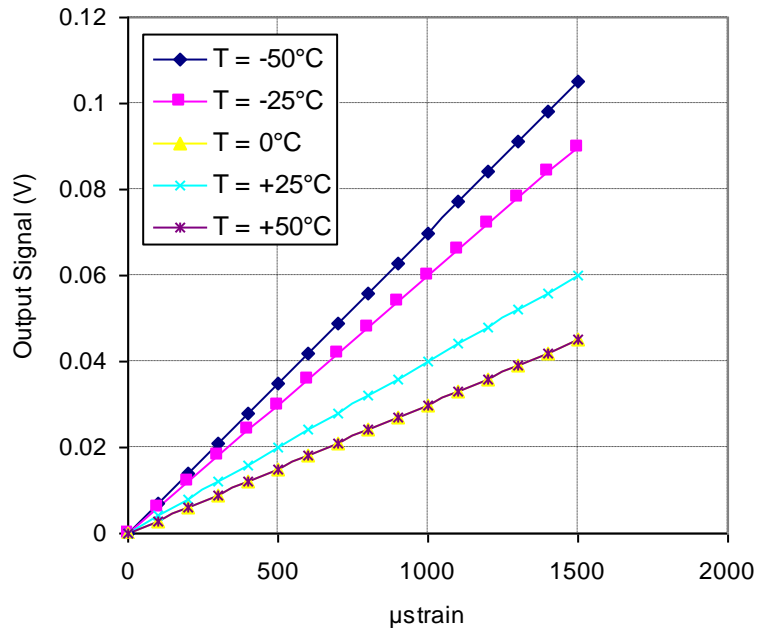
Figure 66 Simplified calibration curves at different temperatures for doping concentration of 5×10^{18} /cm^3 (Design 3)
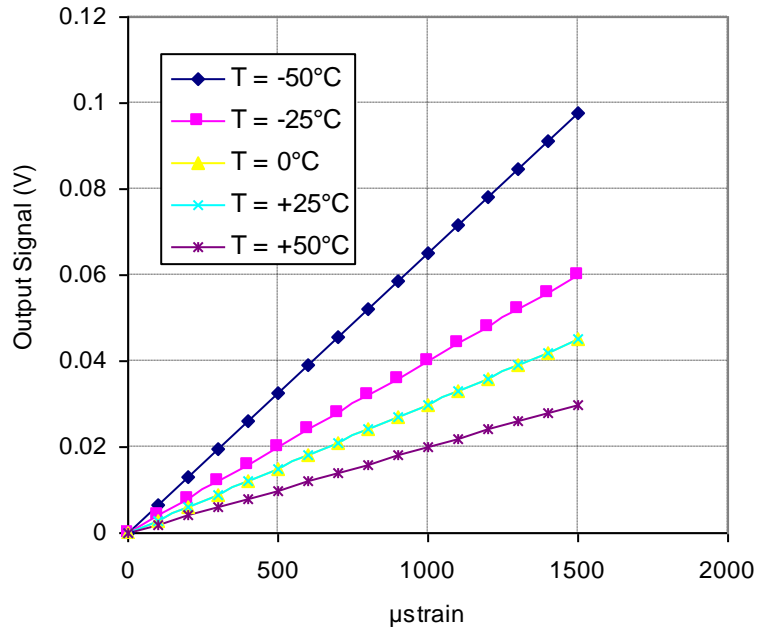
Figure 67 Simplified calibration curves at different temperatures for doping concentration of 1×10^{19} /cm^3 (Design 3)
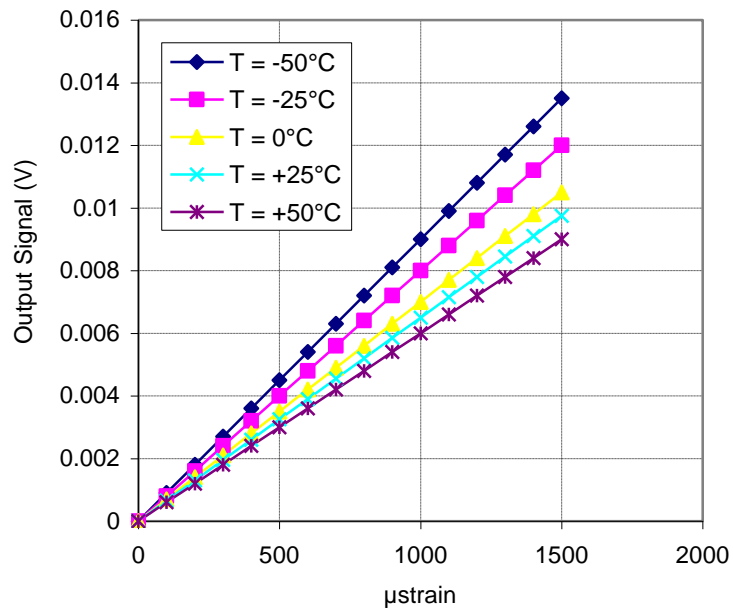
Figure 68 Simplified calibration curves at different temperatures for doping concentration of 5×10^{19} /cm^3 (Design 3)
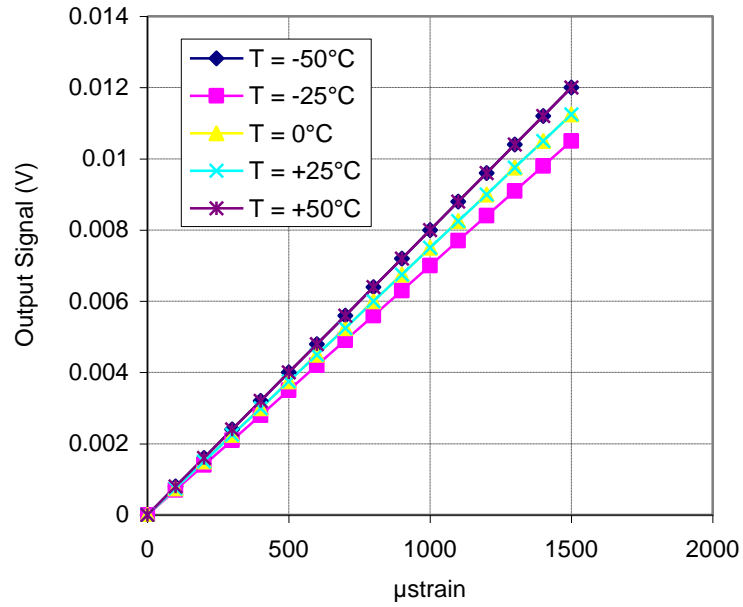
Figure 69 Simplified calibration curves at different temperatures for doping concentration of 1×10^{20} /cm^3 (Design 3)
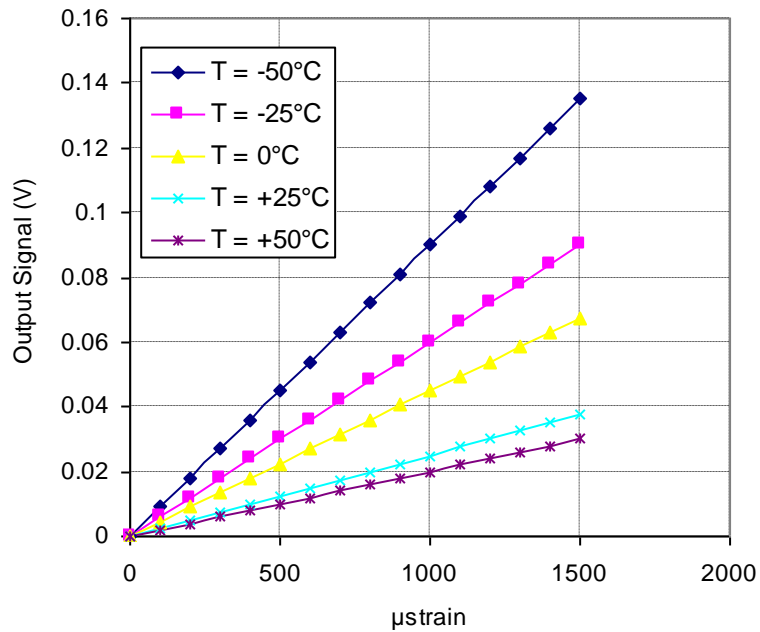
Figure 70 Simplified calibration curves at different temperatures for doping concentration of 1×10^{18} /cm^3 (Design 4)
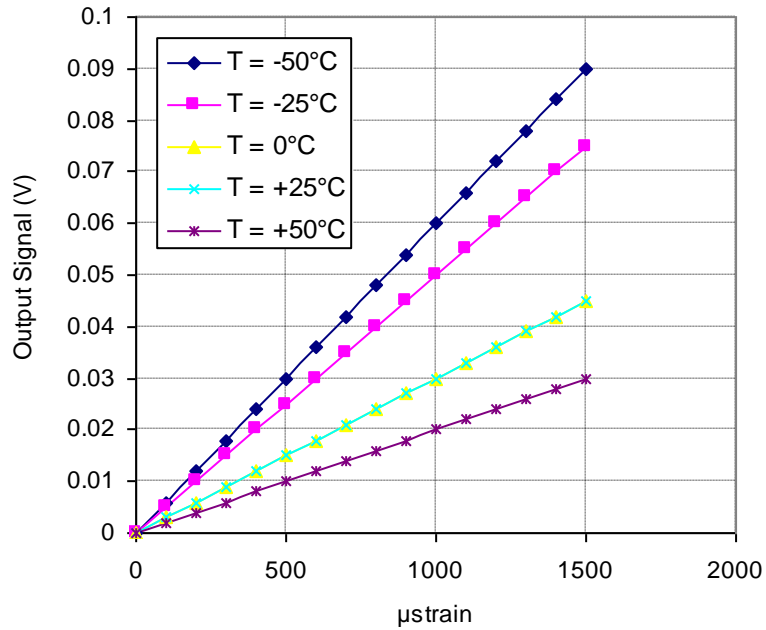
Figure 71 Simplified calibration curves at different temperatures for doping concentration of 5×10^{18} /cm³ (Design 4)
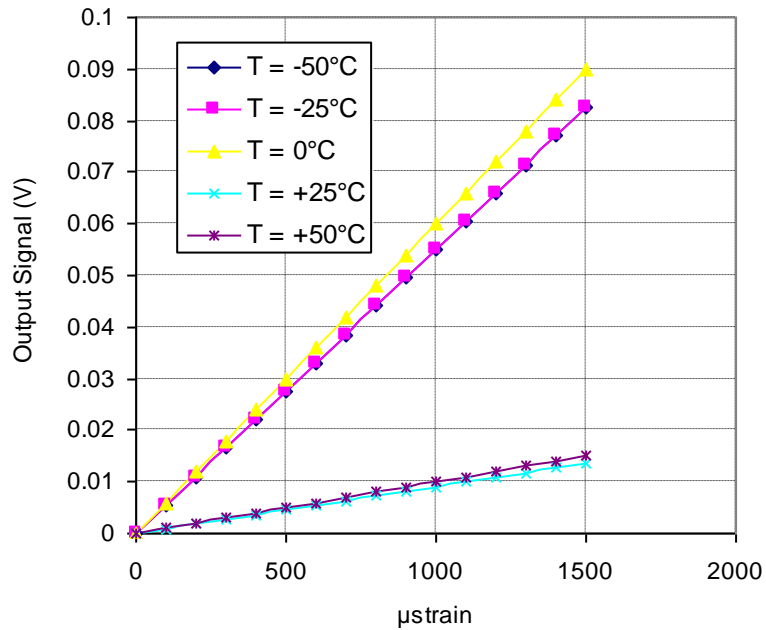
Figure 72 Simplified calibration curves at different temperatures for doping concentration of 1×10^{19} /cm³ (Design 4)
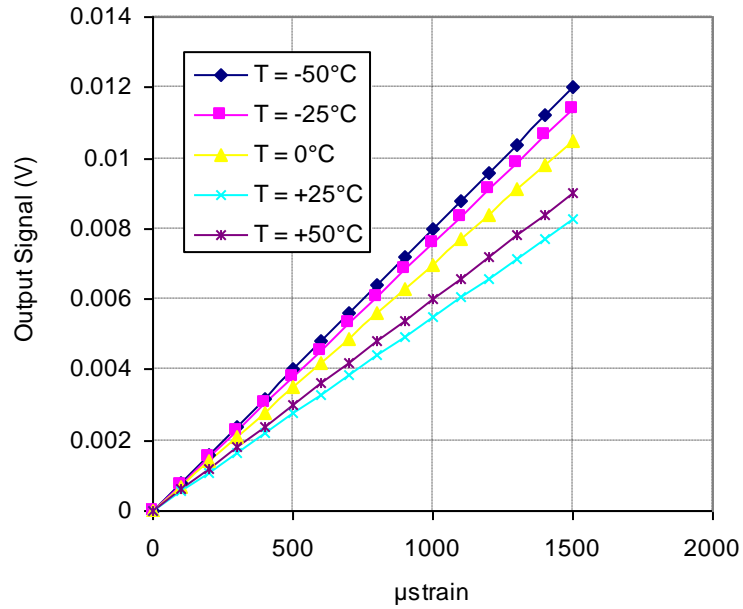
Figure 73 Simplified calibration curves at different temperatures for doping concentration of 5×10^{19} /cm^3 (Design 4)
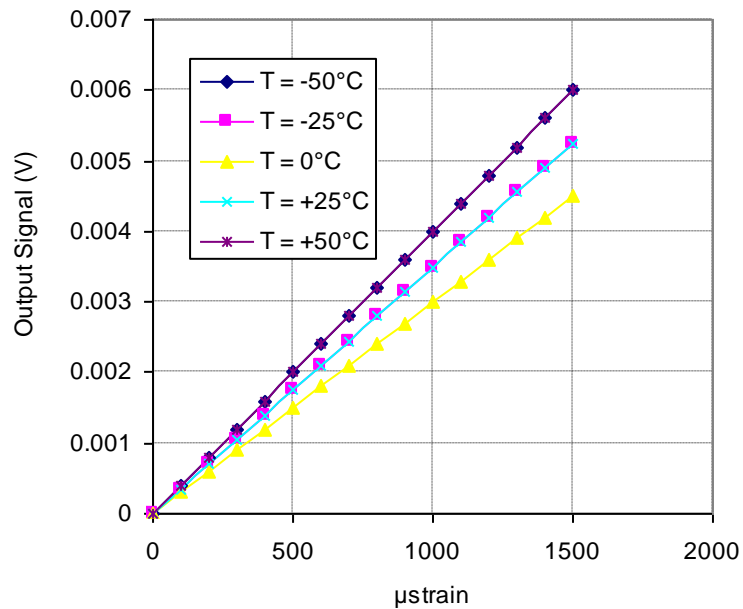
Figure 74 Simplified calibration curves at different temperatures for doping concentration of 1×10^{20} /cm^3 (Design 4)

Table 8 Summary of sensitivity values at different temperatures and doping concentrations

(Design 1)

Temperature (°C)	Sensing Sensitivity (V/με)				
	1×10^{18} (atoms/cm³)	5×10^{18} (atoms/cm³)	1×10^{19} (atoms/cm³)	5×10^{19} (atoms/cm³)	1×10^{20} (atoms/cm³)
-50	9.00E-05	8.00E-05	5.50E-05	8.50E-06	7.50E-06
-25	7.00E-05	6.50E-05	4.00E-05	7.00E-06	6.00E-06
0	6.00E-05	4.00E-05	3.50E-05	7.20E-06	5.60E-06
25	5.00E-05	3.50E-05	2.50E-05	5.50E-06	6.00E-06
50	3.50E-05	3.00E-05	2.80E-05	5.50E-06	5.00E-06

Table 9 Summary of sensitivity values at different temperatures and doping concentrations

(Design 2)

Temperature (°C)	Sensing Sensitivity (V/με)				
	1×10^{18} (atoms/cm³)	5×10^{18} (atoms/cm³)	1×10^{19} (atoms/cm³)	5×10^{19} (atoms/cm³)	1×10^{20} (atoms/cm³)
-50	7.00E-05	5.00E-05	3.50E-05	1.00E-05	7.00E-06
-25	3.00E-05	4.00E-05	3.00E-05	8.00E-06	5.00E-06
0	4.00E-05	2.70E-05	2.50E-05	7.00E-06	6.00E-06
25	3.00E-05	2.50E-05	2.00E-05	6.00E-06	6.00E-06
50	2.00E-05	2.00E-05	2.00E-05	5.00E-06	4.00E-06

Table 10 Summary of sensitivity values at different temperatures and doping concentrations

(Design 3)

Temperature (°C)	Sensing Sensitivity (V/με)				
	1×10^{18} (atoms/cm³)	5×10^{18} (atoms/cm³)	1×10^{19} (atoms/cm³)	5×10^{19} (atoms/cm³)	1×10^{20} (atoms/cm³)
-50	9.00E-05	7.00E-05	6.50E-05	9.00E-06	8.00E-06
-25	8.00E-05	6.00E-05	4.00E-05	8.00E-06	7.00E-06
0	6.00E-05	3.00E-05	3.00E-05	7.00E-06	7.50E-06
25	4.50E-05	4.00E-05	3.00E-05	6.50E-06	7.50E-06
50	3.50E-05	3.00E-05	2.00E-05	6.00E-06	8.00E-06

Table 11 Summary of sensitivity values at different temperatures and doping concentrations

(Design 4)

Temperature (°C)	Sensing Sensitivity (V/µε)				
	1×10^{18} (atoms/cm^3)	5×10^{18} (atoms/cm^3)	1×10^{19} (atoms/cm^3)	5×10^{19} (atoms/cm^3)	1×10^{20} (atoms/cm^3)
-50	9.00E-05	6.00E-05	5.50E-05	8.00E-06	4.00E-06
-25	6.00E-05	5.00E-05	5.50E-05	7.60E-06	3.50E-06
0	4.50E-05	3.00E-05	6.00E-05	7.00E-06	3.00E-06
25	2.50E-05	3.00E-05	9.00E-06	5.50E-06	3.50E-06
50	2.00E-05	2.00E-05	1.00E-05	6.00E-06	4.00E-06

Table 12 Summary of sensitivity values at different temperatures and doping concentrations

(Design 5)

Temperature (°C)	Sensing Sensitivity (V/µε)				
	1×10^{18} (atoms/cm^3)	5×10^{18} (atoms/cm^3)	1×10^{19} (atoms/cm^3)	5×10^{19} (atoms/cm^3)	1×10^{20} (atoms/cm^3)
-50	5.00E-05	7.00E-05	4.00E-05	5.00E-05	1.00E-06
-25	3.00E-05	2.50E-05	1.00E-05	4.00E-05	1.00E-06
0	1.00E-05	9.00E-06	3.00E-05	5.00E-05	1.50E-06
25	9.50E-06	1.00E-05	1.00E-05	6.00E-05	1.00E-06
50	8.00E-06	9.10E-06	7.80E-06	4.00E-06	2.00E-06

Table 13 Summary of sensitivity values at different temperatures and doping concentrations

(Design 6)

Temperature (°C)	Sensing Sensitivity (V/µε)				
	1×10^{18} (atoms/cm^3)	5×10^{18} (atoms/cm^3)	1×10^{19} (atoms/cm^3)	5×10^{19} (atoms/cm^3)	1×10^{20} (atoms/cm^3)
-50	5.00E-05	4.50E-05	5.00E-05	4.00E-05	5.00E-06
-25	4.00E-05	4.00E-05	3.00E-05	3.40E-05	4.00E-06
0	3.50E-05	3.00E-05	2.50E-05	3.00E-05	6.00E-06
25	2.00E-05	1.00E-05	9.58E-06	5.00E-06	5.50E-06
50	9.50E-06	9.00E-06	8.00E-06	7.50E-06	4.00E-06

7.5.   Effect of Alignment Errors

Successful application of piezoresistive sensors requires properly designed sensing chips and the awareness of potential sources of error during the sensor application. In particular, rotational alignment error, during fabrication and installation, can be considered one of the most important sources of errors. Another factor that can cause significant variability, when comparing results, is the purity of the used silicon substrates and the oxygen levels in the silicon samples. The effects of crystallographic misalignment and thermal errors were not mentioned in most of the published literature; however, Jaeger and Suhling [45] showed that temperature variations and measurement errors can play a pivotal role in determining accuracy of the results obtained during both calibration and application of piezoresistive stress sensors. Therefore, the goal of this section is to evaluate the sensitivity of the fabricated sensing chip to alignment/rotational errors, which can affect the sensor output signal. FEA simulation was used to analyze the effect of rotational error on the sensor output signal. The alignment error around the center of the chip is plotted versus the % signal error in Figure 75. It is clear that about 4.5^o alignment error can introduce error in the sensor output signal of about 2%, which is an acceptable value. Therefore, the current sensor design can be considered to have low sensitivity to rotational errors within $\pm4.5^o$ misalignment. It is also noted that the induced error due to the rotational misalignment is non-linear.
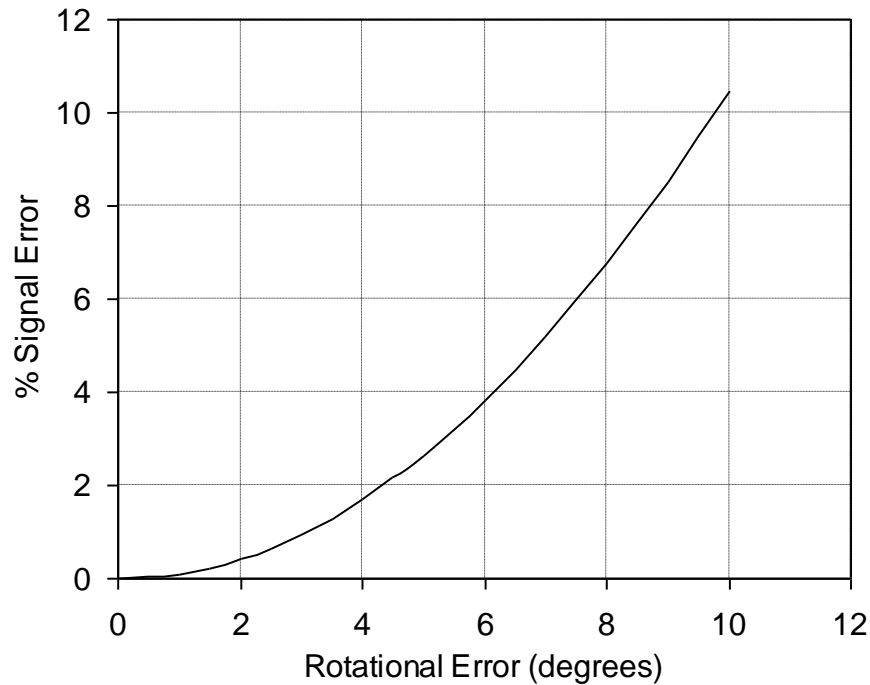
Figure 75 FEA results showing the effect of alignment/rotational error on the sensor output signal. The rotational error is measured from [110] direction, number of FEA runs = 16

7.6. Results of Flip Chip Packaging

Although the current study did not focus on packaging, a few samples were packaged and tested. The proposed packaging scheme for the developed sensing chip utilizes flip-chip technology. General steps of the flip-chip process are illustrated in Figure 50. As shown, the contact pads on the top surface of the sensing chip are attached to the lower surface of the packaging pcb. The sensor output signal is acquired through the contact pads on the lower surface of the pcb. Therefore, another pcb is specially designed to meet the requirements of the flip-chip steps. The packaging pcb has two sets of contact pads, on both surfaces, as shown in Figure 50. The lower set of pads is the mirror image of the pads on the MEMS sensing chip, while the other set of pads meet the requirements of the

DAQ board. Figure 76 illustrates the designed pcb, unpackaged sensing chip and a packaged sensing chip.

To attach the sensing chip pads to the pcb pads, conductive epoxy was considered. However, lateral short circuiting between adjacent contact pads was a critical limitation to the success of the packaging process. Therefore, anisotropic conductive epoxy is used. The working concept of the anisotropic conductive adhesive is illustrated in Figure 50. The pcb acts as an intermediate layer between the MEMS sensor and the DAQ system. The thickness of the pcb utilized in the flip-chip packaging in this study is 1/16 inch, approximately 1.60 mm.

Specimens of packaged sensors are tested at room temperature for two doping concentrations, 1×10^{19} atoms/cm^3 and 1×10^{20} atoms/cm^3. The testing results are shown in Figure 77 and Figure 78. As shown, the packaged sensors have lower sensitivity. This effect is the results of the packaging process, which contributed to the sensor overall stiffness. The stiffening process limited the chip deformation and hence the sensing element response. In addition, the response of the packaged sensor is slightly nonlinear compared to the unpackaged sensor. Therefore, further investigation is required to understand the behavior of the packaged chip and to control its characteristics. On top of the recommendations to improve the process are using a thinner packaging pcb to reduce the stiffening effect and exploring the opportunity to develop flexible link between the MEMS sensor and the packing pcb.

Table 14 Sensitivity of unpackaged and packaged MEMS sensors for doping concentrations of 1×10^{19} atoms/cm^3 and 1×10^{20} atoms/cm^3 at room temperature

	Sensitivity (mV/µε/V)	
	1×10^{19} atoms/cm^3	1×10^{20} atoms/cm^3
Unpackaged	0.0200	0.0050
Packaged	0.0034	0.0015
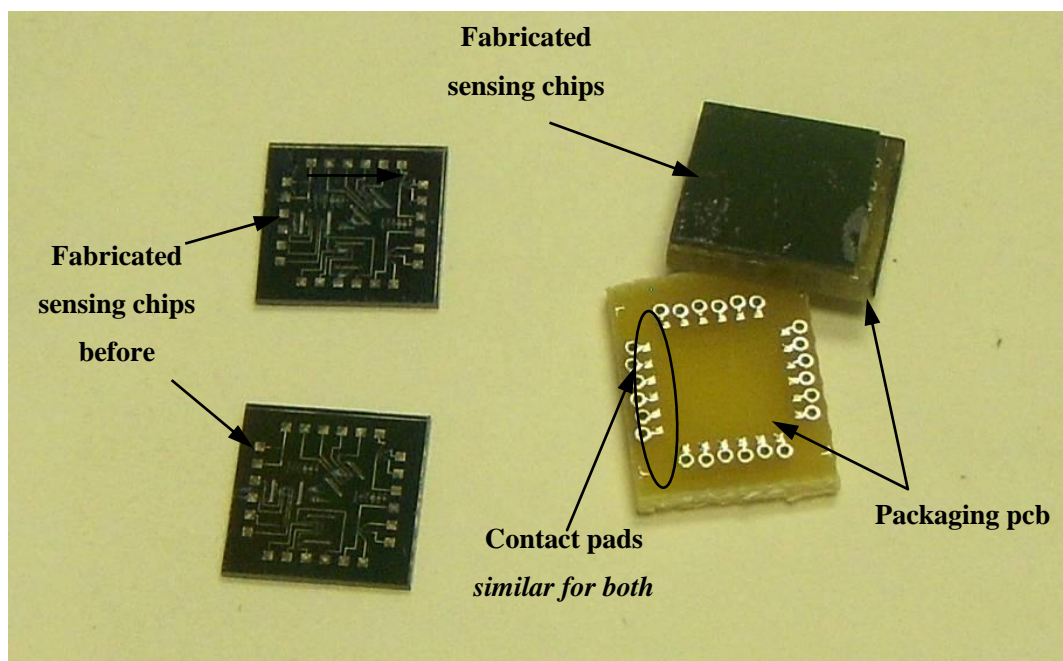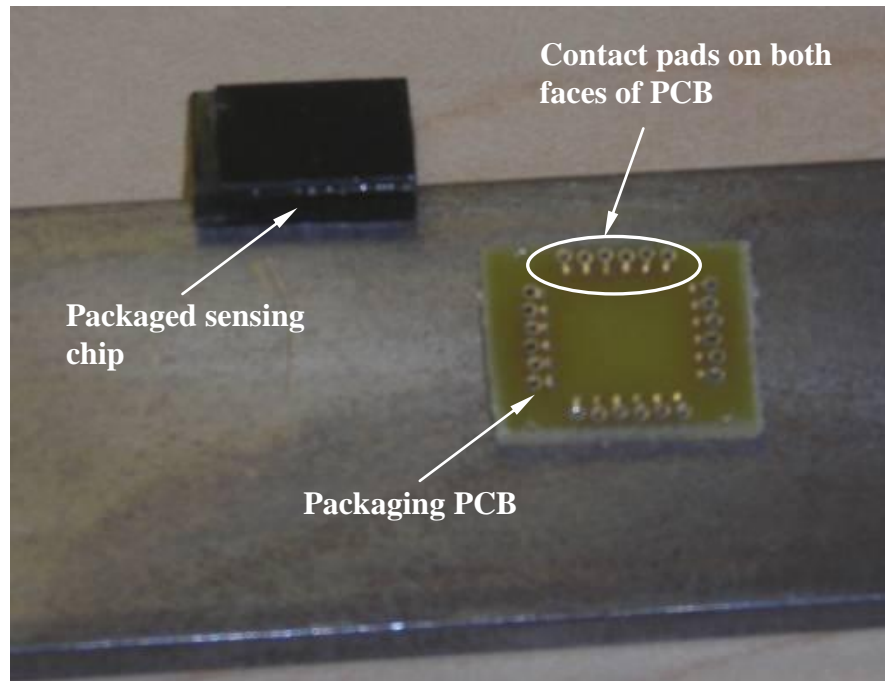
Figure 76 Packaging components (packaging pcb, unpackaged sensing chip, and packaged sensor). Chip dimensions 10mm (length)×10mm (width)×500μm (thickness)
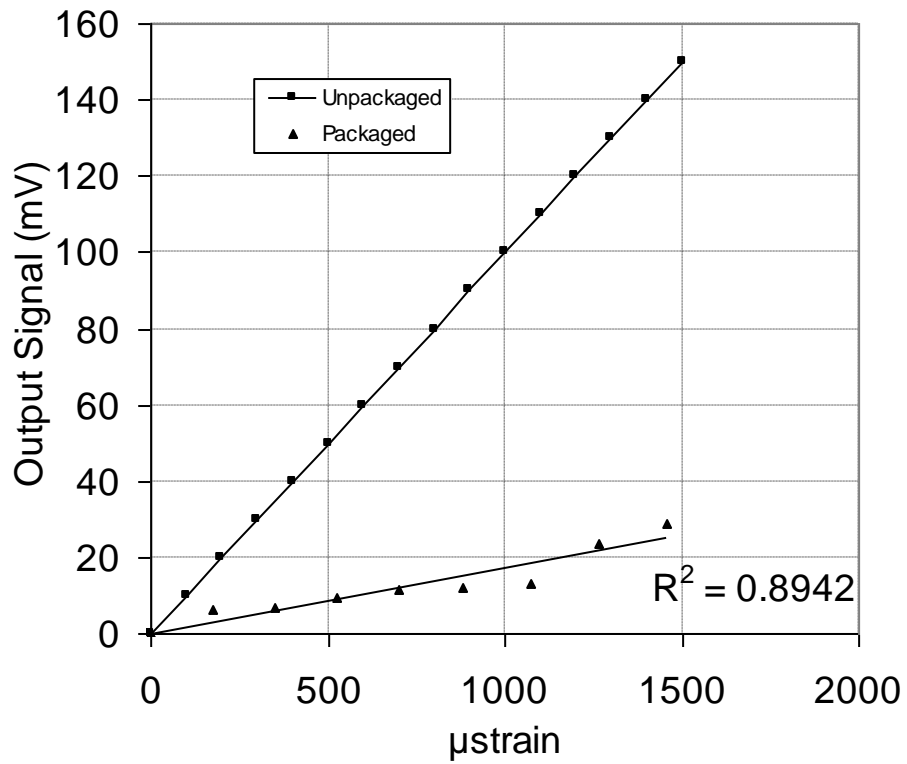
Figure 77 Calibration curve of packaged and unpackaged MEMS sensors, doping concentration of 1×10^{19} atoms/cm^3, input voltage = 5 V. The linear regression line for the packaged sensor was set to zero. R^2 is displayed for the results of the packaged sensor

$R^2 = 0.9345$
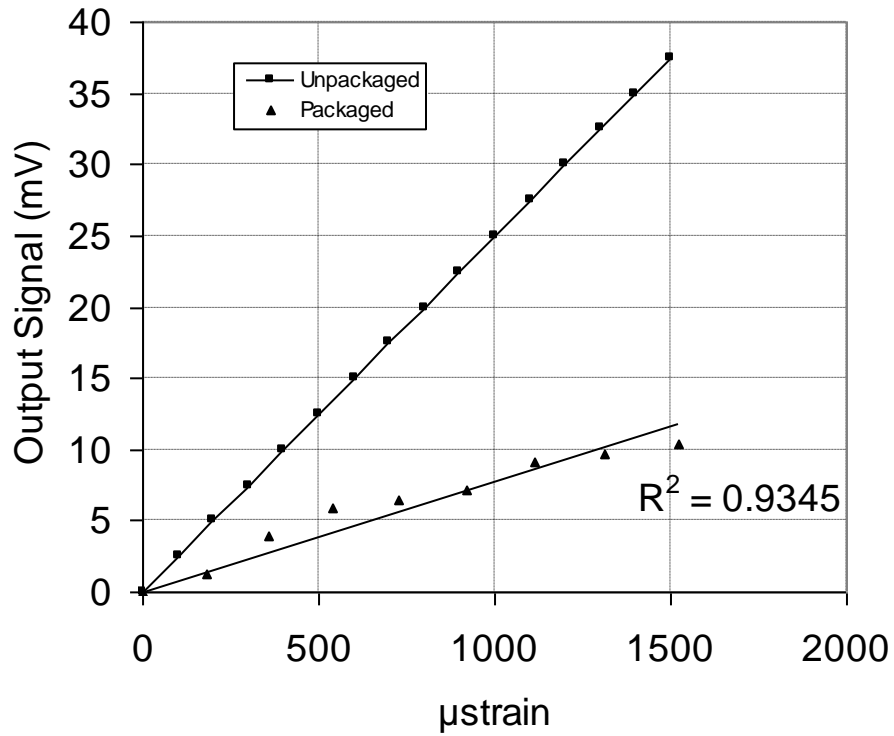
Figure 78 Calibration curve of packaged and unpackaged MEMS sensors, doping concentration of 1×10^{20} atoms/cm^3, input voltage = 5 V. The linear regression line for the packaged sensor was set to zero. R^2 is displayed for the results of the packaged sensor

Chapter 8 – Conclusions

The purpose of this thesis research is to investigate the design of a general-purpose piezoresistive strain sensor, characterize the developed MEMS piezoresistive sensor, and finally, propose packaging scheme for future studies. This chapter presents several key points drawn from this research and proposes recommendations for future work in these areas. In addition, it highlights some point that should be considered in order to improve the results attained in the current research project, which facilitates the migration from research to application.

8.1. Summary of the Current Work

Due to the continuous growth of the silicon-based sensor technology, there exists an obvious trend toward combining MEMS transducers with increasingly sophisticated circuits. These integrated sensing systems are capable of gathering electronic data from the physical world, processing and acting on the information, and transferring the data to other electronic systems which gain intelligence from this process.

In this work, a new MEMS-based piezoresistive strain sensor for structural health monitoring applications is developed. The active sensing material is p-type silicon on a bulk n-type silicon carrier. The sensor is a three-arm rosette that has a temperature self-compensated performance. This sensor is capable of measuring in-plane strains components along orientations of the sensing units. Each sensing unit contains four p-type silicon elements connected in a full-bridge configuration (microbridge) to achieve some level of signal magnification. These elements are aligned along [110] direction and its in-plane transverse, which are convenient crystallographic orientation from microfabrication standpoint. These directions have the highest gauge factor on (100) plane. The sensor was designed to have high impedance, large gauge factor low hysteresis and excellent linearity.

Various methodologies, such as geometry of the sensor silicon carrier and sensing elements' configuration, were employed to develop the new piezoresistive MEMS

strain sensor. A new methodology to realize MEMS piezoresistive sensors was presented. This methodology emphasized the feasibility of using the silicon carrier geometry as a mean to improve the sensor performance while utilizing high doping concentration. To establish such goal, stress concentration regions (SCRs), namely surface trenches, have been introduced in the sensor silicon carrier. These SCRs provided stress or strain concentration. Therefore, by placing the piezoresistive sensing elements in their proximity, the sensor sensitivity can be improved. Six designs of SCRs were considered in this work. Finite element analysis (FEA) method was employed to guide the selection of the SCRs geometry.

Compared with the flat silicon carrier, introducing geometric features in the sensor silicon carrier enhanced the signal strength by more than a factor of three. Moreover, surface trenches minimized the effect of the sensor cross sensitivity (transverse gauge factor), which contribute to the sensor output signal. Furthermore, the noise sources that are most likely to affect the sensor resolution were analyzed at different doping levels and operating temperatures. Simulation results showed that doping concentration of 5×10^{19} atoms/cm^3 has high signal stability over wider temperature range from -50°C to +50°C. In addition, this doping level has the highest signal to noise ratio. It was proved that increasing doping concentration stabilizes the sensor output signal and enhances the signal to noise ratio. The optimum doping concentration based on the sensor design was determined to be 5×10^{19} atoms/cm^3.

Six sensor layouts were successfully designed, fabricated, packaged, tested and calibrated. The testing results showed that increasing doping concentration resulted in substantial loss in the sensor sensitivity, which agrees with all of the published literature. Utilizing doping concentration of 1×10^{20} atoms/cm^3 reduced the sensitivity by about 80% from its value at doping concentration of 1×10^{18} atoms/cm^3. The experimental evaluation showed that fabricated sensors were functional and can serve over temperature range from -50°C to +50°C. Through a comprehensive FEA investigation, it was concluded that the depth of the piezoresistive sensing elements does not have a major influence on the sensor

129

sensitivity. However, minimum piezoresistor thicknesses are favorable to reduce stress gradient perpendicular to the chip surface. As expected, stresses were concentrated around the SCRs. Design 3 showed the most stable performance.

The sensor sensitivity at doping concentration of 1×10^{20} atoms/cm^3 was more than two times higher compared to a 350Ω commercial thin-foil strain gauge. Therefore, the concept of utilizing the geometric features can be applied to develop MEMS piezoresistive strain sensor with low thermal drift and high sensitivity. Moreover, it was demonstrated that selection of the bonding adhesive and the installation procedure plays a pivotal rule in the application of the sensor. Although, analytical modeling showed that the response of this sensor depends on the three piezoresistive coefficients, the influence of the small coefficients (π_{11} and π_{12}) can be neglected for high doping concentrations. In addition, the low power consumption of the MEMS sensor puts it as a strong candidate for wireless sensing applications.

Near-field and far-field strain concepts were discussed to account for signal loss. Moreover, the relationship between the far-field and the near-field strains was experimentally established. Approximately 16% of the applied mechanical strain on the strained surface (far-field strain) is transferred to the sensing elements (near-field strain). The ratio between the far-field to the near-field strain can be improved by one or more of the following actions; wafer thinning, introducing other features in the bottom surface of the sensing chip, and use of SOI wafer while etching the oxide layer underneath the sensing unit.

To verify the FEA modeling process, FEA results were compared to the analytical solution of a flat sensing chip. The maximum % error (at light doping concentration) was less than 5% and the minimum % error (at high doping concentration) was approximately 2%. The experimental results showed that the sensor TCR at doping concentration of 1×10^{20} atoms/cm^3 dropped to approximately 30% of its value at doping concentration of 1×10^{18} atoms/cm^3. The overall sensor TCR followed a logarithmic relationship with the doping level.

In conclusion, high doping concentrations can be employed to develop piezoresistive MEMS sensors and by incorporating stress concentration regions in

the sensor silicon carrier, the measured sensitivity can be enhanced. Sensing elements' configuration, material properties of the bonding adhesive and installation procedure have to be considered in order to efficiently utilize this sensor in various applications. Finally, it goes without saying that packaging scheme shall be further investigated.

The concept of stress concentration can be used to improve the performance of 'virtually' any piezoresistive or piezoelectric sensors, which opens the door to unlimited opportunities to develop new sensors with better sensing and performance characteristics, or to improve existing sensors. This improvement in the sensing and performance characteristics will reflect positively on other applied research fields, e.g. SHM, WSNs.

8.2. Proposed Future Research

This research effort explores the piezoresistive effect as a transduction mechanism to measure mechanical strain under varying temperature conditions. To achieve this goal, the piezoresistive properties of single crystal silicon have been studied over temperature range from -50°C to +50°C for different doping concentrations. The feasibility of employing different mechanisms to enhance the sensing capabilities of the piezoresistive element was investigated. Among the investigated mechanisms are the configuration of the piezoresistive elements and the geometric characteristics of the silicon carrier. These mechanisms are investigated using extensive finite elements study. Later, the simulated sensing chip designs were fabricated using MEMS techniques. The fabricated sensing chips were characterized and tested. Experimental results were compared with the simulation outputs to find out the sources of variability in the development process, if any.

This thesis introduces a new concept, namely geometric gauge factor. The sensor gauge factor can be considered to be the resultant of two components; piezoresistive and geometric gauge factors. The piezoresistive gauge factor depends on material properties, e.g. doping level of sensing elements. On the other hand, the geometric gauge factor, to great extent, depends only on the

characteristics of sensor silicon carrier. Creating geometric features in the sensor silicon carrier develops areas of stress concentration, which in turn increases the differential stress around the piezoresistive sensing elements. Altering the stress field, due to stress concentration, enhances the sensing capabilities of piezoresistive sensors, which results in increased stress/strain sensitivity.

Simulation and experimental results demonstrated the feasibility of the aforementioned concept, geometric gauge factor. Geometric gauge factor does not depend on the doping concentration. Rather, it depends on the layout of the sensor silicon carrier. The high doping concentration and the geometric features combined to stabilize the thermal behavior of the piezoresistive sensing elements at reasonable stress/strain sensitivity. The sensitivity loss due to high doping level is partially recovered by altering stress/strain field around the sensing piezoresistive elements due to increased geometric gauge factor. The results of the current study concluded that high doping concentrations can be employed in mechanical strain measurements under varying temperature conditions. The research findings in this work provide a platform of a systematic approach to develop piezoresistive devices with acceptable sensitivity, resolution, and thermal behavior.

This research effort explores the piezoresistive effect as a transduction mechanism to measure mechanical strain under varying temperature conditions. To achieve this goal, the piezoresistive properties of single crystal silicon have been studied over temperature range from -50°C to $+50^{\circ}$C for different doping concentrations. The feasibility of employing different mechanisms to enhance the sensing capabilities of the piezoresistive element was investigated. Among the investigated mechanisms are the configuration of the piezoresistive elements and the geometric characteristics of the silicon carrier. These mechanisms are investigated using extensive finite elements study. Later, the simulated sensing chip designs were fabricated using MEMS techniques. The fabricated sensing chips were characterized and tested. Experimental results were compared with the simulation outputs to find out the sources of variability in the development process, if any.

8.3. Proposed Future Research

It is the author opinion that the following topics are of high importance to migrate this research effort to applications:

- The I-V characteristic curves should be constructed at various temperatures for the different doping concentrations.

- Further investigation is required to understand the behavior of the packaged chip and to control its characteristics. On top of the recommendations to improve the process are using a thinner packaging pcb to reduce the stiffening effect and exploring the opportunity to develop flexible link between the MEMS sensor and the packing pcb.

- The literature contains extensive data, models, and theories describing the piezoresistive effect in tension and compression. However, existing models fail to predict the piezoresistive behavior of under bending loads. A complete understanding of the piezoresistive effect of silicon and of the factors which influence piezoresistive sensitivity is vital to the design and implementation of innovative piezoresistive sensors. Therefore, investigation of piezoresistive behavior under bending loads is required.

- At the time of this work, due to the unavailability of a stable current source, voltage excitation was used. However, since semiconductor gauges have higher resistance than their thin-foil counterpart, current excitation instead of voltage excitation should be investigated.

- Since the trench depth was determined by a timed etching process, not all of the trenches across the wafer had the same depth. To avoid such problem, Silicon on insulator (SOI) wafers could be used instead; however, this will make the trenches through the sensing chip. Using SOI wafers will have better control over the etch depth compared to using double-side polished wafers.

- Polysilicon may be considered as a sensing material. However, this will require an improved model of piezoresistive behavior of polysilicon.

- Successful implementation of these applications depends upon increased measurement sensitivity, decreased sensor and actuator size, decreased power requirements, more straightforward and reliable calibration techniques, improved dynamic range and sensor bandwidth, and reduced manufacturing costs and complexity. One solution to these design requirements centers on the idea of an integral piezoresistive sensor.

- The piezoresistive MEMS sensor was developed bearing in mind static and quasi-static applications. Therefore, dynamic response was not evaluated. Low-pass filter, with cut off frequency of 100Hz, was used in the conditioning circuit to exclude higher frequency, if any. Evaluation of the sensor dynamic response is a subject of future work.

- Differences in the coefficients of thermal expansion of steel (strained surface), bonding adhesive (M-Bond 200), and silicon substrate suggest that selection of the bonding material plays a crucial role in the long-term drift and hysteresis, which is a subject of a future research in addition to packaging optimization. Additionally, volume and distribution of metal pads can have significant impact on thermal hysteresis of the piezoresistive sensors. In this work, the aluminum pads were moved away from the transduction area, and symmetric pad layout was used to minimize the effect of the thermal stress hysteresis of aluminum pads on silicon.

Appendix A - Finite Element Code

In this project, six sensor designs were considered. Figure A-1 shows the different sensor layouts labeled from Design 1 to Design 6. A three dimensional sample schematic of the sensor design is shown in Figure A-2. These designs can be classified into four different groups. The first group consists from Design 1 and Design 2 to test for the aspect ratio of the sensing unit. The second group consists from Design 2, Design 3 and Design 4 to test for the effect of the surface trenches geometry at the same aspect ratio. The third group consists from Design 4 and Design 5 to test for the aspect ratio of the sensing unit as well as the aspect ratio of the surface trenches. The last group consists from the Design 5 and Design 6 to test for trench geometry at another aspect ratio.

This Appendix provides the code of the finite element (FE) models used in this study. It is noteworthy to mention that the difference between the code files is the geometric part. Therefore, it was imperative to construct this appendix to introduce the full code file of one design, Design 1, and geometry code files of the rest of the designs.
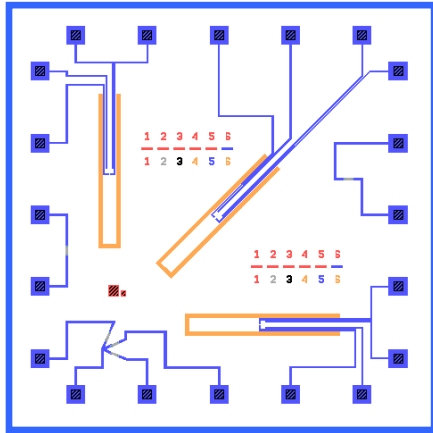
Design 1
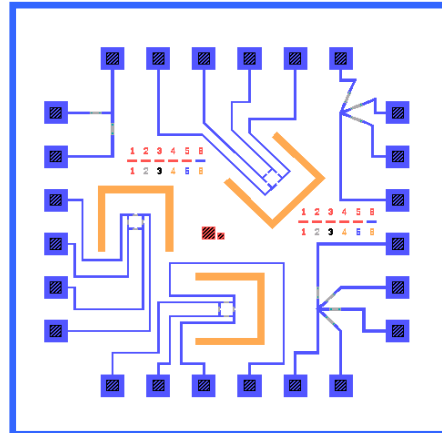
Design 2
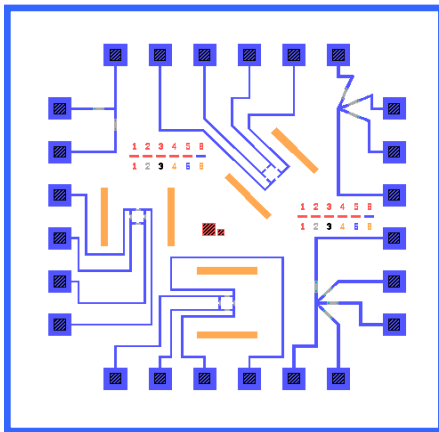
Design 3
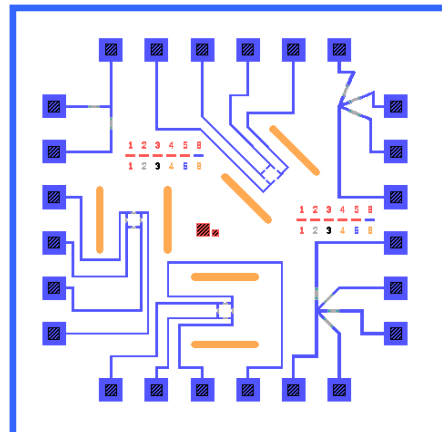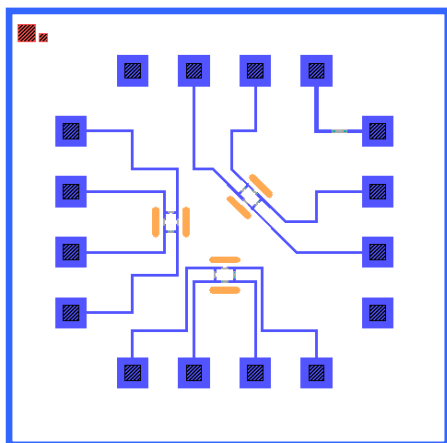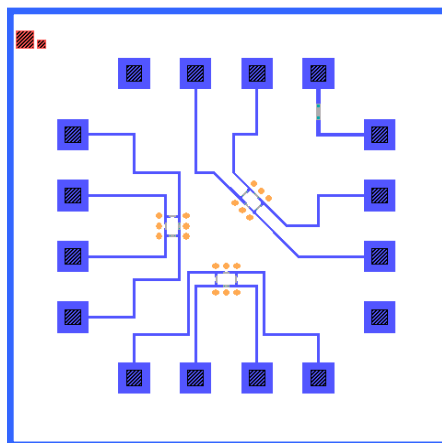
Design 4

Design 5

Design 6

Figure A-1 Schematic of the different sensing chip designs as shown on the microfabrication masks
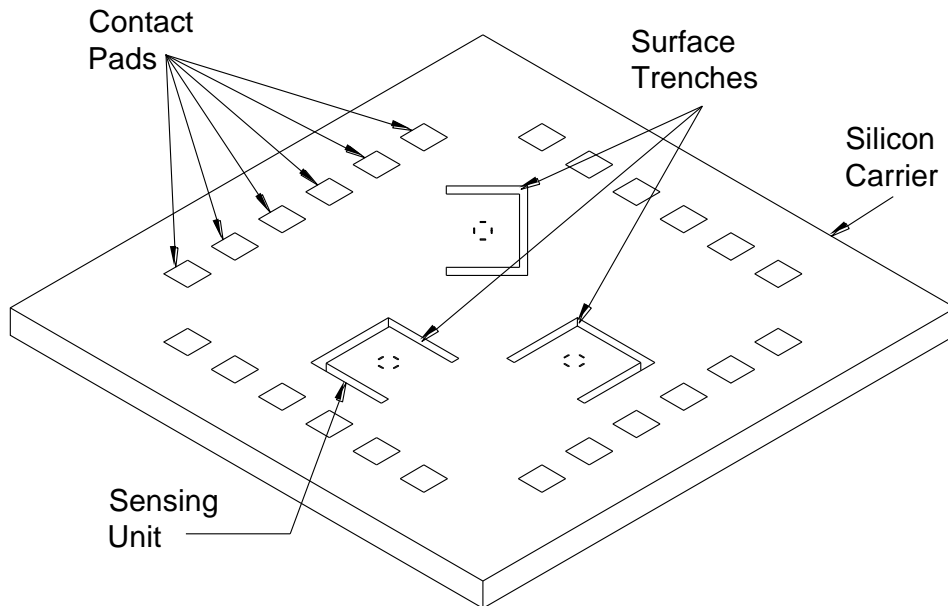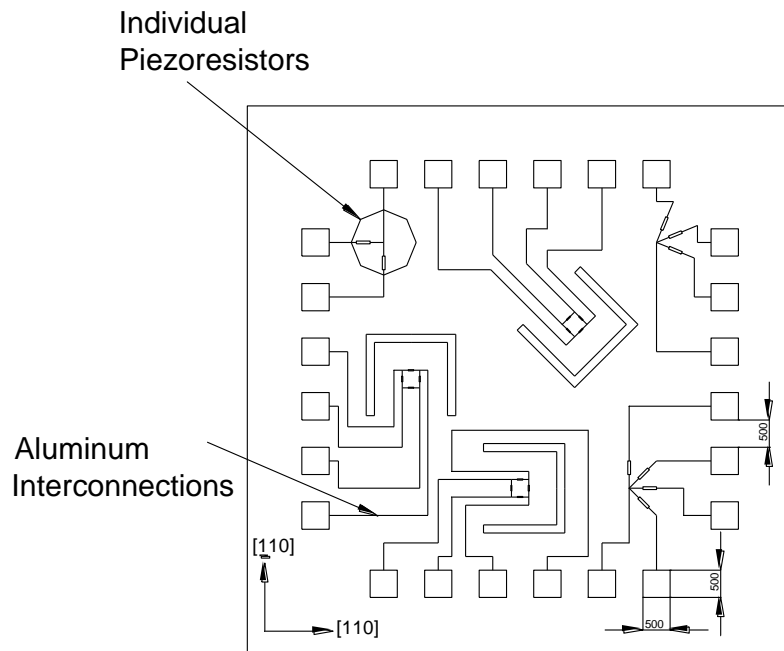
Individual
Piezoresistors

Aluminum
Interconnections

[110]

[110]

500

500

500

Contact
Pads

Surface
Trenches

Silicon
Carrier

Sensing
Unit

*The individual resistor and the aluminum interconnections
are removed from the 3D view for clarity.*

**Figure A-2 Schematic of the sensing chip showing the three sensing units and
the full bridge configuration (Design 2)**
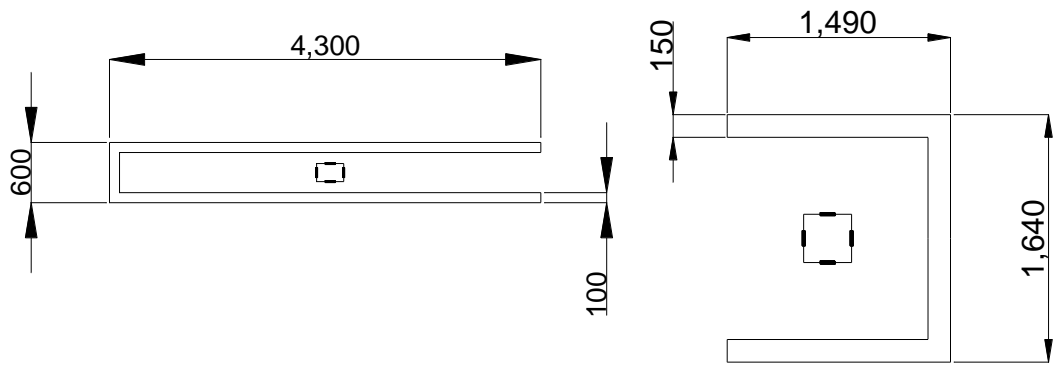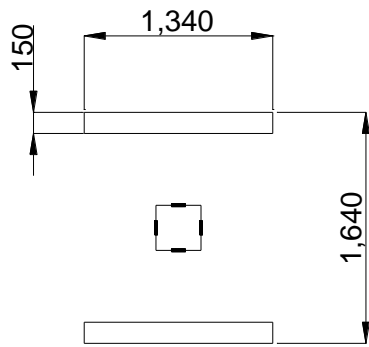
Design 1
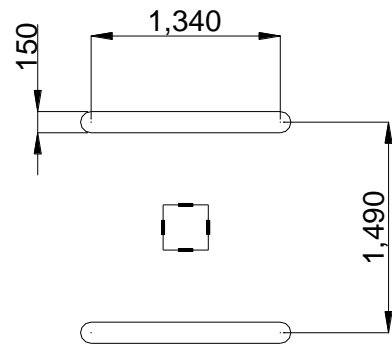
Design 2
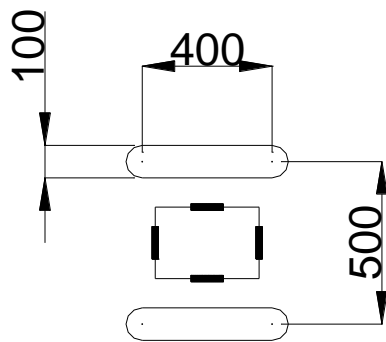
Design 3
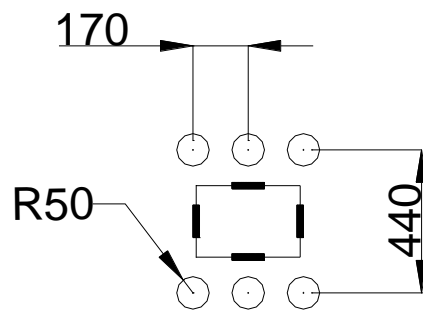
Design 4

Design 5

Design 6

Figure A-3 Schematics of the sensing units of the different sensing chip designs (*All dimensions are in μm)*; depth of all the surface trenches is 100 μm

A1.   Full Code File of Design 1

```
/CONFIG,NPROC,2
/TITLE, SILICON STRAIN GAUGE
/FILNAME,SGAUGE,1


!***********************
!*SCALAR PARAMETERS
!***********************


/PREP7


!*DIMENSIONS
RW=20                       !WIDTH OF EACH PIEZORESISTOR, μm

RL=5*RW                     !LENGTH OF EACH PIEZORESISTOR, μm

RD=1                        !DEPTH OF EACH PIEZORESISTOR, μm

HR=100                      !HOLE RADIUS, μm

HD=100                      !HOLE DEPTH, μm


SW=(8*RL+4*HR)/2            !WIDTH OF SILICON SUBSTRATE, μm

SL=2*(12*RL+2*HR)           !LENGTH OF SILICON SUBSTRATE, μm

SD=500                      !THICKNESS OF SILICON SUBSTRATE, μm


BW=SW                       !WIDTH OF BONDING, μm

BL=SL                       !LENGTH OF BONDING, μm

BD=100                      !DEPTH OF BONDING, μm


M=10         !ASPECT RATIO STRAINED SURFACE TO SILICON CHIP

PW=M*SW      !WIDTH OF THE STRAINED SURFACE (PLATE), μm

PL=M*SL      !LENGTH OF THE STRAINED SURFACE (PLATE), μm
```

PD=1000   !DEPTH OF THE STRAINED SURFACE (PLATE), μm

FD=0.1*SD   !BACK FEATURE DEPTH, μm

!* MATERIAL PROPERTIES

BE=1E-3   !ELASTIC PROPERTIES OF BONDING OF EPOXY, N/μm^2

BNU=0.35   !POISSON'S RATIOS OF THE BONDING OF EPOXY

PE=200E-3   !ELASTIC PROPERTIES OF STRAINED SURFACE, N/μm^2

PNU=0.33   !POISSON'S RATIOS OF THE STRAINED SURFACE

RHO= 7.8E4 !ELECTRICAL RESISTIVITY OF THE SILICON, OHM. μm

C11= 16.57×10^{-2} !STIFFNESS COEFF. OF SILICON <100>, N/μm^2

C12= 6.39×10^{-2}

C44= 7.96×10^{-2}

FACT=1   !SCALING FACTOR FOR PIEZORESISTIVE COEFFICIENTS

P11= FACT*(6.6×10)   !PIEZORESISTIVE COEFF. OF P-TYPE SI

P12= FACT*(-1.1×10)   !DOPING CONCENTRATION IS $\leq$

P44= FACT*(138.1×10)   ! 1×10^{17} ATOMS/CM^3, μm^2/N

!* BOUNDARY CONDITIONS

VS=3   !SUPPLY VOLTAGE, VOLT

VG=0   !GROUND VOLTAGE, VOLT

RHD=0.002*PL   ! DISPLACEMENT OF STRAINED SURFACE, μm

LHD=0   ! DISPLACEMENT OF STRAINED SURFACE, μm

!***

!* P-TYPE MATERIAL PROPERTIES AND ELEMENT DEFINITION

```
!*************************************************************

ET,1,SOLID227,101
TB,ANEL,1,1,21,0
TBTEMP,25
TBDATA,1,C11,C12,C12,0,0,0
TBDATA,7,C11,C12,0,0,0,
TBDATA,12,C11,0,0,0
TBDATA,16,C44,0,0
TBDATA,19,C44,0
TBDATA,21,C44


MP,RSVX,1,RHO


TB,PZRS,1
TBDATA,1,P11,P12,P12
TBDATA,7,P12,P11,P12
TBDATA,13,P12,P12,P11
TBDATA,22,P44
TBDATA,29,P44
TBDATA,36,P44


!*************************************************************
!* SILICON MATERIAL PROPERTIES AND ELEMENT DEFINITION
!*************************************************************


ET,2,SOLID187
TB,ANEL,2,1,21,0
TBTEMP,25
TBDATA,1,C11,C12,C12,0,0,0
TBDATA,7,C11,C12,0,0,0,
```

```
TBDATA,12,C11,0,0,0
TBDATA,16,C44,0,0
TBDATA,19,C44,0
TBDATA,21,C44
```

```
!***************************************************************
!* BONDING MATERIAL PROPERTIES AND ELEMENT DEFINITION
!***************************************************************
```

```
ET,3,SOLID187
MP,EX,3,BE
MP,NUXY,3,BNU
```

```
!***********************************************************
!* STRAINED SURFACE MATERIAL PROPERTIES
!* AND ELEMENT DEFINITION
!***********************************************************
```

```
ET,4,SOLID187
MP,EX,4,PE
MP,NUXY,4,PNU
```

```
SAVE
```

```
! SPECIFY MATERIAL ORIENTATION
LOCAL,11
```

```
LOCAL,12,0,0,0,0,45
```

```
!**************************
!* GEOMETRY DEFINITION
```

!****************************

/PREP7

BLOCK,0,SL,-SW/2,SW/2,0,SD,
BLOCK,0,SL,-SW/2,-SW/2+HR,0,HR,
VSBV,1,2
BLOCK,0,SL,SW/2-HR,SW/2,0,HR,
VSBV,3,1
BLOCK,SL/2-RL,SL/2+RL,-SW/2,SW/2,SD-FD,SD,
VSBV,2,1

!*SENSING BRIDGE
BLOCK,SL/2-RL/2,SL/2+RL/2,RL/2+RL/2,RL/2+RL/2+RW,0,RD,
BLOCK,SL/2-RL/2,SL/2+RL/2,-RL/2-RL/2-RW,-RL/2-RL/2,0,RD,
BLOCK,SL/2-3*RL/2,SL/2-3*RL/2-RW,-RL/2,RL/2,0,RD,
BLOCK,SL/2+3*RL/2,SL/2+3*RL/2+RW,-RL/2,RL/2,0,RD,
VOVLAP,ALL

BLOCK,0,BL,-BW/2,BW/2,SD,SD+BD,
BLOCK,SL/2-RL,SL/2+RL,-SW/2,SW/2,SD-FD,SD,
VADD,3,7

BLOCK,-(PL-SL)/2,(PL-SL)/2+SL,-PW/2,PW/2,SD+BD,SD+BD+PD,
VGLUE,6,8
VGLUE,7,3

SAVE

!************
!* MESHING

143

!************

ESYS,12

!MESH PIEZORESISTORS
TYPE,1
MAT,1
ESIZE,RW/2
MSHAPE,1,3D
VMESH,1,2,1
VMESH,4,5,1

!MESH SILICON
TYPE,2
MAT,2
ESIZE,SW/7
MSHAPE,1,3D
VMESH,6

!MESH BONDING
TYPE,3
MAT,3
ESIZE,BW/3
MSHAPE,1,3D
VMESH,7

!MESH STRAINED SURFACE
TYPE,4
MAT,4
ESIZE,PW/3
MSHAPE,1,3D

```
VMESH,8

/PBC,U,,1
/PBC,VOLT,,1
/PBC,CP,,1
/PNUM,TYPE,1
/NUMBER,1
EPLOT
FINI

SAVE

!*************
!* SOLUTION
!*************

/SOLU
ANTYPE,STATIC

!***************************************
!* BOUNDARY CONDITION APPLICATION
!***************************************

!********************
!* SENSING CIRCUIT
!********************

!SOURCE VOLTAGE TERMINAL

ALLSEL,ALL
ASEL,S, , ,14
```

```
ASEL,A, , ,36
NSLA,S,1
CP,1,VOLT,ALL
*GET,NS,NODE,0,NUM,MIN
AREA, VOLU, PDS,
D,NS,VOLT,VS

!GROUND VOLTAGE TERMINAL
ALLSEL,ALL
ASEL,S, , ,29
ASEL,A, , ,25
NSLA,S,1
CP,2,VOLT,ALL
*GET,NG,NODE,0,NUM,MIN
AREA, VOLU, PDS,
D,NG,VOLT,VG

!1ST OUTPUT CONTACT
ALLSEL,ALL
ASEL,S, , ,11
ASEL,A, , ,30
NSLA,S,1
CP,3,VOLT,ALL
*GET,NO1,NODE,0,NUM,MIN
AREA, VOLU, PDS,

!2ND OUTPUT CONTACT
ALLSEL,ALL
ASEL,S, , ,26
ASEL,A, , ,35
NSLA,S,1
```

```
CP,4,VOLT,ALL
*GET,NO2,NODE,0,NUM,MIN
AREA, VOLU, PDS,

! LEFT BOUNDARY CONDITION FOR THE STRAINED SURFACE
ALLSEL,ALL
ASEL,S, , ,56
NSLA,S,1
D,ALL,UX,LHD
D,ALL,UY,0
D,ALL,UZ,0

! RIGHT BOUNDARY CONDITION FOR THE STRAINED SURFACE
ALLSEL,ALL
ASEL,S, , ,55
NSLA,S,1
D,ALL,UX,RHD
D,ALL,UY,0
D,ALL,UZ,0

NSEL,ALL
CNVTOL,VOLT,1,.0001

SOLVE
FINI

!*********************
!* POST PROCESSING
!*********************

VOA=ABS(VOLT(NO1)-VOLT(NO2))*1000
```

147

```
DR=VOA/VS/1000
SEN=VOA/(VS*(P/PE*1E6))
GF=(DR)/(P/PE)
*STAT
```

A2.　　Geometric Code File of Design 2, Design 3, and Design 4

```
/CONFIG,NPROC,2
/TITLE, SILICON STRAIN GAUGE
/FILNAME,SGAUGE,1


!************************
!*SCALAR PARAMETERS
!************************


/PREP7


!*DIMENSIONS
RW=20                   !WIDTH OF EACH PIEZORESISTOR, μm

RL=5*RW                 !LENGTH OF EACH PIEZORESISTOR, μm

RD=1                    !DEPTH OF EACH PIEZORESISTOR, μm

HR=150                  !HOLE RADIUS, μm

HD=100                  !HOLE DEPTH, μm


SW=2*(10*RL+HR+5*RL+RW+RL+RL/2)!WIDTH OF SI SUBSTRATE, μm

SL=4*(5*RL+RW+RL+RL/2)+30*RL+HR !LENGTH OF SI SUBSTRATE, μm

SD=500                  !THICKNESS OF SILICON SUBSTRATE, μm


BW=SW                   !WIDTH OF BONDING, μm

BL=SL                   !LENGTH OF BONDING, μm
```

BD=100   !DEPTH OF BONDING, μm

M=10   !ASPECT RATIO STRAINED SURFACE TO SILICON CHIP

PW=M*SW   !WIDTH OF THE STRAINED SURFACE (PLATE), μm

PL=M*SL   !LENGTH OF THE STRAINED SURFACE (PLATE), μm

PD=1000   !DEPTH OF THE STRAINED SURFACE (PLATE), μm

FD=0.1*SD   !BACK FEATURE DEPTH, μm

!* MATERIAL PROPERTIES

BE=4.3×10^{-3} !ELASTIC PROPERTIES OF BONDING OF EPOXY, N/μm^2

BNU=0.35   !POISSON'S RATIOS OF THE BONDING OF EPOXY

PE=200×10^{-3} !ELASTIC PROPERTIES OF STRAINED SURFACE, N/μm^2

PNU=0.33   !POISSON'S RATIOS OF THE STRAINED SURFACE

RHO= 7.8×10^{4}!ELECTRICAL RESISTIVITY OF THE SILICON, OHM. μm

C11= 16.57×10^{-2} !STIFFNESS COEFF. OF SILICON <100>, N/μm^2

C12= 6.39×10^{-2}

C44= 7.96×10^{-2}

FACT=1   !SCALING FACTOR FOR PIEZORESISTIVE COEFFICIENTS

P11= FACT*(6.6×10)   !PIEZORESISTIVE COEFF. OF P-TYPE SI

P12= FACT*(-1.1×10)   !DOPING CONCENTRATION IS $\leq$

P44= FACT*(138.1×10)   ! 1×10^{17} ATOMS/CM^3, μm^2/N

!* BOUNDARY CONDITIONS

VS=3   !SUPPLY VOLTAGE, VOLT

VG=0   !GROUND VOLTAGE, VOLT

149

```
RHD=0.002*PL        ! DISPLACEMENT OF STRAINED SURFACE, μm
LHD=0               ! DISPLACEMENT OF STRAINED SURFACE, μm


!************************************************************
!* P-TYPE MATERIAL PROPERTIES AND ELEMENT DEFINITION
!************************************************************


ET,1,SOLID227,101
TB,ANEL,1,1,21,0
TBTEMP,25
TBDATA,1,C11,C12,C12,0,0,0
TBDATA,7,C11,C12,0,0,0,
TBDATA,12,C11,0,0,0
TBDATA,16,C44,0,0
TBDATA,19,C44,0
TBDATA,21,C44


MP,RSVX,1,RHO


TB,PZRS,1
TBDATA,1,P11,P12,P12
TBDATA,7,P12,P11,P12
TBDATA,13,P12,P12,P11
TBDATA,22,P44
TBDATA,29,P44
TBDATA,36,P44


!************************************************************
!* SILICON MATERIAL PROPERTIES AND ELEMENT DEFINITION
!************************************************************
```

```
ET,2,SOLID187
TB,ANEL,2,1,21,0
TBTEMP,25
TBDATA,1,C11,C12,C12,0,0,0
TBDATA,7,C11,C12,0,0,0,
TBDATA,12,C11,0,0,0
TBDATA,16,C44,0,0
TBDATA,19,C44,0
TBDATA,21,C44
```

```
!*************************************************************
!* BONDING MATERIAL PROPERTIES AND ELEMENT DEFINITION
!*************************************************************
```

```
ET,3,SOLID187
MP,EX,3,BE
MP,NUXY,3,BNU
```

```
!*************************************************************
!* STRAINED SURFACE MATERIAL PROPERTIES
!* AND ELEMENT DEFINITION
!*************************************************************
```

```
ET,4,SOLID187
MP,EX,4,PE
MP,NUXY,4,PNU
```

```
SAVE
```

```
! SPECIFY MATERIAL ORIENTATION
LOCAL,11
```

LOCAL,12,0,0,0,0,45

!***************************
!* GEOMETRY DEFINITION
!***************************

BLOCK,0,SL,-SW/2,SW/2,0,SD,
BLOCK,10*RL,23*RL+2*RW,-RL/2-6*RL-RW,-RL/2-6*RL-RW-HR,0,HR,
VSBV,1,2
BLOCK,10*RL,23*RL+2*RW,RL/2+6*RL+RW,RL/2+6*RL+RW+HR,0,HR,
VSBV,3,1
BLOCK,13*RL+RL/2+RW,19*RL+RL/2+RW,-SW/2,SW/2,SD-FD,SD,
BLOCK,SL-23*RL-2*RW,SL-10*RL,-RL/2-6*RL-RW,-RL/2-6*RL-RW-
HR,0,HR,
BLOCK,SL-23*RL-2*RW,SL-
10*RL,RL/2+6*RL+RW,RL/2+6*RL+RW+HR,0,HR,
BLOCK,SL-23*RL-2*RW,SL-23*RL-2*RW-HR,-
(2*HR+13*RL+2*RW)/2,(2*HR+13*RL+2*RW)/2,0,HR

VSEL,S,,,1
VSEL,A,,,2
VSEL,A,,,4
VADD,ALL
VSEL,ALL
VSBV,3,5

!*SENSING BRIDGE
BLOCK,15*RL,15*RL+RW,-RL/2,RL/2,0,RD,
BLOCK,18*RL+RW,18*RL+2*RW,-RL/2,RL/2,0,RD,
BLOCK,16*RL+RW,17*RL+RW,3*RL/2,3*RL/2+RW,0,RD,

BLOCK,16*RL+RW,17*RL+RW,-3*RL/2,-3*RL/2-RW,0,RD,

!*COMPENSATING BRIDGE

BLOCK,15*RL+23*RL+2*RW+HR,15*RL+RW+23*RL+2*RW+HR,-RL/2,RL/2,0,RD,

BLOCK,18*RL+RW+23*RL+2*RW+HR,18*RL+2*RW+23*RL+2*RW+HR,-RL/2,RL/2,0,RD,

BLOCK,16*RL+RW+23*RL+2*RW+HR,17*RL+RW+23*RL+2*RW+HR,3*RL/2,3*RL/2+RW,0,RD,

BLOCK,16*RL+RW+23*RL+2*RW+HR,17*RL+RW+23*RL+2*RW+HR,-3*RL/2,-3*RL/2-RW,0,RD,

VOVLAP,ALL

BLOCK,0,BL,-BW/2,BW/2,SD,SD+BD,

BLOCK,13*RL+RL/2+RW,19*RL+RL/2+RW,-SW/2,SW/2,SD-FD,SD,

VADD,1,11

BLOCK,-(PL-SL)/2,(PL-SL)/2+SL,-PW/2,PW/2,SD+BD,SD+BD+PD,

VGLUE,1,12

VGLUE,12,10

SAVE

A3.   Geometric Code File of Design 5

/CONFIG,NPROC,2

/TITLE, SILICON STRAIN GAUGE

/FILNAME,SGAUGE,1

!***********************

!*SCALAR PARAMETERS

153

```
!*************************

/PREP7

!*DIMENSIONS
RW=20                    !WIDTH OF EACH PIEZORESISTOR, μm
RL=5*RW                  !LENGTH OF EACH PIEZORESISTOR, μm
RD=1                     !DEPTH OF EACH PIEZORESISTOR, μm
HR=100                   !HOLE RADIUS, μm
HD=100                   !HOLE DEPTH, μm


SW=8*RL+4*HR             !WIDTH OF SILICON SUBSTRATE, μm
SL=12*RL+2*HR            !LENGTH OF SILICON SUBSTRATE, μm
SD=500                   !THICKNESS OF SILICON SUBSTRATE, μm


BW=SW                    !WIDTH OF BONDING, μm
BL=SL                    !LENGTH OF BONDING, μm
BD=100                   !DEPTH OF BONDING, μm


M=10        !ASPECT RATIO STRAINED SURFACE TO SILICON CHIP
PW=M*SW     !WIDTH OF THE STRAINED SURFACE (PLATE), μm
PL=M*SL     !LENGTH OF THE STRAINED SURFACE (PLATE), μm
PD=1000     !DEPTH OF THE STRAINED SURFACE (PLATE), μm


FD=0.1*SD   !BACK FEATURE DEPTH, μm


!* MATERIAL PROPERTIES
BE=1E-3     !ELASTIC PROPERTIES OF BONDING OF EPOXY, N/μm²
BNU=0.35    !POISSON'S RATIOS OF THE BONDING OF EPOXY
```

154

PE=200E-3   !ELASTIC PROPERTIES OF STRAINED SURFACE, N/μm^2

PNU=0.33   !POISSON'S RATIOS OF THE STRAINED SURFACE

RHO= 7.8E4 !ELECTRICAL RESISTIVITY OF THE SILICON, OHM. μm

C11= 16.57×10^{-2} !STIFFNESS COEFF. OF SILICON <100>, N/μm^2

C12= 6.39×10^{-2}

C44= 7.96×10^{-2}

FACT=1   !SCALING FACTOR FOR PIEZORESISTIVE COEFFICIENTS

P11= FACT*(6.6×10)   !PIEZORESISTIVE COEFF. OF P-TYPE SI

P12= FACT*(-1.1×10)   !DOPING CONCENTRATION IS $\leq$

P44= FACT*(138.1×10)   ! 1×10^{17} ATOMS/CM^3, μm^2/N

!* BOUNDARY CONDITIONS

VS=3   !SUPPLY VOLTAGE, VOLT

VG=0   !GROUND VOLTAGE, VOLT

RHD=0.002*PL   ! DISPLACEMENT OF STRAINED SURFACE, μm

LHD=0   ! DISPLACEMENT OF STRAINED SURFACE, μm

!**

!* P-TYPE MATERIAL PROPERTIES AND ELEMENT DEFINITION

!**

ET,1,SOLID227,101

TB,ANEL,1,1,21,0

TBTEMP,25

TBDATA,1,C11,C12,C12,0,0,0

TBDATA,7,C11,C12,0,0,0,

TBDATA,12,C11,0,0,0

```
TBDATA,16,C44,0,0
TBDATA,19,C44,0
TBDATA,21,C44


MP,RSVX,1,RHO


TB,PZRS,1
TBDATA,1,P11,P12,P12
TBDATA,7,P12,P11,P12
TBDATA,13,P12,P12,P11
TBDATA,22,P44
TBDATA,29,P44
TBDATA,36,P44
```

!**
!* SILICON MATERIAL PROPERTIES AND ELEMENT DEFINITION
!**

```
ET,2,SOLID187
TB,ANEL,2,1,21,0
TBTEMP,25
TBDATA,1,C11,C12,C12,0,0,0
TBDATA,7,C11,C12,0,0,0,
TBDATA,12,C11,0,0,0
TBDATA,16,C44,0,0
TBDATA,19,C44,0
TBDATA,21,C44
```

!**
!* BONDING MATERIAL PROPERTIES AND ELEMENT DEFINITION
!**

156

```
ET,3,SOLID187
MP,EX,3,BE
MP,NUXY,3,BNU


!***********************************************************
!* STRAINED SURFACE MATERIAL PROPERTIES
!* AND ELEMENT DEFINITION
!***********************************************************


ET,4,SOLID187
MP,EX,4,PE
MP,NUXY,4,PNU


SAVE


! SPECIFY MATERIAL ORIENTATION
LOCAL,11


LOCAL,12,0,0,0,0,45


!***************************
!* GEOMETRY DEFINITION
!***************************


BLOCK,0,SL,-SW/2,SW/2,0,SD,
BLOCK,4*RL+HR,4*RL+HR+4*RL,-2*RL-2*HR,-2*RL,0,HR,
BLOCK,4*RL+HR,4*RL+HR+4*RL,2*RL,2*RL+2*HR,0,HR,


CYL4,4*RL+HR,-2*RL-HR,HR, , , ,HD
CYL4,4*RL+HR,2*RL+HR,HR, , , ,HD
```

CYL4,SL-4*RL-HR,-2*RL-HR,HR, , , ,HD

CYL4,SL-4*RL-HR,2*RL+HR,HR, , , ,HD

VADD,2,3,4,5,6,7

VSBV,1,8

VSBV,2,9

BLOCK,SL/2-RL,SL/2+RL,-SW/2,SW/2,SD-FD,SD,

!*SENSING BRIDGE

BLOCK,SL/2-RL/2,SL/2+RL/2,RL/2+RL/2,RL/2+RL/2+RW,0,RD,

BLOCK,SL/2-RL/2,SL/2+RL/2,-RL/2-RL/2-RW,-RL/2-RL/2,0,RD,

BLOCK,SL/2-3*RL/2,SL/2-3*RL/2-RW,-RL/2,RL/2,0,RD,

BLOCK,SL/2+3*RL/2,SL/2+3*RL/2+RW,-RL/2,RL/2,0,RD,

VOVLAP,ALL

BLOCK,0,BL,-BW/2,BW/2,SD,SD+BD,

BLOCK,SL/2-RL,SL/2+RL,-SW/2,SW/2,SD-FD,SD,

VADD,3,7

BLOCK,-(PL-SL)/2,(PL-SL)/2+SL,-PW/2,PW/2,SD+BD,SD+BD+PD,

VGLUE,6,8

VGLUE,7,3

SAVE

A4. Geometric Code File of Design 6

/CONFIG,NPROC,2

```
/TITLE, SILICON STRAIN GAUGE
/FILNAME,SGAUGE,1


!***********************
!*SCALAR PARAMETERS
!***********************


/PREP7


!*DIMENSIONS
RW=20                    !WIDTH OF EACH PIEZORESISTOR, μm
RL=5*RW                  !LENGTH OF EACH PIEZORESISTOR, μm
RD=1                     !DEPTH OF EACH PIEZORESISTOR, μm
HR=150                   !HOLE RADIUS, μm
HD=100                   !HOLE DEPTH, μm


SW=2*SGL+2*SGW           !WIDTH OF SI SUBSTRATE, μm
SL=4*SGL+SGW+RL+4*RW!LENGTH OF SI SUBSTRATE, μm
SD=500                   !THICKNESS OF SILICON SUBSTRATE, μm


BW=SW                    !WIDTH OF BONDING, μm
BL=SL                    !LENGTH OF BONDING, μm
BD=100                   !DEPTH OF BONDING, μm


M=10          !ASPECT RATIO STRAINED SURFACE TO SILICON CHIP
PW=M*SW       !WIDTH OF THE STRAINED SURFACE (PLATE), μm
PL=M*SL       !LENGTH OF THE STRAINED SURFACE (PLATE), μm
PD=1000       !DEPTH OF THE STRAINED SURFACE (PLATE), μm


FD=0.1*SD     !BACK FEATURE DEPTH, μm
```

159

!* MATERIAL PROPERTIES

BE=4.3×10^{-3} !ELASTIC PROPERTIES OF BONDING OF EPOXY, N/μm^2

BNU=0.35   !POISSON'S RATIOS OF THE BONDING OF EPOXY

PE=200×10^{-3} !ELASTIC PROPERTIES OF STRAINED SURFACE, N/μm^2

PNU=0.33   !POISSON'S RATIOS OF THE STRAINED SURFACE

RHO= 7.8×10^4!ELECTRICAL RESISTIVITY OF THE SILICON, OHM. μm

C11= 16.57×10^{-2} !STIFFNESS COEFF. OF SILICON <100>, N/μm^2

C12= 6.39×10^{-2}

C44= 7.96×10^{-2}

FACT=1   !SCALING FACTOR FOR PIEZORESISTIVE COEFFICIENTS

P11= FACT*(6.6×10)   !PIEZORESISTIVE COEFF. OF P-TYPE SI

P12= FACT*(-1.1×10)   !DOPING CONCENTRATION IS ≤

P44= FACT*(138.1×10)   ! 1×10^{17} ATOMS/CM^3, μm^2/N

!* BOUNDARY CONDITIONS

VS=3   !SUPPLY VOLTAGE, VOLT

VG=0   !GROUND VOLTAGE, VOLT

RHD=0.002*PL   ! DISPLACEMENT OF STRAINED SURFACE, μm

LHD=0   ! DISPLACEMENT OF STRAINED SURFACE, μm

!**

!* P-TYPE MATERIAL PROPERTIES AND ELEMENT DEFINITION

!**

ET,1,SOLID227,101

```
TB,ANEL,1,1,21,0
TBTEMP,25
TBDATA,1,C11,C12,C12,0,0,0
TBDATA,7,C11,C12,0,0,0,
TBDATA,12,C11,0,0,0
TBDATA,16,C44,0,0
TBDATA,19,C44,0
TBDATA,21,C44


MP,RSVX,1,RHO


TB,PZRS,1
TBDATA,1,P11,P12,P12
TBDATA,7,P12,P11,P12
TBDATA,13,P12,P12,P11
TBDATA,22,P44
TBDATA,29,P44
TBDATA,36,P44


!***********************************************************
!* SILICON MATERIAL PROPERTIES AND ELEMENT DEFINITION
!***********************************************************

ET,2,SOLID187
TB,ANEL,2,1,21,0
TBTEMP,25
TBDATA,1,C11,C12,C12,0,0,0
TBDATA,7,C11,C12,0,0,0,
TBDATA,12,C11,0,0,0
TBDATA,16,C44,0,0
TBDATA,19,C44,0
```

TBDATA,21,C44

!**
!* BONDING MATERIAL PROPERTIES AND ELEMENT DEFINITION
!**

ET,3,SOLID187
MP,EX,3,BE
MP,NUXY,3,BNU

!**
!* STRAINED SURFACE MATERIAL PROPERTIES
!* AND ELEMENT DEFINITION
!**

ET,4,SOLID187
MP,EX,4,PE
MP,NUXY,4,PNU

SAVE

! SPECIFY MATERIAL ORIENTATION
LOCAL,11

LOCAL,12,0,0,0,0,45

!****************************
!* GEOMETRY DEFINITION
!****************************

BLOCK,0,SL,-SW/2,SW/2,0,SD,

162

BLOCK,SGL-3*SGW/2,2*SGL+SGW,-(SGL/2+SGW),-SGL/2,0,SGD,

BLOCK,2*SGL,2*SGL+SGW,-SGL/2,SGL/2,0,SGD,

BLOCK,SGL-3*SGW/2,2*SGL+SGW,SGL/2,SGL/2+SGW,0,SGD,

BLOCK,SGL-3*SGW/2,SGL-SGW/2,-SGL/2,(-SGL+SGW)/2,0,SGD,

BLOCK,SGL-3*SGW/2,SGL-SGW/2,(SGL-SGW)/2,SGL/2,0,SGD,

VSBV,1,2

VSBV,7,3

VSBV,1,4

VSBV,2,5

VSBV,1,6

BLOCK,   3*SGL+SGW+RW-SGL/2,3*SGL+SGW+RW+3*RL-SGL/2,-
SW/2,SW/2,SD-FD,SD,

VSBV,2,1

CYL4,3*SGL+SGW-SGL/2,-RL-RW-2*HR,HR, , , ,HD

VSBV,3,1

CYL4,3*SGL+SGW+RW+3*RL/2-SGL/2,-RL-RW-2*HR,HR, , , ,HD

VSBV,2,1

CYL4,3*SGL+SGW+2*RW+3*RL-SGL/2,-RL-RW-2*HR,HR, , , ,HD

VSBV,3,1

CYL4,3*SGL+SGW-SGL/2,RL+RW+2*HR,HR, , , ,HD

VSBV,2,1

CYL4,3*SGL+SGW+RW+3*RL/2-SGL/2,RL+RW+2*HR,HR, , , ,HD

VSBV,3,1

CYL4,3*SGL+SGW+2*RW+3*RL-SGL/2,RL+RW+2*HR,HR, , , ,HD

VSBV,2,1

!*SENSING BRIDGE

BLOCK,3*SGL+SGW-SGL/2,3*SGL+SGW+RW-SGL/2,-RL/2,RL/2,0,RD,

BLOCK,3*SGL+SGW+RW+3*RL-SGL/2,3*SGL+SGW+2*RW+3*RL-SGL/2,-RL/2,RL/2,0,RD,

BLOCK,3*SGL+SGW+RW+RL-SGL/2,3*SGL+SGW+RW+2*RL-SGL/2,-RL,-RL-RW,0,RD,

BLOCK,3*SGL+SGW+RW+RL-SGL/2,3*SGL+SGW+RW+2*RL-SGL/2,RL,RL+RW,0,RD,

!*COMPENSATING BRIDGE

BLOCK,SGL+2*RL,SGL+2*RL+RW,-RL/2,RL/2,0,RD,

BLOCK,SGL+5*RL+RW,SGL+5*RL+2*RW,-RL/2,RL/2,0,RD,

BLOCK,SGL+3*RL+RW,SGL+4*RL+RW,-RL,-RL-RW,0,RD,

BLOCK,SGL+3*RL+RW,SGL+4*RL+RW,RL,RL+RW,0,RD,

VOVLAP,ALL

BLOCK,0,BL,-BW/2,BW/2,SD,SD+BD,

BLOCK,   3*SGL+SGW+RW-SGL/2,3*SGL+SGW+RW+3*RL-SGL/2,-SW/2,SW/2,SD-FD,SD,

VADD,3,11

BLOCK,-(PL-SL)/2, (PL-SL)/2+SL,-PW/2,PW/2,SD+BD,SD+BD+PD,

VGLUE,3,12

VGLUE,12,10

SAVE

Appendix B - Details Microfabrication Process Flow

B1.　Sensor Design and Masks

In this project, six sensor layouts were considered, shown in Figure B-1 and labeled from Design 1 to Design 6. The sensing chip is composed from n-type silicon carrier and p-type sensing elements. Figure B-2 is a 3-D schematic example of Design 2. As shown in this figure, the sensing chip has three sensing units and individual piezoresistive elements. Each sensing unit is composed from a full microbridge configuration, which is formed by four piezoresistive elements. The sensing units are etched along three different orientations with respect to <110>; 0°, 45° and 90°.

The surface trenches are 100 μm in depth with different geometric shapes. Figure B-3 presents the geometric characteristics of the sensing unit of the different sensing chips. The minimum feature size on the mask was 5μm. To ease the handling process of the wafers during microfabrication, no device was designed on a 10mm distance from the wafer wedges. In order to characterize the fabricated wafers, different test structures were included on the designed masks e.g. resistor blocks, resistor rosettes, Greek and Kelvin Crosses, bridges with multiple contacts, doped flat regions…etc, at different orientations.

B2.　Starting Material

The microfabrication process flow utilized 4-inch (100) n-type double side polished silicon substrates with the following specifications:

- Primary flat along <110>
- Thickness of 500±25 μm, total thickness variation less than 1μm
- Bulk resistivity of 10 Ω·cm

It was the original intent to perform back-side etching; therefore, double side polished silicon substrates were selected. However, due to technical limitations,

165

front side etching was performed. Therefore, in the current microfabrication recipe, it was sufficient to have only one polished side.
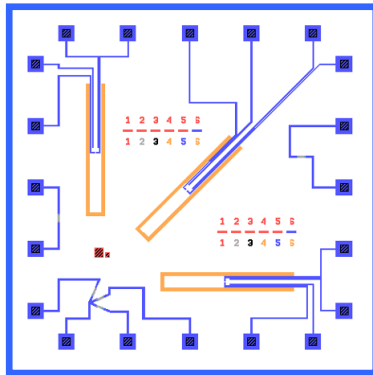
Design 1
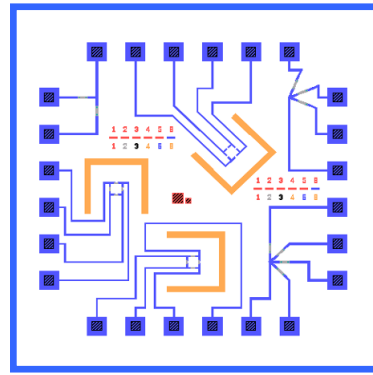
Design 2
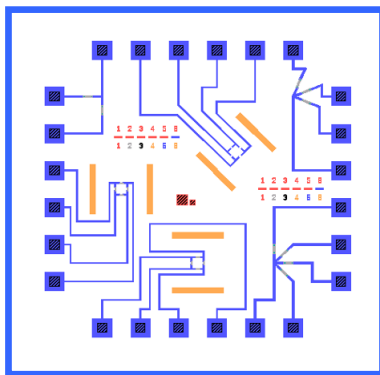
Design 3
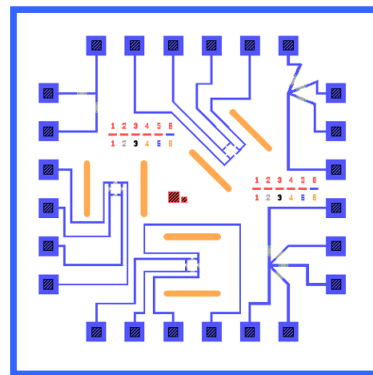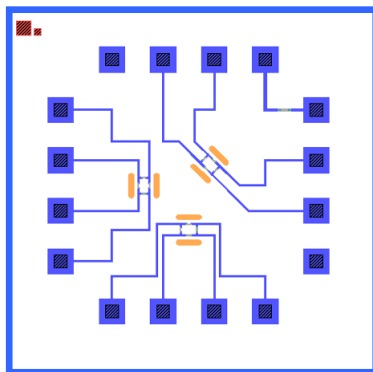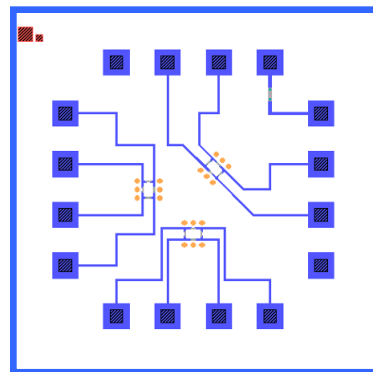
Design 4

Design 5

Design 6

Figure B-1 Layouts of the different sensor designs as shown on the microfabrication masks
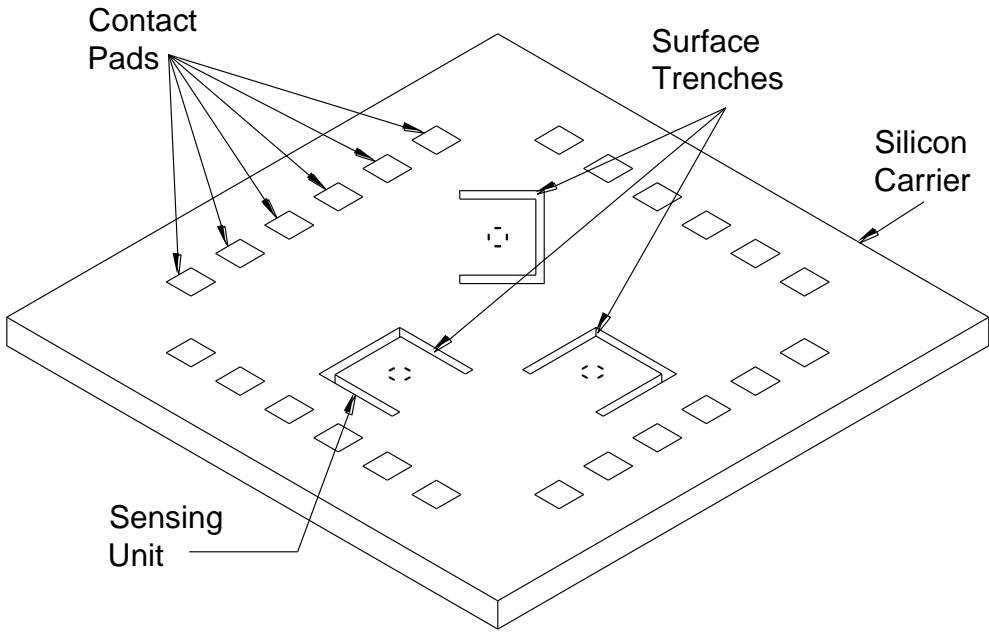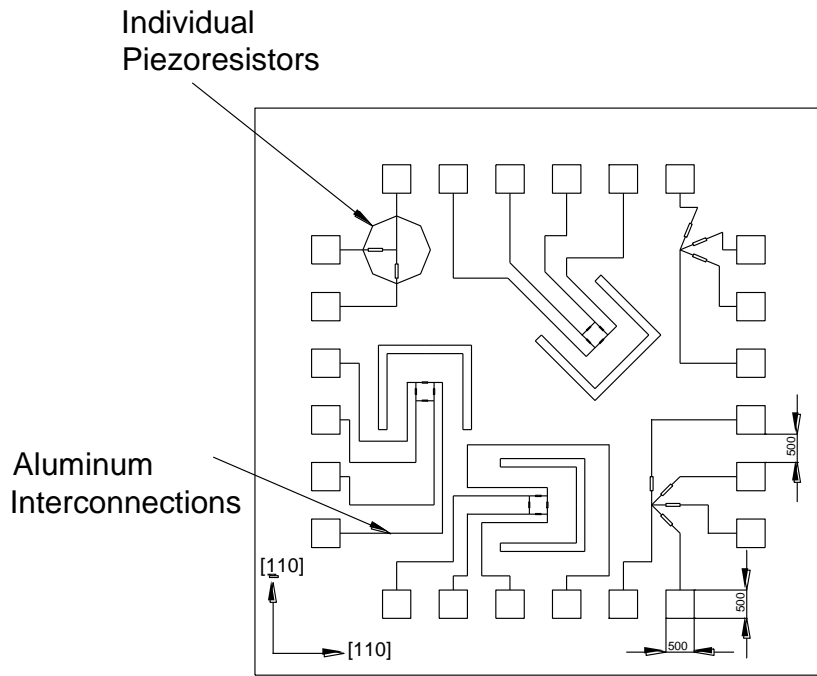
Individual
Piezoresistors

Aluminum
Interconnections

[110]

[110]

500

500

500

Contact
Pads

Surface
Trenches

Silicon
Carrier

Sensing
Unit

The individual resistor and the aluminum interconnections
are removed from the 3D view for clarity.

Figure B-2 Schematic of the sensing chip showing the three sensing units and

the full bridge configuration (Design 2)
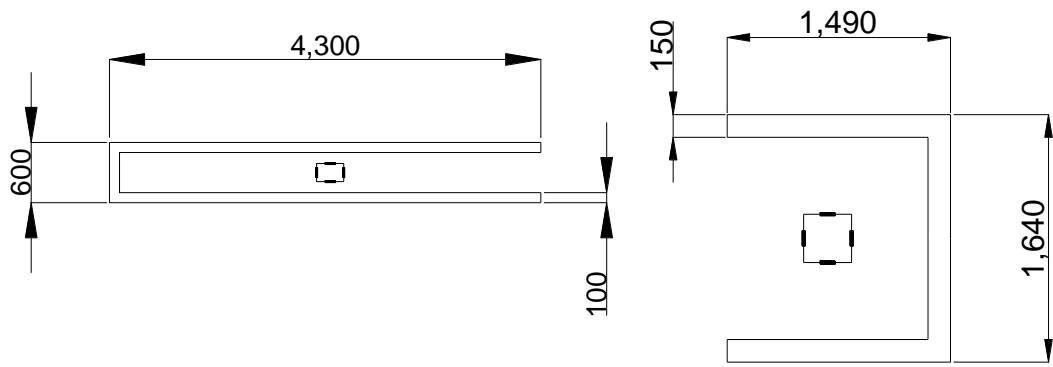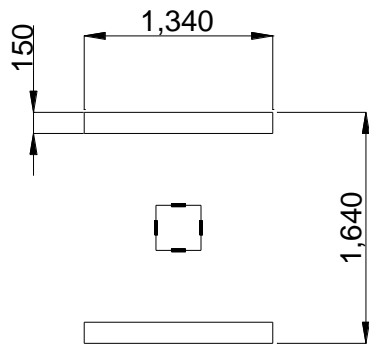
Design 1
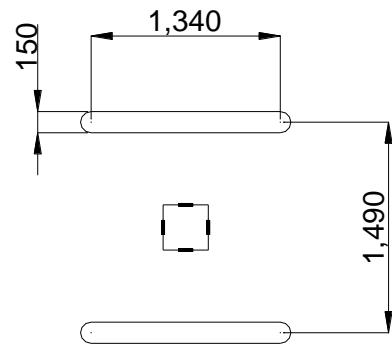
Design 2
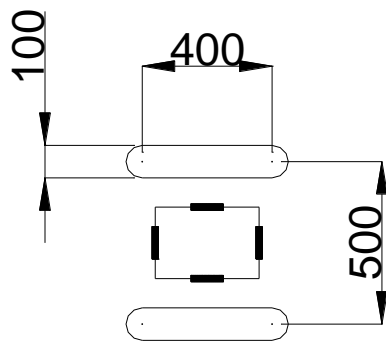
Design 3
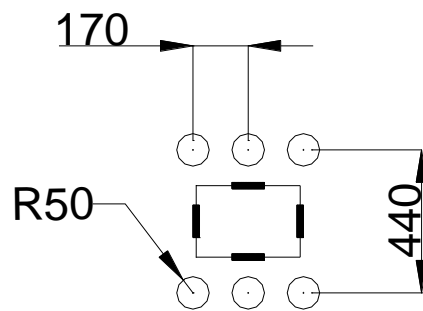
Design 4

Design 5

Design 6

Figure B-3 Schematics of the sensing units of the different sensing chip designs (All dimensions are in μm); depth of all the surface trenches is 100 μm

168

B3.   General Steps

To prototype the different sensor designs, a five-mask microfabrication process flow is used.

Figure B-4 shows a schematic representation of the process flow to prototype the sensing unit. The followings are the general microfabrication steps.

1. Wafer cleaning in piranha solution.

2. Wet thermal oxidation to grow 1200nm of thermal oxide at 1000^oC for 8 hrs in wet N_2 atmosphere. The wafers were loaded in the minibrute furnace. The main power switch, the bubbler heater and the N_2 gas were turned on one after the other i.e. almost at the same time. The flowmeter N_2 of was set at 30.

3. Lithography to pattern the first mask (alignment marks).

4. Reactive Ion Etching (RIE) then Deep Reactive Ion Etching (DRIE) to pattern the first mask in the silicon substrate.

5. Lithography to define the piezoresistors' locations using the second mask (doping windows).

6. RIE to open windows for ion implantation.

7. Boron ion implantation with different doses (5.20×10^{12}, 5.20×10^{13}, 5.20×10^{14}, 5.20×10^{15} and 5.20×10^{16} atoms/cm^2) at energy level of 100 keV to create the p-type regions.

8. Masking oxide layer removal using RIE.

9. Annealing at 1100^oC for 15 minutes. The furnace was ramped to 1100^oC. The flowmeter N_2 of was set at 100. Then, the wafers were loaded at very slow rate ~ 1 inch/min. the 15 minutes were counted after the loading process was completed.

10. Wet thermal oxidation to grow insulating oxide layer for one hour at 1000^oC.

11. Lithography to pattern the contact via for the aluminum contacts using the third mask (contact via openings).

12. RIE to open contact via.

13. Lithography to pattern the surface trenches using the fourth mask (surface trenches).

14. RIE then DRIE to pattern the fourth mask in the silicon substrate to a depth of about 100µm.

15. Aluminum sputtering for 30 minutes to get aluminum layer of thickness 500nm.

16. Lithography to define metallization traces and interconnects using the fifth mask (metallization and interconnections).

17. Aluminum etching.

18. Wafer dicing, preparation for wire bonding and testing.

The fabricated sensing chips and sensing units are shown in Figure B-5 and Figure B-6, respectively. Each sensing chip is a square 10 mm × 10 mm.

B4.   Details of Microfabrication Process Flow

1)   Wafer preparation and cleaning

     i.   Piranha cleaning for 15 minutes

     ii. Dump and rinse 5 times

     iii. BOE for 2 minutes

     iv. Dump and rinse 5 times

     v.   Spin-Rinse-Dry

2)   Wet thermal oxidation using the Minibrute furnace

     i.   8 hours at 1000 ℃, the measured oxide thickness was about 1200nm. The temperature ramped from room temperature ($\sim 22^{o}$C) to maximum temperature in about 45 minutes.

3)   Lithography using mask#1

     i.   YES HMDS oven ~ 15-20minutes at 150 ^{o}C

     ii. Rehydrated for 10-15 minutes

     iii. Solitec Spinner HPR504

1. spread at 400 rpm for 10 seconds. Approximately 15mL were poured on each wafer before the spreading process.
2. spin at 4000 rpm for 40 seconds
3. the measured photoresist thickness was about 1.2-1.3um

    iv. Solitec hotplate contact soft-bake 90 seconds at 115 $^{\circ}$C

    v. Rehydrated for 10-15 minutes

    vi. Oscar mask aligner

        1. Expose for 3 seconds

    vii. Develop the wafer using 354 developer for 20-25 seconds using dip develop process. The amount of developer used was estimated based on the number of processed wafers; however, during the development process, the developer has to cover the wafer.

    viii. Rinse-Dry

    ix. Microscopic check on the development quality

4) Reactive ion etching

    i. STS RIE for 6:45 minutes using OxiTest recipe. This time is more than the actual required time (based on the measured oxide thickness) by extra about 25% to ensure the complete etching on the oxide. The details of the OxiTest recipe are CF4 - 20sccm, CHF3 - 30sccm, 100mT pressure, 300W RF, ~240nm/min SiO_2 etch rate

5) Resist strip

    i. Place wafers in Acetone for 30 minutes

    ii. IPA Rinse

    iii. Dump rinse 5 times

    iv. Spin-Rinse-Dry

v. Alfa-step was used to measure the etch depth in the oxide

6) Deep reactive ion etching

    i. STS ICP DRIE using Precision recipe. The details of the Precision recipe are C4F8 - 65sccm, SF6 - 80sccm, 20mT pressure, 750W ICP power, 20W Platen power, ~1.2μm/cycle Si etch rate

    ii. Chamber conditioning for ~ 20 cycles

    iii. Silicon etching ~ 45 cycles

7) Wafers' cleaning

    i. Place wafers in Acetone for 30 minutes

    ii. IPA Rinse

    iii. Dump rinse 5 times

    iv. Spin-Rinse-Dry

    v. Alfa-step was used to measure the combined etch depth in the oxide and the silicon

8) Lithography using mask#2

    i. YES HMDS oven ~ 15-20minutes at 150 ^{o}C

    ii. Rehydrated for 10-15 minutes

    iii. Solitec Spinner HPR504

        1. spread at 400 rpm for 10 seconds. Approximately 15mL were poured on each wafer before the spreading process.

        2. spin at 4000 rpm for 40 seconds

        3. the measured photoresist thickness was about 1.2-1.3um

    iv. Solitec hotplate contact soft-bake 90 seconds at 115 ^{o}C

    v. Rehydrated for 10-15 minutes

    vi. Oscar mask aligner

1. Expose for 3 seconds

    vii. Develop the wafer using 354 developer for 20-25 seconds using dip develop process. The amount of developer used was estimated based on the number of processed wafers; however, during the development process, the developer has to cover the wafer.

    viii. Rinse-Dry

    ix. Microscopic check on the development quality

9) Reactive ion etching

    i. STS RIE for 6:45 minutes using OxiTest recipe. This time is more than the actual required time (based on the measured oxide thickness) by extra about 25% to ensure the complete etching on the oxide. The details of the OxiTest recipe are CF4 - 20sccm, CHF3 - 30sccm, 100mT pressure, 300W RF, ~240nm/min SiO_2 etch rate

10) Resist Strip

    i. Place wafers in Acetone for 30 minutes

    ii. IPA Rinse

    iii. Dump rinse 5 times

    iv. Spin-Rinse-Dry

11) Boron ion implantation with different doses (5.20×10^{12}, 5.20×10^{13}, 5.20×10^{14}, 5.20×10^{15} and 5.20×10^{16} atoms/cm^2) at energy level of 100 keV to create the p-type regions. These doses were planned to get final doping concentrations of 1×10^{18} atoms/cm^3, 5×10^{18} atoms/cm^3, 1×10^{19} atoms/cm^3, 5×10^{19} atoms/cm^3 and 1×10^{20} atoms/cm^3, respectively. These doses were reviewed by INNOViON ion implantation facility to fit their equipments. The following information was supplied to INNOViON wafer type, implant specie, wafer diameter, dose,

concentration, energy, junction depth and mask thermal oxide thickness.

12) Mask oxide removal
    i. STS RIE for 6:45 minutes using OxiTest recipe

13) Wafers' cleaning
    i. Place wafers in Acetone for 30 minutes
    ii. IPA Rinse
    iii. Dump rinse 5 times
    iv. Spin-Rinse-Dry

14) Annealing (drive in)
    i. Minibrute for 15 minutes at $1100^{o}C$ in dry N_2 environment. The furnace was ramped to $1100^{o}C$. The flowmeter N_2 of was set at 100. Then, the wafers were loaded at very slow rate ~ 1 inch/min. the 15 minutes were counted after the loading process was completed.

15) Wet thermal oxidation using the Minibrute furnace
    i. 1 hour at $1000°C$ in wet N_2 environment

16) Lithography using mask#3
    i. YES HMDS oven ~ 15-20minutes at $150\ ^{o}C$
    ii. Rehydrated for 10-15 minutes
    iii. Solitec Spinner HPR504
        1. spread at 400 rpm for 10 seconds. Approximately 15mL were poured on each wafer before the spreading process.
        2. spin at 4000 rpm for 40 seconds

3. the measured photoresist thickness was about 1.2-1.3um

    iv. Solitec hotplate contact soft-bake 90 seconds at 115 $^{\circ}$C

    v. Rehydrated for 10-15 minutes

    vi. Oscar mask aligner

        1. Expose for 3 seconds

    vii. Develop the wafer using 354 developer for 20-25 seconds using dip develop process. The amount of developer used was estimated based on the number of processed wafers; however, during the development process, the developer has to cover the wafer.

    viii. Rinse-Dry

    ix. Microscopic check on the development quality

17) Reactive ion etching

    i. STS RIE for 6:45 minutes using OxiTest recipe. This time is more than the actual required time (based on the measured oxide thickness) by extra about 25% to ensure the complete etching on the oxide. The details of the OxiTest recipe are CF4 - 20sccm, CHF3 - 30sccm, 100mT pressure, 300W RF, ~240nm/min SiO_2 etch rate

18) Resist strip

    i. Place wafers in Acetone for 30 minutes

    ii. IPA Rinse

    iii. Dump rinse 5 times

    iv. Spin-Rinse-Dry

19) Aluminum Sputtering using Bob Sputtering System

    i. RF biasing 10 min

        1. 700 V DC Bias

2. 20 sccm Argon

        3. 3 e −3 Torr

    ii. Sputter Aluminum for 30min

        1. 300 W

        2. 20 sccm Argon

        3. 3 e −3 Torr

    iii. The measured Aluminum thickness was about 500nm

20) Lithography using mask#4

    i. Solitec Spinner HPR504

        1. spread at 400 rpm for 10 seconds

        2. spin at 4000 rpm for 40 seconds

        3. the measured photoresist thickness was about 1.2-
           1.3um

    ii. Solitec hotplate contact soft-bake 90 seconds at 115 ^{o}C

    iii. Rehydrated for 10-15 minutes

    iv. Oscar mask aligner

        1. Expose for 3 seconds

    v. Develop the wafer using 354 developer for 20-25 seconds
       using dip develop process. The amount of developer used
       was estimated based on the number of processed wafers;
       however, during the development process, the developer
       has to cover the wafer.

    vi. Spin-Rinse-Dry

    vii. Microscopic check on the development quality

21) Wet etch to pattern the metal contacts

    i. Aluminum etch to visible end point ~ 15 minutes at room
       temperature with slight hand agitation

    ii. Dump rinse 5 times

    iii. Place wafers in Acetone for 5 minutes

176

  iv. IPA rinse

  v. Dump rinse 5 times

  vi. Spin-Rinse-Dry

22) Wafers' cleaning

  i. Place wafers in Acetone for 30 minutes

  ii. IPA Rinse

  iii. Dump rinse 5 times

  iv. Spin-Rinse-Dry

23) Wafers annealing

  i. The wafers were annealed using the minibrute furnace at ~ 450 ^{o}C for 20 minutes in dry N_2 atmosphere. The flowmeter N_2 of was set at 100

24) Lithography using mask#5

  i. Solitec Spinner HPR504

   1. spread at 400 rpm for 10 seconds

   2. spin at 4000 rpm for 40 seconds

   3. the measured photoresist thickness was about 1.2-1.3um

  ii. Solitec hotplate contact soft-bake 90 seconds at 115 ^{o}C

  iii. Rehydrated for 10-15 minutes

  iv. Oscar mask aligner

   1. Expose for 3 seconds

  v. Develop the wafer using 354 developer for 20-25 seconds using dip develop process. The amount of developer used was estimated based on the number of processed wafers; however, during the development process, the developer has to cover the wafer.

  vi. Spin-Rinse-Dry

vii. Microscopic check on the development quality

25) Reactive ion etching

    i. STS RIE for 6:45 minutes using OxiTest recipe. This time is more than the actual required time (based on the measured oxide thickness) by extra about 25% to ensure the complete etching on the oxide. The details of the OxiTest recipe are CF4 - 20sccm, CHF3 - 30sccm, 100mT pressure, 300W RF, ~240nm/min SiO_2 etch rate

26) Resist strip

    i. Place wafers in Acetone for 30 minutes

    ii. IPA Rinse

    iii. Dump rinse 5 times

    iv. Spin-Rinse-Dry

27) Deep reactive ion etching

    i. STS ICP DRIE using Precision recipe. The details of the Precision recipe are C4F8 - 65sccm, SF6 - 80sccm, 20mT pressure, 750W ICP power, 20W Platen power, ~1.2μm/cycle Si etch rate

    ii. Chamber conditioning for ~ 20 cycles

    iii. Silicon etching ~ 80 cycles

    iv. The measured etch depth was ~ 94 μm.

28) Wafers' cleaning

    i. Place wafers in Acetone for 30 minutes

    ii. IPA Rinse

    iii. Dump rinse 5 times

    iv. Spin-Rinse-Dry

29) Wafer dicing on a single pass. Then the diced wafers were cleaned and dried.

30) Preparation for wire bonding and testing.

Wafer preparation and cleaning		Mask oxide removal Drive-in Thermal oxidation	
Thermal oxidation		Lithography (mask#3)	
Lithography (mask#1)		RIE	
Reactive ion etching (RIE)		Photoresist strip and cleaning	
Photoresist strip and cleaning		Aluminum sputtering	
Deep reactive ion etching (DRIE)		Lithography (mask#4)	
Lithography (mask#2)		Aluminum etching Photoresist strip and cleaning	
RIE		Lithography (mask#5)	
Photoresist strip and cleaning		RIE Photoresist strip and cleaning	
Boron ion implantation		DRIE Cleaning Dicing	

N-type silicon
Thermal oxide
Photoresist
P-type silicon
Aluminum

Sensing Unit
(Design#2)

Figure B-4 Schematic of the microfabrication process to build the sensing unit
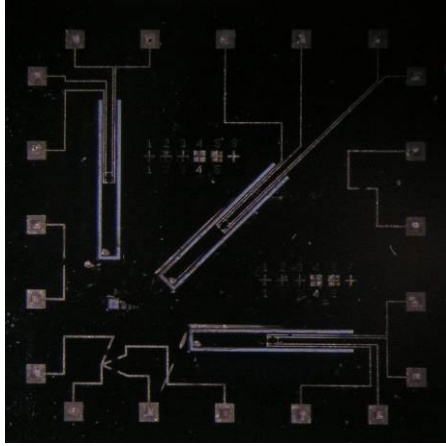
Design 1
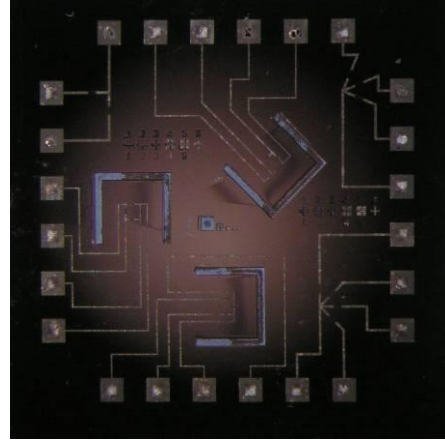
Design 2
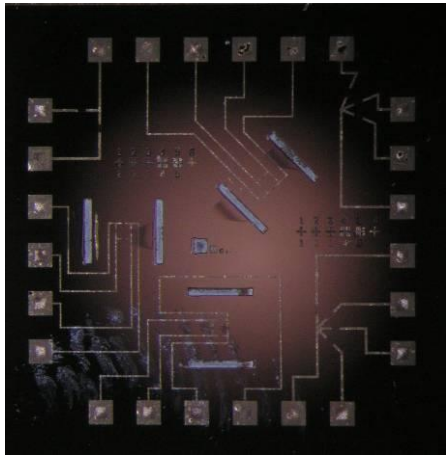
Design 3
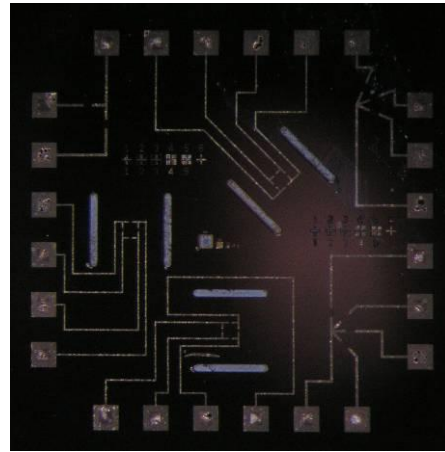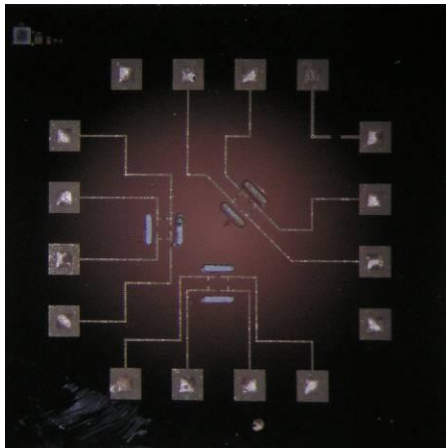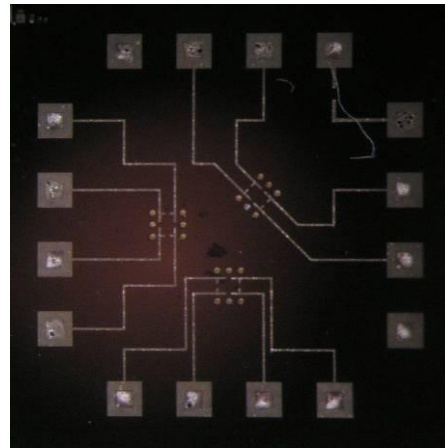
Design 4

Design 5

Design 6

Figure B-5 Fabricated Sensing chips after dicing
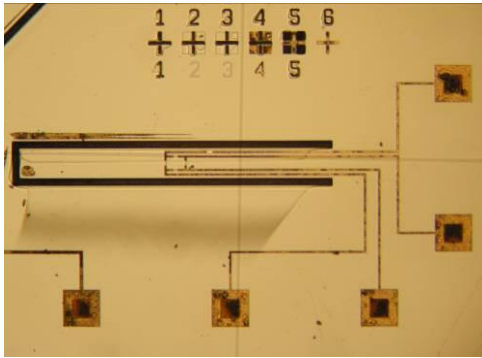
Design 1
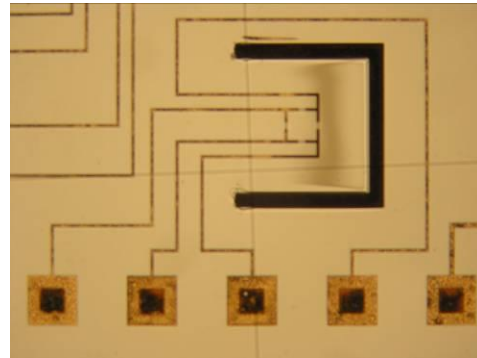
Design 2
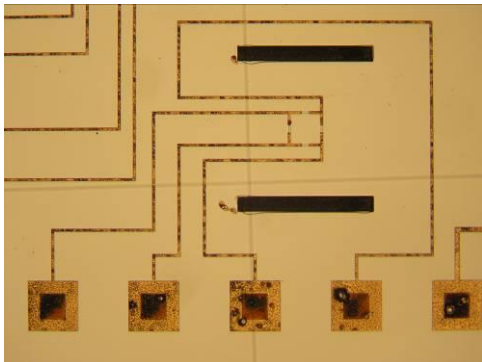
Design 3
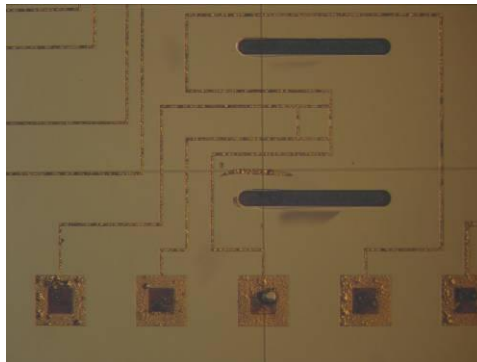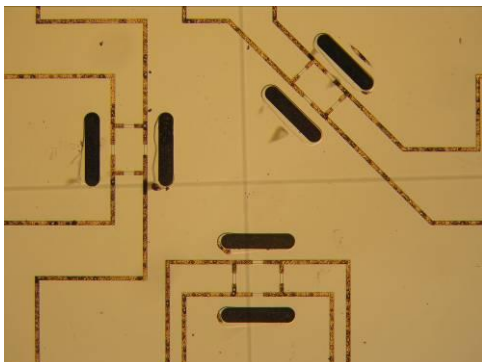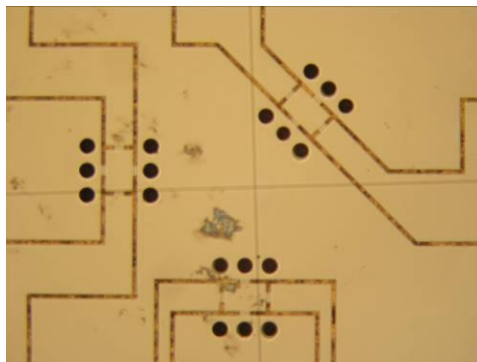
Design 4

Design 5

Design 6

Figure B-6 Fabricated sensing units

Appendix C - Determination of the Stiffness Coefficients

The transformation relations of the reduced index stress and strain components can be presented as

$$\sigma_\alpha = \left[T_{\alpha\beta} \right] \sigma_\alpha^{'} \tag{C-1}$$

$$\varepsilon_\alpha = \left[T_{\alpha\beta}^t \right] \varepsilon_\alpha^{'} \tag{C-2}$$

Inverting equation (C-2) leads to

$$\varepsilon_\alpha^{'} = \left[T_{\alpha\beta}^t \right]^{-1} \varepsilon_\alpha \tag{C-3}$$

Through the use of $\varepsilon_{ij} = S_{ijkl}\, \sigma_{kl}$

$$\varepsilon^{'} = \left[T^t \right]^{-1} S\ \sigma \tag{C-4}$$

Finally, substitution of equation (C-1) into equation (C-4) yields the relations between stress and strain in a rotated primed coordinate system as follows:

$$\varepsilon^{'} = \left[T^t \right]^{-1} S\ T^{\ -1} \sigma^{'} \tag{C-5}$$

If the unprimed coordinate system is assumed, $\left[T^t \right]^{-1}$ and $T^{\ -1}$ in equation (C-5) simplify to unit matrices.

$$\left[S^{'} \right] = \left[T^t \right]^{-1} S\ T^{\ -1} \tag{C-6}$$

By putting $\left[S'\right]=\left[C'\right]^{-1}$, equation (C-6) becomes

$$\left[C'\right]^{-1}=\left[T'\right]^{-1} S \; T^{-1}$$ (C-7)

Inverting equation (C-7) gives

$$\left[C'\right]= T \; C \left[T'\right]$$ (C-8)

Many calculations may be solved with matrix algebra. With respect to the unprimed coordinate system

$$\left[c_{\alpha\beta}\right]=\begin{bmatrix} c_{11} & c_{12} & c_{12} & 0 & 0 & 0 \\ c_{12} & c_{11} & c_{12} & 0 & 0 & 0 \\ c_{12} & c_{12} & c_{11} & 0 & 0 & 0 \\ 0 & 0 & 0 & c_{44} & 0 & 0 \\ 0 & 0 & 0 & 0 & c_{44} & 0 \\ 0 & 0 & 0 & 0 & 0 & c_{44} \end{bmatrix}$$ (C-9)

And with respect to the primed coordinate system

$$\left[C'\right]=\begin{bmatrix} \dfrac{c_{11}+c_{12}}{2}+c_{44} & \dfrac{c_{11}+c_{12}}{2}+c_{44} & c_{12} & 0 & 0 & 0 \\ \dfrac{c_{11}+c_{12}}{2}-c_{44} & \dfrac{c_{11}+c_{12}}{2}+c_{44} & c_{12} & 0 & 0 & 0 \\ c_{12} & c_{12} & c_{11} & 0 & 0 & 0 \\ 0 & 0 & 0 & c_{44} & 0 & 0 \\ 0 & 0 & 0 & 0 & c_{44} & 0 \\ 0 & 0 & 0 & 0 & 0 & \dfrac{c_{11}-c_{12}}{2} \end{bmatrix}$$ (C-10)

Appendix D - Stress-Strain Relationship in Silicon

Silicon exhibits linear elastic material behaviour and the generalized Hooke's Law, the most general formula of linear elastic stress-strain relations, is given by

$$\sigma_{ij} = C_{ijkl}\, \varepsilon_{kl} \tag{D-1}$$

where σ_{ij} and ε_{kl} are the stress and strain components, and C_{ijkl} are the components of the stiffness tensor. Inverting equation (D-1) gives

$$\varepsilon_{ij} = C_{ijkl}\, \sigma_{kl} \tag{D-2}$$

where S_{ijkl} are the compliance components. Also, the transformation relations for the reduced index stress and strain components can be expressed as indicated below

$$\sigma_\alpha = T_{\alpha\beta}^{-1}\, \sigma_\beta' \tag{D-3}$$

$$\varepsilon_\alpha = T_{\alpha\beta}^t\, \varepsilon_\beta' \tag{D-4}$$

where the coefficients $T_{\alpha\beta}$ are elements of a six by six transformation matrix related to the direction cosines for the unprimed and primed coordinate systems. Also, note that σ_α and ε_α are the stress and strain tensor components in the unprimed system, respectively, whereas σ_β' and ε_β' are those components in a rotated primed coordinate system. Inverting equation (D-4) leads to

$$\varepsilon' = \left(T^t\right)^{-1} \varepsilon \tag{D-5}$$

If equation (D-2) is plugged into equation (D-5), the result is

$$\varepsilon' = {T^t}^{-1} S\sigma \tag{D-6}$$

Finally, substitution equation (D-3) into equation (D-6) yields the relations between stress and strain in a rotated primed coordinate system as follows:

$$\varepsilon' = {T^t}^{-1} ST^{-1}\sigma' \tag{D-7}$$

If the unprimed coordinate system is assumed, $(T^t)^{-1}$ and T^{-1} in equation (D-7) simplify to unit matrices. Thus equation (D-7) reduces down to equation (D-2).

Appendix E - Procedure of Data Analysis

The output signal was acquired using a National Instruments® data acquisition (DAQ) box with 8 channels. After the data was collected, the following steps were performed to process the output signal and to interpret the testing results.

The TCR was evaluated by plotting the sensor output signal as a normalized resistance change ($\Delta R/R$) versus testing temperature.

1. The slope of the respective curve was evaluated based on a linear regression model. This slope represents the sensor TCR, which was calculated as part per million (ppm)/^{o}C.

2. The applied mechanical strain on the steel testing specimen was calculated using the applied load and the specimen dimensions and material properties.

3. The strain causation was verified using the thin-foil strain gauge.

4. The temperature effect was removed from the sensor output signal using the evaluated TCR.

5. The sensor output signal was then plotted as output voltage versus strain. Unfortunately, due to the microfabrication limitations there was initial offset in the sensor calibration curve.

6. The offset was removed by subtracting the initial offset from the calibration curve, which resulted in a calibration curve the starts from origin. This is common practice in instrumentation, which should not affect the results accuracy or reliability.

E1. Calibration Curve Simplification

Due to the high sampling rate the calibration curve had thousands of data points, which makes it difficult to handle the experimental data. In addition, as mentioned in item 5, the calibration curve had initial offset. The initial offset was subtracted, as indicated in item 6 above. The final calibration curve is called simplified

calibration curve. Below is an example of the data analysis progress, from raw data to simplified calibration curve.
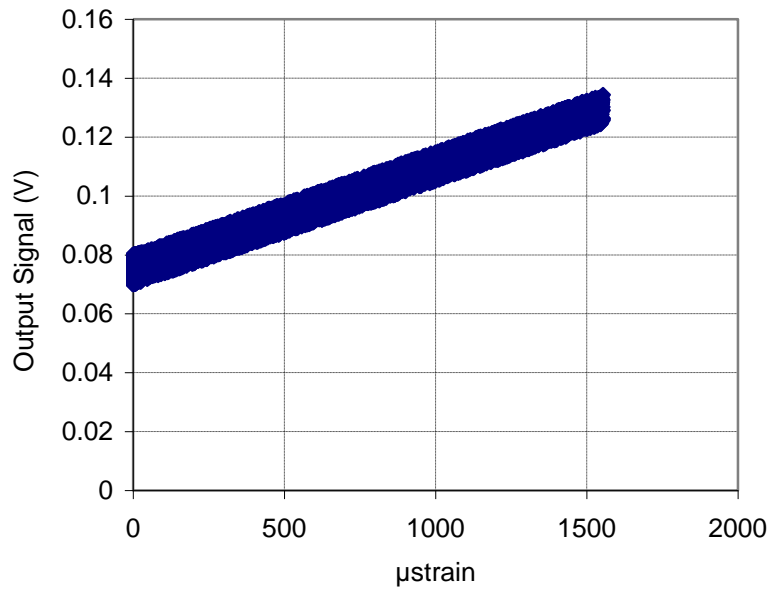
Figure E-1 Sample of a sensor calibration curve, raw data with initial offset
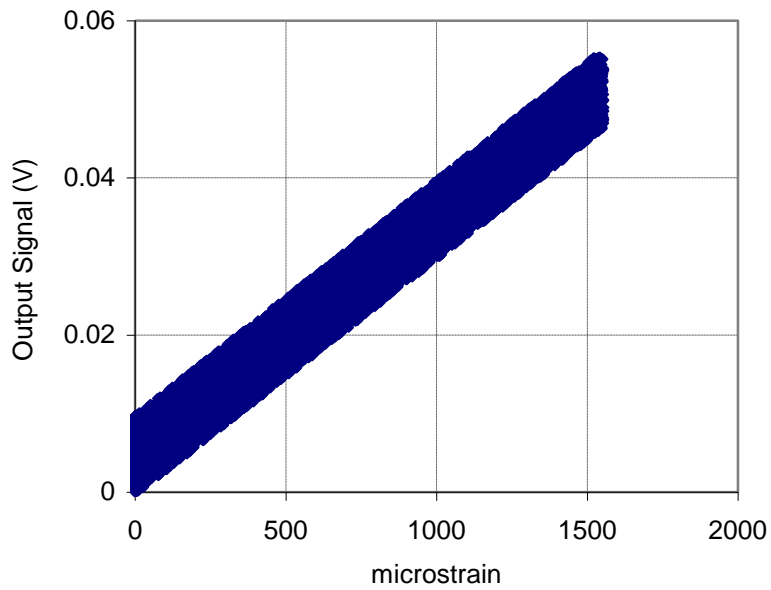
Figure E-2 Sample of a calibration curve, raw data with initial offset removed
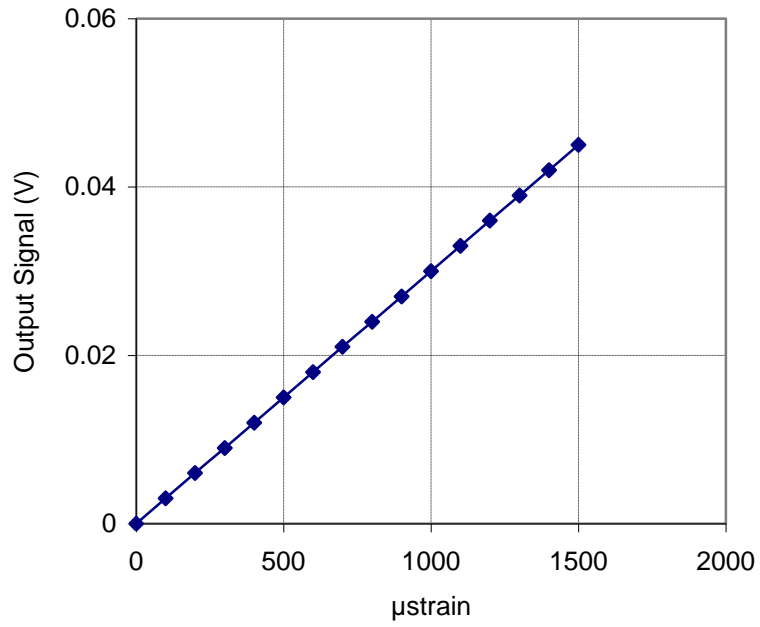
Figure E-3 Sample of a simplified calibration curve

Appendix F - Calibration Results of Different Case Studies

This appendix provides the experimental testing results of the six sensor layouts that were prototyped in this study. The experimental results are presented in six data sets. Each data starts with the sensor layout, as shown on the microfabrication mask, and dimensions if the sensing unit followed by the image of the microfabricated chip. The normalized resistance change versus temperature at load-free condition is then presented to evaluate the temperature coefficient of resistance (TCR) for the five doping levels. Following to the TCR evaluation is relationship between the sensor TCR and the doping level. Finally, the simplified calibration curves are provided. Please refer to Appendix E, Data Analysis Procedure, for definition of simplified calibration curve. Tabulated summary of the sensing chip sensitivity is given.
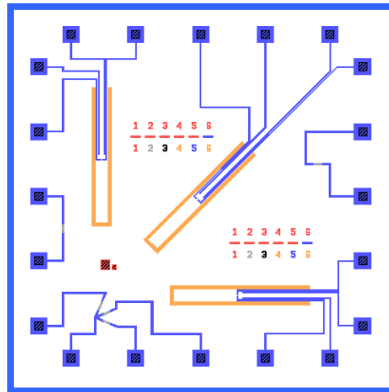
Figure F-1 Layout (Design 1), as shown on the microfabrication masks
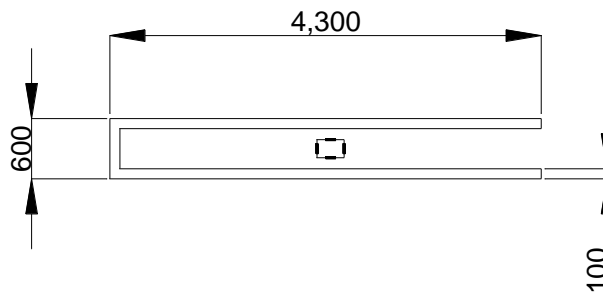
Figure F-2 Schematic of the sensing unit (Design 1), all dimensions are in μm and depth of all the surface trenches is 100 μm
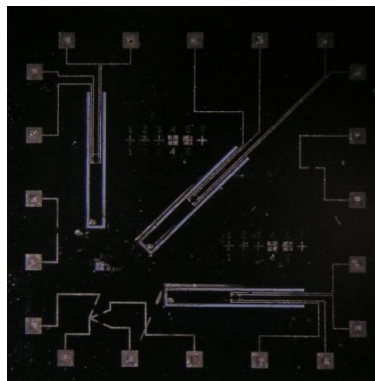
Figure F-3 Fabricated Sensing chip (Design 1) after dicing
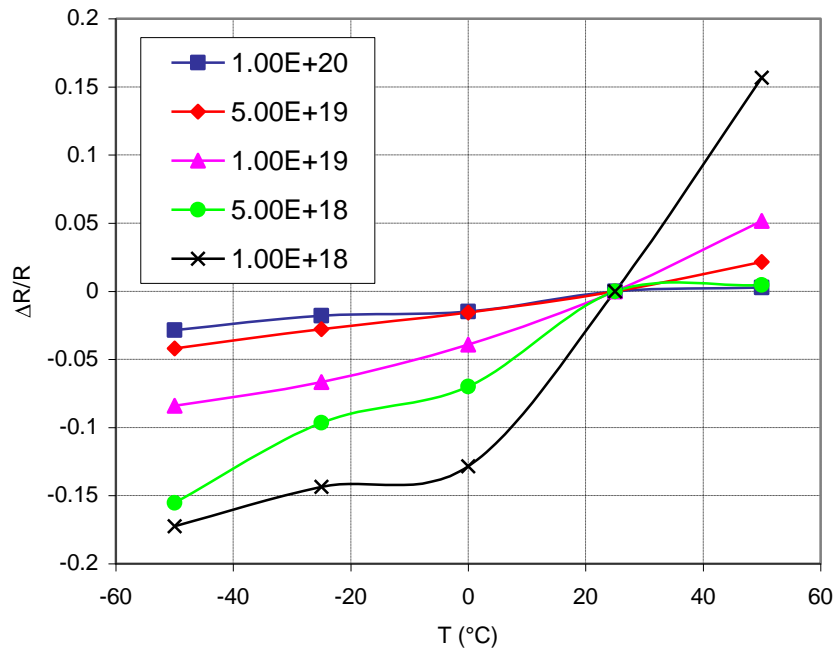
Figure F-4 Normalized resistance change at stress free condition for different doping concentrations, slope of these curves = TCR (Design 1)

$$TCR = -0.0006Ln(N) + 0.0281$$
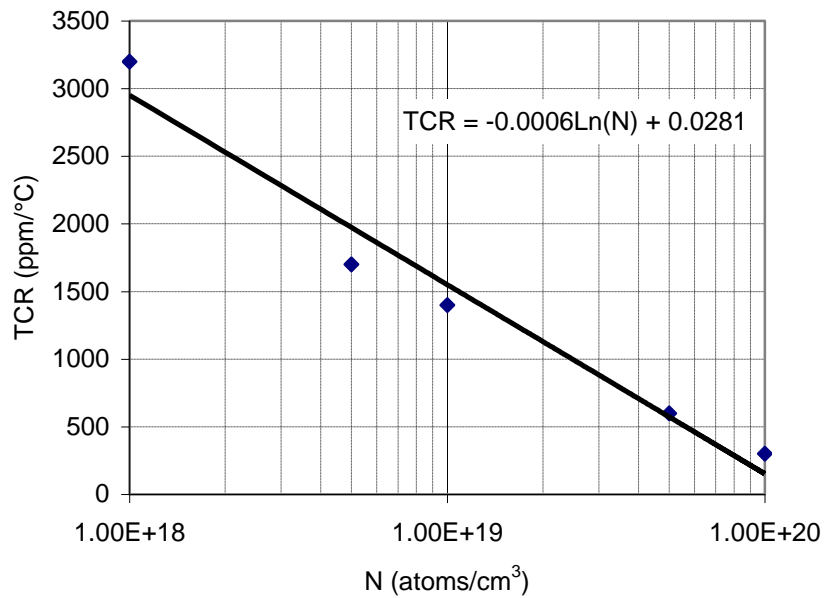
Figure F-5 Temperature coefficient of resistance (TCR) at different doping concentrations to evaluate the sensor TCR, (Design 1)
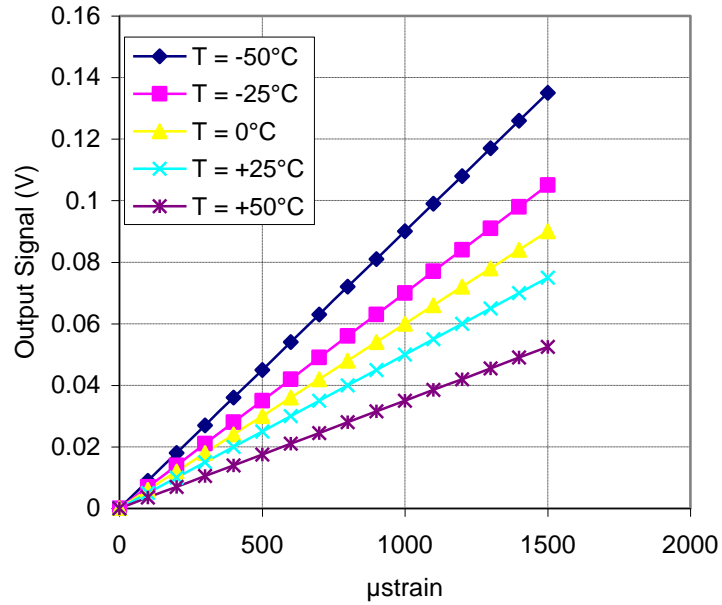
Figure F-6 Simplified calibration curves at different temperatures for doping concentration of 1×10^{18} /cm^3 (Design 1)
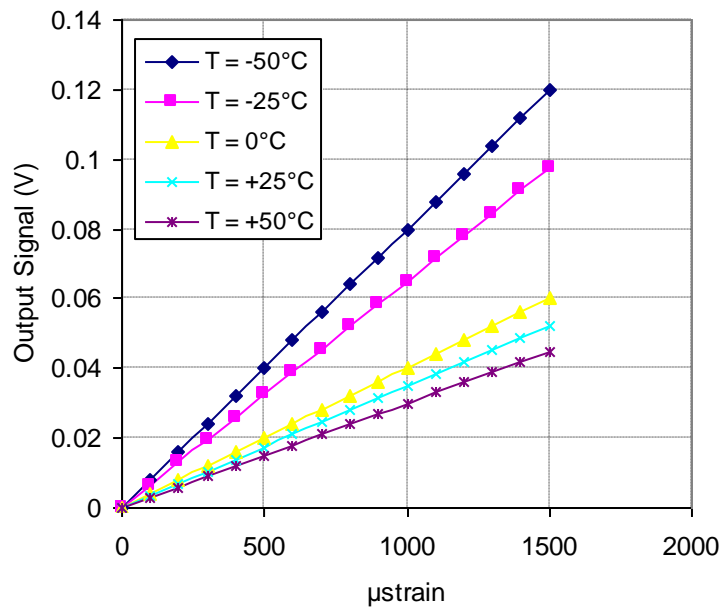
Figure F-7 Simplified calibration curves at different temperatures for doping concentration of 5×10^{18} /cm^3 (Design 1)

192
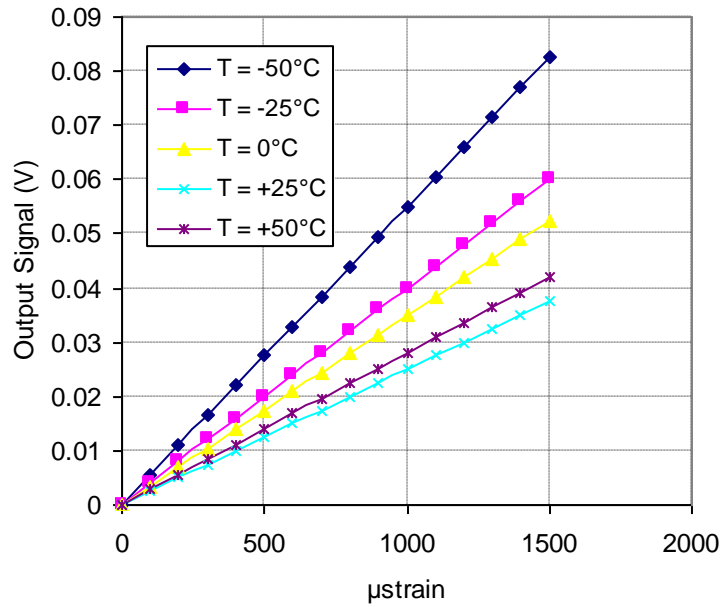
Figure F-8 Simplified calibration curves at different temperatures for doping concentration of 1×10^{19} /cm^3 (Design 1)
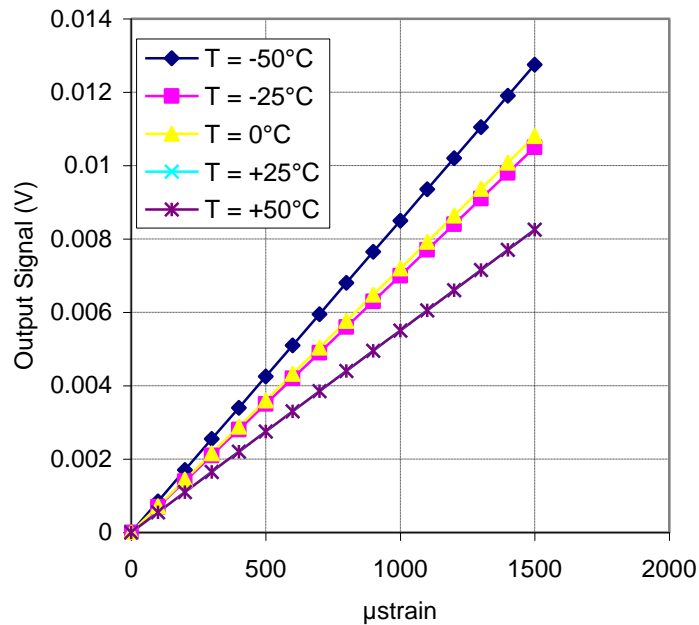
Figure F-9 Simplified calibration curves at different temperatures for doping concentration of 5×10^{19} /cm^3 (Design 1)
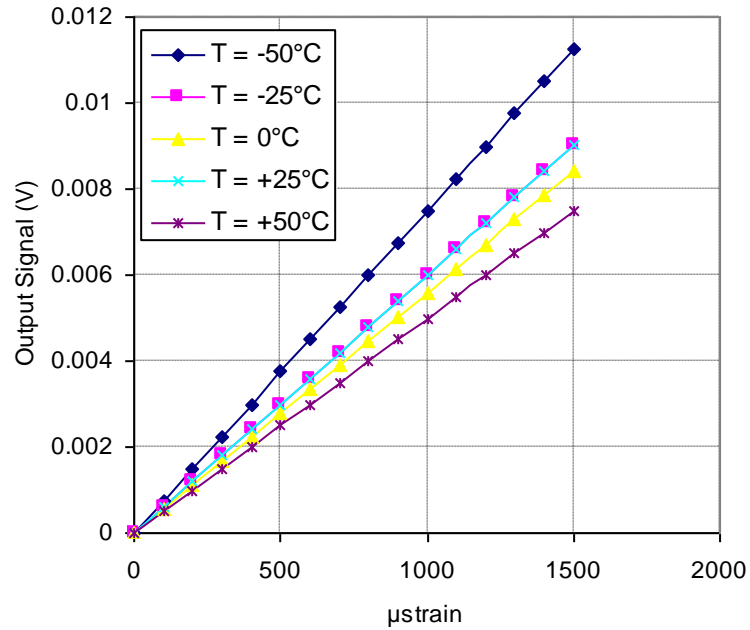
Figure F-10 Simplified calibration curves at different temperatures for doping concentration of 1×10^{20} /cm^3 (Design 1)

Table F-1 Sensitivity values at different temperatures and doping concentrations (Design 1)

Temperature (°C)	Sensing Sensitivity (V/με)				
	1×10^{18} (atoms/cm^3)	5×10^{18} (atoms/cm^3)	1×10^{19} (atoms/cm^3)	5×10^{19} (atoms/cm^3)	1×10^{20} (atoms/cm^3)
-50	9.00E-05	8.00E-05	5.50E-05	8.50E-06	7.50E-06
-25	7.00E-05	6.50E-05	4.00E-05	7.00E-06	6.00E-06
0	6.00E-05	4.00E-05	3.50E-05	7.20E-06	5.60E-06
25	5.00E-05	3.50E-05	2.50E-05	5.50E-06	6.00E-06
50	3.50E-05	3.00E-05	2.80E-05	5.50E-06	5.00E-06

F2. Experimental Data of Layout Design 2
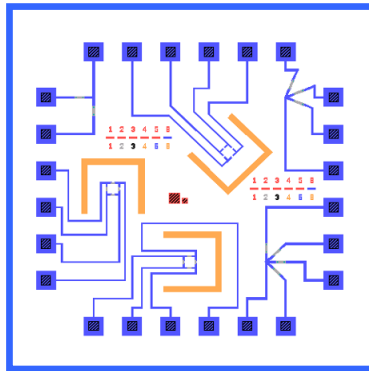
Figure F-11 Layout (Design 2), as shown on the microfabrication masks
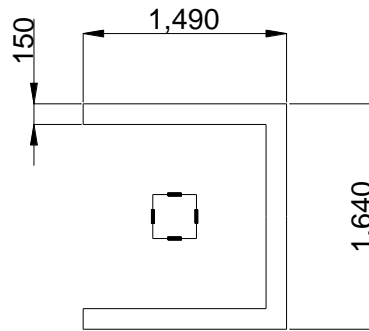
Figure F-12 Schematic of the sensing unit (Design 2), all dimensions are in μm and depth of all the surface trenches is 100 μm
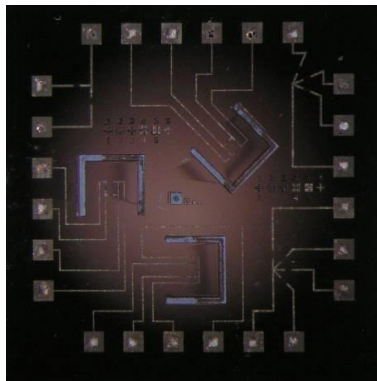

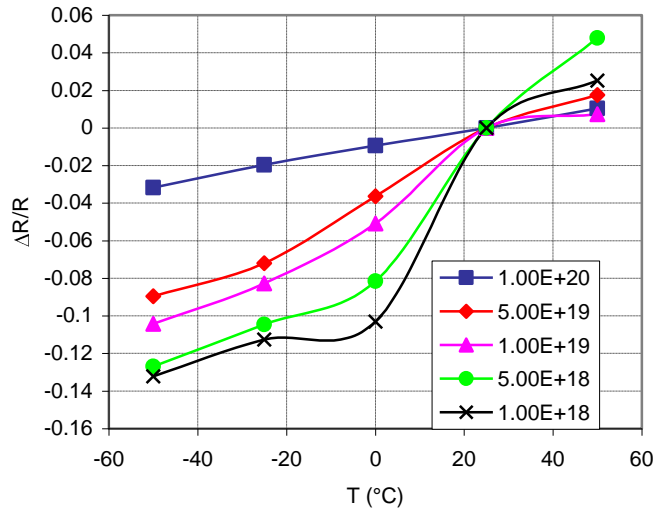
Figure F-13 Fabricated Sensing chip (Design 2) after dicing

Figure F-14 Normalized resistance change at stress free condition for different doping concentrations, slope of these curves = TCR (Design 2)
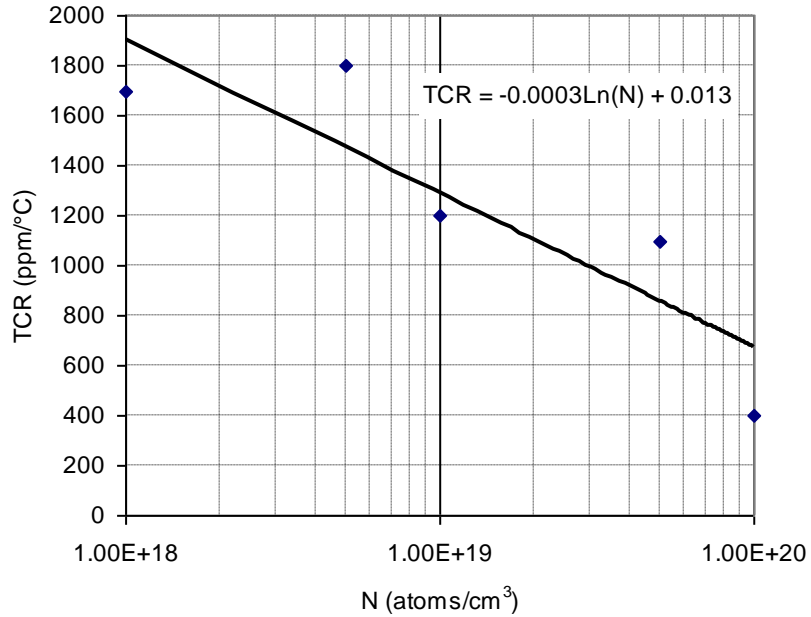

TCR = -0.0003Ln(N) + 0.013

Figure F-15 Temperature coefficient of resistance (TCR) at different doping concentrations to evaluate the sensor TCR, (Design 2)
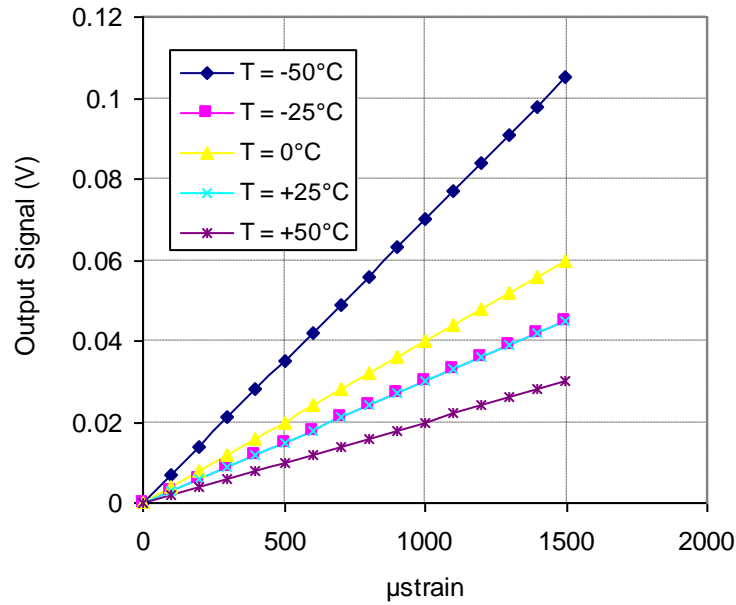
Figure F-16 Simplified calibration curves at different temperatures for doping concentration of 1×10^{18} /cm^3 (Design 2)
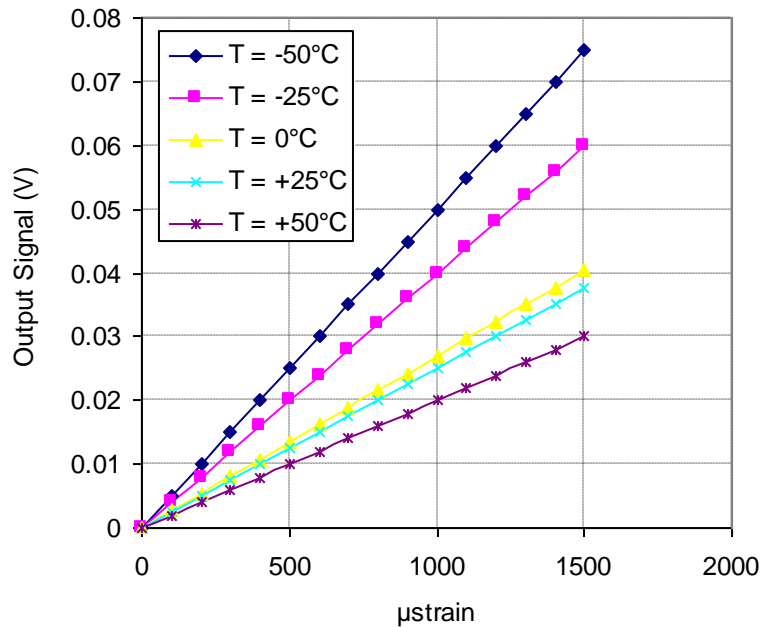

Figure F-17 Simplified calibration curves at different temperatures for doping concentration of 5×10^{18} /cm^3 (Design 2)
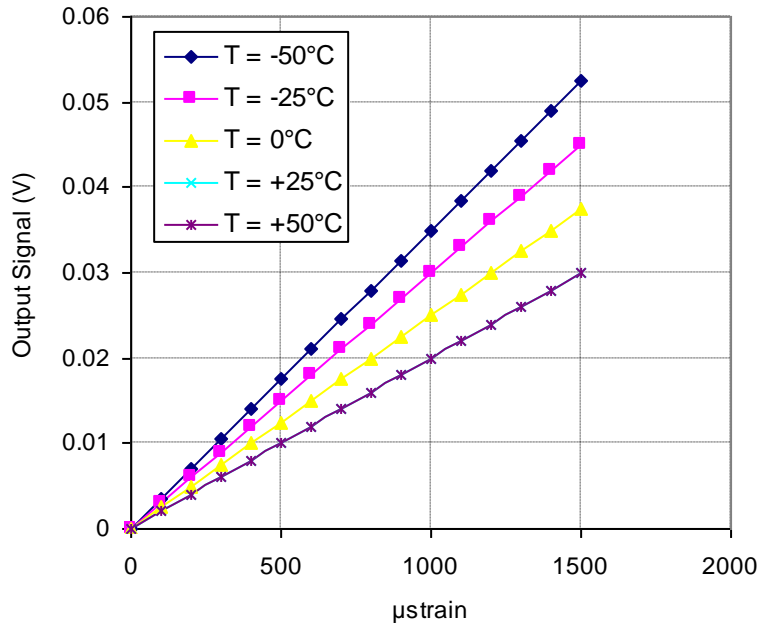
Figure F-18 Simplified calibration curves at different temperatures for doping concentration of 1×10^{19} /cm^3 (Design 2)
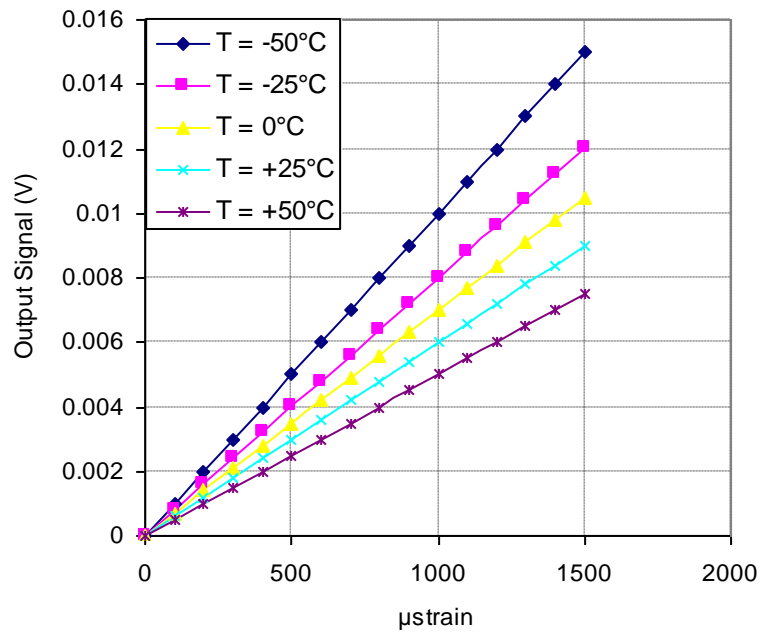

Figure F-19 Simplified calibration curves at different temperatures for doping concentration of 5×10^{19} /cm^3 (Design 2)
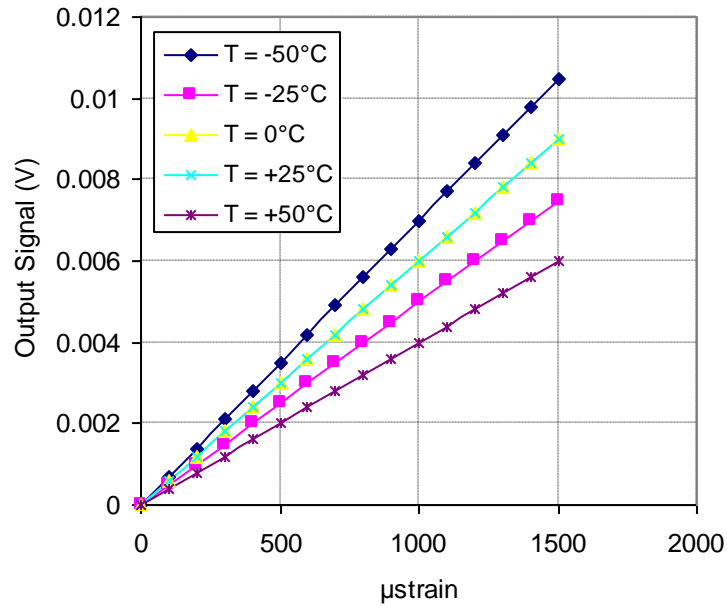
Figure F-20 Simplified calibration curves at different temperatures for doping concentration of 1×10^{20} /cm^3 (Design 2)

Table F-2 Sensitivity values at different temperatures and doping concentrations (Design 2)

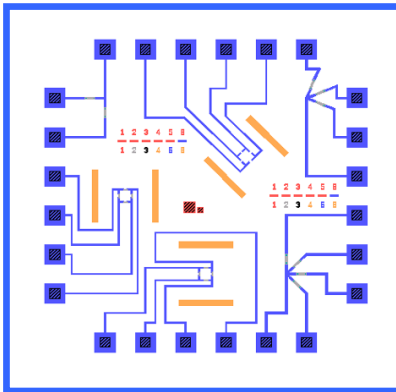| Temperature (^{o}C)	Sensing Sensitivity (V/με)				
	1×10^{18} (atoms/cm^3)	5×10^{18} (atoms/cm^3)	1×10^{19} (atoms/cm^3)	5×10^{19} (atoms/cm^3)	1×10^{20} (atoms/cm^3)
-50	7.00E-05	5.00E-05	3.50E-05	1.00E-05	7.00E-06
-25	3.00E-05	4.00E-05	3.00E-05	8.00E-06	5.00E-06
0	4.00E-05	2.70E-05	2.50E-05	7.00E-06	6.00E-06
25	3.00E-05	2.50E-05	2.00E-05	6.00E-06	6.00E-06
50	2.00E-05	2.00E-05	2.00E-05	5.00E-06	4.00E-06

A3. Experimental Data of Layout Design 3

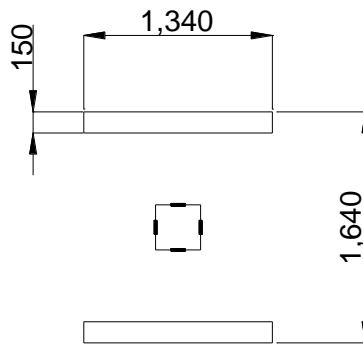**Figure F-21 Layout (Design 3), as shown on the microfabrication masks**

Figure F-22 Schematic of the sensing unit (Design 3), all dimensions are in μm and depth of all the surface trenches is 100 μm
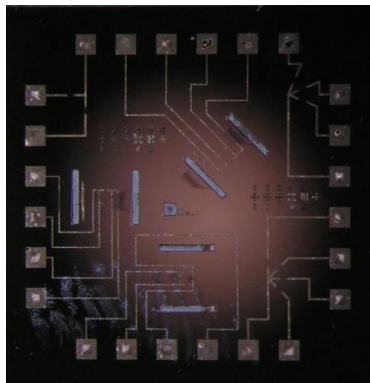

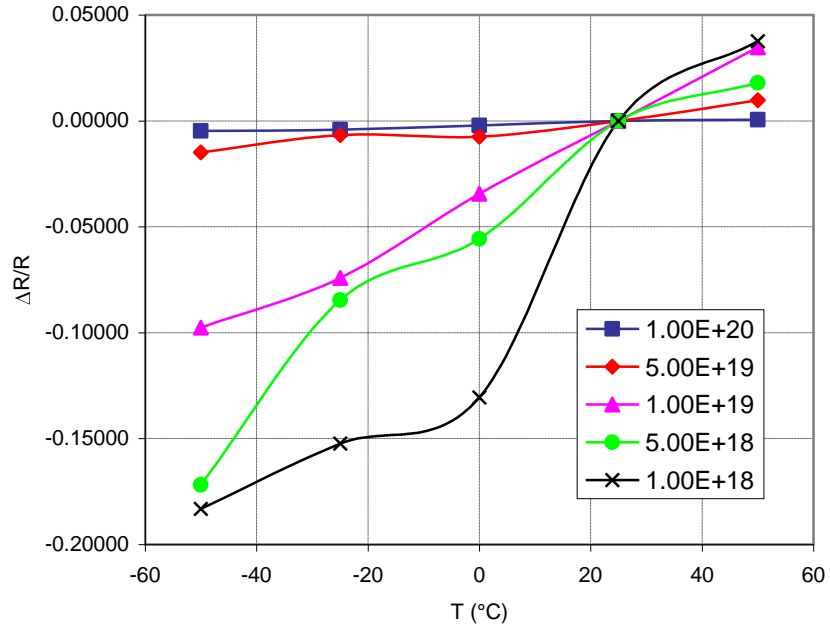**Figure F-23 Fabricated Sensing chip (Design 3) after dicing**

Figure F-24 Normalized resistance change at stress free condition for different doping concentrations, slope of these curves = TCR (Design 3)
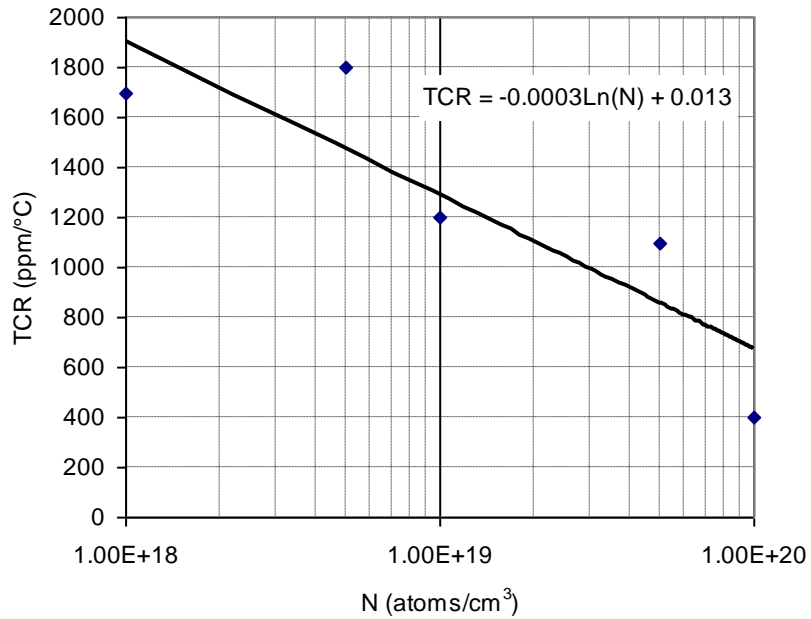

Figure F-25 Temperature coefficient of resistance (TCR) at different doping concentrations to evaluate the sensor TCR, (Design 3)

Figure F-26 Simplified calibration curves at different temperatures for doping concentration of 1×10^{18} /cm^3 (Design 3)

Figure F-27 Simplified calibration curves at different temperatures for doping concentration of 5×10^{18} /cm^3 (Design 3)
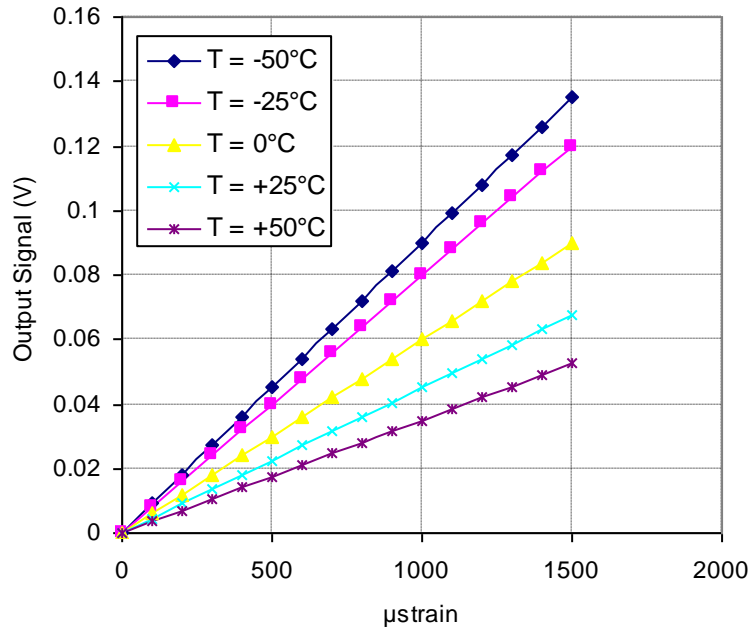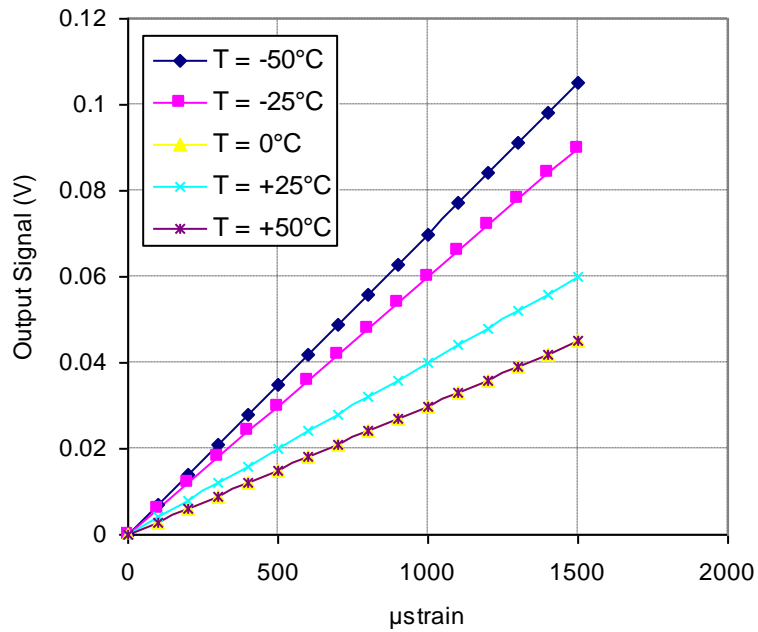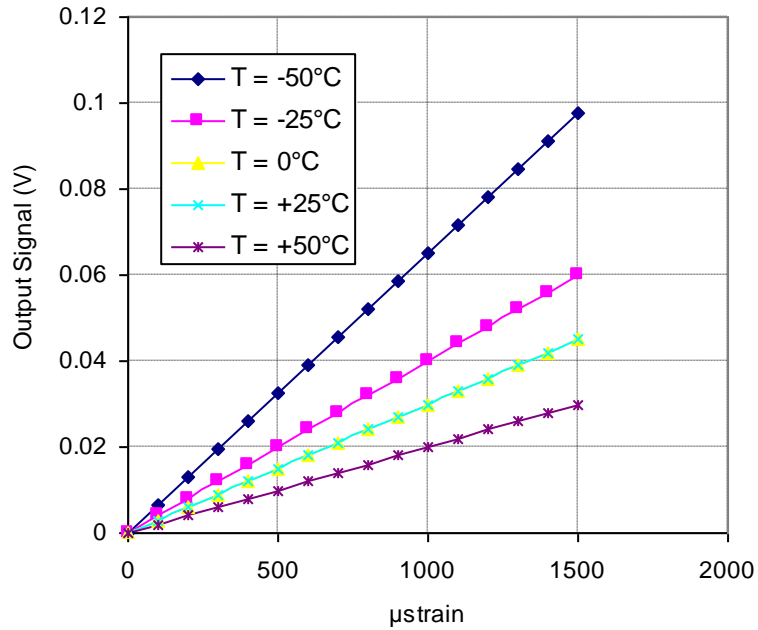
202

Figure F-28 Simplified calibration curves at different temperatures for doping concentration of 1×10^{19} /cm^3 (Design 3)
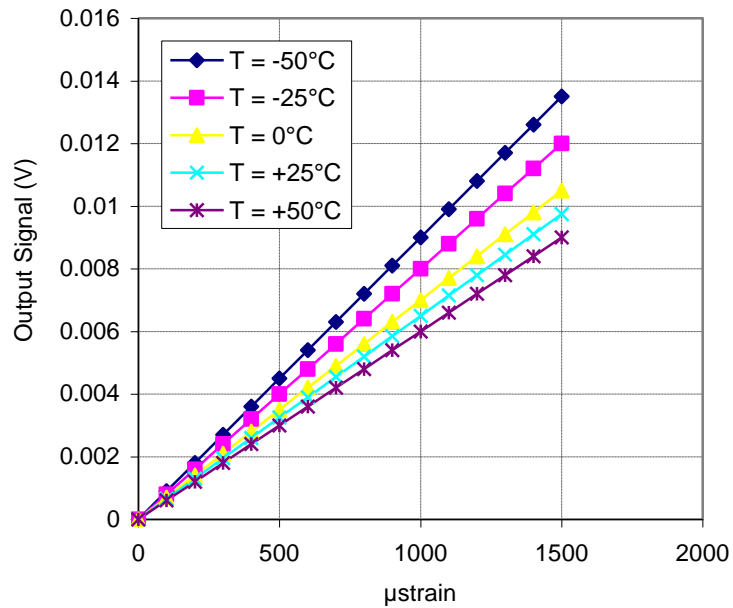

Figure F-29 Simplified calibration curves at different temperatures for doping concentration of 5×10^{19} /cm^3 (Design 3)

Figure F-30 Simplified calibration curves at different temperatures for doping concentration of 1×10^{20} /cm^3 (Design 3)

Table F-3 Sensitivity values at different temperatures and doping concentrations (Design 3)

Temperature (^{o}C)	Sensing Sensitivity (V/µε)				
	1×10^{18} (atoms/cm^3)	5×10^{18} (atoms/cm^3)	1×10^{19} (atoms/cm^3)	5×10^{19} (atoms/cm^3)	1×10^{20} (atoms/cm^3)
-50	9.00E-05	7.00E-05	6.50E-05	9.00E-06	8.00E-06
-25	8.00E-05	6.00E-05	4.00E-05	8.00E-06	7.00E-06
0	6.00E-05	3.00E-05	3.00E-05	7.00E-06	7.50E-06
25	4.50E-05	4.00E-05	3.00E-05	6.50E-06	7.50E-06
50	3.50E-05	3.00E-05	2.00E-05	6.00E-06	8.00E-06

F4. Experimental Data of Layout Design 4
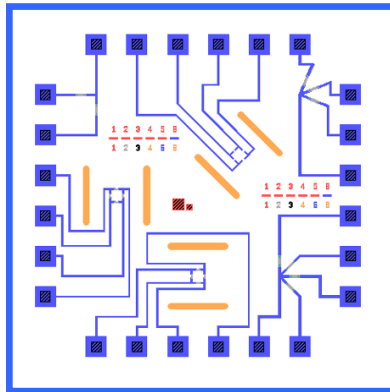
Figure F-31 Layout (Design 4), as shown on the microfabrication masks
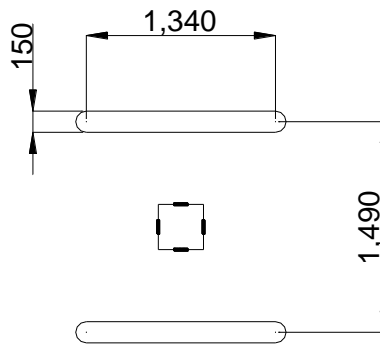
Figure F-32 Schematic of the sensing unit (Design 4), all dimensions are in μm and depth of all the surface trenches is 100 μm

Figure F-33 Fabricated Sensing chip (Design 4) after dicing

Figure F-34 Normalized resistance change at stress free condition for different doping concentrations, slope of these curves = TCR (Design 4)

Figure F-35 Temperature coefficient of resistance (TCR) at different doping concentrations to evaluate the sensor TCR, (Design 4)

Figure F-36 Simplified calibration curves at different temperatures for doping concentration of 1×10^{18} /cm^3 (Design 4)
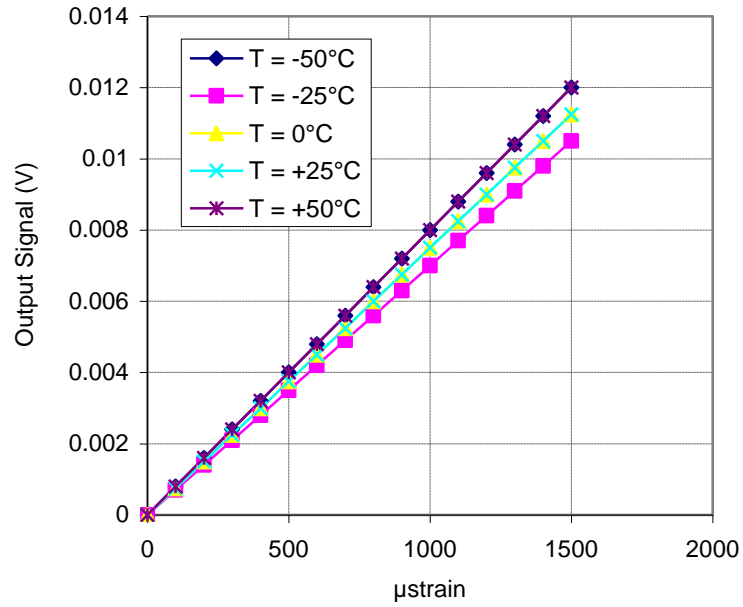

Figure F-37 Simplified calibration curves at different temperatures for doping concentration of 5×10^{18} /cm^3 (Design 4)

207

Figure F-38 Simplified calibration curves at different temperatures for doping concentration of 1×10^{19} /cm^3 (Design 4)

Figure F-39 Simplified calibration curves at different temperatures for doping concentration of 5×10^{19} /cm^3 (Design 4)

Figure F-40 Simplified calibration curves at different temperatures for doping concentration of 1×10^{20} /cm^3 (Design 4)

Table F-4 Sensitivity values at different temperatures and doping concentrations (Design 4)

Temperature (°C)	Sensing Sensitivity (V/με)				
	1×10^{18} (atoms/cm^3)	5×10^{18} (atoms/cm^3)	1×10^{19} (atoms/cm^3)	5×10^{19} (atoms/cm^3)	1×10^{20} (atoms/cm^3)
-50	9.00E-05	6.00E-05	5.50E-05	8.00E-06	4.00E-06
-25	6.00E-05	5.00E-05	5.50E-05	7.60E-06	3.50E-06
0	4.50E-05	3.00E-05	6.00E-05	7.00E-06	3.00E-06
25	2.50E-05	3.00E-05	9.00E-06	5.50E-06	3.50E-06
50	2.00E-05	2.00E-05	1.00E-05	6.00E-06	4.00E-06

F5. Experimental Data of Layout Design 5

Figure F-41 Layout (Design 5), as shown on the microfabrication masks
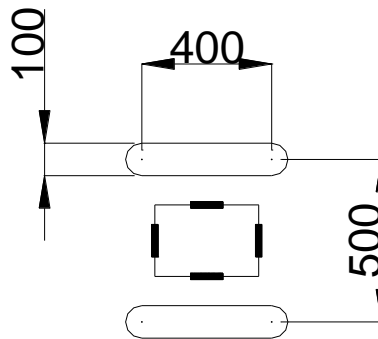
Figure F-42 Schematic of the sensing unit (Design 5), all dimensions are in μm and depth of all the surface trenches is 100 μm
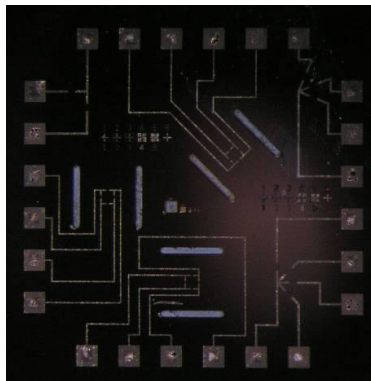

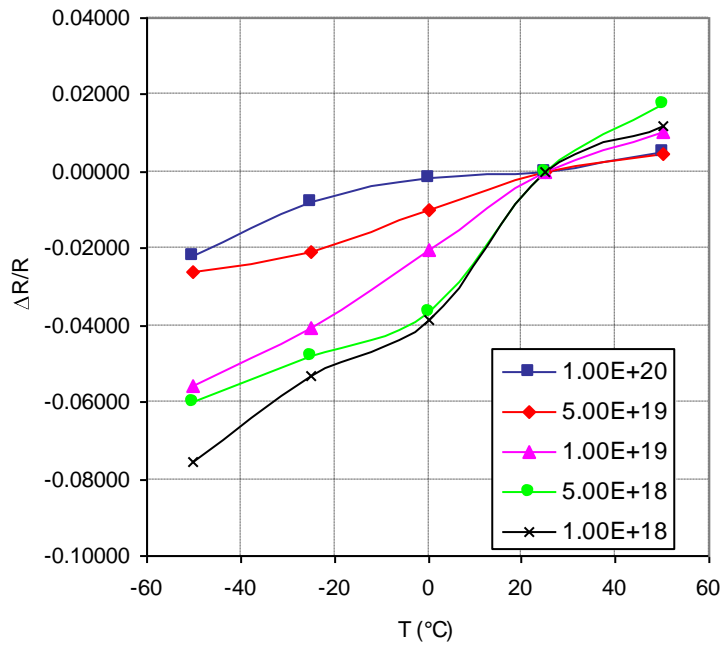
Figure F-43 Fabricated Sensing chip (Design 5) after dicing

Figure F-44 Normalized resistance change at stress free condition for different doping concentrations, slope of these curves = TCR (Design 5)
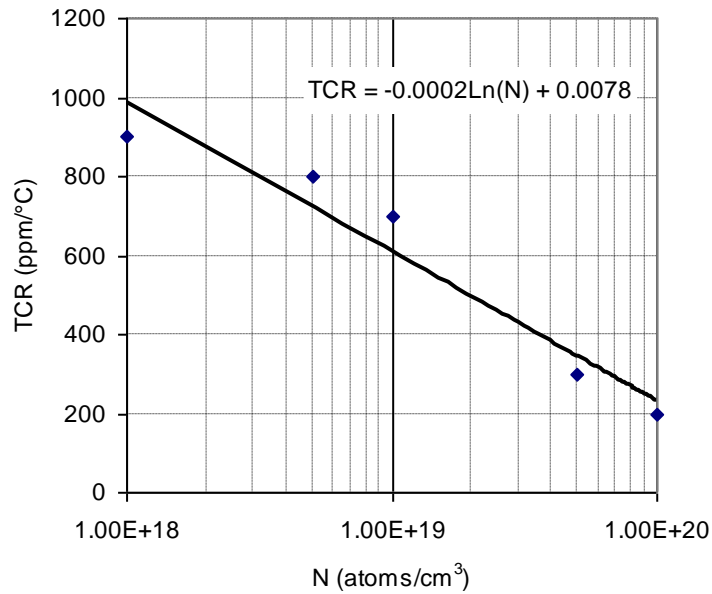

$$TCR = -0.0002Ln(N) + 0.0113$$

Figure F-45 Temperature coefficient of resistance (TCR) at different doping concentrations to evaluate the sensor TCR, (Design 5)
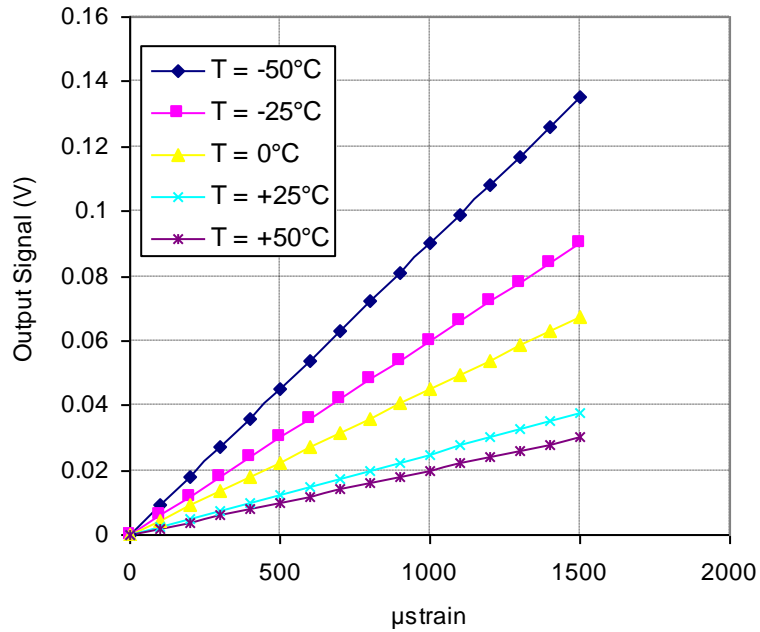
211

Figure F-46 Simplified calibration curves at different temperatures for doping concentration of 1×10^{18} /cm^3 (Design 5)
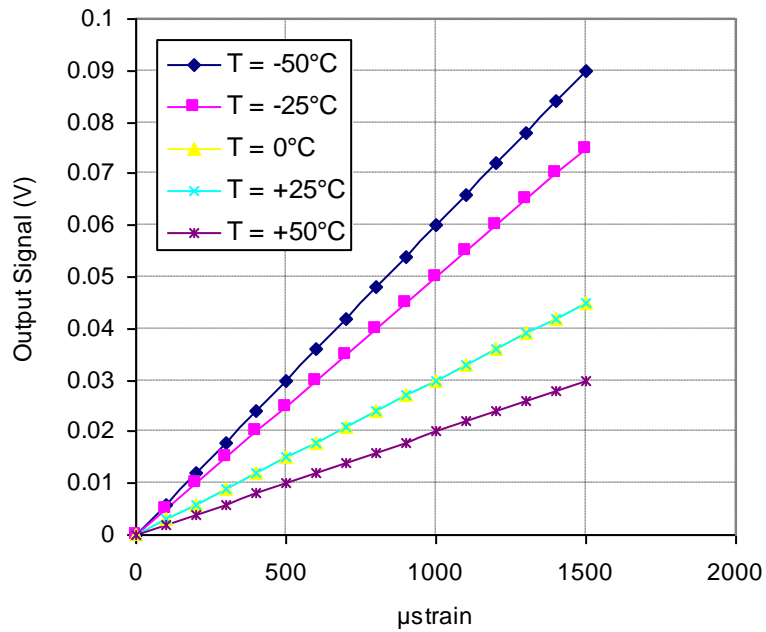

Figure F-47 Simplified calibration curves at different temperatures for doping concentration of 5×10^{18} /cm^3 (Design 5)
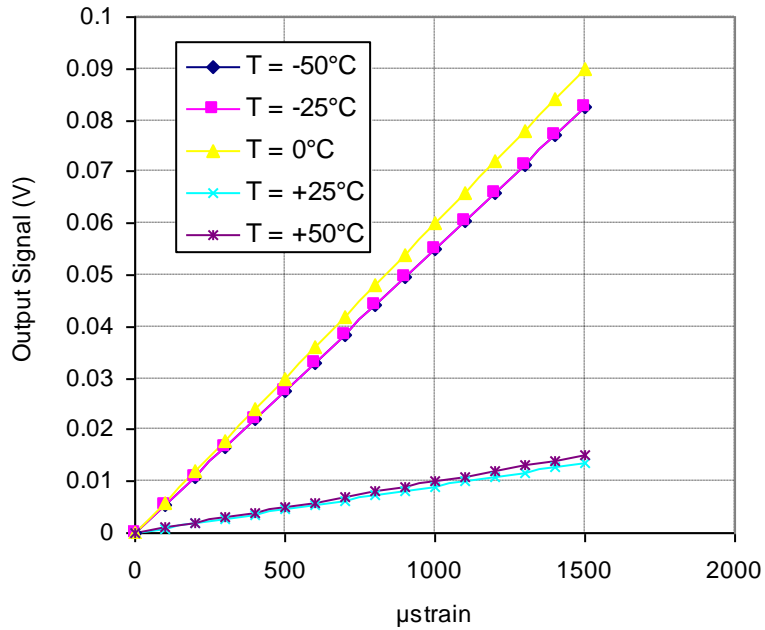
Figure F-48 Simplified calibration curves at different temperatures for doping concentration of 1×10^{19} /cm^3 (Design 5)
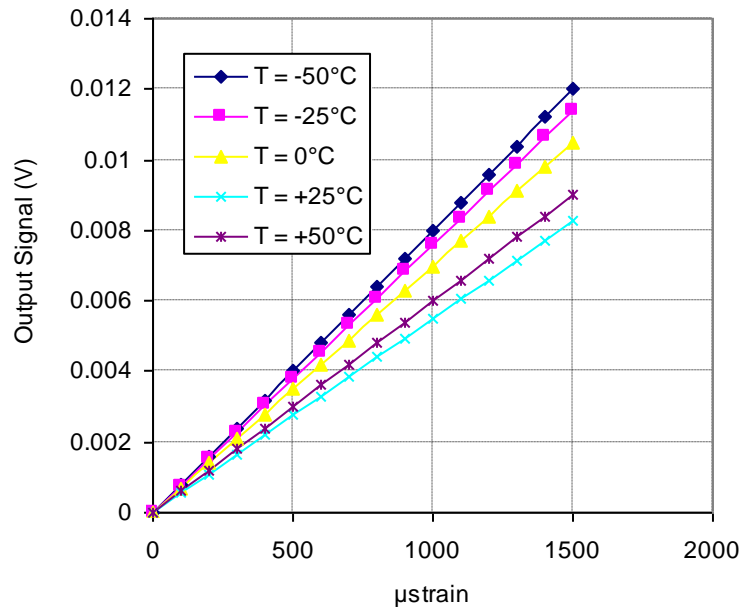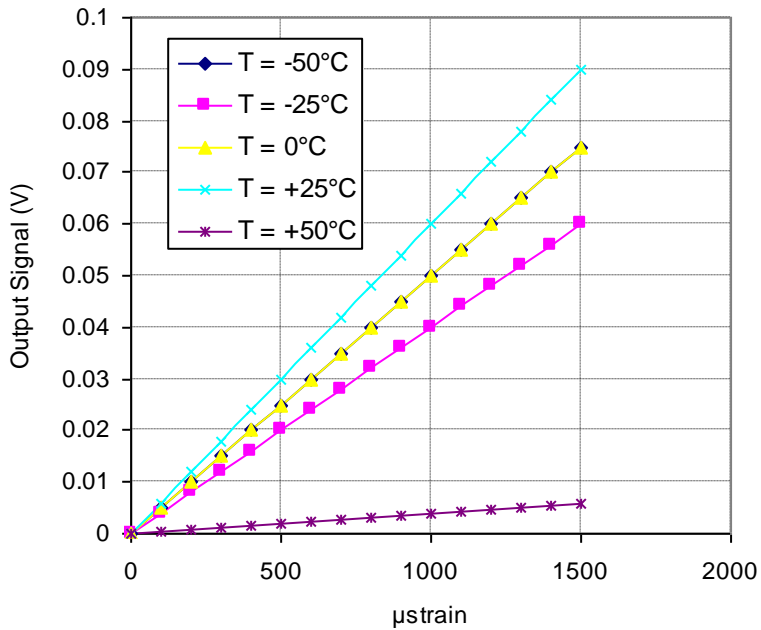

Figure F-49 Simplified calibration curves at different temperatures for doping concentration of 5×10^{19} /cm^3 (Design 5)
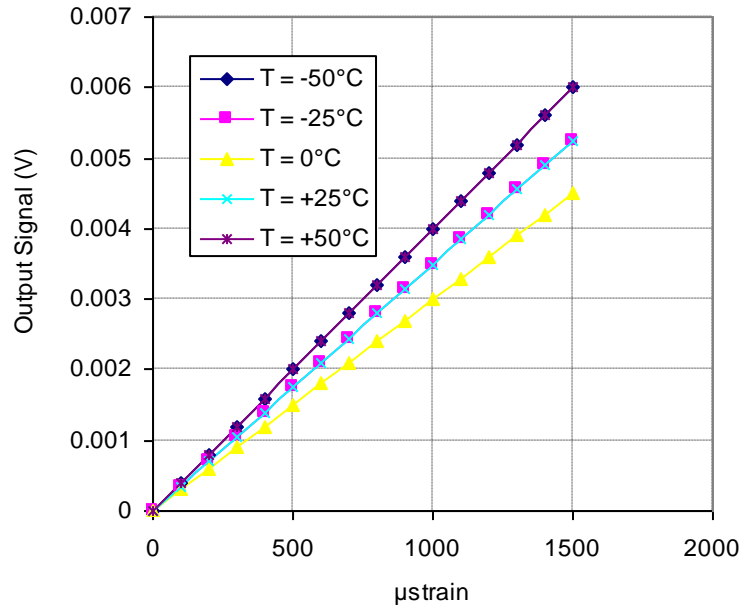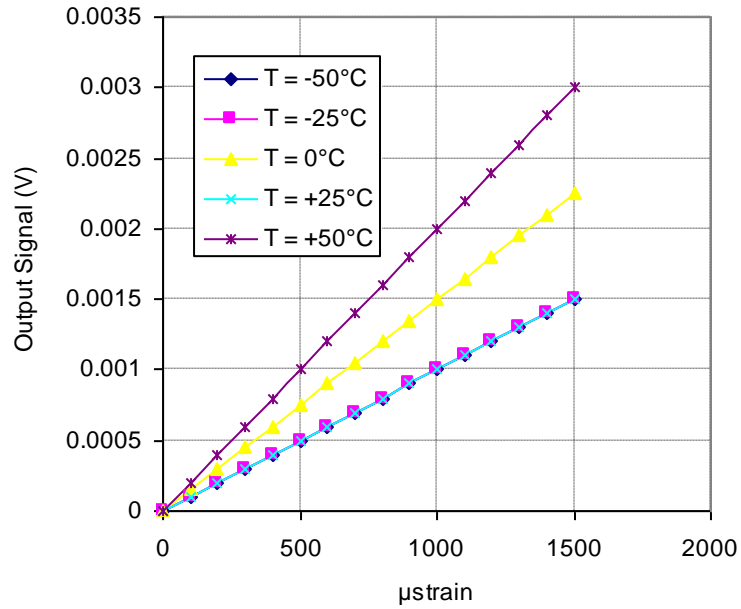
Figure F-50 Simplified calibration curves at different temperatures for doping concentration of 1×10^{20} /cm^3 (Design 5)

Table F-5 Sensitivity values at different temperatures and doping concentrations (Design 5)

Temperature (^{o}C)	Sensing Sensitivity (V/µε)				
	1×10^{18} (atoms/cm^3)	5×10^{18} (atoms/cm^3)	1×10^{19} (atoms/cm^3)	5×10^{19} (atoms/cm^3)	1×10^{20} (atoms/cm^3)
-50	5.00E-05	7.00E-05	4.00E-05	5.00E-05	1.00E-06
-25	3.00E-05	2.50E-05	1.00E-05	4.00E-05	1.00E-06
0	1.00E-05	9.00E-06	3.00E-05	5.00E-05	1.50E-06
25	9.50E-06	1.00E-05	1.00E-05	6.00E-05	1.00E-06
50	8.00E-06	9.10E-06	7.80E-06	4.00E-06	2.00E-06

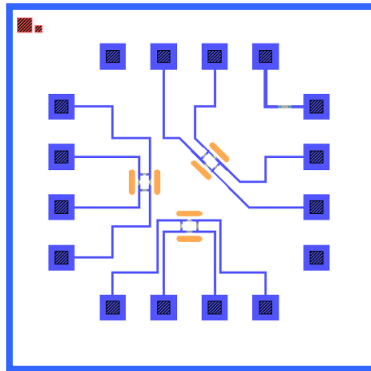**F6. Experimental Data of Layout Design 6**
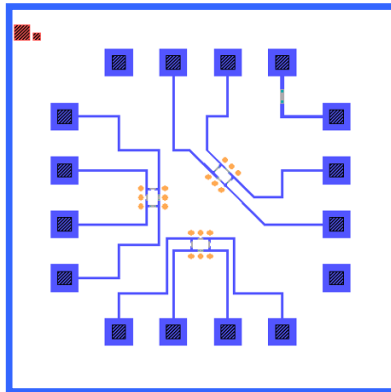
**Figure F-51 Layout (Design 6), as shown on the microfabrication masks**
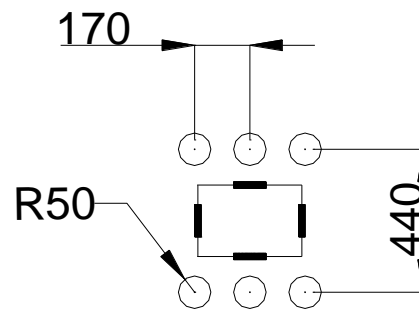
Figure F-52 Schematic of the sensing unit (Design 6), all dimensions are in μm and depth of all the surface trenches is 100 μm
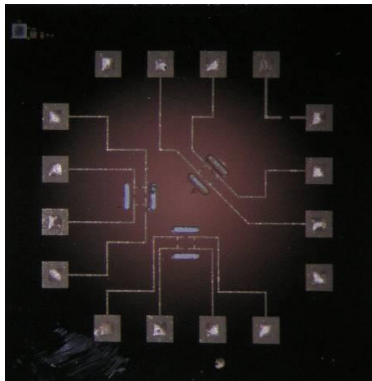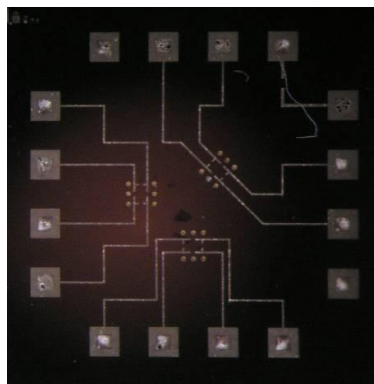

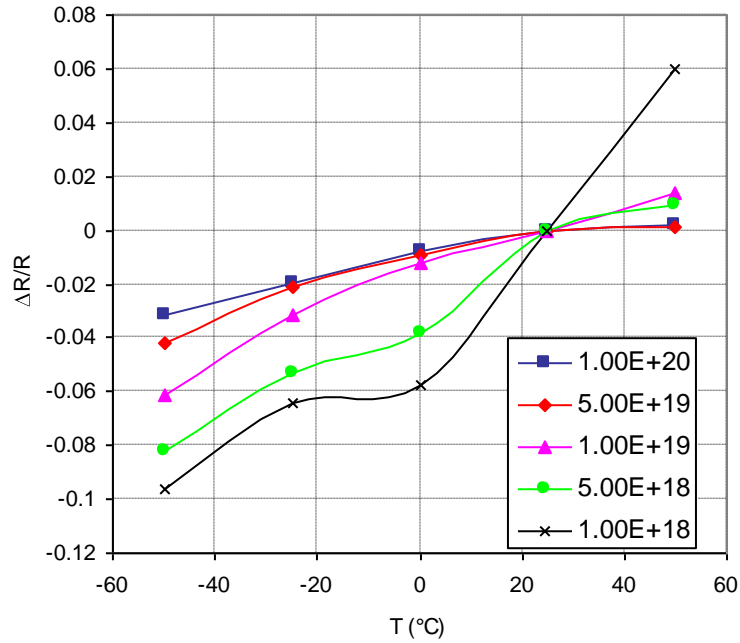
Figure F-53 Fabricated Sensing chip (Design 6) after dicing
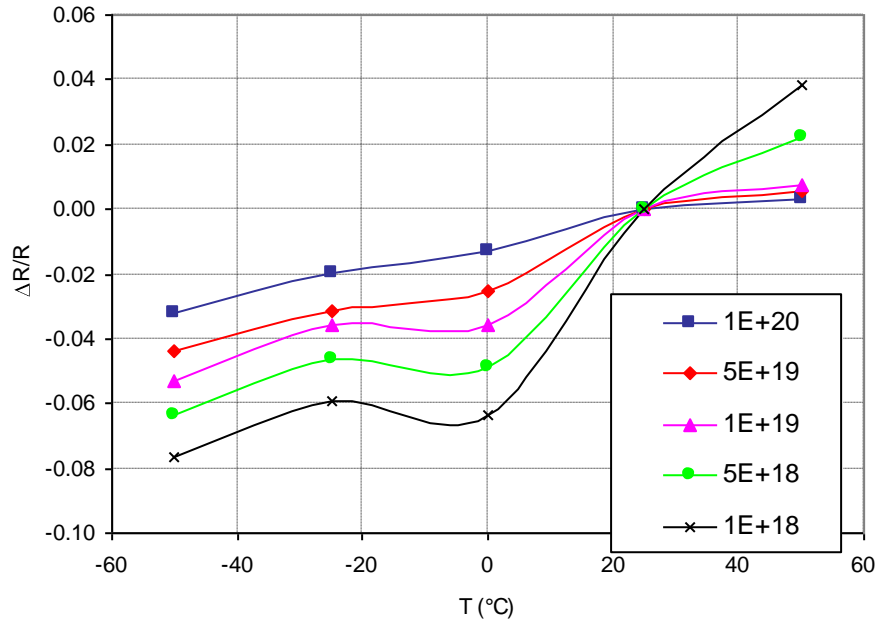
Figure F-54 Normalized resistance change at stress free condition for different doping concentrations, slope of these curves = TCR (Design 1)

$$TCR = -0.0002 Ln(N) + 0.0083$$
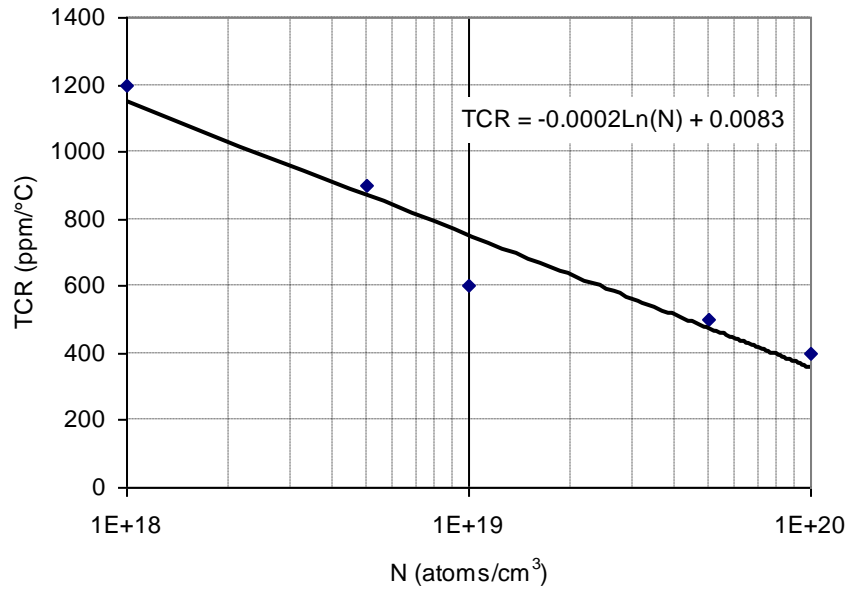
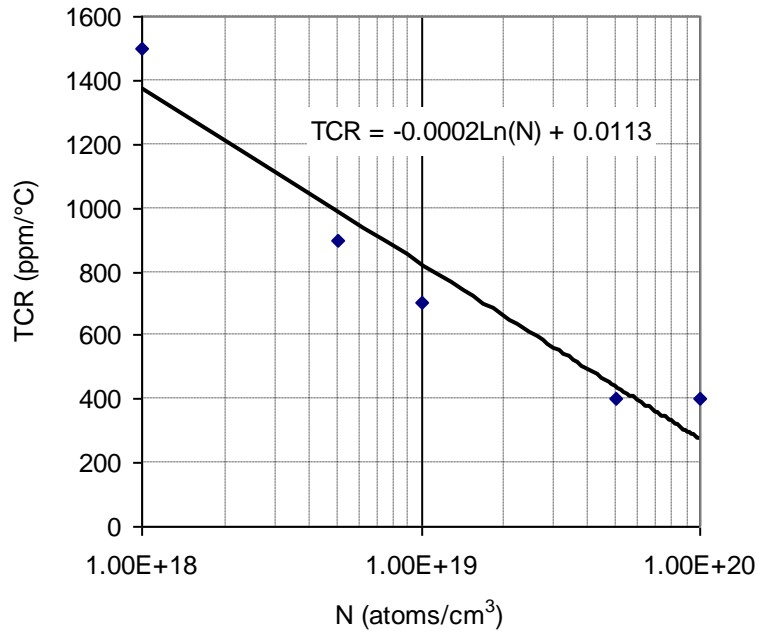**Figure F-55 Temperature coefficient of resistance (TCR) at different doping concentrations to evaluate the sensor TCR, (Design 1)**
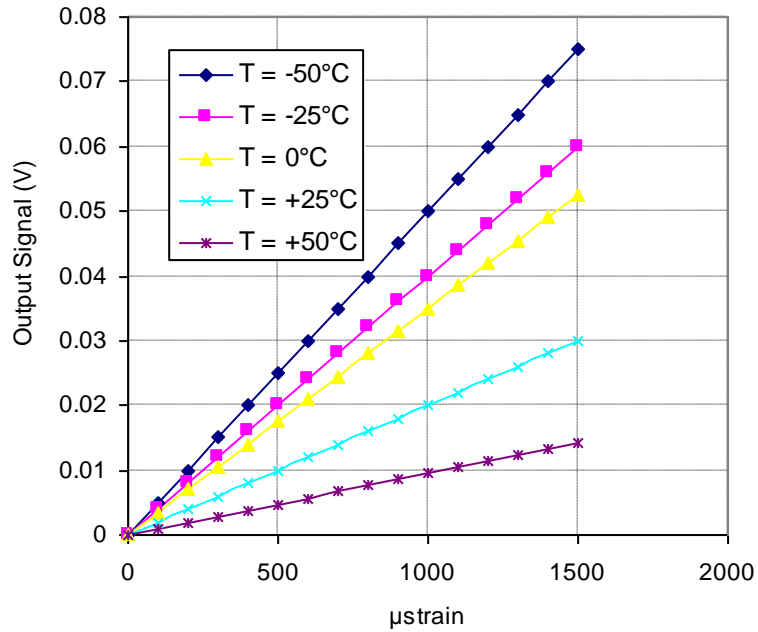
Figure F-56 Simplified calibration curves at different temperatures for doping concentration of 1×10^{18} /cm^3 (Design 1)
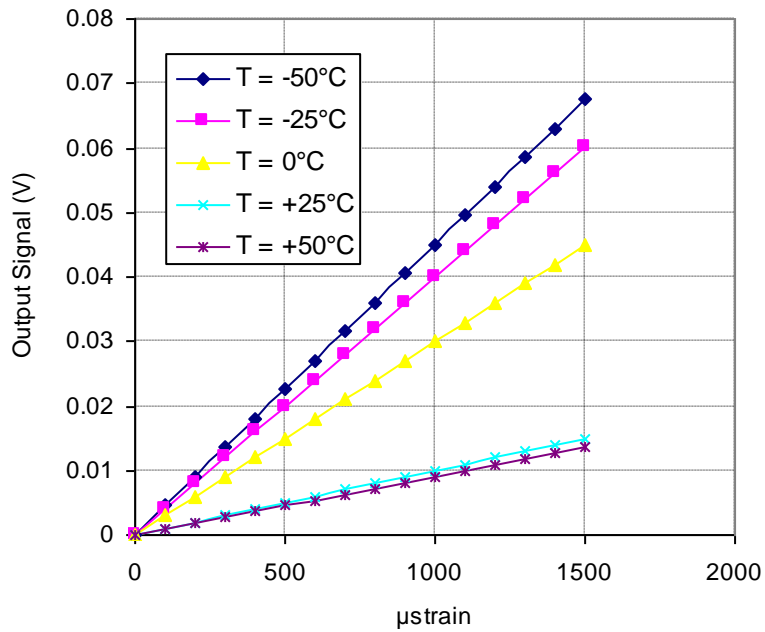
Figure F-57 Simplified calibration curves at different temperatures for doping concentration of 5×10^{18} /cm^3 (Design 1)

217
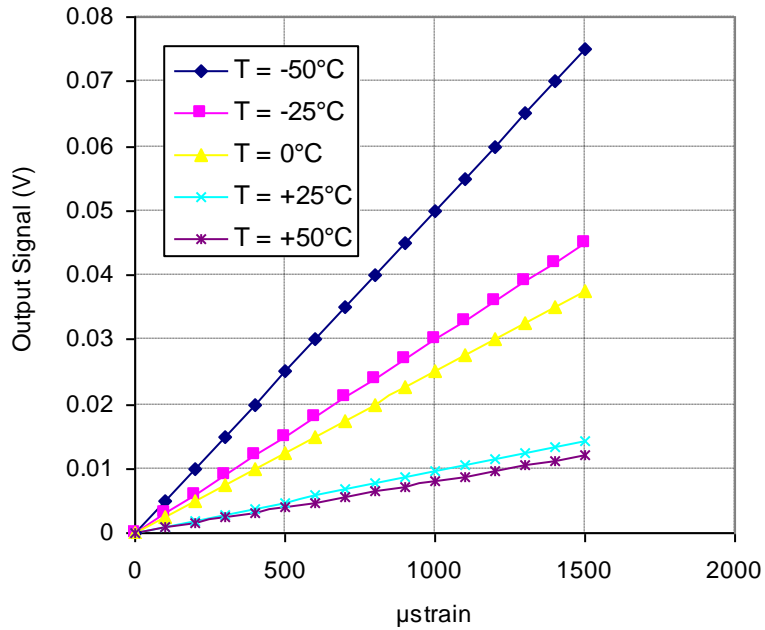
Figure F-58 Simplified calibration curves at different temperatures for doping concentration of 1×10^{19} /cm^3 (Design 1)
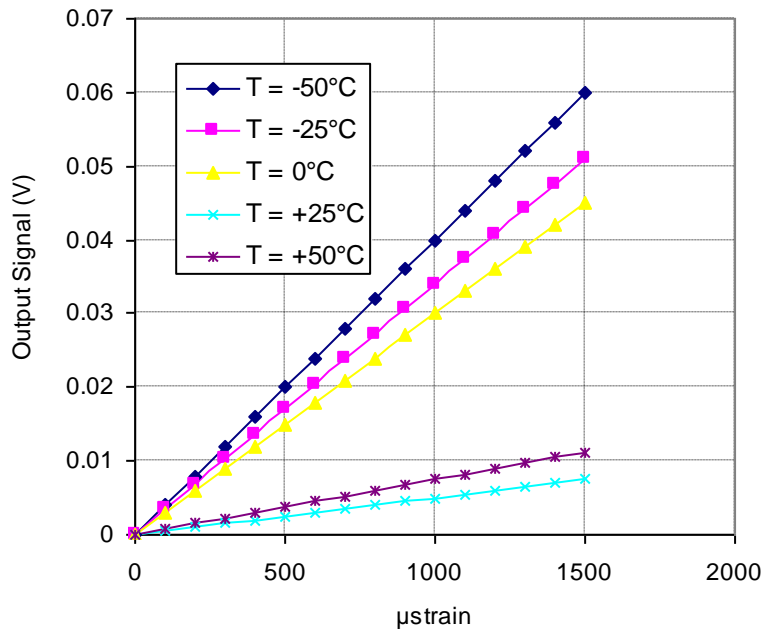
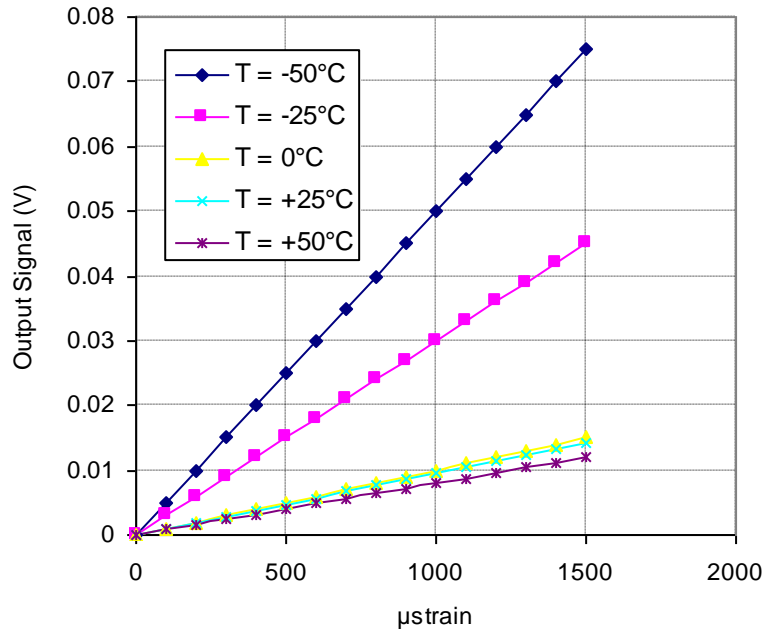**Figure F-59 Simplified calibration curves at different temperatures for doping concentration of 5×10^{19} /cm^3 (Design 1)**
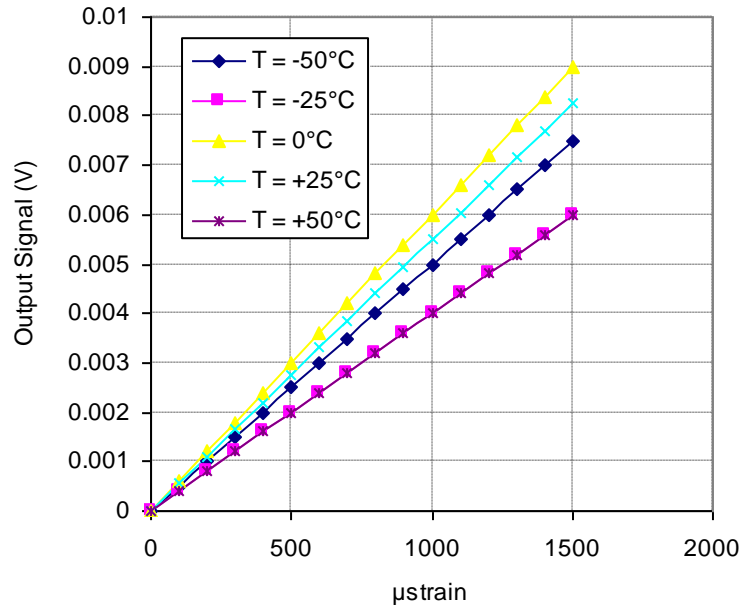
Figure F-60 Simplified calibration curves at different temperatures for doping concentration of 1×10^{20} /cm^3 (Design 1)
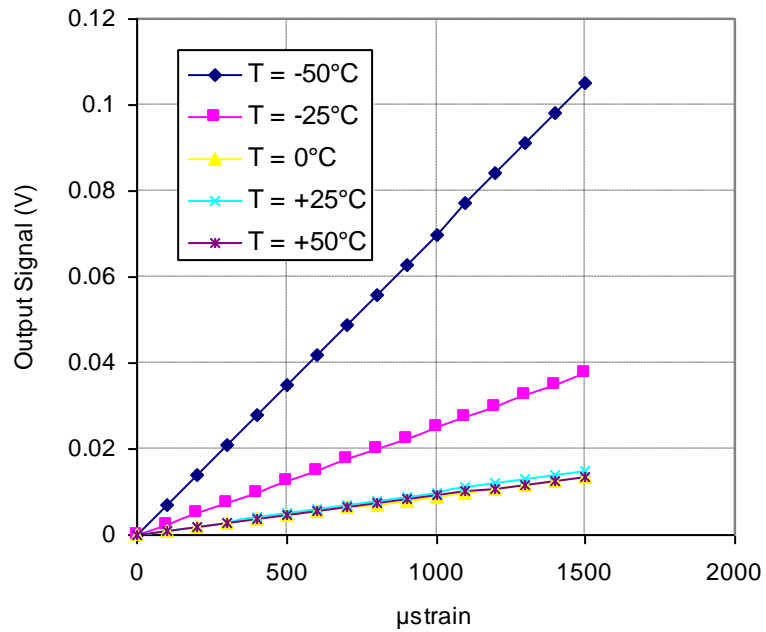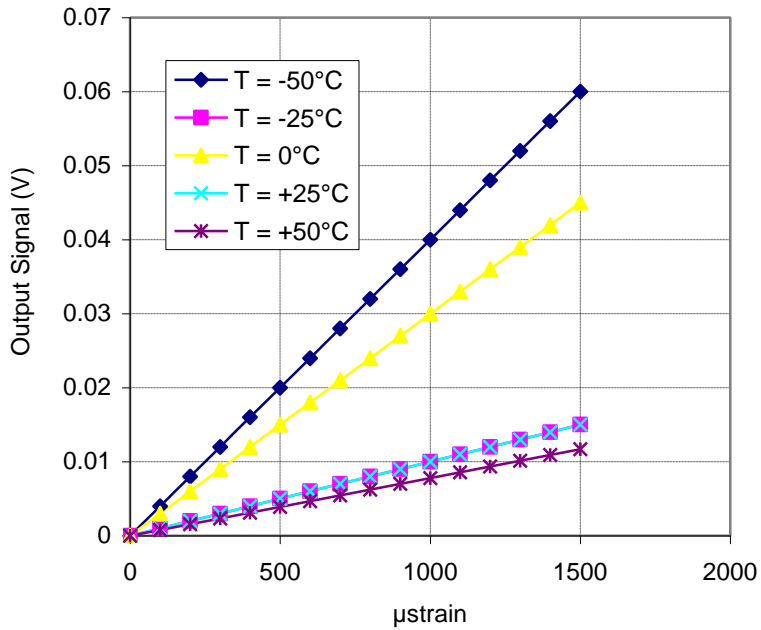
Table F-6 Sensitivity values at different temperatures and doping concentrations (Design 6)

Temperature (^{o}C)	Sensing Sensitivity (V/µε)				
	1×10^{18} (atoms/cm^3)	5×10^{18} (atoms/cm^3)	1×10^{19} (atoms/cm^3)	5×10^{19} (atoms/cm^3)	1×10^{20} (atoms/cm^3)
-50	5.00E-05	4.50E-05	5.00E-05	4.00E-05	5.00E-06
-25	4.00E-05	4.00E-05	3.00E-05	3.40E-05	4.00E-06
0	3.50E-05	3.00E-05	2.50E-05	3.00E-05	6.00E-06
25	2.00E-05	1.00E-05	9.58E-06	5.00E-06	5.50E-06
50	9.50E-06	9.00E-06	8.00E-06	7.50E-06	4.00E-06

Appendix G - Journal Publications

This research project has resulted in four journal publications [28-31]:

1. A. A. S. Mohammed, W. A. Moussa, and E. Lou, "High Sensitivity MEMS Strain Sensor: Design and Simulation," *Journal of Sensors*, vol. 8, pp. 2642-2661, 2008.
2. A. A. S. Mohammed, W. A. Moussa, and E. Lou, "Optimization of Geometric Characteristics to Improve Sensing Performance of MEMS Piezoresistive Strain Sensors," *Journal of Micromechanics and Microengineering*, vol. 20, pp. 015015, 2010.
3. A. A. S. Mohammed, W. A. Moussa, and E. Lou, "High-Performance Piezoresistive MEMS Strain Sensor with Low Thermal Sensitivity," *Journal of Sensors*, vol. 11, pp. 1819-1846, 2011.
4. A. A. S. Mohammed, W. A. Moussa, and E. Lou, "Development and Experimental Evaluation of a Novel Piezoresistive MEMS Strain Sensor," *Journal of Sensors IEEE*, vol. 11, pp. 2220 - 2232, 2011.

List of References

[1]   B. F. Spencer, "Smart Sensing Technology: Opportunities and Challenges," *Structural Control Health Monitoring*, vol. 11, pp. 349-368, 2004.

[2]   D.-D. Ho, K.-D. Nguyen, P.-Y. Lee, D.-S. Hong, S.-Y. Leea, J.-T. Kim, S.-W. Shin, C.-B. Yun, and M. Shinozuka, "Wireless structural health monitoring of cable-stayed bridge using Imote2-platformed smart sensors," presented at Sensors and Smart Structures Technologies for Civil, Mechanical, and Aerospace Systems, 2012.

[3]   H. Jo, J. Park, B. F. S. Jr., and H.-J. Jung, "Design and validation of high-precision wireless strain sensors for structural health monitoring of steel structures," presented at Sensors and Smart Structures Technologies for Civil, Mechanical, and Aerospace Systems, 2012.

[4]   K.-D. Nguyen, P.-Y. Lee, and J.-T. Kim, "Smart PZT-interface for SHM in tendon-anchorage of cable-stayed bridge," presented at Sensors and Smart Structures Technologies for Civil, Mechanical, and Aerospace Systems, 2012.

[5]   A. Gunasekaran, S. Cross, N. Patel, and S. Sedigh, "Recent Enhancements to and Applications of the SmartBrick Structural Health Monitoring Platform," presented at Sensors and Smart Structures Technologies for Civil, Mechanical, and Aerospace Systems, 2012.

[6]   J. Li, T. Nagayama, K. A. Mechitov, and B. F. S. Jr., "Efficient campaign-type structural health monitoring using wireless smart sensors," presented at Sensors and Smart Structures Technologies for Civil, Mechanical, and Aerospace Systems, 2012.

[7]   X. Ning, H. Murayama, K. Kageyama, K. Uzawa, and D. Wada, "Measurement of longitudinal strain and estimation of peel stress in adhesive-bonded single-lap joint of CFRP adherend using embedded FBG sensor," presented at Sensors and Smart Structures Technologies for Civil, Mechanical, and Aerospace Systems, 2012.

[8]   D. k. singh and Mrs.A.Prabha, "Industrial Machine Monitoring using MEMS Technology," presented at 2012 International Conference on Computing, Electronics and Electrical Technologies [ICCEET], 2012.

[9]   C. Jacob, "Capacitive strain sensors for measurement of large strain for structural health monitoring," in *Electrical Engineering*. Arlington: University of Texas at Arlington, 2010, pp. 71.

[10]   X. Yi, R. Vyas, C. Cho, C.-H. Fang, J. Cooper, Y. Wang, R. T. Leon, and M. M. Tentzeris, "Thermal effects on a passive wireless antenna sensor for strain and crack sensing," presented at Sensors and Smart Structures Technologies for Civil, Mechanical, and Aerospace Systems, 2012.

[11]   H. Saboonchi and D. Ozevin, "Numerical Simulation of Novel MEMS Strain Sensor for Structural Health Monitoring," presented at 20th Analysis and Computation Specialty Conference - 2012 ASCE, 2012.

[12]   H. Saboonchi and D. Ozevin, "Numerical Demonstration of MEMS Strain Sensor," presented at Sensors and Smart Structures Technologies for Civil, Mechanical, and Aerospace Systems, 2012.

[13]   H. Sohn, "Laser Based Structural Health Monitoring for Civil, Mechanical and Aerospace Systems," presented at Sensors and Smart Structures Technologies for Civil, Mechanical, and Aerospace Systems, 2012.

[14]   I. F. Akyildiz, W. Su, Y. Sankarasubramaniam, and E. Cayirci, "Wireless sensor networks: a survey," *Computer Networks*, vol. 38, pp. 393-422, 2002.

[15]   H. Tsuda and J. Lee, "Strain and Damage Monitoring of CFRP in Impact Loading using a Fiber Bragg Grating Sensor System," *Composites Science and Technology*, vol. 67, pp. 1353-1361, 2007.

[16]   O. Frazão, L. Marques, J. Marques, J. Baptista, and J. Santos, "Simple Sensing Head Geometry using Fiber Bragg Gratings for Strain-Temperature Discrimination," *Optics Communications*, vol. 279, pp. 68-71, 2007.

[17]   X. Li, C. Zhao, J. Lin, and S. Yuan, "The Internal Strain of Three-Dimensional Braided Composites with Co-Braided FBG Sensors," *Optics and Lasers in Engineering*, vol. 45, pp. 819-826, 2007.

[18]   R. S. Munoz, "Structural health monitoring using embedded fiber optic strain sensors," in *Civil Engineering*. Maine: University of Maine, 2008, pp. 161.

[19]   A. Ivanov, "Multi-parameter fiber optic sensors for structural health monitoring," in *Electrical and Computer Engineering*. Ottawa: Carleton University, 2008, pp. 129.

[20]   W. Ko, D. Young, J. Guo, M. Suster, H. Kuo, and N. Chaimanonart, "A High-Performance MEMS Capacitive Strain Sensing System," *Sensors and Actuators A: Physical*, vol. 133, pp. 272-277, 2007.

[21]   J. Lin, K. Walsh, D. Jackson, J. Aebersold, M. Crain, J. Naber, and W. Hnat, "Development of Capacitive Pure Bending Strain Sensor for Wireless Spinal Fusion Monitoring," *Sensors and Actuators A: Physical*, vol. 138, pp. 276-287, 2007.

[22]   N. Hu, H. Fukunaga, S. Matsumoto, B. Yan, and X. Peng, "An Efficient Approach for Identifying Impact Force Using Embedded Piezoelectric Sensors," *International Journal of Impact Engineering*, vol. 34, pp. 1258-1271, 2007.

[23]   K. Wojciechowski, B. Boser, and A. Pisano, "A MEMS Resonant Strain Sensor Operated in Air," presented at The 17th Annual International Conference on Micro Electro Mechanical Systems (IEEE-MEMS), 2004.

[24]   A. Mohammed and W. Moussa, "Design and Simulation of Electrostatically Driven Microresonator Using Piezoresistive Elements for Strain Measurements," presented at IEEE Transactions, 2005.

[25]   M. Fallah-Rad, "Investigation of embedded sensors and microstrip patch antennas for structural health monitoring," in *Electrical Engineering*. Winnipeg: University of Manitoba, 2008, pp. 197.

[26]   A. Mohammed, W. Moussa, and E. Lou, "Mechanical Strain Measurements Using Semiconductor Piezoresistive Material," presented at The 4th IEEE International Conference on MEMS, Nano and Smart Systems, and The 6th IEEE International Workshop on System-on-Chip for Real-Time Applications, 2006.

[27]   A. Mohammed, W. Moussa, and E. Lou, "A Novel MEMS Strain Sensor for Structural Health Monitoring Applications under Harsh Environmental

Conditions," presented at The 6th International Workshop on Structural Health Monitoring, Stanford, CA, USA., 2007.

[28]   A. A. S. Mohammed, W. A. Moussa, and E. Lou, "High Sensitivity MEMS Strain Sensor: Design and Simulation," *Journal of Sensors*, vol. 8, pp. 2642-2661, 2008.

[29]   A. A. S. Mohammed, W. A. Moussa, and E. Lou, "Optimization of Geometric Characteristics to Improve Sensing Performance of MEMS Piezoresistive Strain Sensors," *Jouranl of Micromechanics and Microengineering*, vol. 20, pp. 015015, 2010.

[30]   A. A. S. Mohammed, W. A. Moussa, and E. Lou, "High-Performance Piezoresistive MEMS Strain Sensor with Low Thermal Sensitivity," *Journal of Sensors*, vol. 11, pp. 1819-1846, 2011.

[31]   A. A. S. Mohammed, W. A. Moussa, and E. Lou, "Development and Experimental Evaluation of a Novel Piezoresistive MEMS Strain Sensor," *Journal of Sensors IEEE*, vol. 11, pp. 2220 - 2232, 2011.

[32]   D. A. Bittle, "Piezoresistive Stress Sensors for Integrated Circuits." Auburn, AL: M.Sc. Thesis, Auburn University, 1990.

[33]   D. A. Bittle, J. C. Suhling, R. E. Beatty, R. C. Jaeger, and R. W. Johnson, "Piezoresistive Stress Sensors for Structural Analysis of Electronic Packaging," *Electronic Packaging*, vol. 113, pp. 203-215, 1991.

[34]   R. C. Jaeger and J. C. Suhling, "Thermally Induced Errors in the Calibration and Application of Silicon Piezoresistive Stress Sensors," *Advances in Electronic Packaging*, vol. 4, pp. 457-470, 1993.

[35]   R. C. Jaeger, J. C. Suhling, T. M. Carey, and R. W. Johnson, "Off-Axis Sensor Rosettes for Measurement of the Piezoresistive Coefficients of Silicon," presented at IEEE Transactions on Components, Hybrids and Manufacturing Technology, 1993.

[36]   R. C. Jaeger, J. C. Suhling, and R. Ramani, "Errors Associated with the Design, Calibration and Application of Piezoresistive Stress Sensors in (100) Silicon," presented at IEEE Transactions on Components, Packaging, and Manufacturing Technology Part B: Advanced Packaging, 1994.

[37]   R. C. Jaeger, J. C. Suhling, and A. A. Anderson, "A (100) Silicon Stress Test Chip with Optimized Piezoresistive Sensor Rosettes," presented at Proceedings - Electronic Components and Technology Conference, 1994.

[38]   Y. Kang, "Piezoresistive Stress Sensors for Advanced Semiconductor Materials." Auburn, AL: Ph.D. Dissertation, Auburn University, 1997.

[39]   M. Suster, J. Guo, N. Chaimanonart, W. Ko, and D. Young, "A Wireless Strain Sensing Microsystem with External RF Power Source and Two-Channel Data Telemetry Capability," presented at Solid-State Circuits Conference, 2007.

[40]   J. Fraden, *Handbook of modern sensors : physics, designs, and applications*, 2nd ed ed. New York: AIP Press: Springer, 1996.

[41]   J. Brugger, M. Despont, C. Rossel, H. Rothuizen, P. Vettiger, and M. Willemin, "Microfabricated Ultrasensitive Piezoresistive Cantilevers for Torque Magnetometry," *Sensors and Actuators A: Physical*, vol. 73, pp. 235-242, 1999.

[42]   D. R. Edwards, K. G. Heinen, S. Groothuis, and J. Martinez, "Shear Stress Evaluation of Plastic Packages," *IEEE Transactions on Components, Hybrids, and Manufacturing Technology*, vol. 10, pp. 618-627, 1987.

[43]   S. A. Gee, V. R. Akylas, and W. F. v. d. Bogert, "The Design and Calibration of a Semiconductor Strain Gauge Array," presented at Proceedings of the 1988 IEEE International Conference on Microelectronic Test Structures (ICMTS), 1988.

[44]   S. A. Gee, W. F. v. d. Bogert, and V. R. Akylas, "Strain-Gauge Mapping of Die Surface Stresses," presented at IEEE Transactions on Component, Hybrids and Manufacturing Technology, 1989.

[45]   B. Jaroszewicz, K. Domanski, D. Tomaszewski, P. Janus, A. Kudla, B. Latecki, A. Kociubinski, M. Nikodem, J. Katcki, M. Wzorek, J. Marczewski, and P. Grabiec, "Application of Ion Implantation for Mono-Si Piezoresistors Manufacturing in Silicon MEMS Technology," *Vacuum*, vol. 78, pp. 263-267, 2005.

[46]   R. Jumpertz, A. Hart, O. Ohlsson, F. Saurenbach, and J. Schelten, "Piezoresistive sensors on AFM cantilevers with atomic resolution," *Microelectronic Engineering*, vol. 41-42, pp. 441-444, 1998.

[47]   S. Majcherek, T. Leneke, and S. Hirsch, "A silicon test chip for the thermomechanical analysis of MEMS packagings," *MicroNanoReliability 2007*, vol. 15, pp. 191-200, 2009.

[48]   W. P. Mason and R. N. Thurston, "Use of Piezoresistive Materials in the Measurement of Displacement, Force and Torque," *Acoustical Society*, vol. 29, pp. 1096-1957, 1957.

[49]   A. A. S. Mohammed, W. A. Moussa, and E. Lou, "Mechanical Strain Measurements Using Semiconductor Piezoresistive Material," presented at 2006 International Conference on MEMS, NANO and Smart Systems, ICMENS, 2006.

[50]   M. Nagy, C. Apanius, and J. Siekkinen, "A User Friendly, High-Sensitivity Strain Gauge," *J. Sensors*, vol. 18, pp. 20-27, 2001.

[51]   W. G. Pfann and R. N. Thurston, "Semiconducting Stress Transducers Utilizing the Transverse and Shear Piezoresistance Effects," *Journal of Applied Physics*, vol. 32, pp. 2008-2019, 1961.

[52]   L. J. Spencer, L. James, W. F. Schroen, G. A. Bednarz, J. A. Bryan, T. D. Metzgar, R. D. Cleveland, and R. D. Edwards, "New Quantitative Measurements of IC Stress Introduced by Plastic Packages," *19th Annual Reliability Physics Symposium*, pp. 74-80, 1981.

[53]   Y. Su, A. G. R. Evans, A. Brunnschweiler, G. Ensell, and M. Koch, "Fabrication of improved piezoresistive silicon cantilevers probes for the atomic force microscope," *Sensors and Actuators A: Physical*, vol. 60, pp. 163-167, 1997.

[54]   J. C. Suhling, M. T. Carey, R. W. Johnson, and R. C. Jaeger, "Stress measurement in microelectronic packages subjected to high temperatures," presented at Manufacturing Processes and Materials Challenges in Microelectronic Packaging, 1991.

[55]   R. N. Thurston, "Use of Semiconductor Transducers in Measuring Strains, Accelerations, and Displacements," *Physical Acoustics*, vol. 1, pp. 215-235, 1964.

[56]   T. Toriyama and S. Sugiyama, "Analysis of Piezoresistance in p-Type Silicon for Mechanical Sensors," *Microelectromechanical Systems*, vol. 11, pp. 598-604, 2002.

[57]   R. E. Beatty, R. C. Jaeger, J. C. Suhling, R. W. Johnson, and R. D. Butler, "Evaluation of Piezoresistive Coefficient Variation in Silicon Stress Sensors using a 4PB Test Fixture," presented at IEEE Transactions on Component, Hybrids and Manufacturing Technology, 1992.

[58]   R. E. Beaty, J. C. Suhling, C. A. Moody, D. A. Bittle, R. W. Johnson, R. D. Butler, and R. C. Jaeger, "Calibration Considerations for Piezoresistive-Based Stress Sensors," *Proceedings of 40th Electronic Components and Technology Conference*, vol. 1, pp. 797-806, 1990.

[59]   C. H. Cho, R. C. Jaeger, and J. C. Suhling, "Characterization of the Temperature Dependence of the Piezoresistive Coefficients of Silicon from -150°C to +125°C," *IEEE Sensors*, vol. 8, pp. 1455-1468, 2008.

[60]   Y. Kanda, "Piezoresistance Effect of Silicon," *Sensors and Actuators: A Physical*, vol. 28, pp. 83-91, 1991.

[61]   Y. Kanda, "A Graphical Representation of the Piezoresistance Coefficients in Silicon," *IEEE Transactions Electronic Devices*, vol. ED-29, pp. 64-70, 1982.

[62]   E. Lund and T. Finstad, "Measurement of the Temperature Dependency of the Piezoresistance Coefficients in p-type Silicon," *Advances in Electronic Packaging*, vol. 26, pp. 215-218, 1999.

[63]   F. J. Morin, T. H. Geballe, and C. Herring, "Temperature Dependence of the Piezoresistance of High-Purity Silicon and Germanium," *Physical Review*, vol. 10, pp. 525-539, 1956.

[64]   O. Slattery, D. O'Mahoney, E. Sheehan, and F. Waldron, "Sources of Variation in Piezoresistive Stress Sensor Measurements," *IEEE Transactions on Components and Packaging Technologies*, vol. 27, pp. 81-86, 2004.

[65]   O. N. Tufte and E. L. Stelzer, "Piezoresistive Properties of Silicon Diffused Layers," *Journal of Applied Physics*, vol. 34, pp. 3322-3327, 1963.

[66]   O. N. Tufte and E. L. Stelzer, "Piezoresistive Properties of Heavily Doped n-Type Silicon," *Physical Review*, vol. 133, pp. A1705-A1716, 1964.

[67]   C.-F. Chu, "Piezoresistive Properties of Boron and Phosphorous Implanted Layers in Silicon," in *Electrical Engineering and Applied Physics*: Case Western Reserve University, 1978, pp. 221.

[68]   J. C. Greenwood, "Instrument Science and Technology: Silicon in Mechanical Sensors," *J. Phys. E: Sci. Instrum.*, vol. 21, pp. 1114-1128, 1988.

[69]   K. Matsuda, "Nonlinear Piezoresistance Effects in Silicon," *Journal of Applied Physics*, vol. 73, pp. 1838-1847, 1993.

[70]   A. Boukabache and P. Pons, "Doping Effects on Thermal Behaviour of Silicon Resistor," *Electronics Letters*, vol. 38, pp. 342-343, 2002.

[71]   C. S. Smith, "Piezoresistance effect in germanium and silicon," *Physical Review*, vol. 94, pp. 42-49, 1954.

[72]   M. J. Sundaresan, P. F. Pai, A. Ghoshal, M. J. Schulz, F. Ferguson, and J. H. Chung, "Methods of distributed sensing for health monitoring of composite material structures," *Composites Part A: Applied Science and Manufacturing*, vol. 32, pp. 1357-1374, 2001.

[73]   J. A. Guemes and J. M. Menendez, "Response of Bragg grating fiber-optic sensors when embedded in composite laminates," *Compos Sci Technol*, vol. 62, pp. 959-966, 2002.

[74]   S. Takeda, Y. Okabe, T. Yamamoto, and N. Takeda, "Detection of edge delamination in CFRP laminates under cyclic loading using small-diameter FBG sensors," *Compos Sci Technol*, vol. 63, pp. 1885-1894, 2003.

[75]   D. C. Seo and J. J. Lee, "Effect of embedded optical fiber sensors on transverse crack spacing of smart composite structures," *Composite Structures*, vol. 32, pp. 51-58, 1995.

[76]   A. Todoroki and Y. Tanaka, "Delamination identification of cross-ply graphite/epoxy composite beams using electric resistance change method," *Compos Sci Technol*, vol. 62, pp. 629-639, 2002.

[77]   A. Todoroki, Y. Tanaka, and Y. Shimamura, "Delamination monitoring of graphite/epoxy laminated composite plate of electric resistance change method," *Compos Sci Technol*, vol. 62, pp. 1151-1160, 2002.

[78]   D. C. Seo and J. J. Lee, "Damage detection of CFRP laminates using electrical resistance measurement and neural network," *Composite Structures*, vol. 47, pp. 525-530, 1999.

[79]   W. S. N. Trimmer, "Microrobots and micromechanical systems," *Sensors and Actuators*, vol. 19, pp. 267-287, 1989.

[80]   C. Herring and E. Vogt, "Transport and Deformation-Potential Theory for Many-Valley Semiconductors with Anisotropic Scattering," *Physics Review*, vol. 101, pp. 944-961, 1956.

[81]   C. Herring, "Transport Properties of Multi-valley Semiconductor," *Bell System Technical Journal*, vol. 34, pp. 237, 1955.

[82]   C. S. Smith, "Macroscopic Symmetry and Properties of Crystals," *Solid State Physics*, vol. 6, pp. 175-249, 1958.

[83]   "An Overview of Silicon Micromachining and Related Applications," *Special Issue of IEEE Proceedings*, vol. 86, 1998.

[84]   P. F. Indermuhle, G. Schurmann, G. A. Racine, and N. F. d. Rooij, "Fabrication and Characterization of Cantilevers with Integrated Sharp Tips and Piezoelectric Elements for Actuation and Detection for Parallel AFM Applications," *Sensors and Actuators A: Physical*, vol. 60, pp. 186-190, 1997.

[85]   W. L. Price, "Extension of van der Pauw's Theorem for Measuring Specific Resistivity in Discs of Arbitrary Shape to Anisotropic Media," *Journal of Physics D: Applied Physics*, vol. 5, pp. 1127-1132, 1971.

[86]   E. N. Adams, "Elastoresistance in p-type Ge and Si," *Physical Review*, vol. 96, pp. 803-804, 1954.

[87]   W. D. Callister, *Materials Science and Engineering: An Introduction*. USA: John Wiley & Sons, 1985.

[88]   P. W. Bridgman, "The effect of homogeneous mechanical stress on the electrical resistance of crystals," *Physical Review*, vol. 42, pp. 858-863, 1932.

[89]   W. Paul and G. L. Pearson, "Pressure Dependence of the Resistivity of Silicon," *Physical Review*, vol. 98, pp. 1755-1757, 1955.

[90]   J. H. Taylor, "Pressure Dependence of Resistance of Germanium," *Physical Review*, vol. 80, pp. 919-920, 1950.

[91]   J. Richter and O. Hansen, "Piezoresistance of Silicon and Strained $Si_{0.9}$ $Ge_{0.1}$," *Elsevier Preprint*, pp. 1-18, 2004.

[92]   K. Yamada, M. Nishihara, S. Shimada, M. Tanabe, M. Shimazoe, and Y. Matsouka, "Nonlinearity of the Piezoresistance Effect of P-Type Silicon Diffused Layers," *IEEE Transactions on Electron Devices*, vol. 29, pp. 71-77, 1982.

[93]   J. T. Lenkkeri, "Nonlinear effects in the Piezoresistivity of p-Type Silicon," *Physical State Solids*, vol. 136, pp. 373-385, 1986.

[94]   Z. Gniazdowski and P. Kowalski, "Practical Approach to Extraction of Piezoresistance of Piezoresistance Coefficient," *Sensors and Actuators:A*, vol. 68, pp. 329-332, 1998.

[95]   S. Kozlovskiy and I. Boiko, "First-order Piezoresistance Coefficients in Silicon Crystals," *Sensors and Actuators: A Physical*, vol. 118, pp. 33-43, 2006.

[96]   B. P. Pisciotta and C. Gross, "The effects of incomplete annealing on the temperature dependence of sheet resistance and gage factor in aluminum and phosphorus implanted silicon on sapphire," *Solid-State Electronics*, vol. 19, pp. 135-143, 1976.

[97]   H. Blanchard, C. d. R. lseli, and R. S. Popovic, "Compensation of the Temperature-Dependent Offset Drift of a Hall Sensor," *Sensors and Actuators: A*, vol. 60, pp. 10-13, 1997.

[98]   G. Blasquez, P. Pons, and A. Boukabache, "Capabilities and Limits of Silicon Pressure Sensors," *Sensors and Actuators*, vol. 17, pp. 387-403, 1989.

[99]   J. Dzmban, A. Gbrecka-Drzazga, U. Llpowicz, W. Indyka, and J. Wqsowslu, "Self-Compensating Piezoresistive Pressure Sensor," *Sensors and Actuators: A*, vol. 41-42, pp. 368-374, 1994.

[100]   J. Gakkestad and H. Jakorsen, "A Front End CMOS Circuit for a Full-bridge Piezoresistive Pressure Sensor," *Sensors and Actuators: A*, vol. 25-27, pp. 859-863, 1991.

[101]   J. Gakkestad, P. Ohlckers, and L. Halbo, "Compensation of Sensitivity Shift in Piezoresistive Pressure Sensors using Linear Voltage Excitation," *Sensors and Actuators: A*, vol. 49, pp. 11-15, 1995.

[102]   J. Gakkestad, P. Ohlckers, and L. Halbo, "Effects of Process Variations in a CMOS Circuit for Temperature Compensation of Piezoresistive Pressure Sensors," *Sensors and Actuators: A*, vol. 48, pp. 63-71, 1995.

[103]   O. J. Gregory and Q. Luo, "A Self-Compensated Ceramic Strain Gage for Use at Elevated Temperatures," *Sensors and Actuators: A*, vol. 88, pp. 234-240, 2001.

[104]   G. Kowalski, "Miniature Pressure Sensors and Their Temperature Compensation," *Sensors and Actuators*, vol. 11, pp. 367-376, 1987.

[105]   B.-N. Lee, K.-N. Kim, H.-D. Park, and S.-M. Shin, "Calibration and temperature compensation of silicon pressure sensors using ion-implanted trimming resistors," *Sensors and Actuators: A*, vol. A72, pp. 148-152, 1999.

[106]   H. Muro, H. Kaneko, S. Klyota, and P. J. French, "Stress Analysis of SiO,/Si Bi-Metal Effect in Silicon Accelerometers and its Compensation," *Sensors and Actuators: A*, vol. 34, pp. 43-49, 1992.

[107]   R. P. Son, J. K. Atkmson, and J. D. Turner, "A Novel Model for the Temperature Characteristic of a Thick-Film Piezoresistive Sensor," *Sensors and Actuators: A*, vol. 41-42, pp. 460-464, 1994.

[108]   Y. TakashimaL, T. Adachi, T. Yoshino, and T. Yamada, "A Temperature Compensation Method for Piezoresistive Sensors," *JSAE Review*, vol. 18, pp. 301-322, 1997.

[109]   Q. Wang, J. Ding, and W. Wang, "Fabrication and Temperature Coefficient Compensation Technology of Low Cost High Temperature Pressure Sensor," *Sensors and Actuators: A*, vol. 120, pp. 468-473, 2005.

[110]   K. Suzuki, H. Hasegawa, and Y. Kanda, "Origin of the Linear and Nonlinear Piezoresistance Effects in P-Type Silicon," *Japan Journal of Applied Physics*, vol. 23, pp. L871-L874, 1984.

[111]   B. Kloeck and N. F. d. Rooij, "Mechanical Sensors," in *Semiconductor Sensors*, S. M. Sze, Ed.: John Wiley & Sons, 1994, pp. 153-199.

[112]   G. T. A. Kovacs, "Micromachined Transducers: Sourcebook." New York: McGraw-Hill, 1998, pp. 911.

[113] "http://en.wikipedia.org/wiki/File:Indices_miller_plan_exemple_cube.png," Last Access: March 13th, 2013 at 5:00 PM.

[114] G. L. Bir and G. E. Pikus, *Symmetry and Strain - Induced Effects in Semiconductors*. New York: Wiley, 1974.

[115] W. P. Mason, *Piezoelectric Crystals and Their Application to Ultrasonic*. Princeton: D. Van Nostrand, 1956.

[116] A. K. M. Mian, "Application of the Van der Pauw Structure as a Piezoresistive Stress Sensor." Auburn, AL: Ph.D. Dissertation, Auburn University, 2000.

[117] L. J. v. d. Pauw, "Determination of Resistivity Tensor and Hall Tensor of Anisotropic Shape," 1961.

[118] L. E. Hollander, G. L. Vick, and T. Diesel, "The Piezoresistive Effect and its Applications," *The Review of Scientific Instruments*, vol. 31, pp. 323-327, 1960.

[119] S. Sze, *Semiconductor Sensors*. New York: John Wiley and Sons, 1994.

[120] L. L. Howell, *Compliant Mechanisms*. USA: John Wiley and Sons, 2002.

[121] J. W. Gardner, *Microsensors: Principles and Applications*. USA: John Wiley and Sons, 1994.

[122] P. French, "Polysilicon: a Versatile Material for Microsystems," *Sensors and Actuators A:*, vol. 99, pp. 3-12, 2002.

[123] P. Ciureanu and S. Middelhoeck, *Thin Film Resistive Sensors*. New York: Institute of Physics Publishing, 1992.

[124] C. A. Brebbia, *Finite Element Systems: A Handbook*, 3[ed] ed. U.K.: Springer-Verlag, 1985.

[125] T. R. Chandrupatla and A. D. Belegundu, *Introduction to Finite Elements in Engineering*. Toronto: Prentice Hall, 2002.

[126] K. H. Huebner, *The Finite Element Method for Engineers*. USA: John Wiley & Sons, 1975.

[127] O. C. Zienkiewicz, *The Finite Element Method*, 3rd ed. UK: McGraw-Hill Book Company Ltd, 1978.

[128] M. H. Bao, "Micro Mechanical Transducers: Pressure Sensors, Accelerometers and Gyroscopes," *Amsterdam : New York : Elsevier*, vol. 8, pp. ch.5, 2000.

[129] K. Peterson, "Silicon as a Mechanical Material," *Proceedings of IEEE*, vol. 5, pp. 420-457, 1982.

[130] R. Hull, *Properties of Crystalline Silicon*. London: Institution of Engineering and Technology, 1999.

[131] W. C. O'Mara, R. B. Herring, and L. P. Hunt, "Handbook of Semiconductor Silicon Technology." Park Ridge: Noyes Publications, 1990.

[132] O. Hansen and A. Boisen, "Noise in Piezoresistive Atomic Force Microscopy," *Nanotechnology*, vol. 10, pp. 51-60, 1999.

[133] J. A. Harley and T. W. Kenny, "*1/f* Noise Consideration for the Design and Process Optimization of Piezoresistive Cantilevers," *Microelectromechanical Systems*, vol. 9, pp. 226-235, 2000.

[134] F. Bordoni, "Noise in Sensors," *Sensors and Actuators*, vol. A21-A23, pp. 17-24, 1990.

[135] X. M. Yu, J. Thaysen, O. Hansen, and A. Boisen, "Optimization of Sensitivity and Noise in Piezoresistive Cantilevers," *J. Applied Physics*, vol. 92, pp. 6296-6301, 2002.

[136] A. A. S. Mohammed, W. A. Moussa, and E. Lou, "High Sensitivity MEMS Strain Sensor: Design and Simulation," *Sensors*, vol. 8, pp. 2642-2661, 2008.

[137] "http://www.vishaypg.com/micro-measurements/ Last Access on."

[138] A. T. Fiory, S. G. Chawda, S. Madishetty, N. M. Ravindra, A. Agarwal, K. K. Bourdelle, J. M. McKinley, H.-J. L. Gossmann, and S. P. McCoy, "Boron and Phosphorus Dopant Diffusion in Crystalline Si by Rapid Thermal Activation," presented at 11th Workshop on Crystalline Silicon Solar Cell Materials and Processes, Estes Park, Colorado, 2001.

[139] J. M. David and M. G. Buehler, "A numerical analysis of various cross sheet resistance resistor test structure," *Solid State Electronics*, vol. 20, pp. 539-543, 1977.

[140] "ASTM E 8/E 8M-08, Standard Test Methods for Tension Testing of Metallic Materials," 2008, American Society for Testing Materials.

[141] O. N. Tufte and E. L. Stelzer, "Piezoresistive Properties of Silicon Diffused Layers," *Journal of Applied Physics*, vol. 34, pp. 313-318, 1963.

[142] Z. Wang, K. Tian, Y. Zhou, L. Pan, C. Hu, and L. Liu, "A high-temperature silicon-on-insulator stress sensor," *Journal of Micromechanics and Microengineering*, vol. 18, pp. 1-11, 2008.

[143] M. Olszacki, C. Maj, M. A. Bahri, J-CMarrot, A. Boukabache, P. Pons, and A. Napieralski, "Experimental Verification of Temperature Coefficients of Resistance for Uniformly Doped P-type Resistors in SOI," *Micromechanics and Microengineering*, vol. 20, pp. 064008, 2010.

[144] Z. W. Zhong, X. Zhang, B. H. Sim, E. H. Wong, P. S. Teo, and M. K. Iyer, "Calibration of a piezoresistive stress sensor in [100] silicon test chips," presented at 4th Electronics Packaging Technology Conference, 2002.

[145] "ASTM E 251-92, Standard Test Methods for Performance Characteristics of Metallic Bonded Resistance Strain Gages," 1992 (R 2003), American Society for Testing Materials.